

ELECTRON IMPACT IONIZATION CROSS SECTIONS FOR CARBON VAPOR

by

KANG-LUNG WANG

B.S., Cheng-Kung University, Taiwan

M.S., Massachusetts Institute of Technology

SUBMITTED IN PARTIAL FULFILLMENT OF THE

REQUIREMENTS FOR THE DEGREE OF

DOCTOR OF PHILOSOPHY

at the

MASSACHUSETTS INSTITUTE OF TECHNOLOGY

August 1970

Signature of Author \_\_\_\_\_

Department of Electrical Engineering, August 24, 1970

Certified by \_\_\_\_\_

Thesis Supervisor

Accepted by \_\_\_\_\_

Chairman, Departmental Committee on Graduate Students

Archives



ELECTRON IMPACT IONIZATION CROSS SECTIONS FOR CARBON VAPOR

by

KANG-LUNG WANG

Submitted to the Department of Electrical Engineering on August 24, 1970 in partial fulfillment of the requirements for the Degree of Doctor of Philosophy.

ABSTRACT

Ionization cross sections for carbon vapor were measured using a chopped molecular beam technique.

Fragmentation of polymer species in the carbon vapor was studied using a time-of-flight technique in the frequency domain. Phase differences were then referred to the highest significant polymer in which fragment ions are negligible. The experiments showed that fragmentation is responsible for less than 10% of the total ion current. The cross sections were then deduced by subtracting the fragment ions. Absolute values were calibrated at an electron energy of 500 eV using the total ion current, the neutral beam intensity, and ion ratios in conjunction with the additivity rule.

Comparison with theoretical calculations showed that the Born and Born-Ochkur approximations yield high values while the classical Cryzinski and Lotz empirical calculations result in values which are too low.

Threshold behavior was investigated with an electron monochromator. The appearance potentials were found to be  $11.3 \pm 0.1$ ,  $12.05 \pm 0.1$ , and  $12.1 \pm 0.1$  V for  $C_1^+$ ,  $C_2^+$ , and  $C_3^+$  respectively.

A Knudsen cell carbon source with water cooling was built to generate the neutral carbon beams. Charged particle traps were carefully designed to prevent ion leakage from the Knudsen cell region into the ionization chamber. The traps reduced the stray ion current to about  $10^{-13}$  amp. An Auger trap reduced the stray electron current to a comparable value.

A simple electron gun was used for electron energies above 35 eV; for low energies an electron monochromator of the cylindrical mirror type provided an energy spread of less than 0.1 eV.

Total ion collection was calculated in terms of acceptance and emittance concepts. It is shown that total collection can be achieved with an extraction voltage of only 15 volts for a neutral beam at a temperature of 2500°K.

The detection efficiency and count loss in the electron multiplier and counter was calibrated by the use of generating functions and compared with experimental results. Most of the loss can be attributed to missed counts at the ion conversion dynode. The detection system was used at over 90% efficiency to avoid possible uncertainties.

Neutral beam intensities were determined by using a highly sensitive film thickness monitor. Attempts to measure ratios of the various effusing neutral species were not successful due to close polymer ion ratios.

THESIS SUPERVISOR: C.K. Crawford

Associate Professor of Electrical Engineering

#### ACKNOWLEDGMENTS

It has been a great pleasure to associate with Professor C. K. Crawford for these years. For not only his generosity and advice during this dissertation research but also his encouragement and guidance throughout the graduate study, I am deeply indebted.

Thanks are also extended to Mrs. Janice O. Morgan for her enthusiasm in polishing the wording and for her patience in typing this manuscript.



TO MY PARENTS

AND MY WIFE

學不可以已

TABLE OF CONTENTS

	Page
List of Illustrations .....	8
List of Symbols .....	13
I. Introduction .....	16
II. Theoretical Treatment of Measurement Methods .....	21
II.1 Time-of-Flight Studies .....	22
II.2 Considerations in Chopper Design .....	31
II.2.1 Overlap Criteria .....	31
II.2.2 Phase Separability .....	32
II.2.3 Transmission .....	33
II.3 Time-of-Flight in the Quadrupole Mass Spectrometer	34
II.4 Neutral Beam Intensity Determination .....	37
III. General Description of the System and Instrumentation	42
III.1 Vacuum System .....	42
III.2 Instrumentation .....	42
III.3 Source Testing Diagram and Nomenclature .....	46
IV. Carbon Vapor Source .....	51
IV.1 Atomic or Molecular Beam intensities .....	51
IV.2 Design of the Source .....	54
IV.2.1 Concentric Radiation Shields .....	56
IV.2.2 Spiral Radiation Shields .....	58
IV.3 Tests of Power Consumption .....	59
IV.3.1 Electrical Characteristics .....	59
IV.3.2 Temperature-Power Relation .....	63

IV.4	Power Controlling .....	65
IV.4.1	Emission Control .....	65
IV.4.2	Constant-Power Power Supply .....	70
IV.5	Charged Particle Traps .....	73
IV.6	Source Tests with the Mass Spectrometer .....	81
IV.6.1	Background Ions in the Source .....	81
IV.6.2	Source Induced Multiplier Noise .....	86
V.	Electron Source and Tests .....	89
V.1	Electron Gun and Collector .....	89
V.2	Electron Beam Control .....	98
V.3	Coaxial Cylinder Mirror Electron Monochromator	100
V.4	Source Requirements and Acceptance-Emittance Matching	121
V.4.1	Emission System .....	121
V.4.2	Acceptance of the Monochromator .....	123
VI.	Ion Extraction Optics .....	128
VI.1	Total Ion Collection and Ion Optics .....	128
VI.2	Emittance and Acceptance of Ion Optics .....	136
VI.3	Potential Penetrations and Draw-Out Voltage Effects	143
VII.	Signal Detection and Associated Instrumentation .....	146
VII.1	Electron Multiplier Construction and Tests .....	146
VII.2	Ion Counter .....	148
VII.3	Atomic Beam Detection .....	156
VII.4	Signal Detection .....	160
VII.4.1	Reference Channel .....	160
VII.4.2	Signal Channel .....	160

VII.5	Signal-to-Background Ratio	161
VIII.	Ionization Cross Sections	165
VIII.1	Fragmentation Experiments	165
VIII.2	Ionization Cross Section Data	167
VIII.3	Threshold Behavior	173
VIII.4	Data Collection and Probable Errors	179
VIII.4.1	Procedures	179
VIII.4.2	Possible Errors and Uncertainties	180
VIII.5	Theoretical Approximation and Estimation	181
VIII.6	Empirical Formulation	191
VIII.7	Comparison and Discussion	192
IX	Summary and Future Improvement	193
Appendix 1	Calibration Experiments Using Copper	195
Appendix 2	Retarding Potential Method	199
Appendix 3	Influence of a Circular Aperture	204
Appendix 4	Knudsen Cell II Control	205
Appendix 5	Constant-Power Power Supply	208
Appendix 6	Neutral Beam Intensity Ratios	210
Appendix 7	Instruments and Power Supplies	212
References		214
Biographical Note		223

LIST OF ILLUSTRATIONS

Figure

- 1 Catenation patterns of carbon due to different kinds of sources.
- 2 The waveform of the chopper function  $s(t)$ .
- 3 Normalized Detection function for an impulse function.
- 4 Phase angle for the Fourier transform for normalized detection function.
- 5 Block diagram of a phase sensitive detector.
- 6 Waveforms of the corresponding points in Fig. 5.
- 7 Chopper for study of fragmentation.
- 8 Energy distribution of the ion source and the quadrupole mass spectrometer
- 9 Phase difference including time-of-flight in the mass spectrometer
- 10 (a) Block diagram of the vacuum system and signal processing.  
(b) Photograph of the sources  
(c) Photograph of the neutral beam source
- 11 (a) Wiring circuits for source testing.  
(b) Wiring circuitry for monoenergetic electron source.
- 12 Neutral beam source assembly
- 13 Construction of spiral radiation shields
- 14 Schematic wiring diagram for source testing
- 15 Diode emission characteristics
- 16 Difference of characteristics for slow and fast tracing
- 17 Emission from the filament and shields as functions of the Knudsen cell power

- 18 Required Power vs Temperature
- 19 Wiring diagram of electron bombardment source
- 20  $\text{Log} (i_{ks} P_{kc}^{-2/5})$  vs  $P_{KC}^{-1/5}$  plot
- 21 Diagram of constant power operation
- 22 Characteristics of constant-power and its operation with a Knudsen cell
- 23 Ion current partially retarded by ion trap voltage
- 24 Declining current characteristics for  $V_{IC} = 0$  and  $V_{IC} = 80$  V
- 25 Plot of collected ion current vs  $\frac{1}{T}$ .
- 26 Performance of ion trap with Auger trap inoperative
- 27 Characteristics of the Auger trap
- 28  $\text{Na}^+$  as a function of  $\frac{1}{T}$
- 29 Potential diagram of Na and  $\text{Na}^+$  on a tantalum surface
- 30 Electron gun assembly
- 31 Electron Collector Assembly
- 32 Lens properties of electron gun
- 33 (a) Retarding potential study of the electron gun  
(b) Secondary electron from the collector
- 34 Current from the electron collector shield
- 35 Schematic diagram for electron gun tests
- 36 Electron beam profile with half high contour
- 37 (a) Profile for a clean surface  
(b) Profile for a contaminated surface
- 38  $i_1$  and  $i_2$  with respect to total emission current
- 39 Schematic diagram of electron beam controller

- 40 Characteristics of the electron beam controller
- 41 Electron monochromator assembly
- 42 Overall view of the monochromator
- 43 View of the inner cylinder disassembled
- 44 Close-up of the electron gun
- 45 Electron gun partially disassembled
- 46 Assembly details of the electron gun
- 47 Close-up of the injection lens
- 48 View of the dismantled injection lens
- 49 Assembly for monochromator tests
- 50 (a) Wiring diagram for tests of the monochromator  
(b) Part of the wiring diagram with auto-differentiation using a modulation technique
- 51 Mirror voltage with respect to the beam energy
- 52 Beam profiles from the monochromator
- 53 Half width of the energy spread from the monochromator
- 54 Retarding potential results of the electron beam from the monochromator
- 55 Half width of the electron beam measured with the RPD method
- 56 (a) Acceptance of the cylindrical monochromator in the  $\alpha$ -direction  
(b) Acceptance of the cylindrical monochromator in the  $\rho$  plane
- 57 Layout of the electron gun
- 58 Construction of the ionizer
- 59 (a) Total ion collector current with respect to the extracting voltage for the Pb atomic beam



- 59 (b) Total ion collector current with respect to extracting  
voltage for background gases
- 60 Current collected as a function of  $V_{ID}$  with the electron gun  
off
- 61 Properties of the ion injection lens
- 62 Effect of the ion energies on the mass spectrometer sensitivity
- 63 Transmission of ion optical system with respect to ion energy
- 64 Relation of the spectrometer output and the electron beam  
current
- 65 Configuration of the entire ion optical system
- 66 Acceptance area of the total ion collector current at  $Q_1$ -plane
- 67 z-axis emittance of the ion sources
- 68 Acceptance of the ion injection system,
- 69 Threshold behavior of Ar at different  $V_{ID}$
- 70 Electron multiplier using EMI Venetian dynode
- 71 Gain of the electron multiplier vs the overall voltage
- 72 Detection efficiency of the counter
- 73 Secondary electron yield of BeCu by  $Cu^+$  ions
- 74 Counting efficiency shown as a function of multiplier voltage
- 75 Circuit for lamp-phototransistor pair
- 76 Signal output displaced with a waveform eductor
- 77 (a) Background spectra when the chopper is moved to interrupt  
the beam
- (b) Atomic beam spectra by the chopped beam technique
- 78 Phase differences due to T-O-F with respect to  $V_{EE}$

- 79 Ionization cross section for  $C_1^+$
  - 80 Ionization cross section for  $C_2^+$
  - 81 Ionization cross section for  $C_3^+$
  - 82 Ionization cross section for  $C_1^{++}$
  - 83 Cross section ratios for various molecules to atoms
  - 84 Threshold cross section for  $C_1^+$
  - 85 Threshold cross section for  $C_2^+$
  - 86 Threshold cross section for  $C_3^+$
  - 87 Threshold cross section for  $C_1^{++}$
  - 88 Calculated cross sections using the Cryzinski approximation
  - 89 Calculated cross sections using Born and Born-Ochkur approximations
- 
- A.1 (a) Spectrometer output when cooling
  - (b) Spectrometer output when heating at constant power
  - (c) Spectrometer output showing the melting point
  - A.2 Schematic diagram of a conventional RPD technique
  - A.3 Revised form of a RPD method
  - A.4 Convolution of two circles
  - A.5 Block diagram of Knudsen cell II control
  - A.6 Circuitry of the Knudsen cell control
  - A.7 Block diagram of the constant-power power supply
  - A.8 General characteristics of the constant-power power supply

LIST OF SYMBOLS

Symbol	Definition
$A_s$	Area of the neutral beam source aperture
B	Brightness
$D_n$	$n^{\text{th}}$ dynode of the electron
$E_d$	Activation energy
$F_{\text{ol}}^+$	Fundamental frequency component of the Fourier transform of ion current pulses
$\bar{G}$	Average gain of the electron multiplier
$G_k(s)$	Generating function for k stages
$I_1^+$	Ion current due to the singly charged species $C_1^+$
$I_b$	Total ion collector current due to backgrounds
$M_o$	$1.6605 \times 10^{-27}$ kg
N	Atomic mass number
$P_1$	Pressure near the source
$P_2$	Pressure near the pump
$P_{\text{KC}}$	Knudsen cell power
$P_k(n)$	Probability of generating n electrons at the $k^{\text{th}}$ stage when the first stage is under the impact of a single electron
$R_o$	Resolution
$T_{\text{KC}}$	Knudsen cell temperature
$U_o$	Initial ion energy in the ionizer
$U_k$	Ionization potential for the $k^{\text{th}}$ shell

$a_o$	radius of a hydrogen atom ( $5.2905 \times 10^{-9}$ cm)
b	length of confining aperture for neutral beam (4.1mm)
c	overlap factor of individual T-O-F pulse
e	electron charge ( $1.6021 \times 10^{-19}$ coulomb)
f	chopper revolution per second
$f_n$	chopper frequency
h	Planck constant ( $6.6257 \times 10^{-34}$ joule-sec)
$i_{KC}$	Knudsen cell bombardment current
k	Boltzmann constant ( $1.3806 \times 10^{-23}$ joule/K°)
$\ell$	width of the confining aperture for neutral beam (1.91 mm)
$\ell_e$	effective length of T-O-F from the ionizer to the electron multiplier
$\ell_{ID}$	path of flight in the ionizer
$\ell_{IE}$	path of flight in the injection electrode
$\ell_{IF}$	path of flight in the ion focusing electrode
$m_\alpha$	mass of $C_\alpha$
$n_\alpha$	neutral beam intensity of $C_\alpha$
$q_K$	number of electrons in the $k^{th}$ shell
$s(t)$	shutter function of the chopper
$t^*$	$\frac{t}{\beta z}$
$t_{ID}$	time-of-flight through the path $\ell_{ID}$
$t_{IE}$	time-of-flight through the path $\ell_{IE}$
$t_{IF}$	time-of-flight through the path $\ell_{IF}$
$\Delta t$	half width of Maxwellian distribution pulses
$\Delta t^*$	$\frac{\Delta t}{\beta z}$

$\bar{v}_b$	average velocity of the neutral beam
$z$	path of the time-of-flight for neutral particles
$\alpha$	secondary electron yield under ion impact
$\beta$	$\sqrt{\frac{m_\alpha}{2kT}}$
$\gamma$	secondary electron yield under electron impact
$\eta_\alpha$	detection sensitivity for the species $C_\alpha \stackrel{\Delta}{=} i\lambda\sigma_\alpha^+ A\phi_0$
$\theta$	angle subtending the transmitting portion
$\theta_{21}$	phase difference for $C_2^+$ and $C_1^+$
$\theta_{31}$	phase difference for $C_3^+$ and $C_1^+$
$v_0$	threshold
$\xi$	ratio of charge to unit atomic mass ( $e/M_0$ )
$\sigma_\alpha^{n+}$	$n^{\text{th}}$ order ionization cross section for a neutral species $C_\alpha$
$\tau_c$	closing time of the shutter function
$\tau_c^*$	$\frac{\tau_c}{\beta z}$
$\tau_0$	period of the shutter function
$\tau_0^*$	$\frac{\tau_0}{\beta z}$
$\phi$	neutral beam flux intensity (particles/cm <sup>2</sup> -sec)
$\psi$	work function
$\omega$	angular velocity ( $2\pi f$ )
$\omega^*$	$\beta z \omega$
$\Gamma$	transmission of the shutter function $s(t)$

## I. INTRODUCTION

The study of electron impact ionization cross section is of interest in plasma physics, mass spectrometer calibration, and high temperature chemistry. Recently, work on atomic carbon has been increased drastically because of its application in vehicle re-entry physics.

Since Tate and Smith<sup>1</sup> began their pioneer work, there has been a vast amount of literature in this field. Several good reviews have appeared for the experimental work<sup>2-9</sup>. In particular, McDaniel<sup>10</sup> presented an excellent description of the experimental work up to 1963. Recently, a critical review including the evaluation of the absolute cross sections of atoms and diatomic molecules was given by Kieffer and Dunn<sup>11</sup>. A large amount of theoretical work in this field has also been accomplished<sup>3,12,13</sup>. A quite complete bibliography of the low energy cross sections has been compiled by Kieffer<sup>14</sup>.

Prior to this work however, only incomplete relative measurements have been made for carbon. Studies of absolute values had not even been attempted. Although several approximate calculations have been made<sup>15,16,94,95,101</sup>, accuracy of these calculations cannot be assured since discrepancies amounting to 50% are common between these calculations and measurements for other elements.

The evaporation of carbon to produce a neutral atomic beam of high intensity, necessary for the study of its ionization cross sections, requires a detailed understanding of the high temperature properties

of carbon. Several investigators have studied vapor pressure and other thermochemical quantities (particularly in the early fifties). However, the results reported from various groups have been so divergent that none can be considered reliable.<sup>17-22</sup> Comparison of graphite evaporation by Knudsen's and Langmuir's methods for example, yields a two order of magnitude discrepancy in vapor pressure.<sup>19,20</sup> This discrepancy might be explained by the difference in the evaporation coefficient used by different workers. Brewer<sup>22</sup> (Langmuir source) used an evaporation coefficient of 0.3 while Thorn and Winslow<sup>23</sup> (Knudsen source) suggested that the evaporation coefficient might be as low as 0.15 for monomers. Thermodynamical calculations<sup>24</sup> based on the molecular orbital theory predict that the evaporation coefficients will decrease rapidly for increasing molecular size, and vary for different crystallographic surfaces. In more recent investigations different coefficients for  $C_1$ ,  $C_2$ , and  $C_3$  from different crystallographic surfaces have actually been confirmed.<sup>25,26</sup> Although quantitative disagreement still exists, it can be concluded that the departure from unity is considerable; the results of the Knudsen cell method are not reliable when a large effusion orifice is used. The evaporation of carbon appears to be a complicated process.

Mass spectrometric and optical emission spectra studies have revealed that the composition of carbon vapor consists of a variety of molecular species.<sup>27-32</sup> In the carbon vapor generated by a Knudsen cell, Chupka and Ingram have found  $C_1^+$ ,  $C_2^+$ ,  $C_3^+$ ,  $C_4^+$ , and  $C_5^+$  in the proportions of 1 to 0.5 to 6 to 0.02 to 0.10 (at 2127°C.). Their ratio

of effusion hole area to the total cell area was about 1 to 1500. The respective abundances of molecular species were then computed assuming relative ionization cross sections of 1, 2, 3, 4, and 5 respectively. The lack of accurate cross section data, however, prevented a precise determination of the vapor pressure. In a later study<sup>29</sup>  $C_3^+$  appeared as the dominant species at an electron energy of 17 eV as previously observed by Chupka and Ingram. At a temperature of 2127°C, the relative intensities were measured as 1 to 0.25 to 4.25 to  $1.25 \times 10^{-3}$  to  $2.5 \times 10^{-3}$ . The appearance potentials were observed as  $11.3 \pm 0.2$ ,  $12.0 \pm 0.6$ , and  $12.6 \pm 0.1$  eV respectively. Subsequent investigations using a similar technique have been reported.<sup>25,33</sup> In the case of Knudsen effusion<sup>33</sup>, the relative abundance and appearance potentials agreed with those previously reported. Recent work by Wachi and Gilmartin (1970)<sup>85</sup> showed that different samples resulted in different ion intensity ratios for polymers. For any one of these samples, the ratios remained almost constant over a certain range of temperature.

Some carbon studies using spark source mass spectrometers have been made.<sup>35-37</sup> Ions as heavy as  $C_{32}^+$  have been observed. However there seems to be a major disagreement among workers on the relative intensities of  $C_2^+$  and  $C_3^+$ . Baun et al observed that  $C_2^+$  is more abundant than  $C_3^+$ , while  $C_2^+$  is dominant in the work of Dornenburg et al.

A laser beam has also been used<sup>38</sup> for high temperature evaporation. The main advantage of laser heating is that higher temperatures can be obtained using low power. Mass spectrometric analysis<sup>39</sup> of the resulting



vapor from carbon shows polymeric ions up to  $C_{14}^+$  but the catenation pattern is different from that obtained with a spark source. The relative intensities of the various peaks, however, do not vary significantly for different graphite samples.

Published catenation patterns for different methods are shown in Fig. 1. The literature is still somewhat sparse.

This literature review suggests that a neutral beam generated by any one of several methods contains not only atomic carbon but also polymer species. The existence of these polymers introduces fragmentation processes and thereby complicates the measurement, because of the fragmented ion contribution to the simple ionization process.

It can also be seen that no absolute ionization cross section measurements have ever been made. Most mass spectrometric studies involved relative intensities of ion species, and then assumed cross section values to determine the vapor pressure of each carbon polymer. (The intent of these studies was to find the relative abundance of polymers.) No results for processes such as double ionization or fragmentation have been reported.

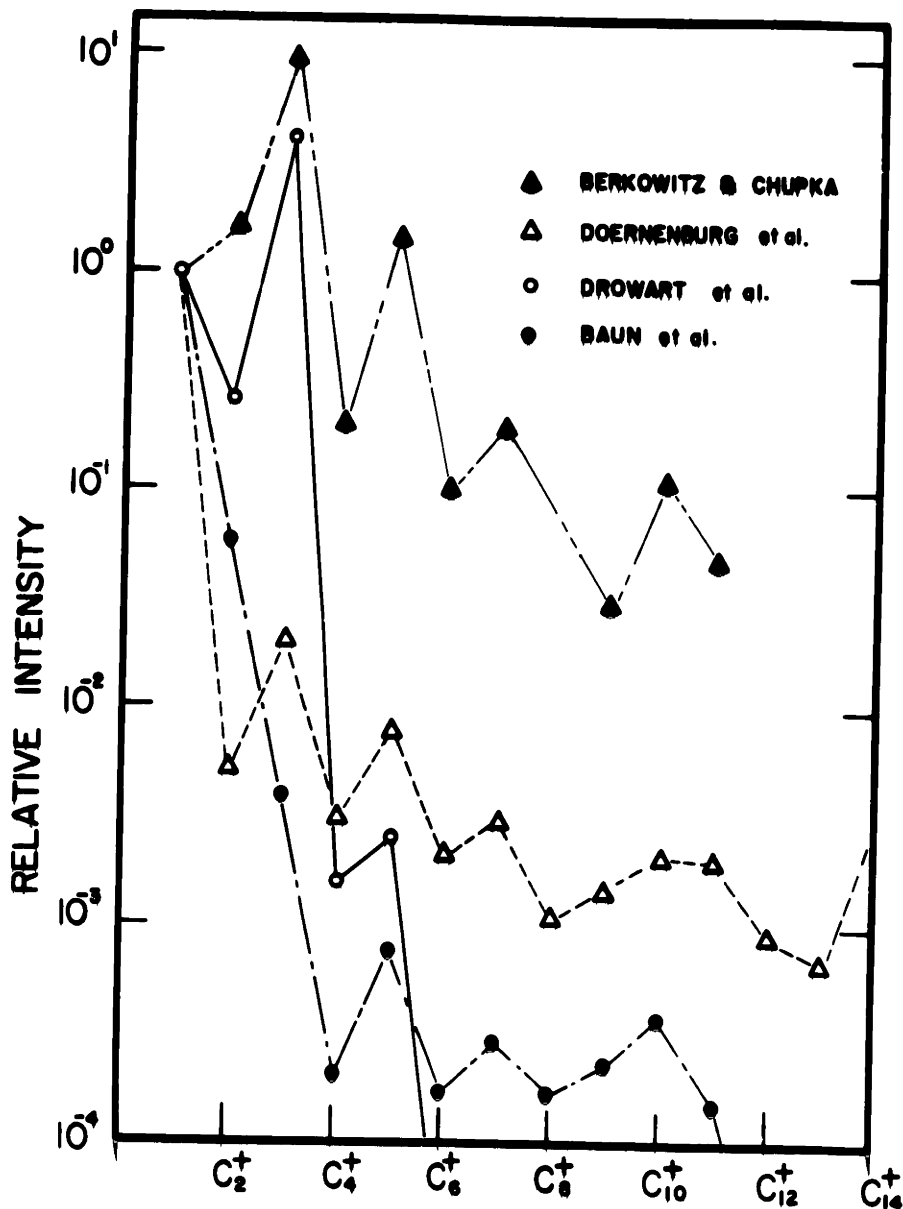


Fig. 1 Catenation patterns of carbon due to different kinds of sources (all results are normalized to 1 at C<sub>1</sub><sup>+</sup>). ▲ indicates the composition of the laser generated beam (Berkowitz, et al<sup>39</sup>); △ shows the beam produced by a spark source (Doerenburg, et al<sup>37</sup>); ○ is from a Knudsen cell source (Drowart, et al<sup>29</sup>); ● indicates the beam generated by a radio frequency spark source (Baun, et al<sup>36</sup>). In first case, C<sub>1</sub>, C<sub>2</sub>, C<sub>3</sub>, and C<sub>5</sub> are dominant; C<sub>1</sub> and C<sub>3</sub> in the second; C<sub>1</sub>, C<sub>2</sub>, and C<sub>3</sub> in the third; and C<sub>1</sub> and C<sub>2</sub> in the last.

## II. THEORETICAL TREATMENT OF MEASUREMENT METHODS

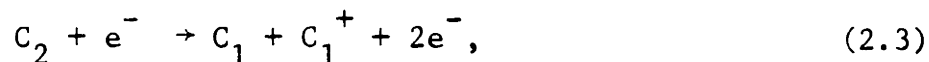
The capability of studying simple ionization processes such as



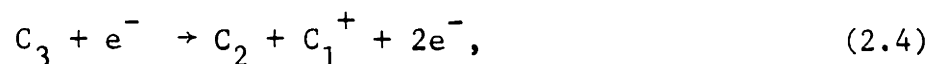
and



relies on the possibility of separating the desired ions from those of other processes. For example, in determining the cross section of process (2.1), the contribution of  $C_1^+$  from other processes such as the fragmentation of higher polymers,



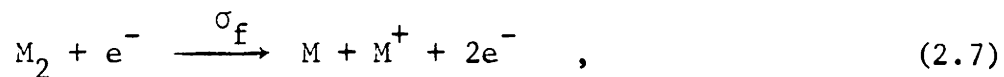
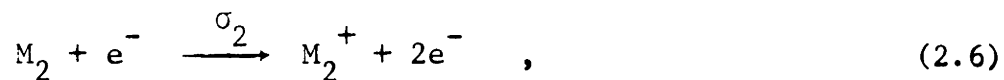
and



should be eliminated. Furthermore, in calculating the absolute ionization cross section, the relative abundances of  $C_1$ ,  $C_2$ , and  $C_3$  (neutral intensities) must be known. Note that polymerization and fragmentation can be considered negligible during transit in the mass spectrometer, since the background pressure and collision cross sections are so low that very few collisions occur.

In order to separate the monoatomic ion contribution from the fragmentation of various higher polymers, several schemes can be used. Kohl et al<sup>40</sup> have studied two species of Bismuth vapor by a proportional

method. Consider the following reactions, where M is any element:



with cross section  $\sigma_1$ ,  $\sigma_2$ , and  $\sigma_f$  respectively. Assuming the ratio of  $\sigma_1$  to  $\sigma_2$  is independent of the impact energy measured relative to the threshold (experimentally observed as approximately true for some simpler elements such as hydrogen) then below the threshold potential of the fragmentation process,  $\sigma_1/\sigma_2$  can be established and extrapolated to higher energies. Then  $\sigma_1$  can be determined and the fragmentation cross section can also be deduced.

Some other studies for Ge,<sup>41</sup> Se,<sup>42</sup> and S,<sup>43</sup> have used theoretical estimates of cross sections in their determination of species ratios, and did not consider fragmentation effects.

### II.1 Time-of-Flight Studies

The confirmation of the Maxwellian velocity distribution of a molecular beam by Ko,<sup>44</sup> and Miller and Kusch<sup>45</sup> has revealed another technique for measuring molecular compositions. The resolution of a composite velocity distribution into those of its polymers by least square fitting has enabled Miller and Kusch,<sup>45</sup> and subsequent workers,<sup>46</sup> to measure the compositions of alkali halide and alkali fluoride vapors. This analysis was based on the validity of the Maxwellian

distribution for each component and the complete surface ionization of alkali salts by a hot tungsten wire. Most of the results show the predominant monomers and dimers. In some cases, the best fit requires some trimers. As higher polymers are encountered, it becomes difficult to make a realistic best fit.

The following method will be used in the study of ionization cross sections having three polymers. A similar technique was used by Boyer et al<sup>47</sup> in studying alkali salts. The central idea of the present method lies in the phase differences resulting from the Fourier transform of Maxwellian distributions of polymer species.

Consider the velocity distribution of molecules effused through an orifice from a Knudsen cell under the conditions of molecular flow. The effused intensity (for  $\alpha$  polymer having mass  $m_\alpha$ ) with the velocity between  $v$  and  $v + dv$  can be expressed as<sup>48</sup>

$$\phi(v)dv = \frac{\phi_\alpha m_\alpha v^3}{2(kT)^2} \exp\left(-\frac{m_\alpha v^2}{2kT}\right) dv, \quad (2.8)$$

where  $\phi_\alpha$  is the molecule flux for the species  $\alpha$  ( $\alpha = 1, 2, 3$ ) and  $T$  is the source temperature. When the ionization chamber is at a distance  $z$  from the chopper, the time-of-flight (TOF) from  $z = 0$  to  $z$  for particles possessing velocity  $v$  is  $t$ . Thus between time  $t$  and  $t + dt$  those particles which reach the region  $z$  must possess a velocity between  $(v - dv)$  and  $v$  at  $z = 0$  (i.e.  $-(v)dv$ ). Changing the variables, Equ. 2.8 becomes

$$-\phi(v)dv = \phi(t)dt$$

$$= \frac{\phi_{\alpha}^m \alpha^2}{2(kT)^2} \frac{z^4}{t^5} \exp\left(-\frac{m_{\alpha}}{2kT} \cdot \frac{z^2}{t}\right) dt, \quad (2.9)$$

or

$$= 2\phi_{\alpha} \beta_{\alpha}^4 \frac{z^4}{t^5} \exp\left(-\frac{\beta_{\alpha}^2 z^2}{t}\right) dt, \quad (2.10)$$

$$\phi(t) = 2\phi_{\alpha} \beta_{\alpha}^4 \frac{z^4}{t^5} \exp\left(-\frac{\beta_{\alpha}^2 z^2}{t}\right), \quad (2.11)$$

where  $\beta_{\alpha}^2 = \frac{m_{\alpha}}{2kT}$ , and therefore  $\beta_{\alpha}^2 = \alpha\beta_1^2$ .

With the shutter function  $s(t)$  shown in Fig. 2, the distribution at  $z$  due to the spike shown in the shaded area can be expressed as

$$\Delta\phi(t) = 2s(\tau) \frac{\phi_{\alpha} \beta_{\alpha}^4 z^4}{(t - \tau)^5} \exp\left[-\left(\frac{\beta_{\alpha} z}{t - \tau}\right)^2\right] \Delta\tau. \quad (2.12)$$

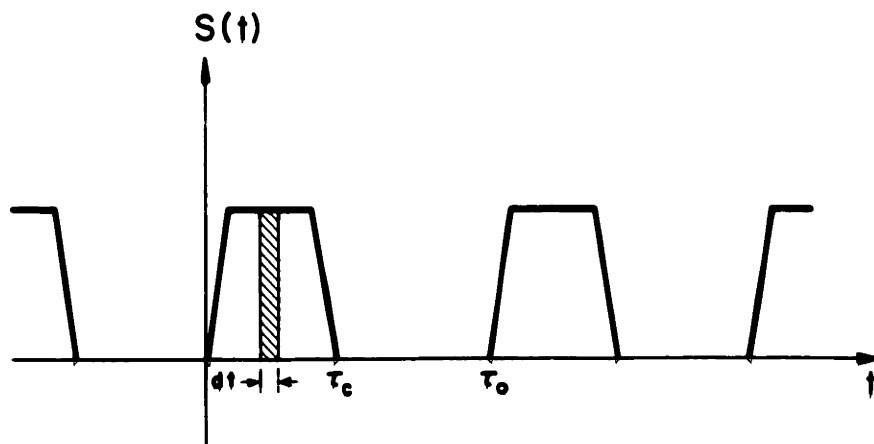


Fig. 2 The waveform of the chopper function  $s(t)$

The superposition of the spikes leads to a Green integral (convolution integral)

$$\phi(t) = \int_{-\infty}^t 2s(\tau) \frac{\phi_{\alpha} \beta_{\alpha}^4 z^4}{(t - \tau)^5} \exp - \left(\frac{\beta_{\alpha} z}{t - \tau}\right)^2 d\tau, \quad (2.13)$$

or

$$\phi(t) = \int_0^{\infty} 2s(t - \tau) \frac{\phi_{\alpha} \beta_{\alpha}^4 z^4}{\tau^5} \exp - \left(\frac{\beta_{\alpha} z}{\tau}\right)^2 d\tau. \quad (2.14)$$

Here the intensity function will be a periodic function, if the shutter is designed to prevent pulses from overlapping.

Since detection is carried out by electron ionization, the ion current for singly charged particles can be described by

$$I_{\alpha}^{+} = n_{\alpha} i \lambda \sigma_{\alpha}^{+} = \frac{\phi(t)}{\bar{v} \phi_{\alpha}} i \lambda \sigma_{\alpha}^{+} = \frac{\phi(t)}{\bar{v} \phi_{\alpha}} \eta_{\alpha} \quad ; \quad (2.15)$$

$$\eta_{\alpha} = \text{detection sensitivity} = i \lambda \sigma_{\alpha}^{+} \phi_{\alpha},$$

where  $n_{\alpha}$ , and  $\sigma_{\alpha}^{+}$  are the density of polymer  $C_{\alpha}$  and the single ionization cross section, respectively;  $i$ , the electron current ionizing the neutral beam;  $\lambda$ , the path of interaction; and  $\eta_{\alpha}$  the detection sensitivity.

Note that in the case of  $n_{\alpha}$  for  $\alpha > 1$ , the cross section may include fragmentation products. Similar to (12) and (13), the ion current for the gate  $s(\tau)\Delta\tau$  may be obtained as,

$$I_{\alpha}^{+}(t) = \int_0^{\infty} 2\eta_{\alpha} s(t - \tau) \frac{\beta_{\alpha}^4 z^3}{\tau^4} \exp - \left(\frac{\beta_{\alpha} z}{\tau}\right)^2 d\tau. \quad (2.16)$$

The detected current for an impulse shutter function follows immediately

$$I_{\alpha}^{+}(t) \Big|_{\delta} = 2\eta_{\alpha} \frac{\beta_{\alpha}^4 z^3}{t^4} \exp - \left(\frac{\beta_{\alpha} z}{t}\right)^2. \quad (2.17)$$

Setting  $t^* = \frac{t}{\beta_{\alpha} z}$  , (2.18)

where  $t^*$  is dimensionless time, we have

$$I_{\alpha}^{+}(t^*) = 2\eta_{\alpha} \frac{(t^*)^{-4}}{z} \exp - \left(\frac{1}{t^*}\right)^2 . \quad (2.19)$$

Define a normalized function,

$$N(t^*) \triangleq \frac{I_{\alpha}^{+} z}{2\eta} = \left(\frac{1}{t^*}\right)^4 \exp - \left(\frac{1}{t^*}\right)^2 , \quad (2.20)$$

which is plotted in Fig. 3.

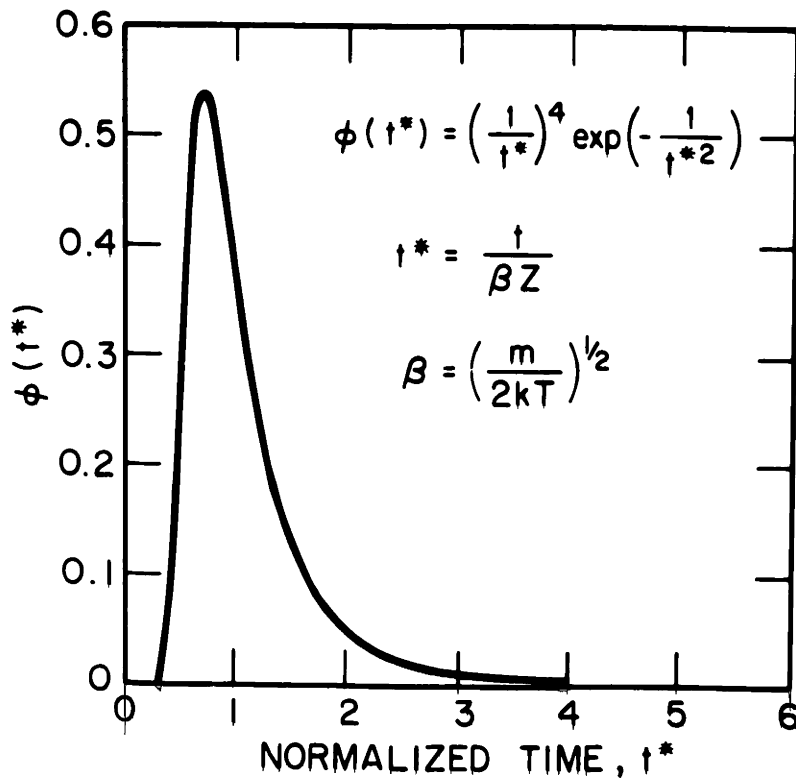


Fig. 3 Normalized detection function for an impulse shutter function



The most probable time is

$$t_{mp} = \sqrt{2\beta_{\alpha}z} \quad , \quad (2.21)$$

while the half width can be calculated as

$$\Delta t = 0.645 \beta_{\alpha}z \text{ or} \quad (2.22a)$$

$$\Delta t^* = 0.645 \quad (2.22b)$$

The fundamental frequency of a phase-sensitive detector output will be given by

$$F_{\alpha 1}^+ = \frac{2\eta}{z\tau_0} (\beta z)^2 \int_0^{\tau_c^*} s(x) e^{-j\omega\beta z x} dx \cdot \int_0^{\infty} \frac{1}{y} e^{-\frac{1}{y^2}} e^{-j\omega\beta z y} dy \quad (2.23)$$

or

$$F_{\alpha 1}^+ = \frac{2\eta}{z\tau_0} (\beta z)^2 \int_0^{\tau_c^*} e^{-j\omega^* x} s(x) dx \int_0^{\infty} \frac{1}{y} e^{-\frac{1}{y^2}} e^{-j\omega^* y} dy \quad (2.24)$$

$$= |F_{\alpha 1}^+| \angle F_{\alpha 1} \quad ,$$

where  $\omega^* = \omega\beta z$ .

For different polyatomic species,  $F_{\alpha 1}$  will be different. Define

$$\psi_{\alpha} = \int_0^{\tau_c^*} e^{-j\omega^* x} s(x) dx = |\psi_{\alpha}| \angle \psi_{\alpha} \quad (2.25)$$

$$\Phi_{\alpha} = \int_0^{\infty} \frac{1}{y} \exp -\frac{1}{y^2} e^{-j\omega^* y} dy = |\Phi_{\alpha}| \angle \Phi_{\alpha} \quad (2.26)$$

The function  $\psi_{\alpha}$  for a rectangular shutter function can be calculated as

$$\psi_{\alpha} = -90^{\circ} + \tan^{-1} \left( \frac{\sin \omega \tau_c}{1 - \cos \omega \tau_c} \right)$$

which is independent of  $\beta_{\alpha}$  (i.e. independent of the species).

The phase angle of  $\Phi_{\alpha}(\omega)$  obtained by numerical integration is shown in Fig. 4.

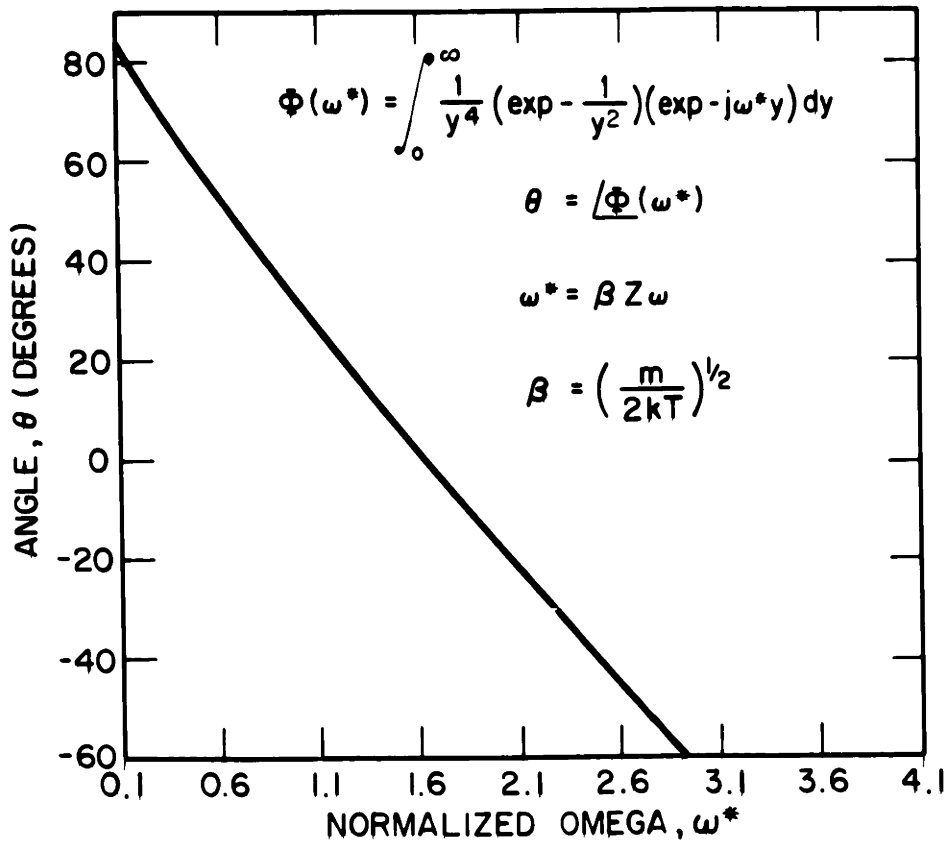


Fig. 4 Phase angle of the Fourier transform for a normalized detection function

In practice, as will be discussed later,  $\omega^*$  should lie in the range shown in Fig. 4.

The advantages of the present method lie in its simplicity (only conventional beam modulation is required) and in the enhanced signal-to-noise ratio due to the synchronous detection. A velocity selector is not needed, and the fitting problem is much easier since the sinusoidal function has two zero crossings. The functional diagram of a phase sensitive detector and the corresponding wave forms is shown in Figs. 5 and 6.

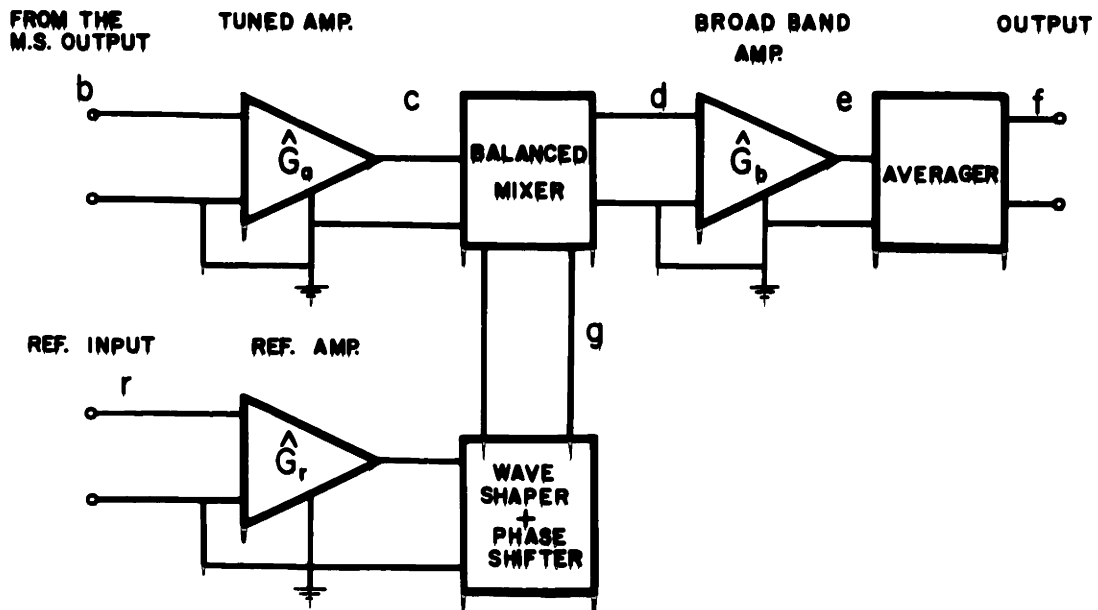


Fig. 5 The block diagram of a phase sensitive detector.

The effectiveness of this method depends largely on how efficiently the components can be separated out. This separation can be performed by comparing the experimental and the calculated phase values. Note that as the number of polymers increases, the method becomes less

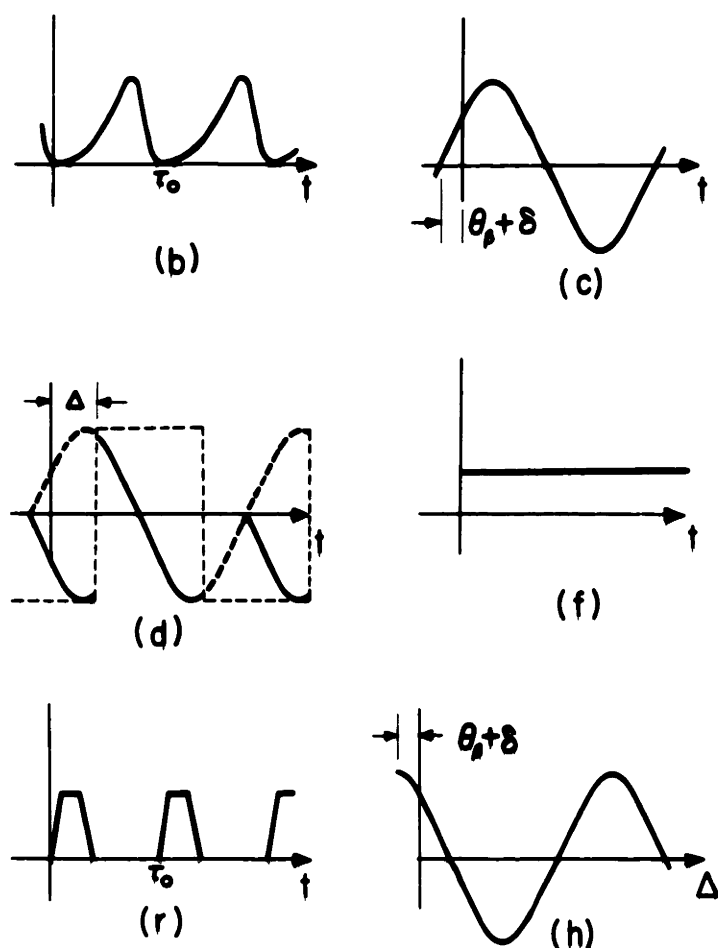


Fig. 6 The wave forms at the corresponding points in Fig. 5; (b) the time-of-flight wave at the input; (c) the fundamental component of the Fourier transform from the input wave form; (d) the dotted rectangular wave is the output at the point d which is the product from the outputs of c and g; (e) is the input wave to the reference amplifier; (f) indicates the output from the averager (constant in time); and (g) the output is a cosine function of the phase shifter  $\Delta$ .

effective. As will be discussed in Chapter VIII,  $C_3^+$  is always taken as a reference and phase differences are then referred to  $C_3^+$  (the highest significant polymer).

Other techniques using direct display of the time-of-flight method through synchronized gates are possible.<sup>41,42</sup>

## II.2 Considerations in Chopper Design

The design of the chopper is based on its specific application. Several important features emerge as first considerations.

II.2.1 Overlap Criteria--To avoid the overlapping of individual T-O-F pulses due to finite periods, the chopping period should be set reasonably large. Define  $c$  as the overlap factor

$$\tau_o^* \geq c \cdot \Delta t^* \quad (2.27)$$

Now, for a shutter function  $s(t)$  as in Fig. 2 with a half width  $\tau_h$ , define the resolution

$$R = \frac{\Delta t^*}{\tau_h^*} \quad (2.28)$$

Introducing the transmission of the shutter function

$$\Gamma = \frac{\tau_h^*}{\tau_o^*} = \frac{\tau_h}{\tau_o} = \frac{n \theta}{2\pi} \quad (2.29)$$

where  $n$  is the number of slots, and  $\theta$  is the angle subtending the transmitting portion to be cut away. Substituting (2.28) and (2.29) into (2.27) one obtains,

$$n\theta \leq \frac{2\pi}{Rc} \quad . \quad (2.30)$$

This gives the upper bound of  $n$  . The value of  $R$  will, in general, depend on specific applications of T-O-F to be used. For an accurate velocity distribution measurement a rather high  $R$  (e.g.  $R > 5$ ) is required.<sup>49</sup> In the present case, since measurement of the distribution function is not intended,  $R$  will be set at only 1 or 2. The  $c$  value used is greater than 3.

To guarantee a desired high resolution from (2.28), set:

$$\tau_h^* \leq R\Delta t^* \quad (2.31)$$

which gives the lower bound of  $\tau_h$ .

Note that

$$\begin{aligned} \tau_h &= \frac{\Gamma}{nf} \quad ; \\ \tau_h^* &= \frac{\Gamma}{nf\beta z} = \frac{\Gamma}{nf^*} \end{aligned} \quad (2.32)$$

Substituting into Equ. 2.30

$$nf^* \leq \frac{\Gamma}{R\Delta t^*} \quad (2.33a)$$

or

$$nf \leq \frac{\Gamma}{R\Delta t} \quad (2.33b)$$

II.2.2 Phase Separability--From Fig. 4, the phase difference of  $\phi_\alpha$  between  $C_1^+$  and  $C_3^+$  can be approximated as

$$\theta_{13} = (\omega_3^* - \omega_1^*) \frac{105^\circ}{2} = 52.5^\circ (\beta_3 - \beta_1) z\omega \quad (2.34)$$

$\beta$ 's are intrinsic to atomic masses and temperature. The sensitivity of the phase difference is proportional to  $z$  and  $\omega$ . However, increasing  $z$  will be accompanied by an intensity attenuation of  $\frac{1}{z^2}$ . Thus one would like to keep  $z$  to a reasonably short distance. Thus, a high  $\omega$  is required.

On the other hand, consider the practical range of  $\omega^*$ . From (2.27) it follows that

$$\frac{2\pi}{\omega^*} \geq c\Delta t^* \quad (2.35)$$

or

$$\omega^* \leq \frac{2\pi}{c\Delta t^*}$$

In fact, the lower bound of  $\omega^*$  will also be determined by the accuracy and transmission of T-O-F. For practical purposes  $z$  was set at 7 cm. As  $z$  is fixed,  $\Delta t$  is almost determined (e.g.  $\Delta t^* = 0.654$ ). Set  $c = 3$ ,  $\omega^* \leq 3.25$ .

II.2.3 Transmission--For a sensitive experiment, high transmission is necessary. To optimize without excessive overlapping, set

$$\Gamma \cong 0.2$$

From the considerations above,  $z = 7\text{cm}$ . Again as  $z$  is fixed,  $\Delta t$  is almost determined, e.g., at  $T = 2400^\circ$  for  $C_3$

$$\beta_3 = \sqrt{\frac{m_1}{2kT}} = 9.497 \times 10^{-6} \text{ sec/cm}$$

$$t_3 = 4.3414 \times 10^{-5} \text{ sec.}$$

Setting R equal to 1, (2.33b) yields

$$nf < 5 \times 10^3 \text{ Hz.}$$

From (2.30) it follows that

$$n\theta \leq \frac{2\pi}{3} \quad .$$

If f is chosen to be variable from 200 to 400 Hz, then one concludes that

$$n = 16$$

$$\theta \cong 5^\circ$$

The chopper is shown in Fig. 7. Slots are skewed  $22.5^\circ$  with respect to the radius for convenience in mounting the chopper motor.

### II.3 Time-of-Flight in the Quadrupole Mass Spectrometer

Since the injection energy to the quadrupole type of mass spectrometer is usually low, the time-of-flight in the spectrometer should also be taken into consideration in addition to the transit time from the atomic source to the ionizer. Because the axial momentum of particles in the mass spectrometer is conserved, one can estimate the transit time by looking at the momentum distribution (or equivalently,



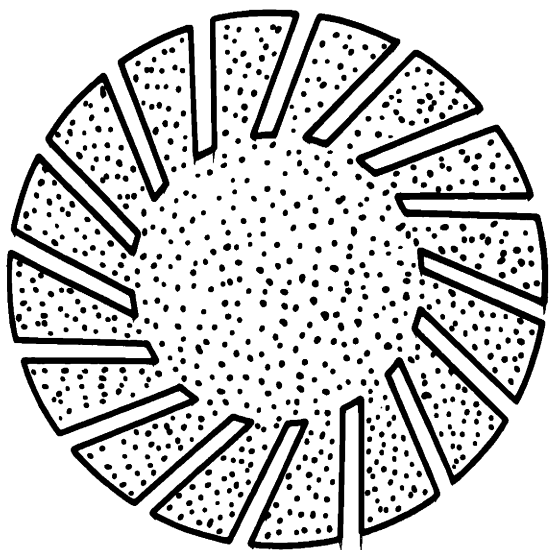


Fig. 7 Chopper for study of fragmentation (16 cuts)

energy distribution) in the system shown in Fig. 8. Note that the initial ion energy is usually very small compared to the energy at extraction. During the time-of-flight in the spectrometer, unlike the time from the source to the ionizer, the dispersion remains unchanged (i.e. pure time delay). The function of the ionizer is to change the distribution from the z axis to the x axis.

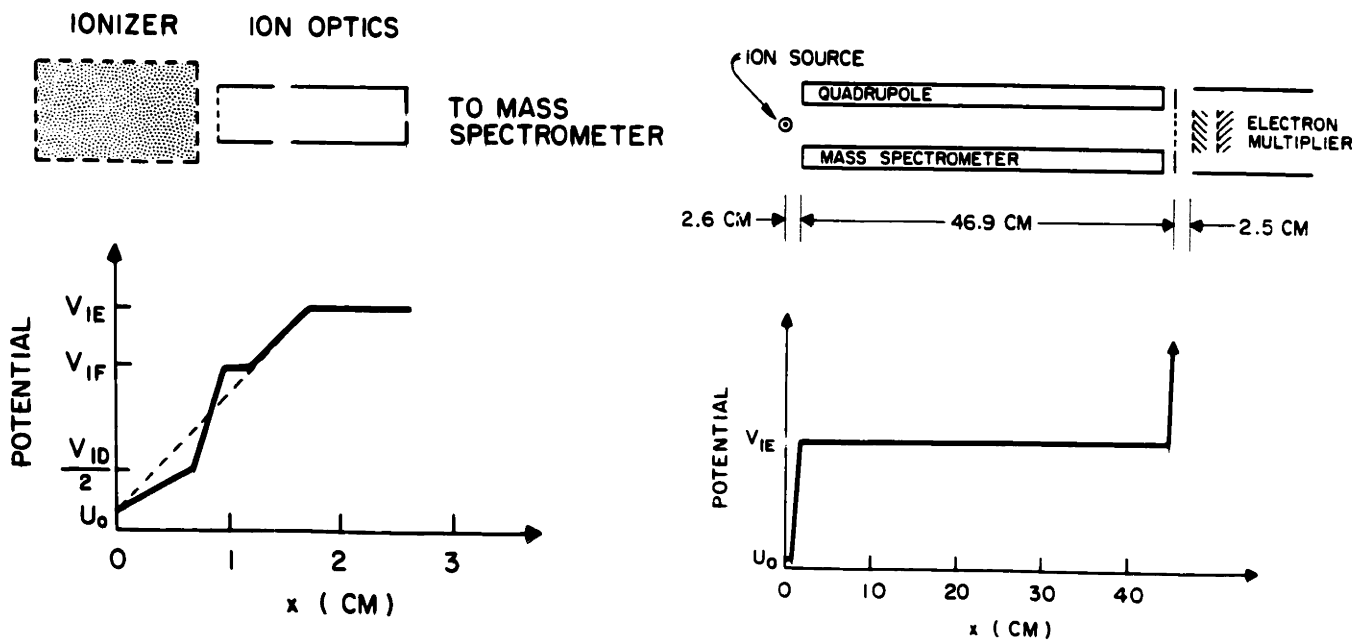


Fig. 8 Energy distribution of the ion source and the mass spectrometer

For particles with velocity  $v$ , the time-of-flight in a quadrupole mass spectrometer of length  $l_M$  (essentially a drift from the viewpoint of axial motion) can be expressed as

$$t_M = \frac{l_M}{v} = l_M \sqrt{\frac{N}{2\xi(V_{IE} + U_0)}} \quad ; \quad (2.37)$$

$$\xi = \frac{e}{M_0}$$

where  $N$  is atomic mass number;  $M_0$  is unit atomic mass ( $C^{12} = 12.0000$ ); and  $U_0$  is the initial energy (possibly including a small contact voltage and x component momentum).

Since  $l_{ID}$ ,  $l_{IF}$ ,  $l_{IE}$  are much shorter than  $l_M$ , the time-of-flight can be estimated very well by linearizing the momentum distribution as shown in Fig. 8. Thus

$$t_{ID} = l_{ID} \left( \frac{2N}{\xi(V_{ID} + U_0)} \right)^{1/2} \quad ; \quad (2.38a)$$

$$t_{IF} = l_{IF} \left( \frac{2N}{\xi(V_{IF} + V_{IE} + 2U_0)} \right)^{1/2} \quad ; \quad (2.38b)$$

$$t_{IE} = l_{IE} \left( \frac{2N}{\xi(V_{IF} + V_{IE} + 2U_0)} \right)^{1/2} \quad ; \quad (2.38c)$$

Ordinarily,  $U_0$  is negligible. In addition to small values of  $l_{ID}$ ,  $l_{IF}$ , and  $l_{IE}$ , all  $V_{ID}$ ,  $V_{IF}$  are adjusted for focusing (to give the maximum spectrometer output) according to  $V_{IE}$  (i.e. approximate linear relationships with  $V_{IE}$  are established).

One may therefore approximate the total time as,

$$\Sigma t = \lambda_e \left( \frac{N}{\xi V_{IE}} \right)^{1/2} ; \quad (2.39)$$

where

$$\lambda_e = \frac{\lambda_{ID}}{\sqrt{\frac{r_1}{2}}} + \frac{\lambda_{IF}}{\sqrt{\frac{r_2}{2}}} + \frac{\lambda_{IE}}{\sqrt{\frac{r_3}{2}}} + \frac{\lambda_M}{\sqrt{2}} \quad (2.40)$$

and  $r_1$ ,  $r_2$ , and  $r_3$  are proportional constants.

If one transforms this time to a phase angle with a given chopping frequency, the difference of phase angles in addition to the contribution from the source to the ionizer (e.g. between  $C_1$  and  $C_3$ ,  $\theta_{31}$ ) is

$$\Sigma \theta_{31} = \frac{360 \lambda_e}{\tau_o} \left( \frac{1}{\xi V_{IE}} \right)^{1/2} (\sqrt{N_3} - \sqrt{N_1}) + \theta_{31}' \quad (\text{degrees}) \quad (2.41)$$

where  $\theta_{31}'$  is the phase difference from the T-O-F in the neutral beam.

In the case of

$$T = 2460^\circ\text{K}, \quad z = 5.5\text{cm}, \quad nf = 5\text{KHz}$$

(2.41) is plotted in Fig. 9 together with the experimental results as a function of  $V_{IE}$ . The existence of radial momenta due to focusing effects will be discussed in detail.

#### II.4 Neutral Beam Determination

The remainder of the problem consists of the determination of  $n_1$ ,  $n_2$ , and  $n_3$ , the intensities of the neutral  $C_1$ ,  $C_2$ , and  $C_3$  species. This information cannot be obtained from the intensities of the ion

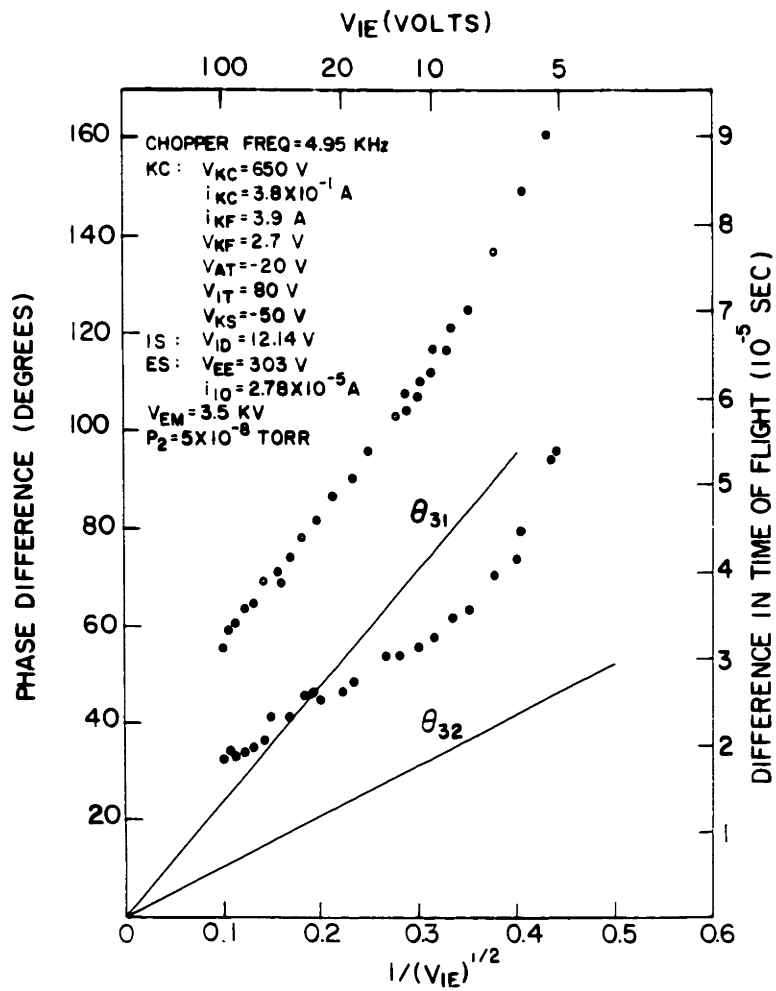


Fig. 9 Phase difference of  $C_3$  and  $C_1$  including time-of-flight in the mass spectrometer

species, since that procedure would require known ionization cross sections which are the experimental task of the present experiment. From a weight gain measurement at the atomic trap or crystal deposition monitor (as will be discussed in Chapter VII), one has

$$\begin{aligned}\phi_1 + \phi_2 + \phi_3 &= \bar{\phi} && \text{at } T \\ \phi_1' + \phi_2' + \phi_3' &= \bar{\phi}' && \text{at } T' \\ \phi_1'' + \phi_2'' + \phi_3'' &= \bar{\phi}'' && \text{at } T''\end{aligned}\tag{2.42a}$$

or

$$\begin{aligned}n_1 \bar{v}_1 + n_2 \bar{v}_2 + n_3 \bar{v}_3 &= \bar{\phi} \\ n_1' \bar{v}_1' + n_2' \bar{v}_2' + n_3' \bar{v}_3' &= \bar{\phi}' \\ n_1'' \bar{v}_1'' + n_2'' \bar{v}_2'' + n_3'' \bar{v}_3'' &= \bar{\phi}''\end{aligned}\tag{2.42b}$$

where  $\phi_i$  is the beam intensity (particles/cm<sup>2</sup>-sec) for  $C_i$  whose average velocity is  $\bar{v}_i$  and whose density is  $n_i$  (particles/cm<sup>3</sup>).

Define

$$\frac{n_i'}{n_i} = \frac{I_i'}{I_i} = \chi_i' \quad ; \quad \frac{n_i''}{n_i} = \frac{I_i''}{I_i} = \chi_i'' \quad .\tag{2.43a}$$

These values can be determined by observing the relative peak height in the mass spectrometer, since the cross sections do not depend on the temperature of the source. From the kinetics, it follows,

$$\frac{\bar{v}_2}{\bar{v}_1} = \frac{\bar{v}_2'}{\bar{v}_1'} = \frac{\bar{v}_2''}{\bar{v}_1''} = \frac{\overline{M_1}}{\overline{M_2}} = \frac{1}{\sqrt{2}} \quad , \quad (2.43b)$$

$$\frac{\bar{v}_3}{\bar{v}_1} = \frac{\bar{v}_3'}{\bar{v}_1'} = \frac{\bar{v}_3''}{\bar{v}_1''} = \frac{\overline{M_1}}{\overline{M_3}} = \frac{1}{\sqrt{3}} \quad .$$

Then Equ. 2.42b becomes,

$$\begin{aligned} n_1 + n_2 + n_3 &= \frac{\Phi}{\bar{v}_1} = N \\ r_1' n_1 + r_2' n_2 + r_3' n_3 &= \frac{\Phi'}{\bar{v}_1'} = N' \\ r_1'' n_1 + r_2'' n_2 + r_3'' n_3 &= \frac{\Phi''}{\bar{v}_1''} = N'' \end{aligned} \quad (2.44)$$

where  $r_1 = \chi_1$ ,  $r_2 = \frac{\chi_2}{\sqrt{2}}$ , and  $r_3 = \frac{\chi_3}{\sqrt{3}}$  .

The solutions are

$$n_1 = \frac{1}{\Delta} \begin{vmatrix} N_1 & 1 & 1 \\ N_2 & r_2' & r_3' \\ N_3 & r_2'' & r_3'' \end{vmatrix} \quad ; \quad (2.45a)$$

$$n_2 = \frac{1}{\Delta} \begin{vmatrix} 1 & N & 1 \\ r_1' & N' & r_3' \\ r_2'' & N'' & r_3'' \end{vmatrix} \quad ; \quad (2.45b)$$

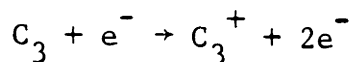
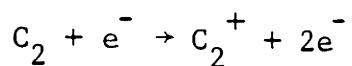
$$n_3 = \frac{1}{\Delta} \begin{vmatrix} 1 & 1 & N \\ r_1' & r_2' & N' \\ r_1'' & r_2'' & N'' \end{vmatrix} \quad ; \quad \text{and} \quad (2.45c)$$

$$\Delta = \begin{vmatrix} 1 & 1 & 1 \\ r_1' & r_2' & r_3' \\ r_1'' & r_2'' & r_3'' \end{vmatrix} \quad . \quad (2.45d)$$

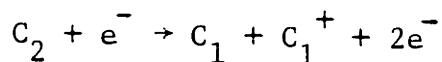
Thus, the ionization cross section for (2.3) is

$$\sigma_1^+ = \frac{I_1^+}{\lambda i n_1} \quad .$$

This procedure is carried out at a specific energy, where absolute calibration is required. Similarly the cross section for the processes



can be obtained in the same manner. Some other processes such as



can be found if the  $C_1^+$  contribution from these species is detectable.

In conclusion, the present technique requires (1) the separation of ion contributions from different neutral polymers and (2) the determination of the relative abundance of neutral polymers.

### III. GENERAL DESCRIPTION OF THE SYSTEM AND INSTRUMENTATION

#### III.1 Vacuum System

The vacuum system (approximately 20 liters in volume) is composed of an NRC VHS-4 4" oil diffusion pump backed by a mechanical roughing pump and a Granville-Phillips cryogenic trap. The trap is maintained at liquid nitrogen temperature to reduce back streaming of pump oil; the pumping speed in front of the trap is about 160 liters/sec. The pressure near the mass spectrometer is about 5 times lower than that near the source which is about  $7 \times 10^{-8}$  torr. When the carbon source was operated at a temperature of  $2700^{\circ}\text{K}$ , the pressure rose to about  $10^{-7}$  torr (or higher).

Minor cracking of the diffusion pump oil was still observed in the mass spectra from 50 to 200 amu. Small amounts of contamination were formed as film deposition on the electrodes after long periods of electron impact. The system and the instrumentation are shown in Fig. 10.

An automatic leak system was installed in the mass spectrometer in conjunction with the ionization gauge controller to regulate the system pressure, and to introduce necessary gases for calibration.

#### III.2 Instrumentation

Fig. 10(a) shows the processing of signals and the block diagram of sources. The sources consist of

- (1) an electron gun and a collector with a feedback control circuit to keep the electron collector current constant while



- the beam energy is changed,
- (2) an ion collector with which absolute ion current can be measured; and an ion optical injection system for the mass spectrometer,
  - (3) an atomic trap or crystal film thickness monitor to measure the neutral beam intensity (and density),
  - (4) an ionization chamber in which the electron beam intersects the neutral beam, (Ions thus produced can be extracted to either the ion collector or the mass spectrometer.)
  - (5) a Knudsen cell which produces a collimated neutral beam using electron bombardment heating with an emission stabilized power supply.

Photographs are shown in Figs. 10(b) and 10(c). The total ion current was measured using a Keithly 601 electrometer with a sensitivity of  $10^{-14}$  amp. Ions thus produced may be injected through the quadrupole mass spectrometer and detected by an EMI Venetian type electron multiplier. The resulting amplified signal may either be further amplified electronically or counted with each count corresponding to a single particle. Particle counting was used to eliminate the unknown secondary yield of ionic impact on the first dynode. The output of the counter was then passed through a PAR HR-8 lock-in amplifier along with a reference signal from a lamp-and-phototransistor combination at the neutral beam source. The chopper was driven by a Globe hysteresis motor which was driven in turn by a 50 watt 400 Hz power amplifier.



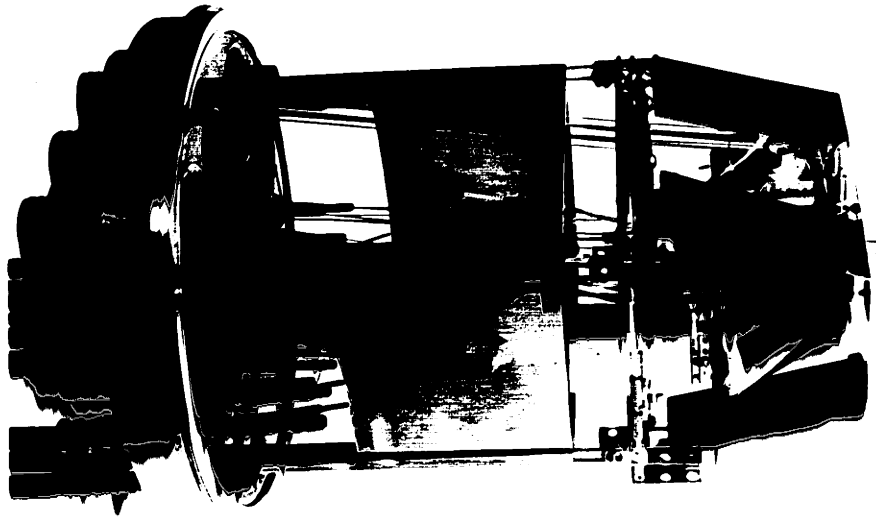


Fig. 10(b) Photograph of the sources, including the electron beam and the ion optical system.



Fig. 10(c) The neutral beam source. (Details of the parts shown in Figs. 10(b) and 10(c) will be given in subsequent chapters.)

### III.3 Source Testing Diagram and Nomenclature

The wiring diagram for tests and operation is shown in Fig. 11(a). Fig. 11(b) shows the low energy electron source including a cylindrical electron monochromator to provide low electron energy spread. In studying threshold behavior, the monochromator replaces the electron gun shown in Fig. 11(a). All the measured quantities are listed in Table I.

TABLE I

#### Electron Source (E.S.)

##### (a) Electron guns and collectors

$V_{EA}$	accelerates electrons before entering the ionization chamber
$V_{EC}$	suppresses secondary electrons from the collector
$V_{ED}$	provides the confining potential for the ionizer and initial ion energy to the ion injection lens
$V_{EE}$	approximately controls the electron energy inside the ionization chamber
$V_{EF}$	controls the potential of the second lens electrode with respect to the filament to provide electron focus
$V_{EG}$	provides normally negative potential on the electron grid aperture to control the beam current
$V_{5C}$	provides the retarded potential for the electron beam in order to study the beam energy
$i_{EC}$	measures the filament supply current

TABLE I Cont'd.

$i_{14}$  measures the electron emission current

$i_{10}$  measures the electron beam current

(b) Electron Monochromator

$V_{EL}$  provides the potential for the central electrode of the injection einzel lens for focusing

$V_{EO}$  provides the potential of the outside cylinder for the monochromator

$V_{EU}$  controls the voltage of the compensation electrodes

$V_{EP}$  controls the operating beam energy of the monochromator

Ion Source (I.S.)

$V_{IC}$  provides the necessary retarded potential for the ion collector

$V_{ID}$  controls the ion draw-out potential necessary to sweep the ions into the mass spectrometer or into the total ion collector

$V_{IE}$  approximately controls the axial ion energy in the mass spectrometer or at the total ion collector

$V_{IF}$  provides a crude ion focus to inject ions into the mass spectrometer

$V_{ES}$  establishes potential on the electron suppressor grid to prevent Auger electrons from leaving the ion collector

$V_{CF}$  controls the potential on the chamber frame with respect to potential on the wire-wound ionization chamber

TABLE I Cont'd.

Knudsen Cell (K.C.)

- $V_{KC}$  provides the electron bombardment energy
- $V_{KS}$  maintains the bias voltage of the shield
- $V_{IT}$  supplies the retarded potential for ions coming out of the Knudsen cell and prevents them from entering the ionizer
- $V_{AT}$  provides the retarded potential for Auger electrons from the Knudsen cell source

Mass Spectrometer and Detection

- DC offsets the mass spectrometer corresponding to mass number  $50 \times \frac{DC}{1000}$  in the present particular mass range of 50 amu
- DC/AC measures the resolution of the mass spectrometer
- $V_{EM}$  supplies the necessary potential for the electron multiplier

Details of the tests and operation will be described in subsequent chapters. Power supplies and instruments used in measurement are tabulated with the laboratory indices shown in Appendix 7.



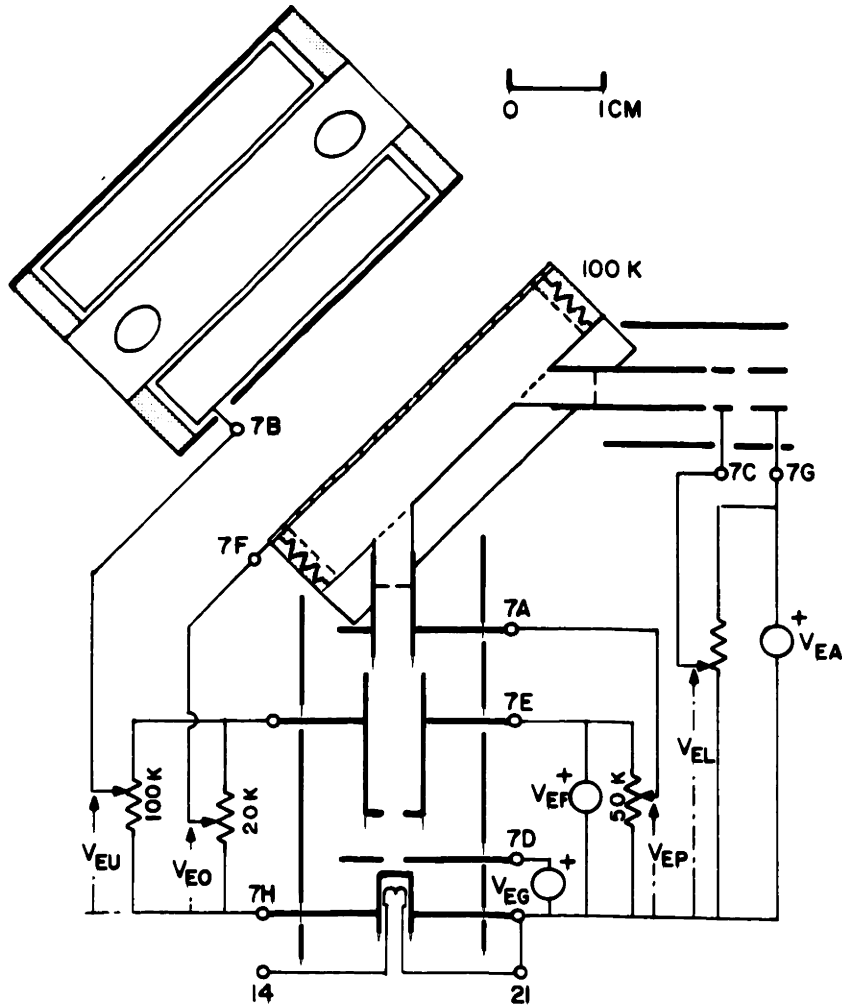


Fig. 11(b) Monoenergetic source for study of threshold behavior



IV. THE CARBON VAPOR SOURCE AND ITS TESTS

IV.1 Atomic or Molecular Beam Intensity

According to the gas kinetic theory, the total number of molecules (atoms) escaping per second through an aperture of area  $A_s$  can be obtained by integration over the cosine law as,

$$N = n_s \bar{v} \frac{A_s}{4} \quad (4.1)$$

Introducing

$$\bar{v} = \left(\frac{8kT}{\pi m}\right)^{1/2} \quad \text{and} \quad n = \frac{P_s}{kT}$$

(4.1) becomes,

$$N = 3.51 \times 10^{22} \frac{P_s A_s}{(MT)^{1/2}} \quad (\text{molecules/sec}). \quad (4.2)$$

Along the  $z$  axis, the beam intensity is simply

$$\begin{aligned} \phi(\theta = 0) &= \frac{n_s \bar{v} A_s}{4\pi z^2} = \frac{N}{\pi z^2} \\ &= 1.115 \times 10^{22} \frac{P_s A_s}{z^2 (MT)^{1/2}} \quad (\text{particles/cm}^2\text{-sec}) \quad (4.3) \end{aligned}$$

where  $P_s$  is in mm Hg,  $M$  is the mass number, and  $A_s$  is in  $\text{cm}^2$ .

The neutral density at the ionizer can be obtained as

$$n_i = \frac{\phi}{v_b} = \frac{1.115 \times 10^{22} P_s A_s}{v_b z^2 (MT)^{1/2}}, \quad (4.4a)$$

$$\bar{v}_b = \sqrt{\frac{9\pi}{8} \frac{kT}{m}} \quad ,$$

or

$$\begin{aligned} n_i &= \frac{2n_s A_s}{3\pi^2 z^2} \quad (\text{molecules/cm}^3) \\ &= 6.56 \times 10^{17} \frac{P_s A_s}{T_s z^2} \quad . \end{aligned} \quad (4.4b)$$

The signal-to-background ratio for the total ion collection can be formulated as

$$S = \frac{I_i}{I_b} = \frac{\sigma_i n_i \ell_i}{\sigma_b n_b \ell_b} \quad . \quad (4.5)$$

In the case of background gases, the impact length is defined by the width of the ionizer (0.7 cm). For an atomic beam, the impact length is equal to the confining aperture (0.191 cm). For estimation purposes, it is assumed that  $\sigma_s = \sigma_b$ . One can obtain the highest tolerable background as

$$P_b \leq \frac{2}{3\pi^2} \frac{A_s}{z^2} \frac{1}{s} \frac{T_b}{T_s} \frac{\ell_i}{\ell_b} P_s \quad . \quad (4.6)$$

when  $T_b = 300^\circ\text{K}$ ,  $T_s = 2400^\circ\text{K}$ ,  $z = 5 \text{ cm}$ ,  $A_s = 7.9 \times 10^{-2} \text{ cm}^2$ , and  $S = 2$ , the result is that

$$P_b \leq 3.65 \times 10^{-6} P_s \quad . \quad (4.7)$$

For a reasonable  $P_b$ , say  $10^{-7}$  torr, the source pressure is

$$P_s \geq 2.74 \times 10^{-2} \quad (\text{torr}) \quad .$$

On the other hand, from section VII.3, the detection limit of a neutral beam requires that  $\phi_i = 10^{15}$  particles/cm<sup>2</sup>-sec (or  $n_i = 10^{10}$  particles/cm<sup>3</sup>). From Equ. 4.3,  $P_s \geq 8.4 \times 10^{-3}$  torr (for C<sub>3</sub>).

The required source pressure is governed more strongly by the requirement set by background gases than that set by the limit sensitivity of neutral particle detection.

It should be noted that the estimation mentioned above was made on the basis of an ideal effusion aperture and molecular flow condition ( $\lambda \gg R$ ) which is not quite true at  $P_s = 2.74 \times 10^{-2}$  torr.

The intensity can be enhanced and the sample consumption can be simultaneously reduced if multichannel effusers are used. In this case, when  $\lambda \gg a$ ,  $\lambda \leq d$ , the neutral density and beam intensity can be expressed as

$$\phi(\theta = 0) = \frac{2^{1/4} AT \bar{v} n_s^{1/2}}{8\pi\delta d^{1/2} z^2} \quad , \quad (4.8)$$

and

$$n_i = \frac{2^{1/4} AT \bar{v} n_s^{1/2}}{8\pi\delta d^{1/2} z^2 v_b} \quad (4.9)$$

where  $a$  is the width of the aperture;  $d$ , the length of the effusers; and  $T$ , the transmission.

More explicitly, at  $\delta = 3 \times 10^{-8}$  cm,  $d = 0.2$  cm,

$$n_i = 9.33 \times 10^{15} \frac{A_s P_s^{1/2}}{T_s^{1/2} z^2}$$

For  $P_s = 2.74 \times 10^{-2}$  torr, Equ. 4.10 yields  $n_i \approx 10^{11}$  particles/cm<sup>3</sup> while Equ. 4.4 gives  $n_i \approx 3.8 \times 10^{10}$  particles/cm<sup>3</sup>. However, due to multichannel effusion, the beam intensity can be further increased by raising the source pressure.

#### IV.2 Design of the Source

An atomic beam source for vaporizing carbon has been designed and built. Since the source will be operated in the range from 2000 to 2800°K, several problems should be considered. First, since the heat loss is dominated by radiation, it is imperative to have the most effective radiation shields obtainable. Second, to avoid overheating of other parts in the vicinity of the source, which may result in tremendous amounts of outgassing, the source should have special cooling. A water-cooled jacket made of copper was chosen because of its high thermal conductivity. A coil of 3.2 mm OD copper tubing was used as the cooling jacket. The source used high efficiency electron bombardment heating. The Knudsen cell itself, with a 3.2 mm orifice, was made out of a single piece of tantalum and was spot welded to a circular aperture in the chamber. Two Knudsen cells were used; one is 0.635 cm in diameter and the other is 0.4 cm. This entire source assembly is shown in Fig. 12.

Charged particle traps consisting of separate ion and Auger traps, are also shown in the Figure. The ion trap was intended to trap ions which might leak from the source while the Auger trap pro-

Auger electron emission resulting from ion impact.

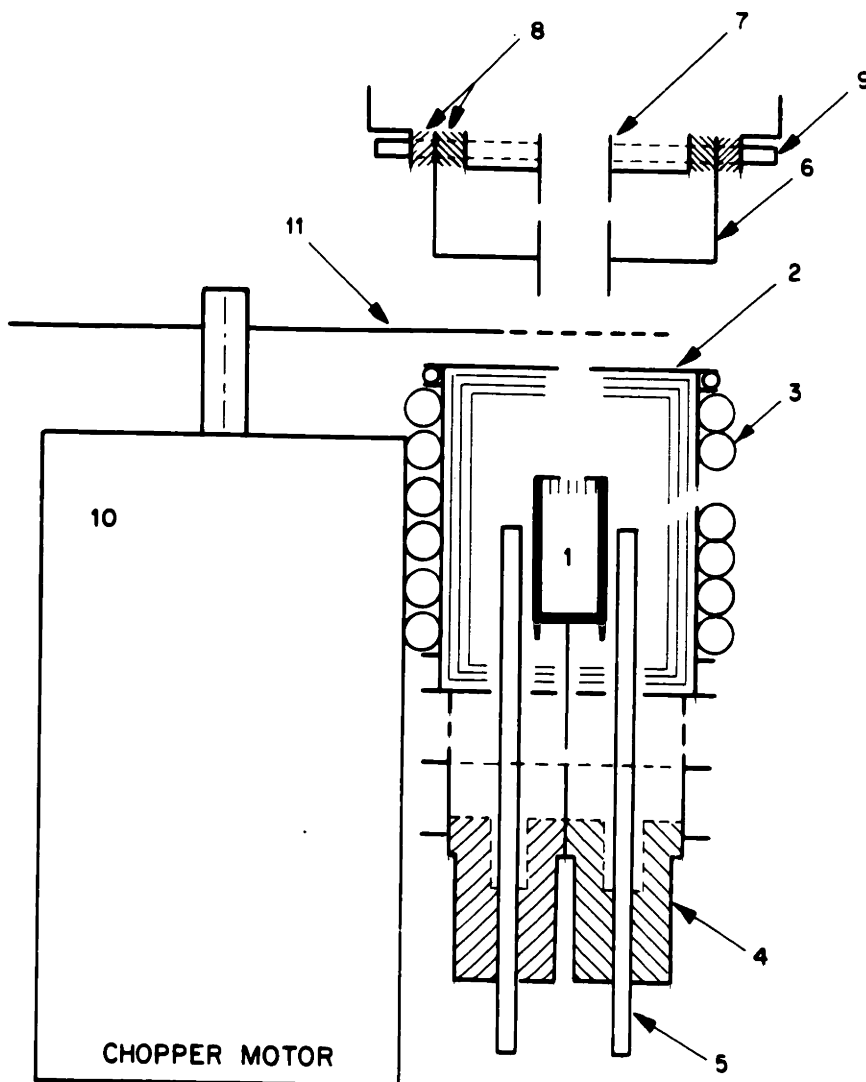


Fig. 12 Neutral beam source assembly: 1) Tantalum Knudsen cell; 2) heat shields (made from 0.076 mm Ta foil); 3) copper cooling coils; 4) filament feedthroughs; 5) filament supports; 6) ion trap; 7) Auger trap; 8) and 9) ceramic rods and spacers; 10) chopper motor; 11) chopper disc

IV.2.1 Concentric Radiation Shields--Shields were made of tantalum foil (.076 mm thick) in concentric cylindrical forms (about 2.5 cm in diameter). Adjacent layers were separated by spot-welding four small tantalum chips ( $0.0725 \text{ cm}^2$  in area and 0.05 cm thick) on the edges. A series of 3.2 mm holes punched through the shields allowed temperature measurement using an optical pyrometer.

Assuming negligible conduction losses, the power required may be estimated by means of the Stefan-Boltzman equation:

$$P = \frac{\sigma A_1 (T_1^4 - T_2^4)}{\frac{1}{\epsilon_1} + \frac{A_1}{A_2} \left[ \frac{1}{\epsilon_2} - 1 \right]} \quad (4.11)$$

where  $\epsilon_1$  is the emissivity of the Knudsen cell (area  $A_1$ , temperature  $T_1$ ),  $\epsilon_2$  is the emissivity of the first heat shield (area  $A_2$ , temperature  $T_2$ ) and  $\sigma$  is the Stefan-Boltzman constant. For equal emissivities and areas, the radiated power is inversely proportional to  $n + 1$ <sup>52</sup> (n being the number of heat shields). In the present case however, a large difference in area between the first shield and the Knudsen cell greatly reduces the effectiveness of the shields.

The above equation contains  $T_2$  which is unknown. This temperature and the temperatures of the other shields may be eliminated by noting that the radiated power is approximately conserved, and that the shields have approximately equal areas. Thus:

$$P = a(T_1^4 - T_2^4) = b(T_2^4 - T_3^4) = b(T_3^4 - T_4^4) = b(T_4^4 - T_5^4) \quad (4.12)$$

where

$$\frac{A_2}{A_3} \approx \frac{A_3}{A_4} \approx \frac{A_4}{A_5} \approx 1 \quad , \quad (4.13)$$

$$a \equiv \frac{A_1}{\frac{1}{\epsilon} + \frac{A_1}{A_2} \left[ \frac{1}{\epsilon} - 1 \right]} \quad , \quad (4.14)$$

and

$$b \equiv \frac{A_2}{\frac{1}{\epsilon} + \left[ \frac{1}{\epsilon} - 1 \right]} \quad . \quad (4.15)$$

The result is

$$P = \frac{a}{3\frac{a}{b} + 1} (T_1^4 - T_5^4) \quad (4.16)$$

$$= \frac{a}{3\frac{a}{b} + 1} T_1^4 = \gamma P_0 \quad (\text{Since } T_1 \gg T_5) \quad . \quad (4.17)$$

Here  $P_0 = aT_1^4$  is the power required with a single shield, while

$$\gamma \equiv \frac{1}{3\frac{a}{b} + 1} \quad . \quad (4.18)$$

It is interesting to observe that  $\gamma$  is only a weak function of emissivity for  $\frac{A_2}{A_1} > 4$ . For example, using  $\epsilon = 0.0816$  (Knudsen cell of 0.635 cm in diameter), one obtains  $\gamma = 0.7$ , in contrast to  $\gamma = 0.68$  using  $\epsilon = 0.7$ . Thus the temperature dependence of the shield emissivity may be neglected in the calculation. Using  $\epsilon = 0.29$ <sup>53</sup> the net radiated

power at  $T_1 = 2400^\circ\text{K}$  can be estimated to be 112 watts.

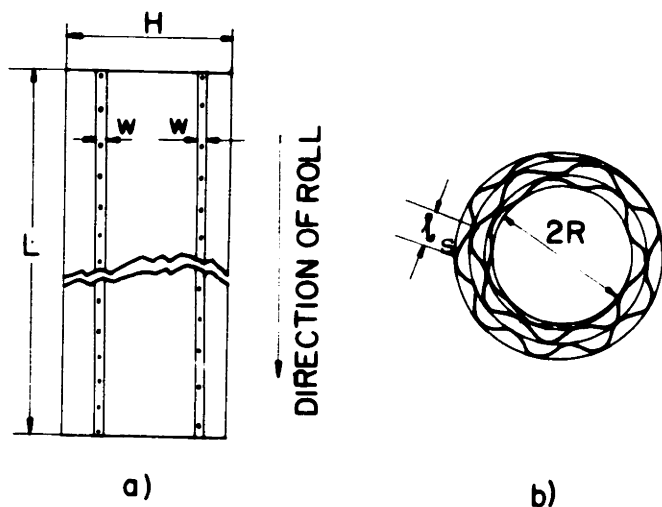
The conduction loss through the shield supports and the filament holder is about 50 watts, while that through the Knudsen cell support is about 5 watts. Radiation losses through the neutral beam aperture and the pyrometer observation hole amount to about 8 watts. Thus the total power required for operation at  $2400^\circ\text{K}$  should be close to 175 watts.

Note that this calculation is approximate. A more precise solution would require a better model of the geometric structure. Note also that coating shield surfaces with a carbon may degrade emissivities and cause an increase in the required power.

IV.2.2 Spiral Radiation Shields--To achieve better radiation shielding, spiral radiation shields have been used due to their compactness and convenience of construction. As shown in Fig. 13, two narrow strips (2.0 mm by width  $W$ ) were spot welded along the edges of a piece of tantalum foil of 0.025 mm thickness, width  $H$  (2.5 cm) and length  $L$  (25 cm). Welding spots were separated by a distance of 6.35 mm. The entire strip (shown in Fig. 13(a)) was then rolled. Fig. 13(b) shows the top view of the resulting shield. An independently removable cylinder was usually placed inside the spiral shield to allow convenient replacement when the shield became contaminated by condensed sample vapors.

The power required here was similar to that in the previous case. The conduction loss in this case was slightly larger because of the spacer





conduction through  $\lambda_s$  and the spiral conduction through the rolled strip. However, the efficiency can be made very large by rolling many times.

Fig. 13 Construction of the spiral radiation shields.  $R$  is the radius of the inner-most shield and  $\lambda_s$  is the conduction path between two shields.

#### IV.3 Tests of Power Consumption

The carbon source previously described has been tested. The source, along with its charged particle traps and a particle collector, was mounted on a second flange in the original ultra high vacuum system. The traps and the collector were mounted on a separate test jig which did not touch the source itself, to prevent the trap from being heated to a high temperature. The collector was carefully shielded to prevent the collection of stray particles. Measurements of the collector to shield resistance showed it to be greater than  $10^{13}$  ohms. A diagram of the experimental arrangement is shown in Fig. 14.

IV.3.1 Electrical Characteristics--For a moderate power input (thus, a moderate temperature), the filament was made of 0.0178 mm tungsten-rhenium wire, and diode emission curves are given in Fig. 15. These

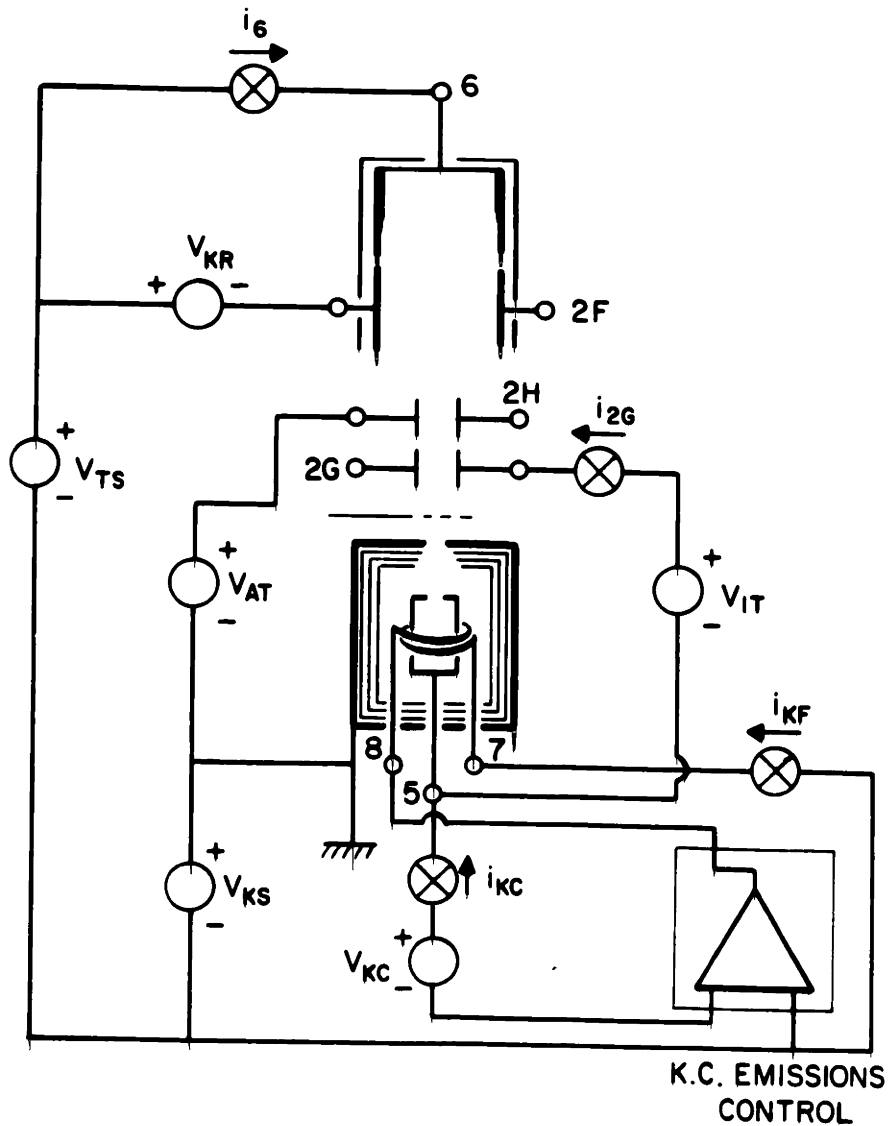


Fig. 14 Schematic wiring diagram of configuration used for source testing

were recorded from an X-Y plotter with a trace time for each curve of less than 5 sec. Fig. 16 shows the difference between slow and fast tracing.

With emission currents between  $3 \times 10^{-1}$  and  $4 \times 10^{-1}$  amp and with

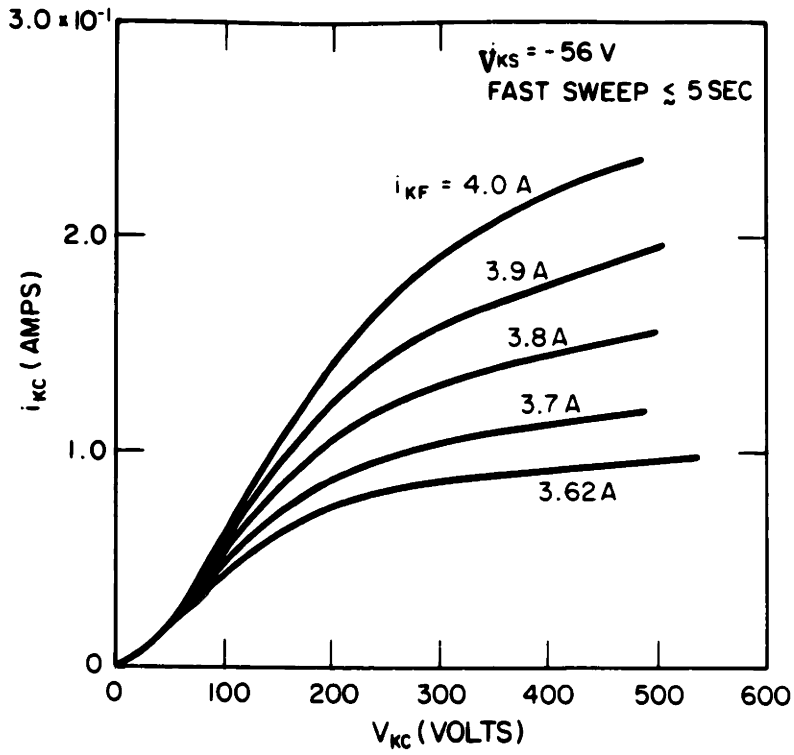
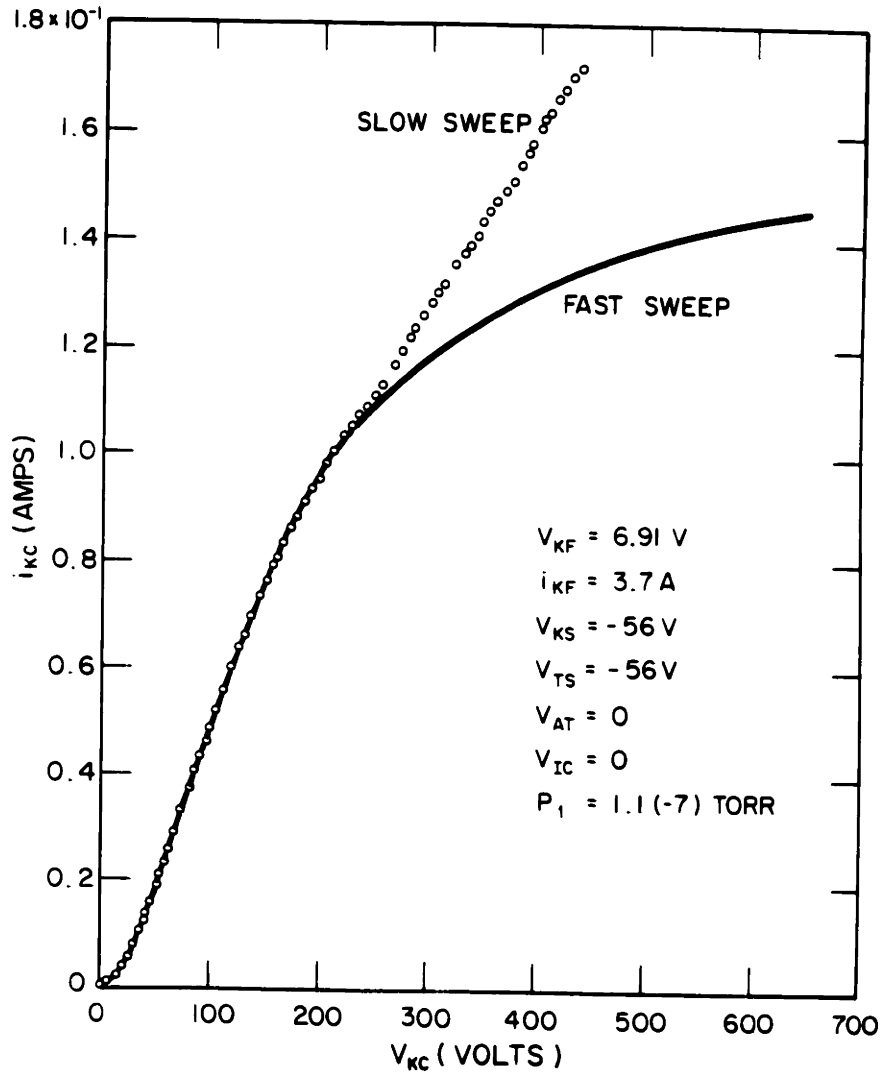


Fig. 15 Diode emission characteristics (fast trace)

Fig. 16 Difference of characteristics for slow and fast tracing



$V_{KC}$  above 400 volts, the Knudsen cell operated close to the region of temperature saturation, governed by the Richardson-Langmuir Law, and in the region where the emission feedback control was operating. For convenience in both these experiments, the filament was first supplied by a constant current source. At low emission (i.e. low K.C. temperature), a reasonably stable current was observed. At higher emission near  $1 \times 10^{-1}$  amp, however, thermal run-away was caused by a positive thermal feedback, raising the filament temperature and thus increasing emission. To solve this problem, a change was made from the constant filament-current mode to a constant filament-voltage mode. Although constant-voltage resulted in better stability, it was still not satisfactory. Thus, a stabilized feedback control was designed to establish a constant emission current (constant  $V_{KC}$ ,  $i_{KC}$  controlled by filament temperature or current); this mode worked well and was used for subsequent experiments.

For high power operation, the filament was changed to a 0.0254 mm W-Re wire. The steady diode characteristics were difficult to obtain because of the use of highly effective heat shields. As the temperature was increased, the first heat shield began to emit electrons. When this happened, both the filament and the shield had to be included in the control loop to make the system stable. (For a detailed discussion see section IV4.) Fig. 17 shows the combined emission from the filament and the shield as functions of power (at constant  $V_{KC}$ ).

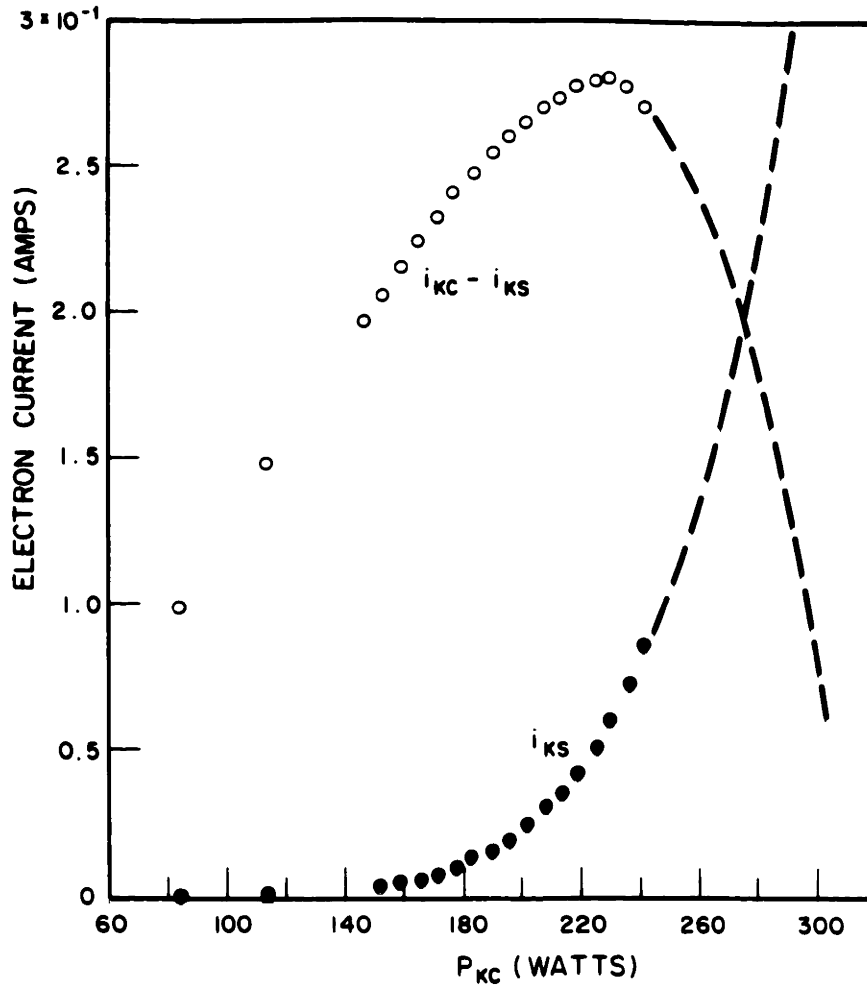


Fig. 17 Emission from the filament and shields as a function of the Knudsen cell power

IV.3.2. Temperature-Power Relation--To investigate the power required, a temperature-power relation was taken, and plotted as in Fig. 18. For the first run, at low temperature, a  $T^4$  dependence was observed which gradually increased to a  $T^5$  (or even higher) dependence by  $1500^\circ\text{K}$ . The  $T^4$  dependence can be explained as a result of the  $T^5$  dependence of radiation loss (temperature dependent emissivity is considered), and the  $T$  dependence of conduction loss. At higher temperatures where radiation is dominant, a dependence between  $T^4$  and  $T^5$  is expected. In the region

from 1400°K to 1700°K, the increase appears to be more rapid than  $T^5$ . This is probably due to the desorption of gases which causes high emissivity.<sup>53</sup>

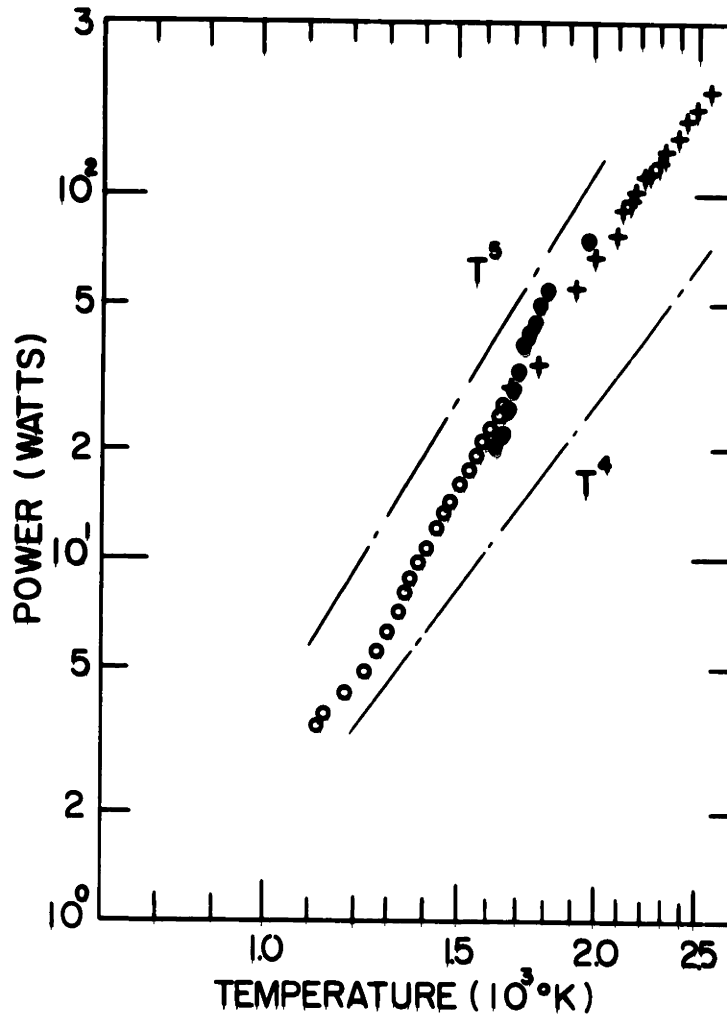


Fig. 18 Required power vs. temperature: o is the power required for the filament only ( $P_{KF}$ ); • is the power required during the first run using both filament and electron bombardment ( $P_{KF}$  plus  $P_{KE}$ ); x is the power required for subsequent runs ( $P_{KF}$  plus  $P_{KE}$ ).

From Fig. 18 it can be observed that 165 watts was required for a temperature of 2400°K. This is very close to the predicted value. Note

also that the heating efficiency of the filament power is almost as effective as the electron bombardment power. A check on the power radiated through the beam aperture and pyrometer observation hole along with extraneous conduction losses was therefore estimated close to 36 watts. These experiments showed that the source was operating satisfactorily.

#### IV.4 Power Controlling

As discussed in the previous section, the electron emission from the shields and the positive thermal radiation feedback result in instability and make the source more difficult to operate at higher temperatures. Feedback control is mandatory to stop drifts and various unstable phenomena, and thus to maintain a stable neutral beam.

##### IV.4.1 Emission Control--In order to have constant power, consider

$$P = i_{KC} \times V_{KC} + i_{KF} V_{KF} = \text{const.}$$

Since  $i_{KF} \times V_{KF}$  is fairly constant and only a small fraction of the total power, constant electron bombardment power can sufficiently imply constant total power. Furthermore, it is still easier to keep emission current constant at constant  $V_{KC}$ . As shown in Fig. 19, the controlled bombardment current  $i_{KC}$  includes the emission current from the heat shields ( $i_{KS}$ ). Failure to do so will result in run-away when the heat shields begin to emit.

At still higher temperatures, as the radiation feedback is increased and the shield thermionic emission becomes dominant, the filament

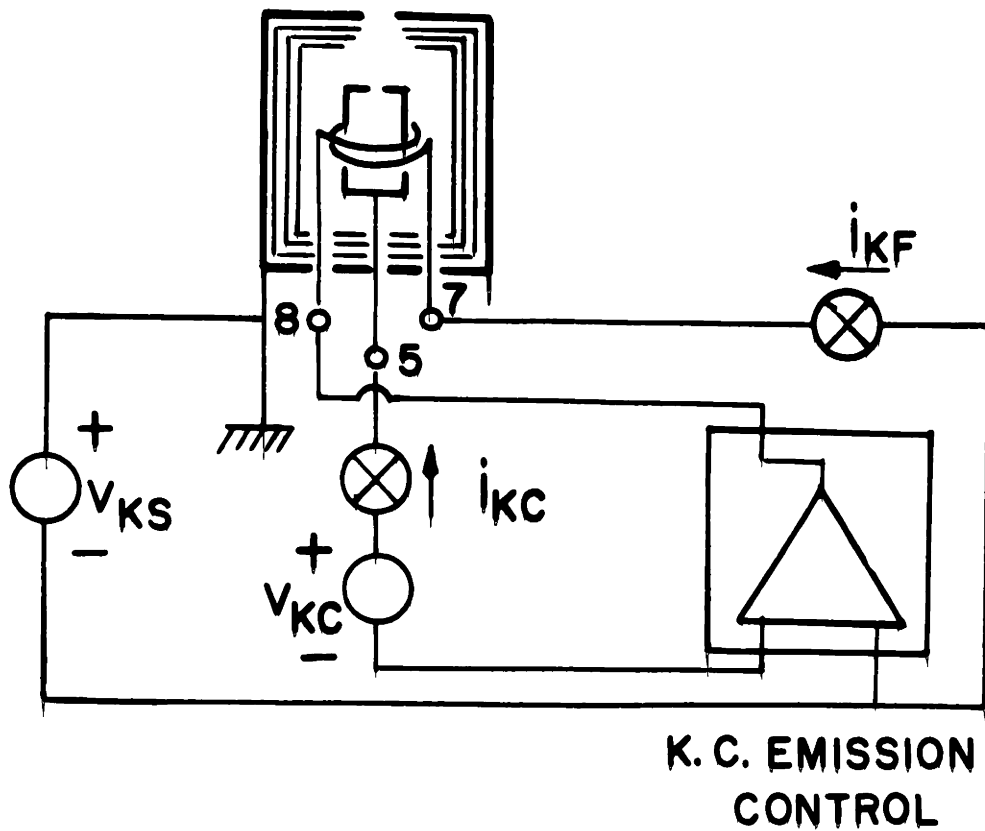


Fig. 19 Wiring diagram of the electron bombardment source

current may be completely turned off. Once this occurs the feedback loop is unable to control the emission and  $i_{KC}$  increases drastically.

To find the cut off point of the filament, let  $T_{KC}$ ,  $T_{KS}$ ,  $T_{KF}$  be temperatures of the Knudsen cell, the innermost shield, and the filament, respectively. Then, from section IV.3.2, if the temperature dependence of emissivity is taken into account, the Stefan Boltzmann equation gives:



$$P_{KC} = c^5 (T_{KC}^5 - T_{KS}^5) \quad , \quad (4.19)$$

$$P_{KF} = d^5 (T_{KC}^5 - T_{KF}^5) + f^5 (T_{KF}^5 - T_{KS}^5) + V_{KF} i_{KF} \quad (4.20)$$

At the cut-off point,  $V_{KF} i_{KF}$  vanishes. Furthermore one can approximate,

$$T_{KS} = \frac{1}{\eta} T_{KC} \quad , \quad (4.21)$$

$$T_{KF} = \frac{1}{\xi} T_{KC} \quad . \quad (4.22)$$

(4.19) and (4.20) become

$$P_{KC} = \alpha^5 T_{KS}^5 = \left(\frac{\xi}{\eta}\right)^5 \alpha^5 T_{KF}^5 \quad (4.23)$$

$$P_{KF} = \beta^5 T_{KF}^5 \quad (4.24)$$

where  $\alpha = c(\eta^5 - 1)^{1/5}$ ;  $\beta = d(\xi^5 - 1)^{1/5} + f(\xi^5 - \eta^5)^{1/5}$ .

Now, the emission at the temperature limit is given by Richardson's Equation,

$$i_{KC} = C T_{KF}^2 e^{-\frac{c_0}{T_{KF}}} + D T_{KS}^2 e^{-\frac{d_0}{T_{KS}}} \quad (4.25)$$

Substituting (4.23) and (4.24) into it, (4.25) may be modified as

$$i_{KC} = A P_{KC}^{2/5} e^{-\frac{a_0}{P_{KC}^{1/5}}} + B P_{KC}^{2/5} e^{-\frac{b_0}{P_{KC}^{1/5}}} \quad , \quad (4.26a)$$

$$P_{KC} = V_{KC} A P_{KC}^{2/5} e^{-\frac{a_o}{P_{KC}^{1/5}}} + (V_{KC} + V_{KS}) B P_{KC}^{2/5} e^{-\frac{b_o}{P_{KC}^{1/5}}} \quad (4.26b)$$

where  $A = \frac{C}{\alpha^2} \left(\frac{\eta}{\xi}\right)^2$ ;  $B = \frac{D}{\alpha^2}$  ;

$a_o = c_o \alpha \left(\frac{\xi}{\eta}\right)$  ;  $b_o = d_o \alpha$

The solution of (4.26) will give  $P_{KC}$  for which the cut-off occurs, provided A, B,  $a_o$ , and  $b_o$  are known. B and  $b_o$  may be readily obtained by plotting  $\log(i_{KS} P_{KC}^{-2/5})$  vs  $P_{KC}^{-1/5}$  as shown in Fig. 20.

$b_o$  is the slope of the plot as

$$b_o = \frac{\Delta \ln(i_{KS} P_{KC}^{-2/5})}{\Delta P_{KC}^{-1/5}} = \frac{\Delta \log(i_{KS} P_{KC}^{-2/5})}{\Delta P_{KC}^{-1/5}} \cdot \ln 10$$

$$= 104.5 \text{ (watt)}^{1/5}$$

$$B = 1.185 \times 10^{16} \text{ (mA watt}^{-2/5}\text{)}$$

That is

$$i_{KS} = 1.185 \times 10^{16} P_{KC}^{2/5} e^{-\frac{104.5}{P_{KC}^{1/5}}} \quad (4.27)$$

$a_o$  and A may be similarly obtained. However it requires a plot of  $(i_{KC} - i_{KS})$  vs  $P_{KC}$  over the cut-off point. Since a constant-power power supply has not yet been built (note that it would not be hard to build as proposed below), no such plot is yet available. Fortunately, because of the higher work function of the filament (W) and the small

area in comparison to the shield,  $i_{KC}$  may be considerably less than  $i_{KS}$  near the cut-off point. Thus, equation 4.26b reduces to

$$P_{KC} = 1.185 \times 10^{13} (V_{KC} + V_{KS}) P_{KC}^{2/5} e^{-\frac{104.5}{P_{KC}^{1/5}}} \quad (4.28)$$

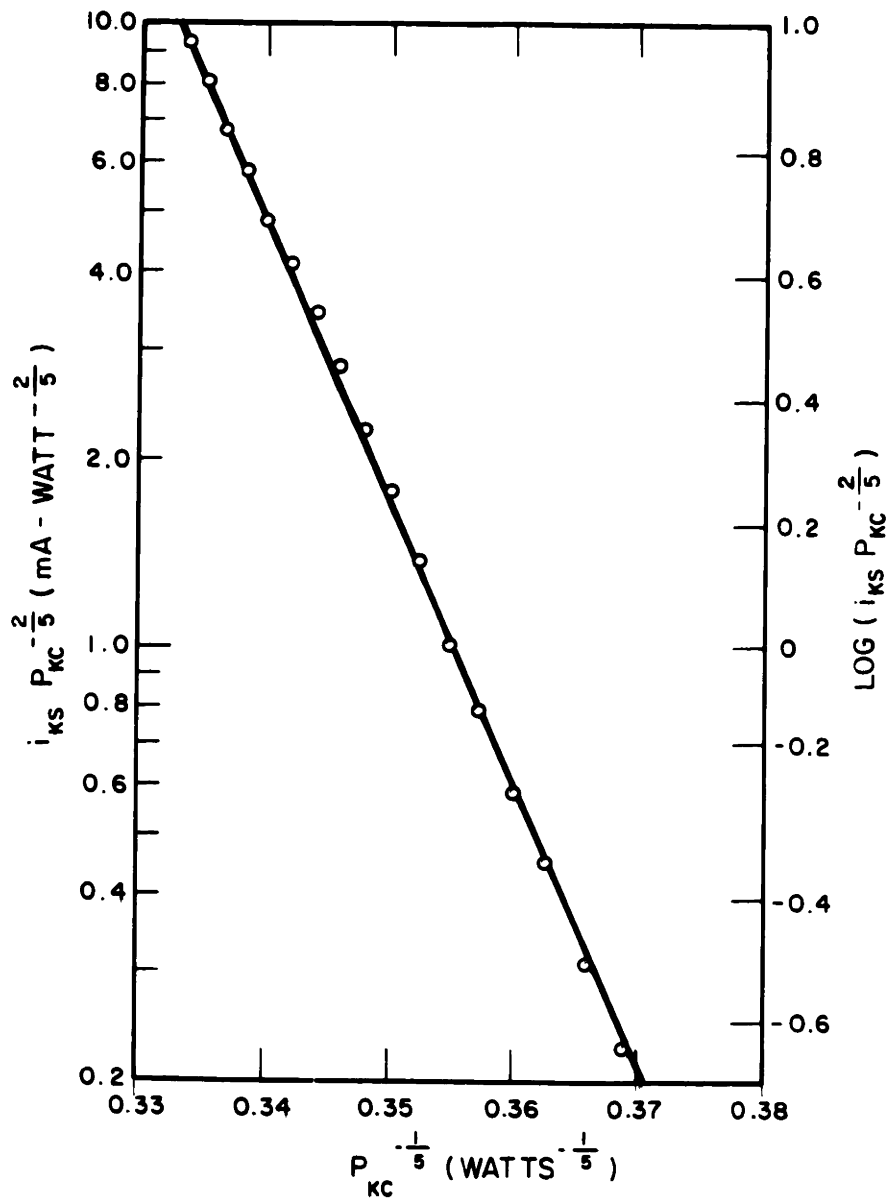


Fig. 20  $\log(i_{KS} P_{KC}^{-2/5})$  vs  $P_{KC}^{-1/5}$  plot. The linear relationship is the result of Richardson's Equation

The solution yields the critical power as

$$P_{cr} = 312 \text{ watts}$$

When this power is reached, a run-away occurs. To avoid this, a specific kind of negative feedback is necessary. In the following section a design for a constant-power power supply is discussed.

IV.4.2 Constant-Power Power Supply--A constant electron bombardment power supply combined with an emission control, as described earlier, is proposed in Fig. 21 along with the characteristics shown in Fig. 22.

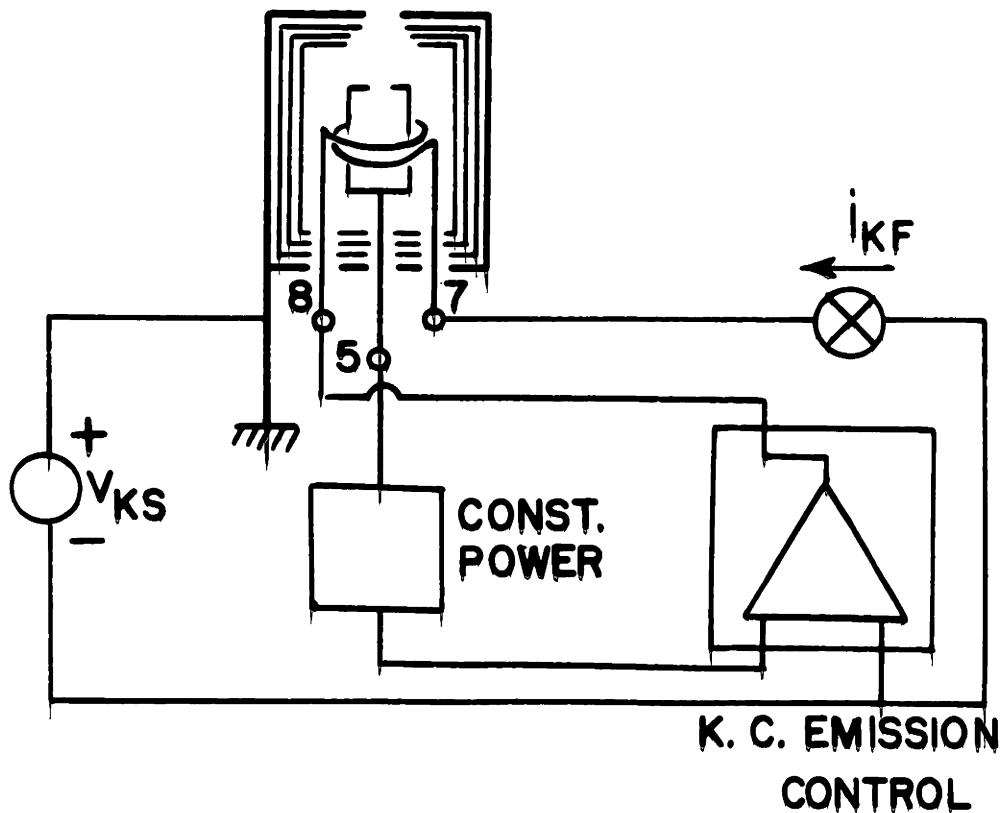


Fig. 21 Diagram of constant power operation

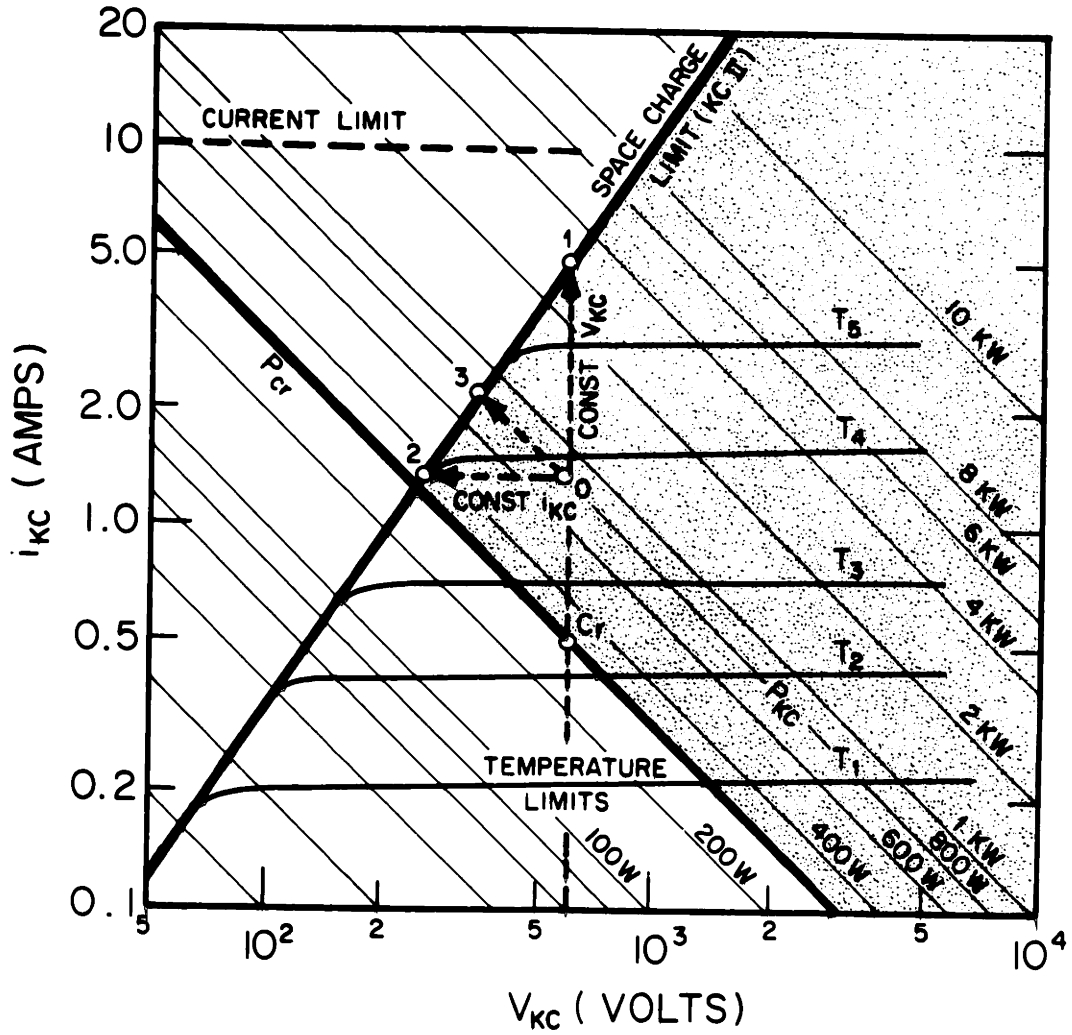


Fig. 22 Characteristics of a constant-power power supply and its operation with the Knudsen cell. The initial operation point is introduced using an emission control by starting at a high filament heating current. The space charge limit line moves up and down depending on the geometry of the source. The critical power depends on the heat shield efficiency.

In Fig. 22  $i_{KC}$  and  $V_{KC}$  are plotted in a log-log scale. The constant power curves (hyperbolas in linear plots) are now straight lines. Space charge lines of the source are given as,<sup>54</sup>

$$i_{KC} = \frac{14.66 \times 10^{-6} \times \ell V^{3/2}}{2} = h V^{3/2} \quad (4.29)$$

with

$$\beta = u - \frac{2u^2}{5} + \frac{11u^3}{120} - \dots \quad \text{and } u = \ln\left(\frac{r}{r_c}\right).$$

These curves are shown with a slope of 3/2 and will move up and down depending on the size of the Knudsen cells: Knudsen cell I (length 2.0 cm; diameter 1.27 cm) and Knudsen cell II (length 2.0 cm and diameter 0.618 cm). Temperature limits are also shown.

In order to turn the source on, first the desired power and constant  $V_{KC}$  are set, and then the filament is turned on. The supply delivers constant  $V_{KC}$  before it reaches the desired power. As the emission reaches the point  $C_r$ , the filament may be turned off by an emission control. Run-away occurs and the system quickly goes from  $C_r$  to 0 and then to 3, the steady state point.

If one does not use a constant-power power supply, but constant  $V_{KC}$  is maintained, the system moves from 0 to 1 which has a much larger power and may cause destruction of the source. On the other hand, if the  $i_{KC}$  limit is maintained, the system goes from 0 to 2, reaching the critical power. This implies that one cannot obtain any higher desired power.

Instead of using an emission control to initiate emission a constant

filament power will also provide stable operation on the space charge limit line while power settings are varied. In this case the characteristics will not be significantly changed, because the filament power is only a portion of the total.

The functional block diagram and circuitry of the supply are presented in Appendix 4.

#### IV.5 Charged Particle Traps

The performance of charged particle traps is important in absolute measurements of electron ionization cross sections.<sup>55</sup> The charged particles coming out of the Knudsen cell, both ions and electrons, must be carefully suppressed. This is the problem especially at higher temperatures. Stray electrons from the electron bombardment source can be retarded by biasing the shield at -30 volts. But while electrons are thus eliminated, alkali ions formed by thermal ionization, along with ions generated by electron impact near the cell, are extracted by this shield bias voltage.

It is observed that the escaping ions are mainly alkali ions. While some also come from impact ionization of either background gas or neutral beam atoms, most ions produced by electron impact are collected by the shield before escaping through the shield aperture due to its geometry.

With a distance of 3.7 mm between the ion trap and the effusion orifice, a stray particle current was observed as plotted in Fig.23. At a temperature lower than 1700°C, the ion trap worked as predicted.

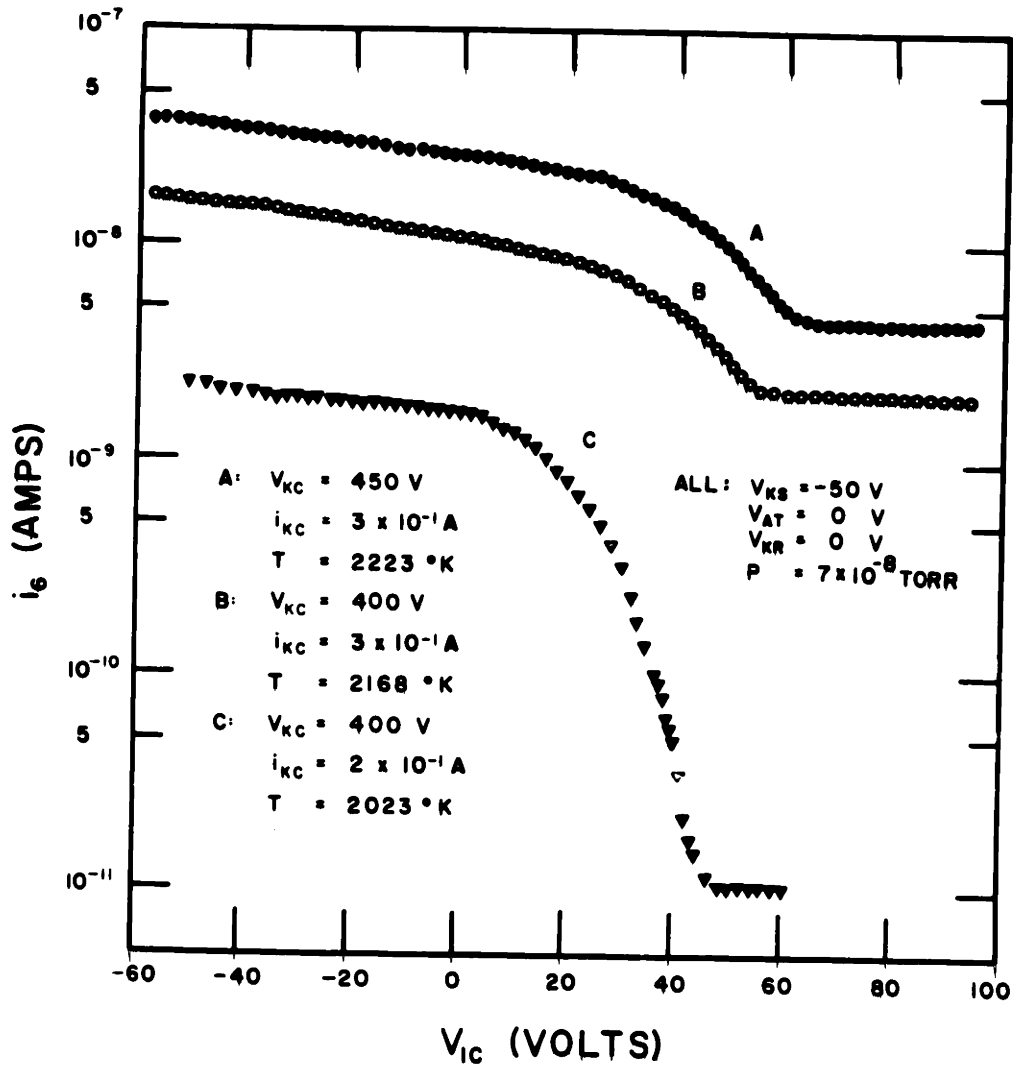


Fig. 23 Ion current ( $I_g$ ) partially retarded by the ion trap voltage. Characteristics are shown for different temperatures; the trap operates satisfactorily below 2200°K.

At higher temperatures however, the stray current greatly increased. This increase took a period of about 15 minutes to reach a steady state, and the higher stray current, amounting to  $10^{-9}$  amp, could not be



reduced by further increasing the trap barrier. Several experiments were then made to find the origin of this current. The results are shown in Figs. 24 and 25. Fig. 24 shows an ion current vs time plot for both  $V_{IC}=0$  and  $V_{IC} = 80$  volts. When  $V_{IC} = 80$  volts a slower initial rate of decline than that of  $V_{IC} = 0$  was observed. The current-temperature relation is shown in Fig. 25. If these ions came from thermal ionization, they ideally should obey the Saha-Langmuir Law,

$$\ln i_+ = \ln eAn + \frac{\psi - V_i}{kT} \quad (4.30)$$

where  $\psi$  and  $V_i$  are the work function of the surface and the ionization potential of the particles respectively. Fig. 25 shows deviations from a straight line behavior (similar deviations have also been observed in the case of Li atoms ionized on a tungsten surface, and were considered to be due to desorption effects<sup>56</sup>). At high temperature however, a reasonably linear characteristic was observed.

It may also be noted that the present behavior may be complicated by diffusion processes. In this latter case (4.30) may be modified to

$$\ln i_+ = C + \frac{\psi - V_i}{kT} + \frac{E_d}{kT} + \frac{\Delta Q}{kT} \quad , \quad (4.31)$$

where C is a constant;  $E_d$  is the activation energy for diffusion<sup>57</sup> ( $\Delta Q$  will be discussed later). Assuming that the ionization potential for Na ions on a tantalum surface is 4.13 eV and the work function for Ta is 5.12 eV, then

$$\psi - V_i = -(5.12 - 4.13) = -0.99 \text{ eV} \quad , \quad (4.32)$$

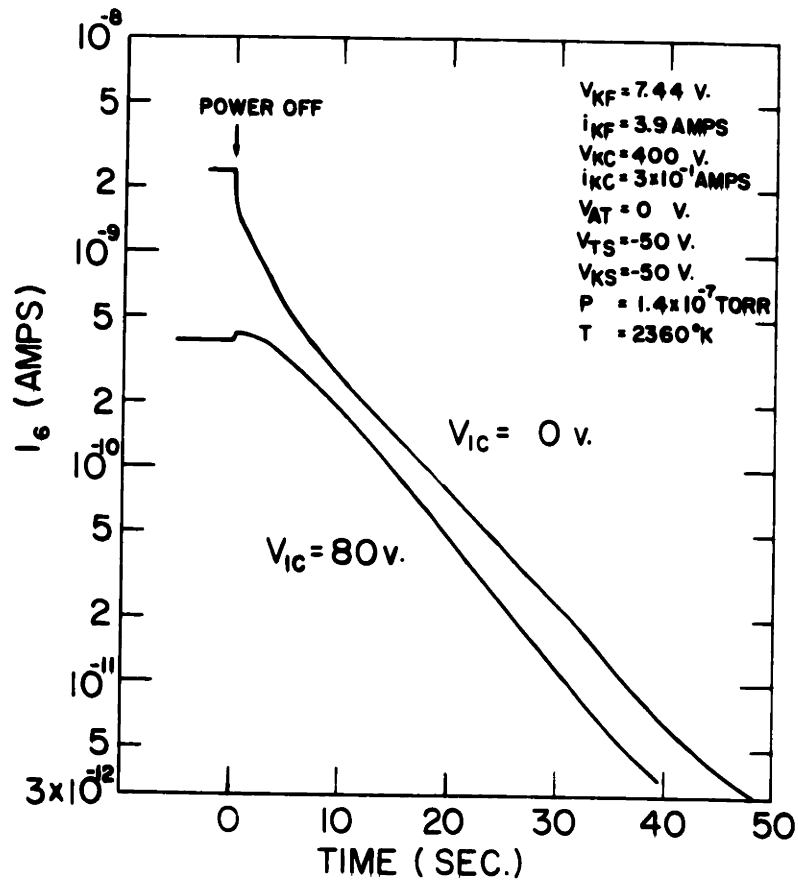


Fig. 24 Declining current characteristics for  $V_{IC} = 0$  and  $V_{IC} = 80$  volts. The ion current from the Knudsen cell and its shields initially dropped at a higher rate, but then approached the rate at which ions were released by the ion trap surfaces.

and using the slope of the plot one obtains,

$$(\psi - V_i) + E_d + \Delta Q = k \frac{d(\ln i^+)}{d(\frac{1}{T})} = \frac{\tan Q}{11605} = \frac{-2.44}{2.3026} = -1.06 \text{ eV} \quad (4.33)$$

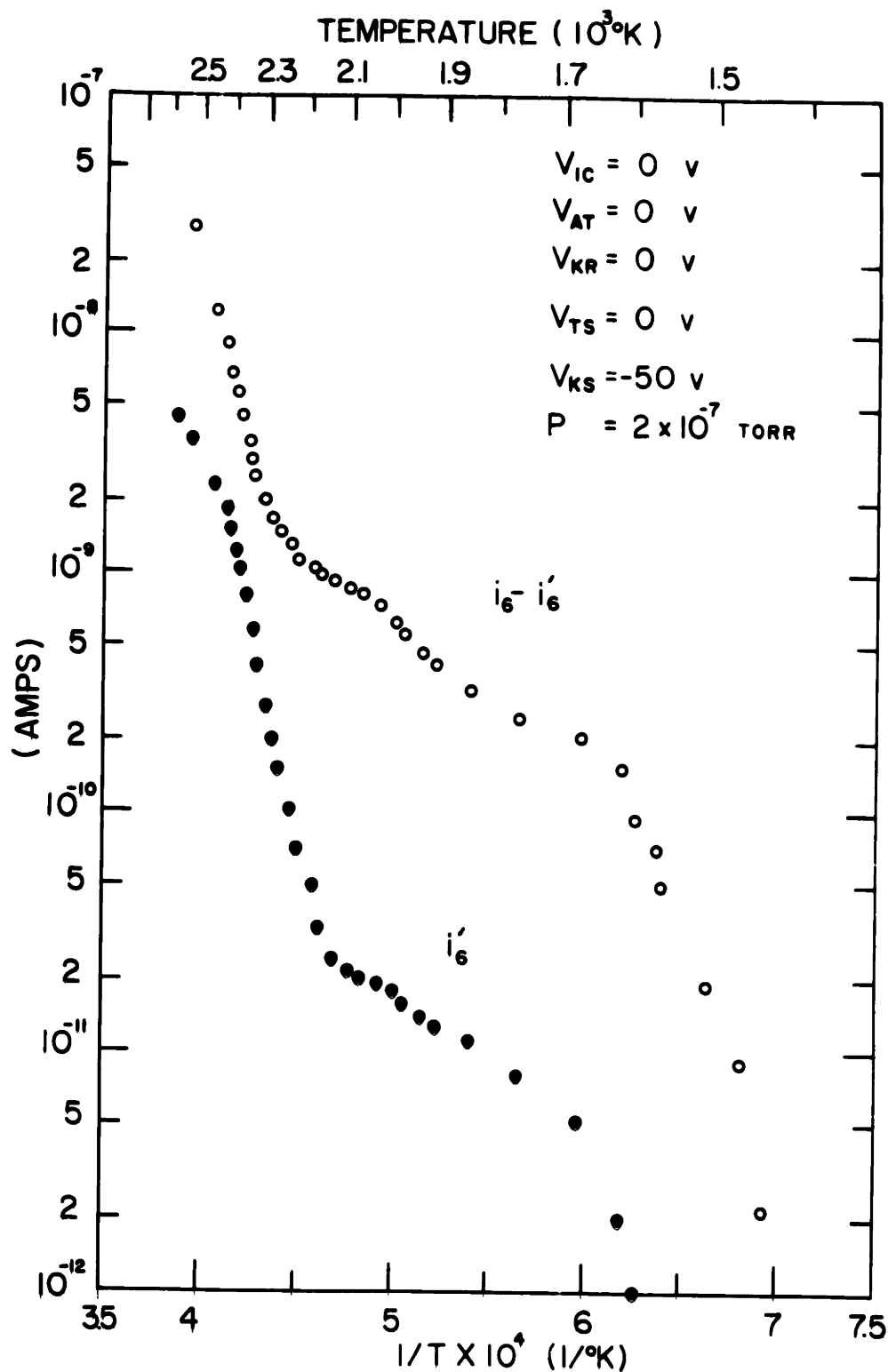


Fig. 25 Plot of collected ion current vs  $1/T$ .  $i_6$  is the current with  $V_{IC} = 0$  volts;  $i'_6$  is the ion current with  $V_{IC} = 80$  volts.

$$E_d + \Delta Q = 0.16 \text{ eV}$$

There is however, no data to verify this activation energy.

The net stray ion current ( $i_6 - i_6'$ ) is also plotted in Fig. 25 and similar features were observed. Recalling the 15 minute stabilization time for this current, the implication is that these may come from the trap and from the top heat shield to the ion collector. This supposition was strongly supported by using a redesigned trap made from a stack of copper plates with a large heat radiating area. The surfaces of this trap did not exceed  $800^\circ\text{K}$  even when receiving 20 watts of power and had a better geometrical configuration to prevent ions from reaching the collector by other paths. At a temperature of  $2500^\circ\text{K}$ , the ion current could be reduced to the order of  $10^{-11}$  amp as shown in Fig. 26.

The intended function of the Auger trap, to provide an electron barrier for electrons resulting from ion impacts, was also investigated. With the initially designed ion trap, the effect of the Auger trap was swamped by the dominant ion current. Results using the redesigned trap are shown in Fig. 27. When it was biased positive, an electron current of  $10^{-8}$  amp was observed. (This current could not have come from the filament because of the strong shield biasing.) Although some of the current was probably caused by Auger emission, most probably came from thermionic emission of the shield. The Auger emission coefficients (at 50 eV energy) are mostly less than 0.3, thus it is unlikely that the large number of electrons observed result solely from the Auger processes.

When the trap was biased at a negative potential and the electron

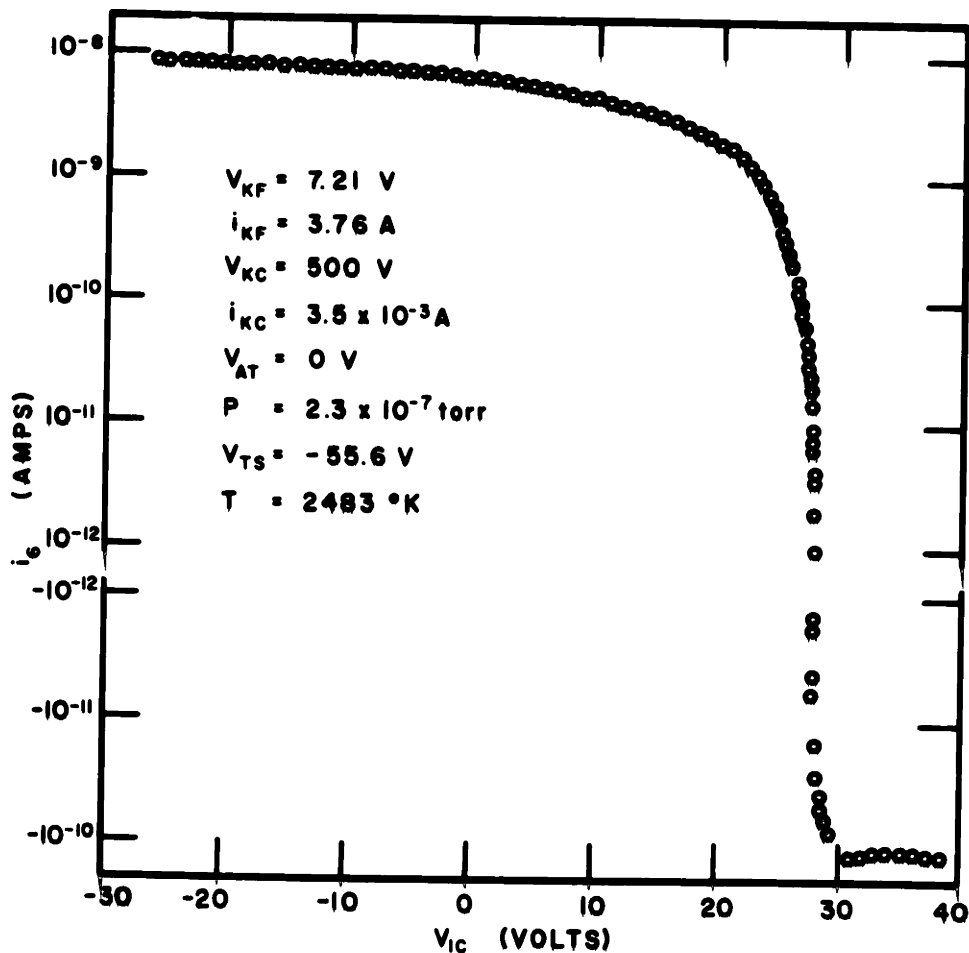


Fig. 26 Performance of the ion trap with the Auger trap inoperative.

An electron current was observed while the ions were retarded.

currents were cut off, a residual ion current of  $3.5 \times 10^{-11}$  amp still remained. This ion current apparently did not come from the Knudsen cell. It was probably due to the leakage ion current coming to the lead of the collector through the sides of the traps collected. In fact, it was found in a later test with the mass spectrometer and the electron and ion sources that careful shielding of the ion collector

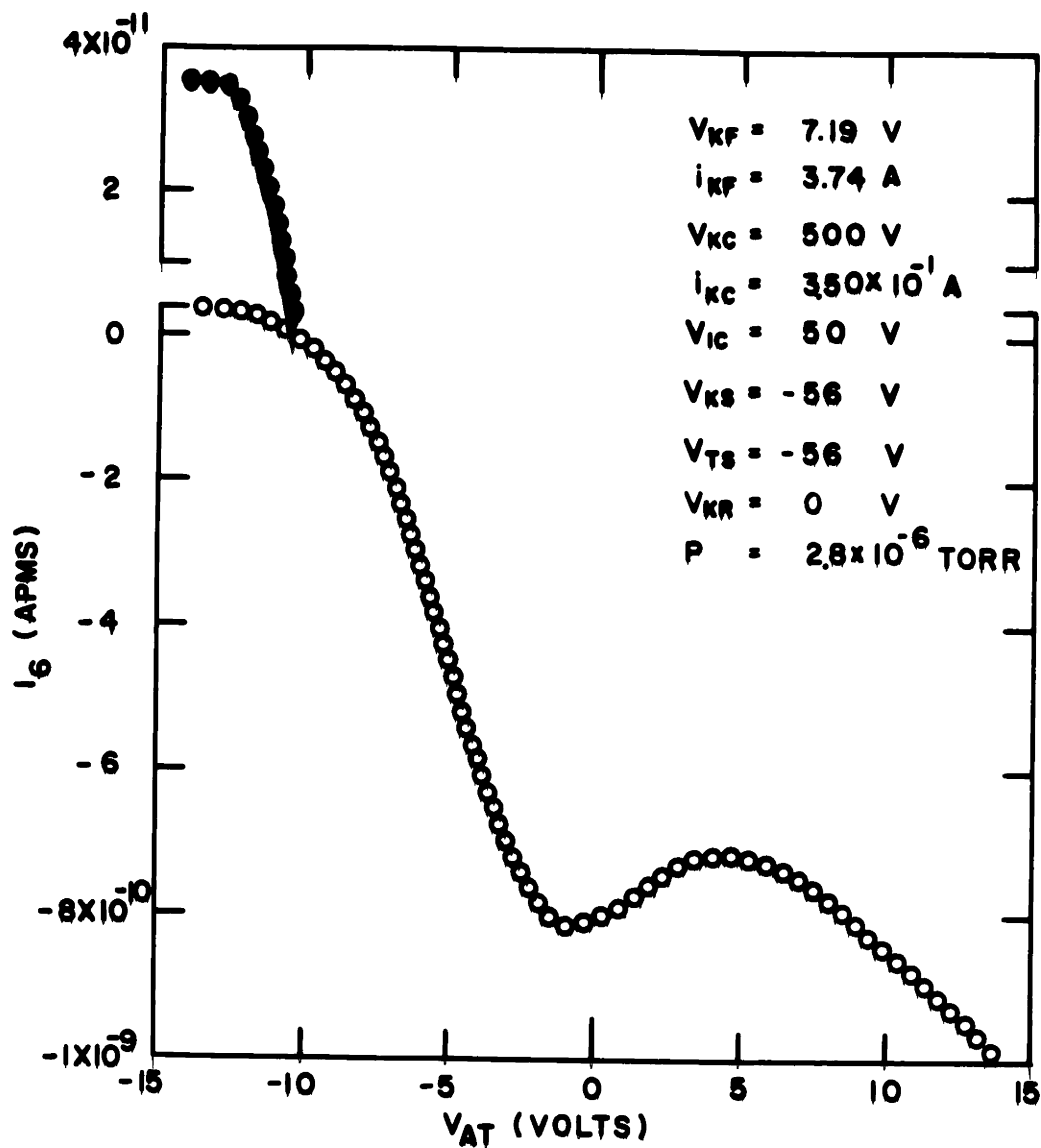


Fig. 27 Characteristics of the Auger trap; the focusing effect of the trap is revealed. At negative biasing, a stray ion current was observed, which probably came from the leakage current through other paths.

lead reduced the residue ion current to about  $2 \times 10^{-13}$  amp.

IV.6 Source Tests with the Mass Spectrometer

IV.6.1 Background Ions in the Source--The carbon source (Knudsen cell geometry) previously tested was investigated further with the mass spectrometer in the main system.

Unwanted ions were emitted from the Knudsen cell (as reported earlier), and these ions entered the ionization chamber when the trap voltages were off. Using the mass spectrometer these ions were mass identified as shown in Table II. The major background spectra immediately after turning the Knudsen cell off were also observed and tabulated in Table III for comparison.

TABLE II

Atomic Mass	18	23	28	36	39
Identification	$H_2O^+$	$Na^+$	$N_2^+$	$C_3^+ + HCl^+$	$K^+$
Counts	$5.5 \times 10^3$	$1.95 \times 10^4$	$4.3 \times 10^3$	$6.5 \times 10^2$	$5 \times 10^2$

Experimental Conditions--Table II

1) Knudsen cell	2) Electron gun--off	3) Ion source
$V_{KC} = 600V$		$V_{ID} = 10V$
$i_{KC} = 350mA$		$V_{IE} = 10V$
$i_{KF} = 5.6A$		$V_{IF} = 9.2V$
$V_{IT} = -180V$		
$V_{AT} = -20V$	4) $P_1 = 4.1 \times 10^{-8}$ torr	
$V_{EM} = 3.5KV$	$P_2 = 2.3 \times 10^{-7}$ torr	

TABLE III

Atomic Mass	17	18	27	28	29	36
Identification	HO <sup>+</sup>	H <sub>2</sub> O <sup>+</sup>	-	N <sub>2</sub> <sup>+</sup>	-	HCl <sup>+</sup>
Counts	4.0 x 10 <sup>3</sup>	1.0 x 10 <sup>5</sup>	3 x 10 <sup>3</sup>	4.2 x 10 <sup>4</sup>	4 x 10 <sup>3</sup>	3.0 x 10 <sup>3</sup>

Experimental Conditions--Table III

- |                         |  |                        |
|-------------------------|--|------------------------|
| 1) Knudsen cell--off    | 2) Electron gun                            | 3) Ion source          |
| V <sub>IT</sub> = -180V | V <sub>EE</sub> = 100V                     | V <sub>ID</sub> = 10V  |
| V <sub>AT</sub> = -20V  | i <sub>10</sub> = 1 x 10 <sup>-6</sup> amp | V <sub>IE</sub> = 10V  |
| V <sub>EM</sub> = 3.5kV |  | V <sub>IF</sub> = 9.2V |
- 4) P<sub>1</sub> = 3 x 10<sup>-8</sup> torr, P<sub>2</sub> = 3 x 10<sup>-7</sup> torr

The majority of ions released were <sup>23</sup>Na<sup>+</sup>, in contrast with the flashable tungsten wire experiment (cf. VI.I), in which the current was predominantly <sup>39</sup>K<sup>+</sup>. Only a small amount of <sup>39</sup>K<sup>+</sup> however was observed.

A comparison of Tables II and III indicates that the rest of the spectra were the result of ionization by electron impact within the source. The relation of <sup>23</sup>Na<sup>+</sup> to the temperature of the Knudsen cell is shown in Fig. 28 where the logarithmic output of the spectrometer is plotted vs. 1/T.

To explain these data, the flashable wire case was considered: K (ionization potential of 4.32 eV) on tungsten (work function of 4.52 eV). The ionization potential (V<sub>i</sub>) of K is lower than the work function (ψ<sub>i</sub>) of tungsten, thus, almost full surface ionization takes place at a



lower temperature (1000°K). At first large amounts of  $K^+$  ions were flashed away from the surfaces. Eventually the  $K^+$  current was reduced to a diffusion-limited surface ionization value. The flashing time constant may be obtained by solving the diffusion equation using the evaporation law.

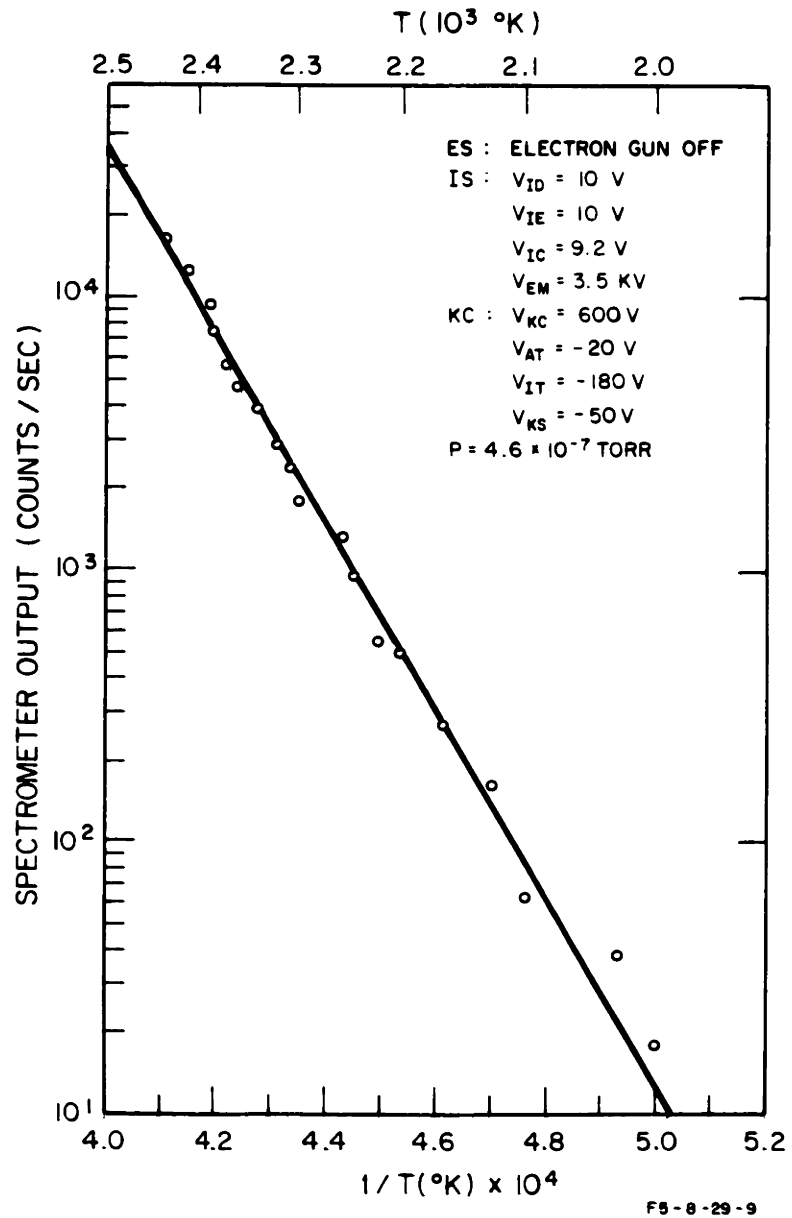


Fig. 28  $Na^+$  as it comes from a Knudsen cell made of Ta. The  $1/T$  relationship is shown.

On the other hand, the ionization potential of Na ( $V_i = 5.12V$ ) is always larger than the work function of tungsten. Surface ionization hardly occurs around  $1000^\circ K$ , thus, most of the alkali metal impurities come out as neutrals. As the temperature is increased however,  $Na^+$  current will increase, according to the Saha-Langmuir Law with the neutral intensity governed by the diffusion process and the evaporation laws. Thus the  $K^+$  ions are dominant in a tungsten surface (even when the impurity concentration of Na is greater than that of K).

In the present case, the ionization potentials of both Na and K are higher than the work function of Ta ( $\psi = 4.13V$ ). The surface coefficients for K and Na are about the same. To have the ion current dominated by  $Na^+$ , the concentration of Na on a Ta surface must be higher than the K impurity. (Note also that a few  $Na^+$  ions may come from electron impact within the source. However, according to Table II and the previous tests, ions from electron bombardment can hardly escape because of the geometrical configuration of the source.) In this case, by looking at the potential energy diagram, Fig. 29, the relation between the ion current and the temperature would be:

$$\begin{aligned}
 i^+ &= A \exp \left[ \frac{e}{kT} (\psi - V_i - \Delta Q) \right] e^{-\frac{E_d}{kT}} \\
 &= A \exp \left[ \frac{e}{kT} (\psi - V_i - \Delta Q - E_d) \right]
 \end{aligned}
 \tag{4.34}$$

where  $E_d$  is the activation energy for sodium to diffuse through the polycrystalline tantalum;  $\Delta Q = E_a - E_i$ , depends also on surface conditions.

From Fig. 28, a measurement of slope shows that

$$\psi - V_i - \Delta Q - E_d = -1.29\text{eV}$$

$$\Delta Q + E_d = 0.3\text{eV}$$

which is about two times the result obtained from the total ion current (Equ. 4.33). This discrepancy is apparently due to the fact that the total ion current includes other species than  $\text{Na}^+$  (e.g.  $\text{K}^+$ ).

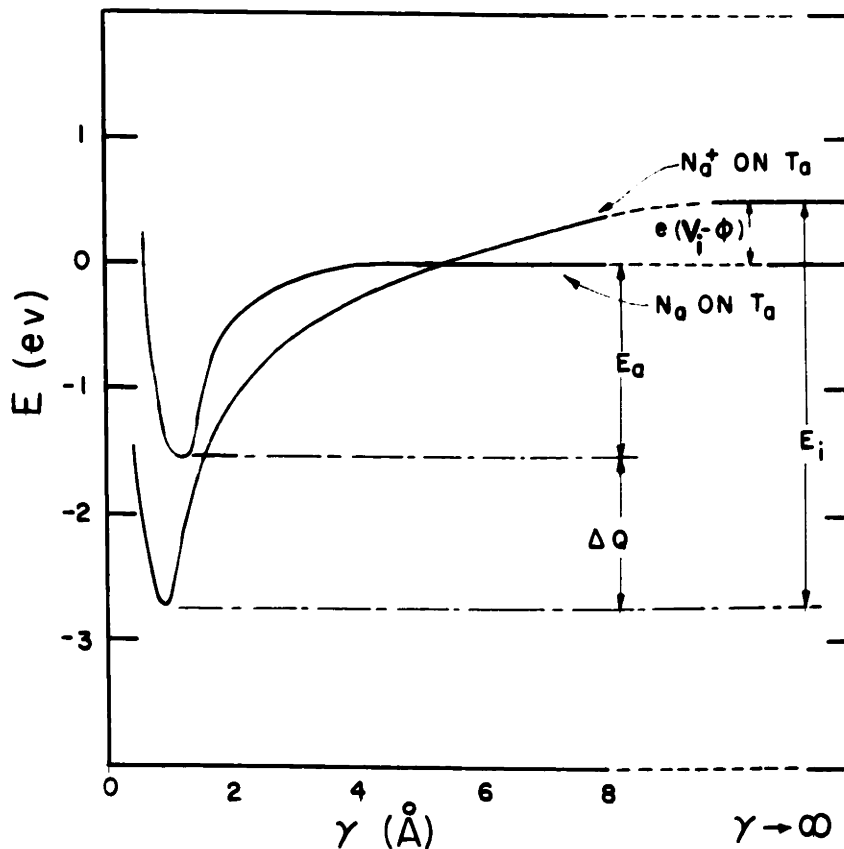


Fig. 29 Potential Energy Diagram of Na and  $\text{Na}^+$  on a Ta surface

The amount of impurity depends, of course, on the metallurgy used in the manufacture of the tantalum or tungsten. Alkali free tungsten has

been obtained.<sup>58</sup>

The present model not only explains the tantalum ion emission in the present case, but also qualitatively explains the ionization chamber extraction grid results<sup>55</sup> and the results of other workers<sup>59</sup>.

IV.6.2. Source Induced Multiplier Noise--Some small coherent background existed when the Knudsen cell was heated. The following observations implied that these counts resulted from neither ions nor electrons:

- 1) They were not mass selectable.
- 2) They persisted when the resolution control was set above infinite resolution.
- 3) They did not depend on any ion source parameter, e.g.  $V_{IE}$ ,  $V_{ID}$ , or  $V_{IF}$  (thus it is hard to believe them to be ions).
- 4) With the electron multiplier biased for ion detection (negative 3.5kV) no electron could possibly reach it.

Only a few possibilities seem likely: first, that the counts were the result of thermal photons scattered through both the ionizer and the spectrometer. Second, that they were the result of soft X-rays generated by electron bombardment of the Knudsen cell. An X-ray photo-effect however would be dependent on the bombarding electron energy. By varying current and voltage at constant power, this was shown not to be the case. Thus, the background is apparently the result of thermal photons. Experimentally it was approximately proportional to the Knudsen cell input power.

Statistical fluctuation made it difficult to verify this proportionality. At such low count rates the analog ratemeter approached its

detection limit. To obtain better data, a digital counter with a longer time base should be used.

A theoretical relationship between the photo-electron flux and temperature can be derived by integrating the product of Fowler's Equation<sup>56</sup> and the Planck radiation distribution function at  $T_K$ , where  $T_K$  is the temperature of the cell.

Assuming  $T_s$  to be the surface temperature of the first dynode, and  $\nu_o$  to be the threshold frequency (equal to  $\frac{e\psi}{h}$  where  $\psi$  is the work function of the first dynode), one has

$$i_\psi \propto \frac{8\pi h}{c^3} \int_{\nu_o}^{\infty} d\nu \frac{\nu^3}{e^{h\nu/kT_{k-1}}} \int_{\omega_a - h\nu}^{\infty} d\omega_x [1 + e^{\frac{\omega_i - \omega_x}{kT_s}}] \quad (4.35)$$

After changing the variable,  $\delta = \frac{h(\nu - \nu_o)}{kT_s}$ , Equ. 4.35 becomes:

$$i_\psi \propto T_s \int_{\nu_o}^{\infty} d\nu \frac{\nu^3}{e^{h\nu/kT_{k-1}}} f(\delta) \quad (4.36)$$

where

$$f(\delta) = \int_{-\infty}^{\delta} \ln(1 + e^t) dt \quad (4.37)$$

At 2400°K and with  $\delta \approx 0$ , the dominant term of Equ. 4.36 after integration becomes:

$$i_\psi \propto T_k^5 \quad (4.38)$$

This equation indicates that the photo-electric emission should be

almost linearly proportional to the input Knudsen cell power, as experimentally observed.

It is also possible that some of these counts came from stray ions scattered through the surroundings of the mass spectrometer. However, because of geometrical configuration, ion scattering should be very small.

## V. ELECTRON SOURCE AND TESTS

A simple electron gun, essentially just a filament, a grid aperture, and an einzel lens, was used for the moderate to high energy studies. A coaxial cylinder electron monochromator was used for low energies and to study threshold behavior. Studies were made on beam profiles, and lens properties, and on electron and other stray effects. A feedback controller to provide a constant beam current as the beam energy varied, was designed and built.

### V.1 Electron Gun and Collector

For studies of ionization cross sections at moderate and high energies, an electron gun consisting of a grid aperture and an einzel lens was used to provide a beam of about 1 to 2 mm in diameter. This assembly is shown in Fig. 30. A W-3%Re wire of 0.0127 mm diameter was used as a directly heated cathode, with a heating current of about 2 amps. After emerging from the einzel lens, the electrons next passed through the ionization chamber, then into an electron collector. A special electrode was used for secondary electron suppression. In order to prevent electron scattering, grids were not used. The electron collector with its shield is shown in Fig. 31. Construction details for the gun and collector are described elsewhere.<sup>55</sup> Beam transmission from the ionizer to the collector was better than 97%. For a beam energy higher than  $V_{EG}$ , the focus voltage ( $V_{EF}$ ) is shown to be proportional to the beam energy as described in Fig. 32. A secondary electron and scattering current equal to about 3% of the primary beam was apparently

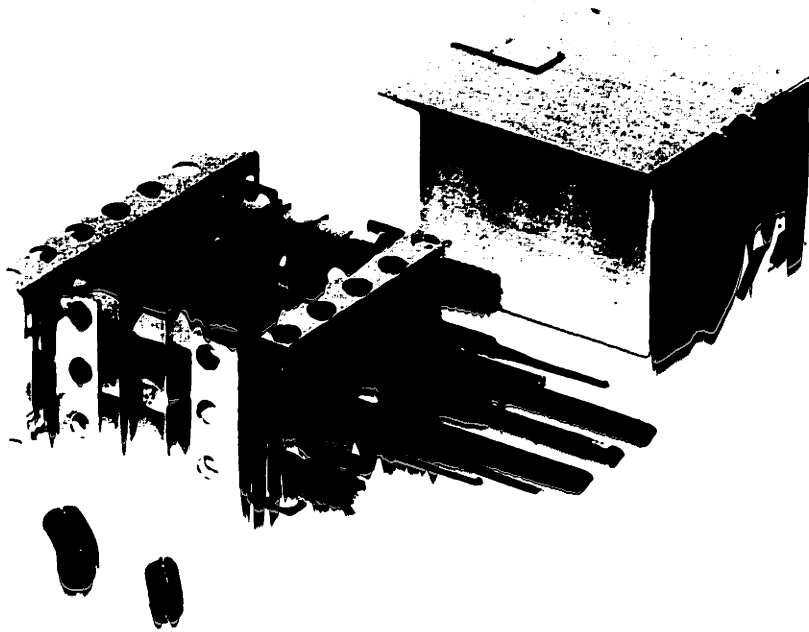


Fig. 30 Electron gun assembly. The shield shown was removed.

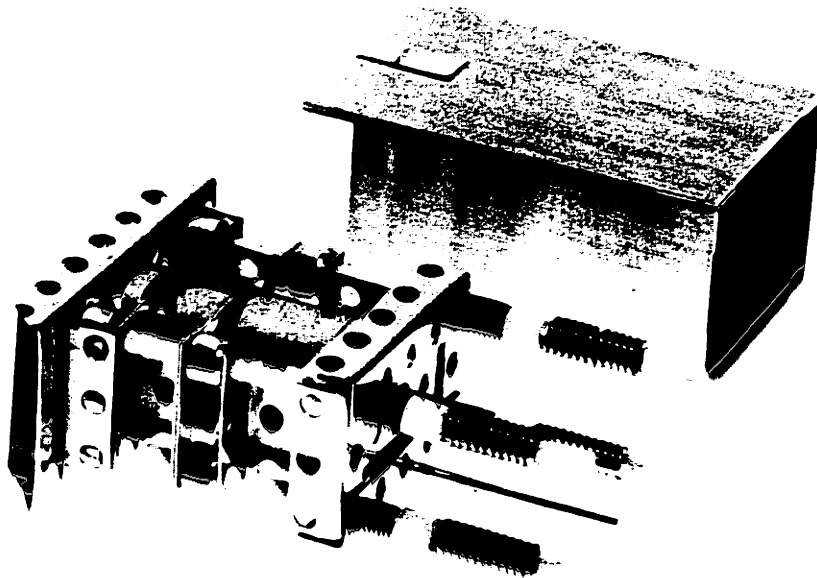


Fig. 31 Electron collector assembly. The shield is held on by friction fit.



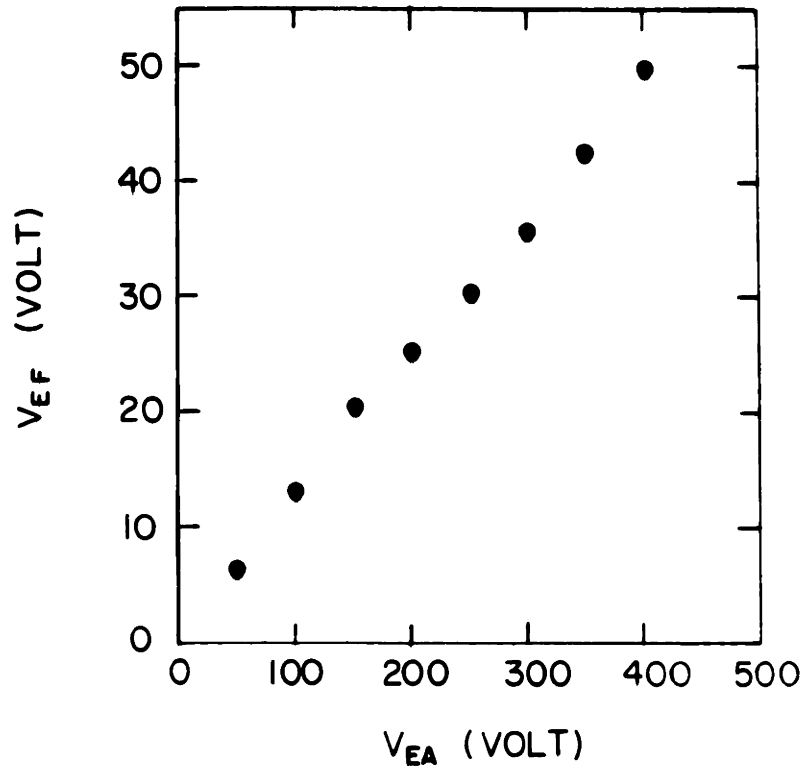


Fig. 32 Lens properties of the electron gun. The focussing voltage required is almost proportional to the beam energy.

due to scattering by the wire forming the ionization chamber main grid.

This effect is illustrated in Fig. 33 (a and b) using a retarding potential.

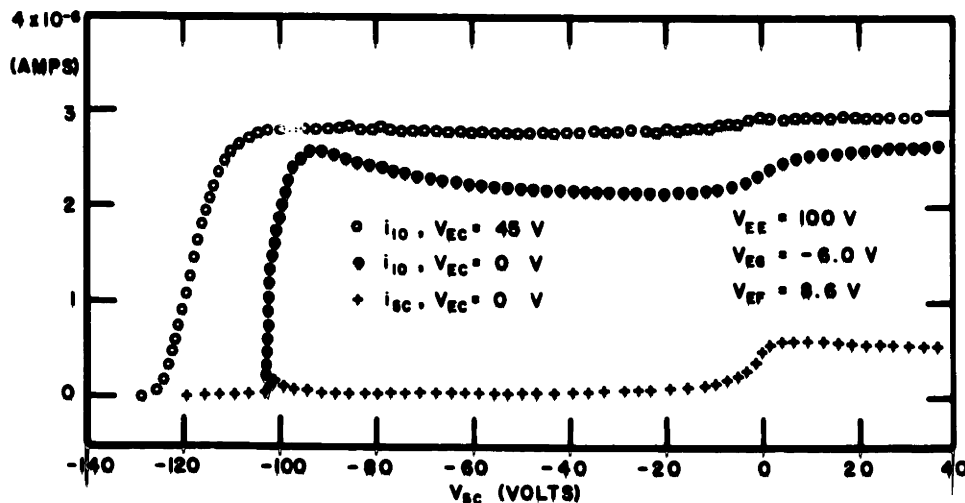


Fig. 33(a) Retarding potential study of the electron gun. Fringing field effect can be noted by the difference between  $V_{EC} = 0$  and  $V_{EC} = 45$  V.

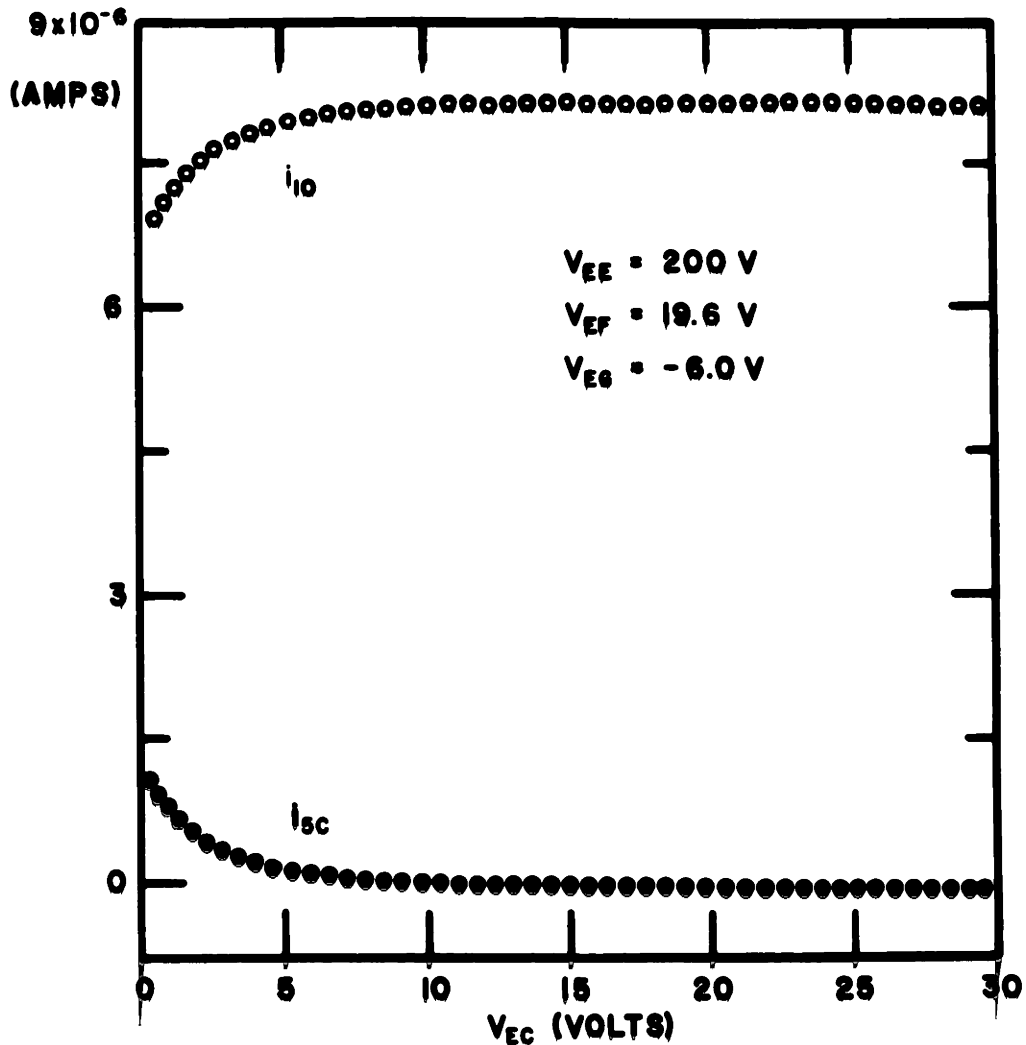


Fig. 33(b) Secondary electron from the collector.  $i_{10}$  indicates the collector current and  $i_{5c}$ , the current to the shield.

No significant number of secondary electrons appeared to escape the positively biased electron collector, however a positive current coming from the secondary electron suppression electrode (and shields) was observed. This probably resulted from photo-electron emission of the electrode under X-ray bombardment which arose from the high-energy electron impacts on the collector surface. Another possible source would

be secondary electrons emitted from the suppressor electrode. Third would be ions produced on the collector surface by electron impact desorption. The positive current increased approximately linearly with the electron beam energy from 100 to 1,000eV as shown in Fig. 34. An X-ray effect could be partially eliminated by using an electron collector with a skew surface. However, the magnitude of this current from all these sources is only about 1% of the total electron current. Thus, no further investigations were felt necessary.

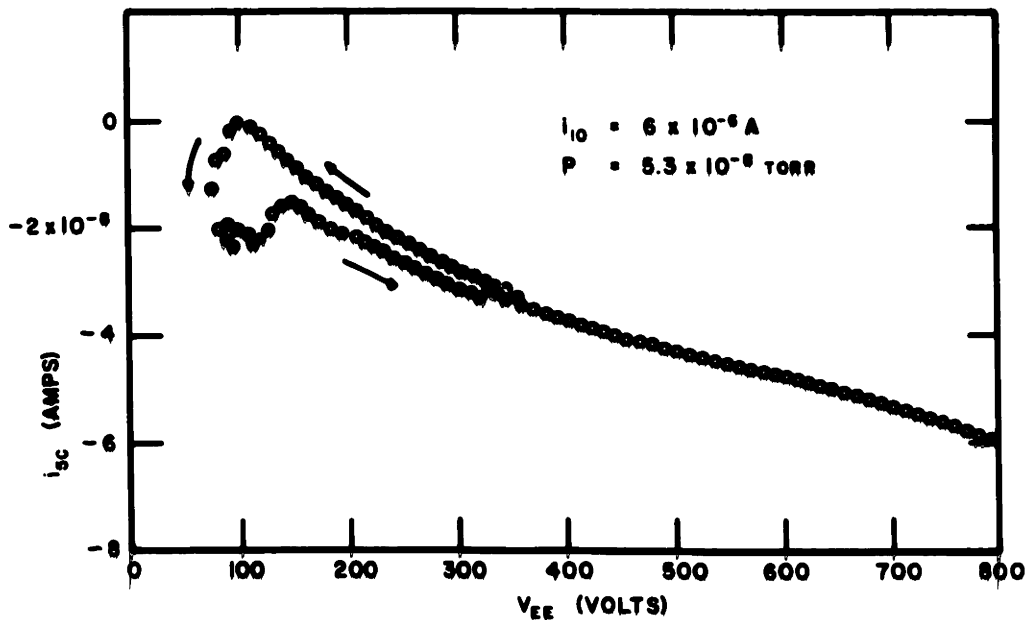


Fig. 34 Current coming from the electron collector shield.

The "loop" is probably due to contamination.

The potential fringing out of the collector shield due to  $V_{EC}$  can be observed in Fig. 33(a) even though the main grid of the ionization chamber should shield the chamber from  $V_{EC}$ . A suppression voltage

$V_{EC}$ , of 10 volts is the optimum for reducing secondary electrons without excessive field penetration.

To further test the gun, a pin hole beam scanner was placed in front of a Faraday cup electron collector, and mounted in another vacuum system. A schematic diagram is shown in Fig. 35. It was again observed

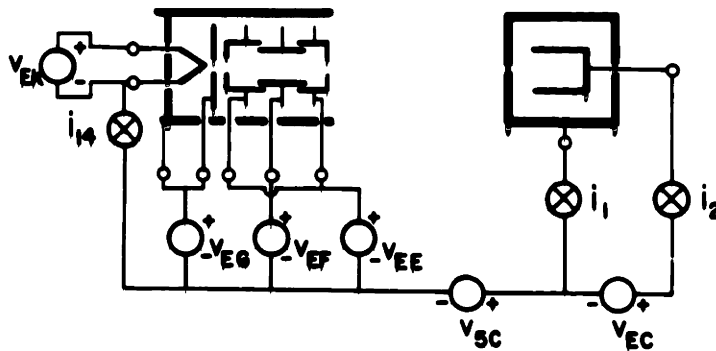


Fig. 35 Schematic diagram for the electron gun test.

that great care is required when operating in a poor vacuum, to avoid the formation of insulating deposits which charge up and seriously disrupt the beam (causing a gradual loss of transmission and fluctuations in the required focus voltage  $V_{EF}$ ). It was also observed that the secondary electron emission was a more significant effect than had been previously anticipated, particularly in the case of uncoated stainless steel surfaces. Several surfaces were coated with Aquadag and various forms of carbon soot in order to reduce these effects. Aquadag-coated surfaces were found to reduce the contamination initially, but deteriorated

with use. Observation of the coated surfaces indicated a destruction of Aquadag by electron bombardment. Carbon coatings are apparently not very stable in low vacuum systems, and may only be suitable in oil free high-vacuum systems. Further experiments with sand-blasted stainless steel showed no degradation; and this material was used for the remaining measurements.

Attempts to add more collimating apertures resulted in so much beam scattering that the profile study indicated a wider divergence than for a single aperture alone.

The density profile of the beam current in the single aperture gun (without Aquadag) is shown in the top of Fig. 36, with the radial half-current-density contour at the bottom. The beam diameter was about 1.6 mm. Contrary to expectations, it was observed that the beam was elliptical in cross section with Y being the major axis. (The hairpin filament was mounted in the X-Z plane.)

The Aquadag-coated surfaces gave similar profiles, however profiles for clean and for contaminated surfaces are illustrated in Fig. 37.

Fig. 38 shows  $i_1$  and  $i_2$  vs  $i_{14}$ . The extraction efficiency of the gun is almost constant over the indicated current range. A retarding potential used to measure the energy spectrum of the beam current, resulting in data similar to that in Fig. 33.

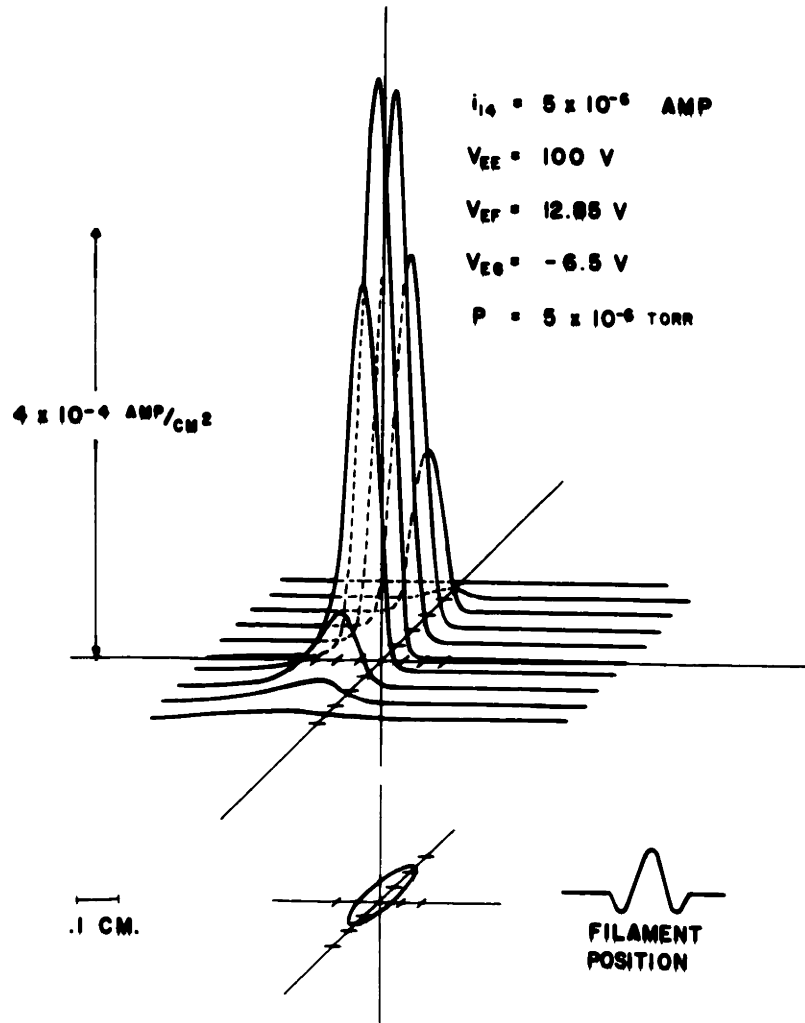


Fig. 36 Electron beam profile with the half high contour. The filament position is also shown on the right below.

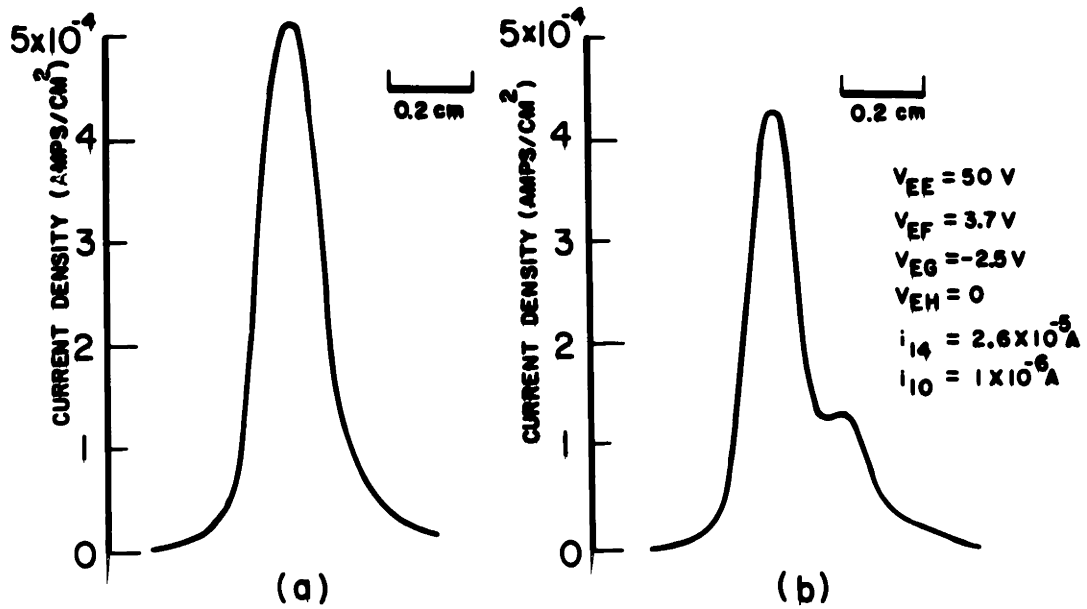


Fig. 37(a) Profile for a clean surface  
(b) Profile for a contaminated surface

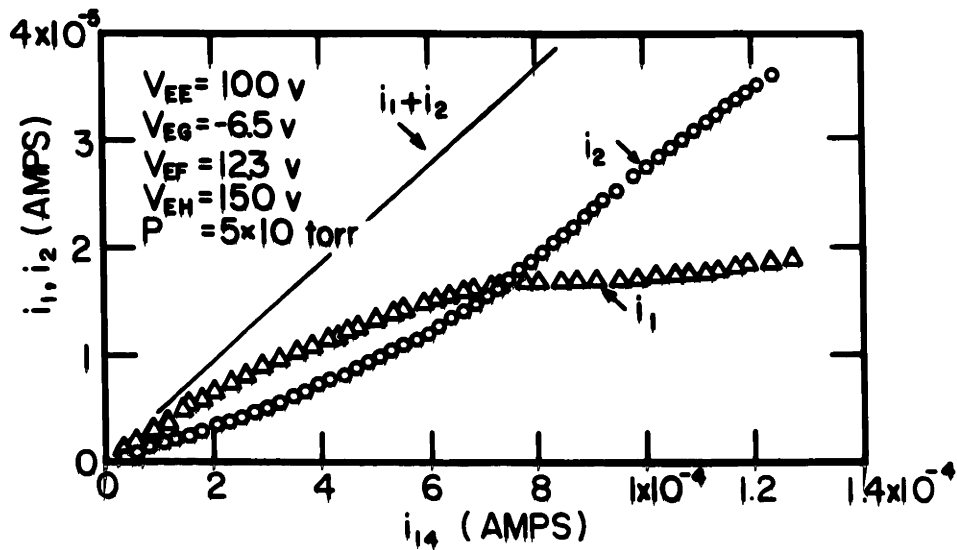


Fig. 38  $i_1$  and  $i_2$  with respect to the total emission current  $i_{14}$ .  
The saturation of  $i_1$  at higher  $i_{14}$  occurs when the space charge effect comes in to widen the beam profile.

## V.2 Electron Beam Control

For convenience in data taking, it is necessary to stabilize the beam current when the electron energy ( $V_{EE}$ ) is varied. To this end, a constant-current feedback control unit was designed and constructed. A schematic is shown in Fig. 39. The controller was made from commercial high-gain operational amplifiers and a Darlington-circuit current amplifier. A Keithly 601 Electrometer was used as the collector current sensor. Because of the high potential difference between the electron collector and the gun cathode, high-voltage reed relays and sampling capacitors were used to bring the signal from collector potential down to cathode potential.

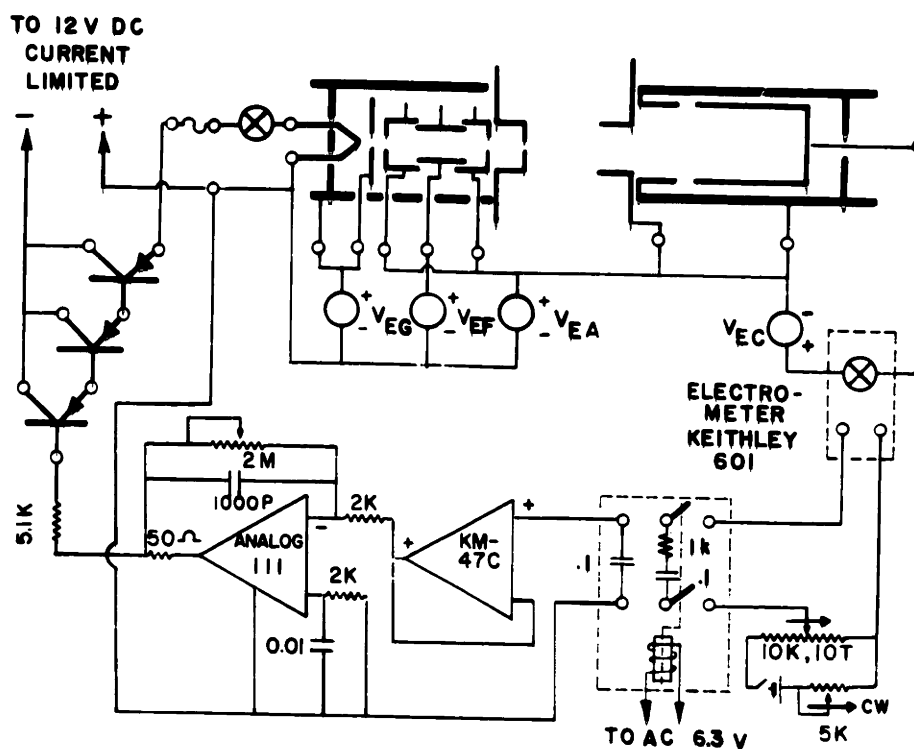


Fig. 39 Schematic diagram of the electron beam controller.



Oscillations occurred for collector currents lower than  $10^{-7}$  amp due to the time constant of the electrometer, the sampling capacitor, and the finite switching time of the reed relay. Thus a compensation network was added, where upon performance was satisfactory with currents from  $10^{-5}$  to  $10^{-8}$  A. The constancy of the collector current with respect to the change in  $V_{EF}$  is displayed in Fig. 40. Overall stability was about 0.4%, depending largely on the differential transfer function of the electron gun.

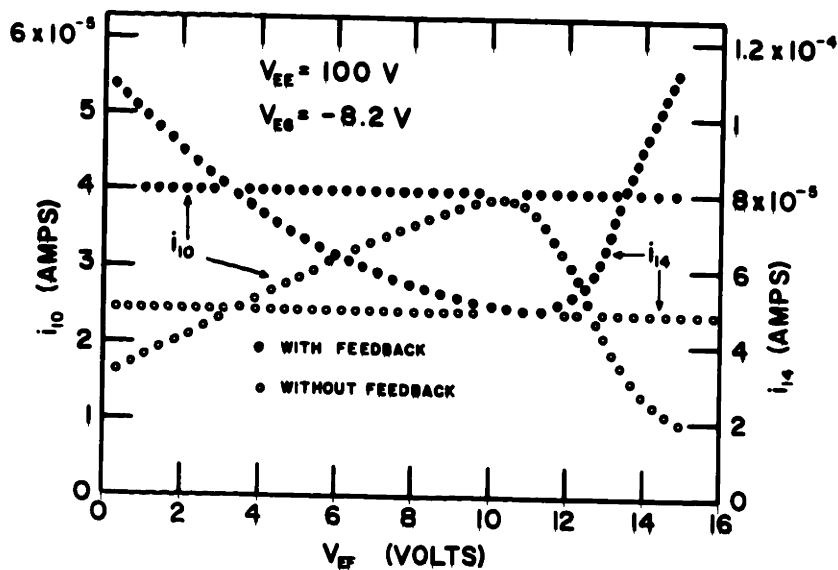


Fig. 40 Characteristics of the electron beam controller.

Without the controller, using a constant filament current supply, the emission current was observed to be almost constant, while the beam current changed with the focus voltage. With the controller, a constant beam current was maintained.

### V.3 Coaxial Cylinder Mirror Electron Monochromator

In order to study the threshold behavior of electron impact phenomena, an electron monochromator with a narrow energy spread is required.

Spherical condenser and cylindrical mirror monochromators, both of which possess two dimensional focusing, were considered. Details of the analysis following the equation of motion have been made for both types. Their advantages may be compared as follows:

- a) It can be shown that the cylindrical mirror monochromator has second order focusing and possesses a third order spherical aberration while the spherical condenser type has first order focusing and possesses a second order spherical aberration.
- b) The reduced dispersion of the cylindrical monochromator at second order focusing is given by<sup>65</sup>

$$d_p = \frac{D}{L} = \frac{5.6a \frac{\Delta E}{E}}{6.12a} = 0.91 \frac{\Delta E}{E}, \quad (5.1)$$

while that for the spherical condenser type is

$$d_p = \frac{D}{2R} = \frac{2R \frac{\Delta E}{E}}{2R} = \frac{\Delta E}{E}. \quad (5.2)$$

Here  $a$  is the radius of the inside cylinder;  $R$  is the radius of the central ray; and  $L$  is the trajectory path in the  $z$  direction. Eqs. 5.1 and 5.2 are almost identical.

- c) Because the cylindrical type possesses a higher order focusing, its acceptance is larger than that of the spherical type in

the  $\theta$ -direction. Furthermore in the median plane its acceptance is a factor of two larger than the spherical type's (since only one-half of the sphere can be used as opposed to a full cylinder for the coaxial type). The acceptance will be calculated in detail in section V.4.

d) In the cylindrical type, rays enter the monochromator at an equipotential surface, therefore there is no fringe field effect.

In summary, a criterion for the choice of a monochromator (or any analyzer) can be stated as:

$$M = PA \quad , \quad (5.3)$$

where M is a figure of merit, P is the resolving power of the analyzer, and A is the acceptance area of the analyzer. This figure of merit is very similar to the gain-bandwidth product for an amplifier. Because of its overall advantages, the cylindrical mirror type monochromator was chosen.

Fig. 41 shows the monochromator with associated electron lenses (including an electron source and an injection lens for the ionizer). Only half of the cylinder was used because of mounting convenience and the resulting reduction in angular divergence. Were the whole cylinder used the output beam would have been shaped like a hollow cone with an angular divergence of almost  $\frac{\pi}{4}$ . Following the Abbe-Helmholtz sine law, it would be difficult to focus this beam onto an ionizer where a small emittance is required.

Some important design quantities are listed below:

Radius of the inside cylinder:  $a = 4.76$  mm

Radius of the outside cylinder:  $b = 11.85$  mm

Theoretical calculated voltage ratio:  $\frac{V_{EA}}{V_{ED}} = 1.323 \frac{1}{\ln(\frac{b}{a})} = 1.44$

Diameter of the energy selection apertures (i)  $d_1 = 0.792$  mm

(ii)  $d_2 = 0.396$  mm

Under the optimal condition for maximum current (as shown in section V.4.2) the calculated effective resolution<sup>60,61</sup> (full width of half magnitude: FWHM):

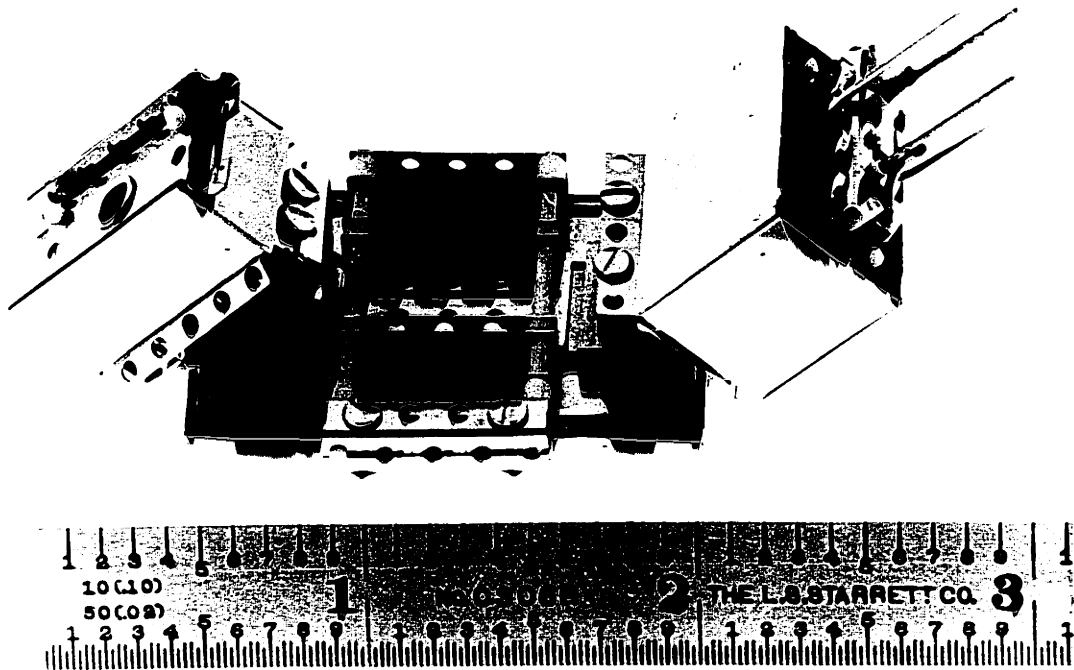


Fig. 41 The electron monochromator assembly. The electron gun is shown at the right and the injection lens at the left.

$$\eta \cong \left( \frac{s + \omega + \rho}{6.2a} \right) \left( \frac{\pi}{4} \right) \quad (5.4)$$

where s: source length along the axis

$\rho$ : radius of the source disc

$\omega$ : selection aperture width or diameter

Since the selection aperture was located perpendicular to the main ray one has

$$\begin{aligned} \omega &= (d/\cos\theta_o) \left( \frac{\pi}{4} \right) \\ \rho &= 0 \end{aligned} \quad (5.5)$$

$$s = (d/\cos\theta_o) \left( \frac{\pi}{4} \right)$$

and

$$\eta = \frac{d}{a} \left( \frac{2}{6.2 \cos\theta_o} \right) \left( \frac{\pi}{4} \right)^2 \quad (5.6)$$

where  $\frac{\pi}{4}$  is due to the circular aperture used (cf Appendix 3).

Thus the resulting resolutions are

$$(i) \text{ for } d_1, \quad \eta_1 = 4.7\%$$

$$(ii) \text{ for } d_2, \quad \eta_2 = 2.35\% \quad .$$

Fig. 42 shows the monochromator partially disassembled. Two coated semicircular discs having approximate resistance surfaces of  $100K\Omega$ , (made by a thick film technique\*) were used both for supporting the

---

\* Author wishes to thank Mr. H. Plicher and Microelectronics Group (Group 77) of Lincoln Laboratory (M.I.T.) for their courtesy in preparing and processing these surface resistors.

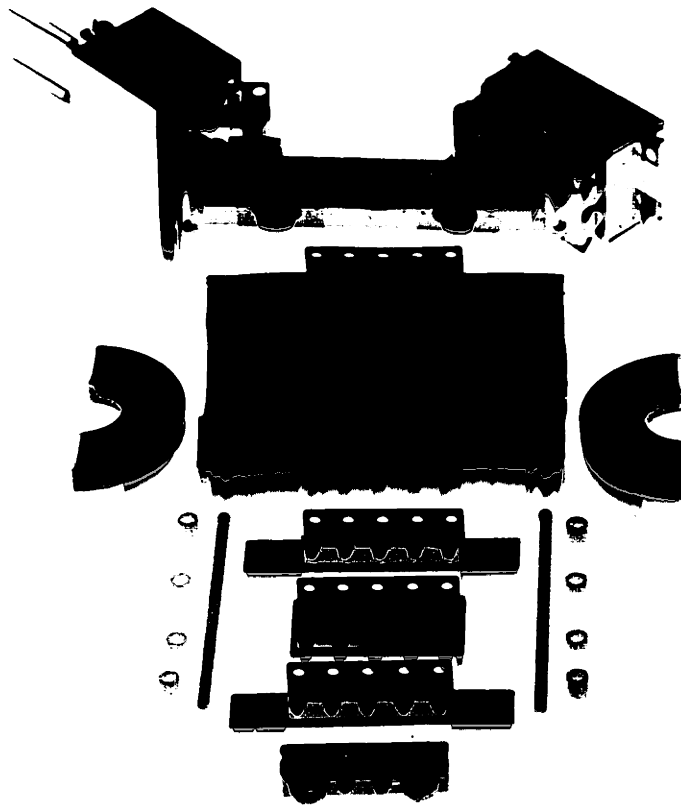


Fig. 42 Overall view of the monochromator. Two thick film resistors are shown in the middle, serving to support the inner cylinder. The contact edges of these resistors are gold-coated. The electron gun and the injection lens are attached to the inner cylinder.

two cylindrical electrodes and as electric field terminating boundaries. The field boundaries in the axial plane are two metal plates whose potential can be adjusted to give maximum transmission. The inner

cylinder was made out of a solid piece of stainless to allow convenient mounting of the associated lens. In Fig. 43, the electron gun is shown at the right and the injection lens at the left.

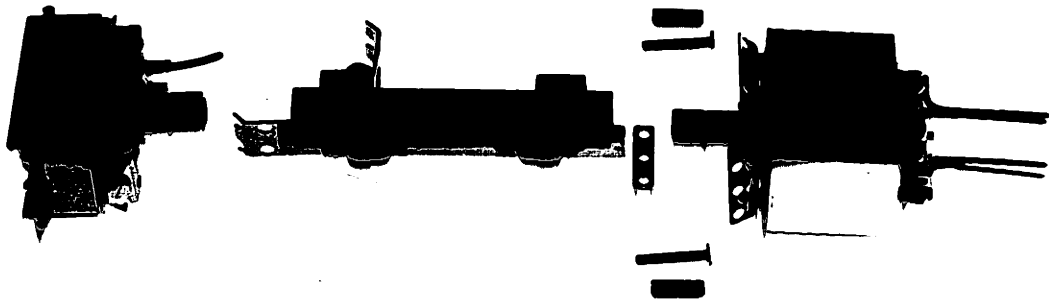


Fig. 43 View of the inner cylinder disassembled. The apertures are spot welded to the lens electrode, and can be readily changed by replacing these electrodes. The electron gun is on the right, the injection lens on the left.

The entrance and exit ports in the inner cylinder are covered with Ni mesh ( $100 \times 100/\text{in}^2$ ). Details of the electron gun are shown in Figs. 44 through 46. The injection lens is shown in Figs. 47 and 48. The monochromator is shielded with one layer of shield  $\mu\mu$  30  $\mu$ -metal\* and one

---

\* obtained from Magnetic Metals Company, Camden, New Jersey

of shieldmu 10 $\mu$  -metal.

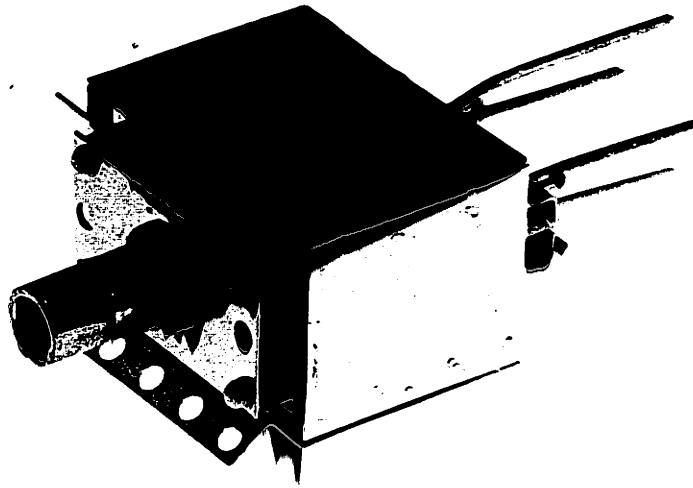


Fig. 44 Close-up of the electron gun.



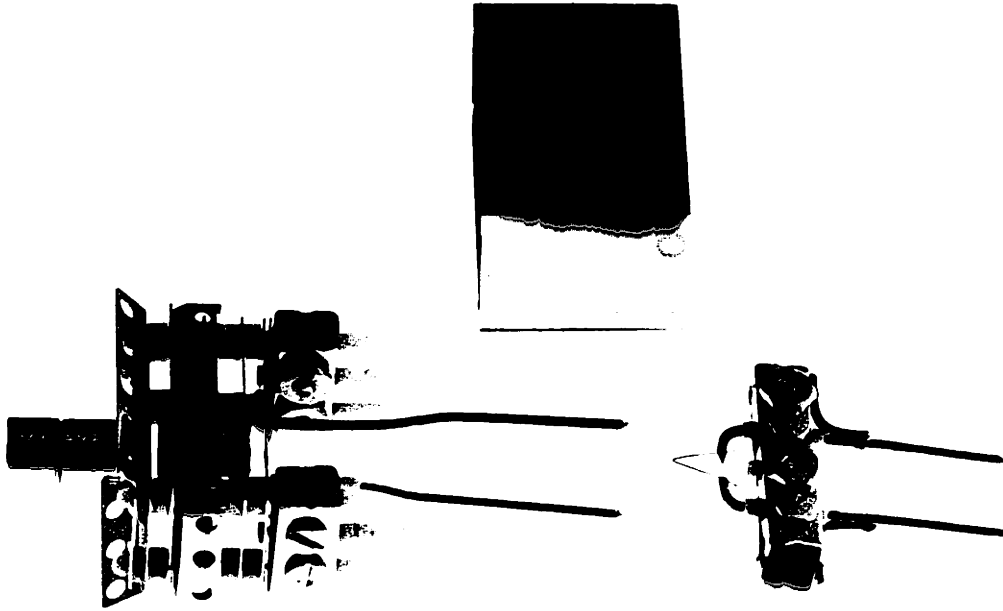


Fig. 45 Partially disassembled electron gun. The shield is a friction fit. The filament can be slid along the two central ceramic rods and then tightened.

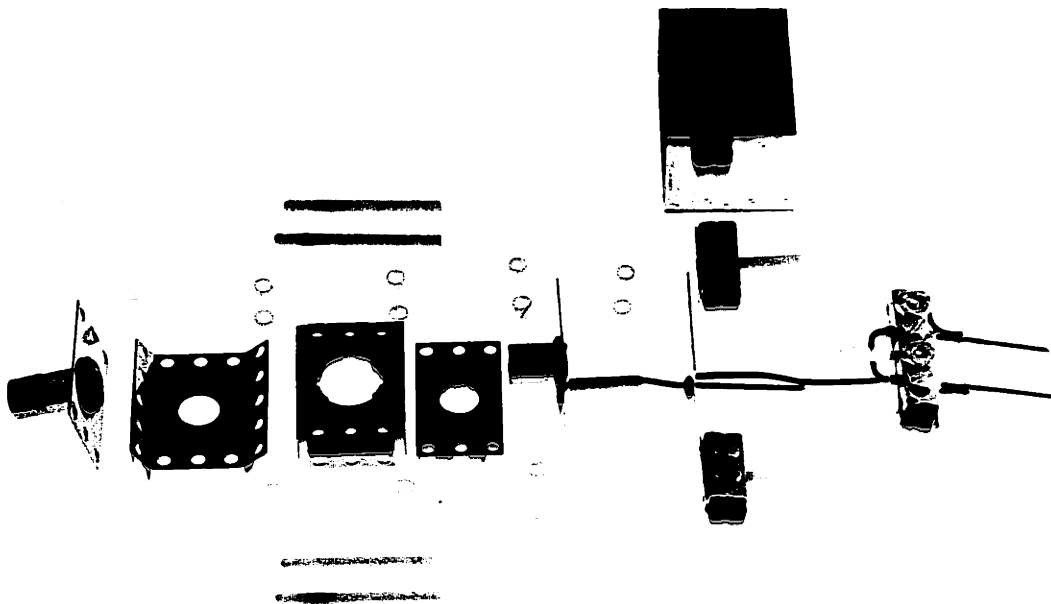


Fig. 46 Assembly details of the electron gun.

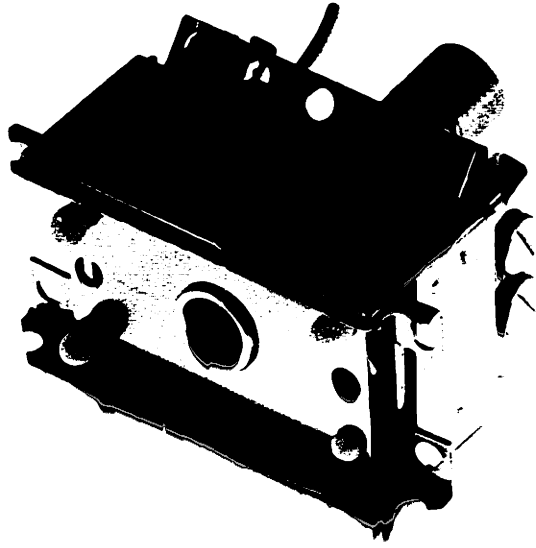


Fig. 47 Close-up of the injection lens

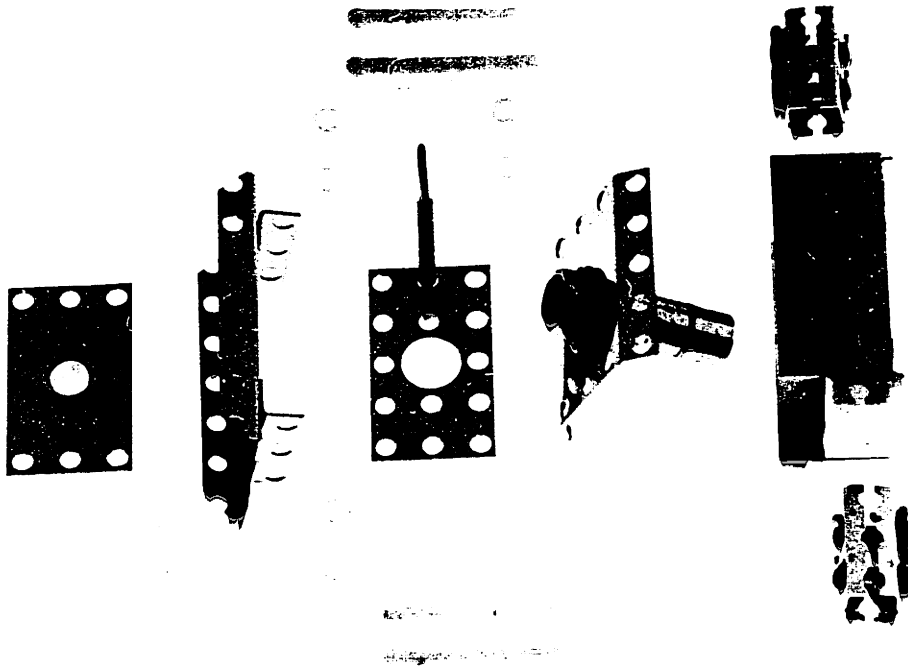


Fig. 48 View of the dismantled injection lens

During the tests, the monochromator was mounted on a 6-in. flange along with a parallel-grid retarding potential analyzer in a high vacuum system (as shown in Fig. 49). A wiring diagram is shown in Fig. 50 with notation as shown in Table IV. Fig. 51 shows the linear relationship between the beam energy and the deflection voltage ( $\frac{V_{EA}}{V_{ED}} = 1.42$ ) in good agreement with the calculated value 1.44.

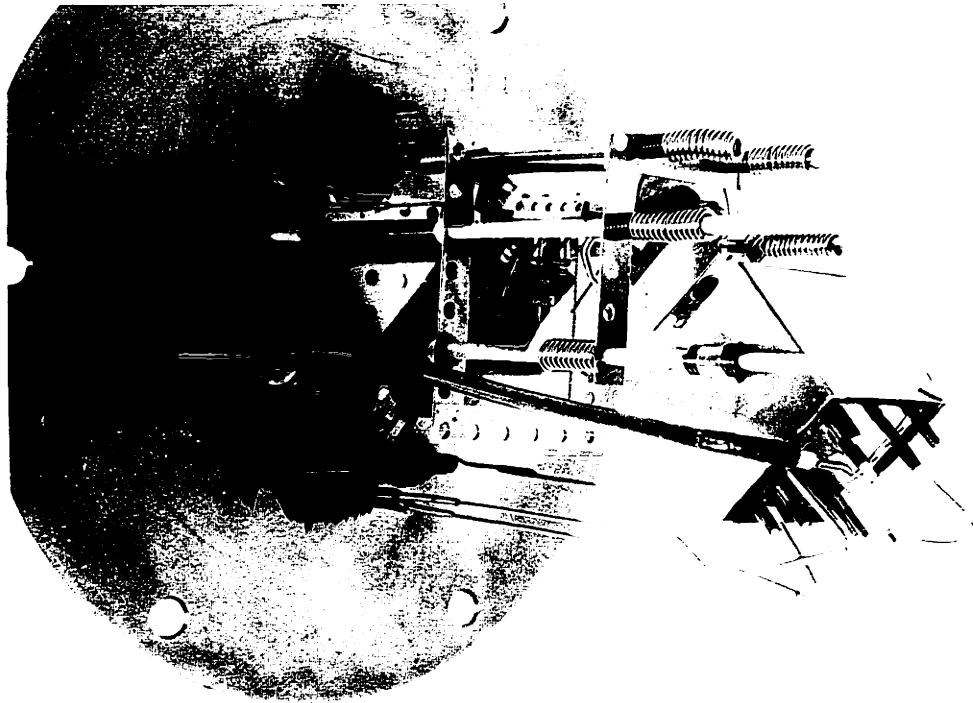


Fig. 49 Assembly for the monochromator test. Also shown is a parallel-grid retarding potential analyzer.

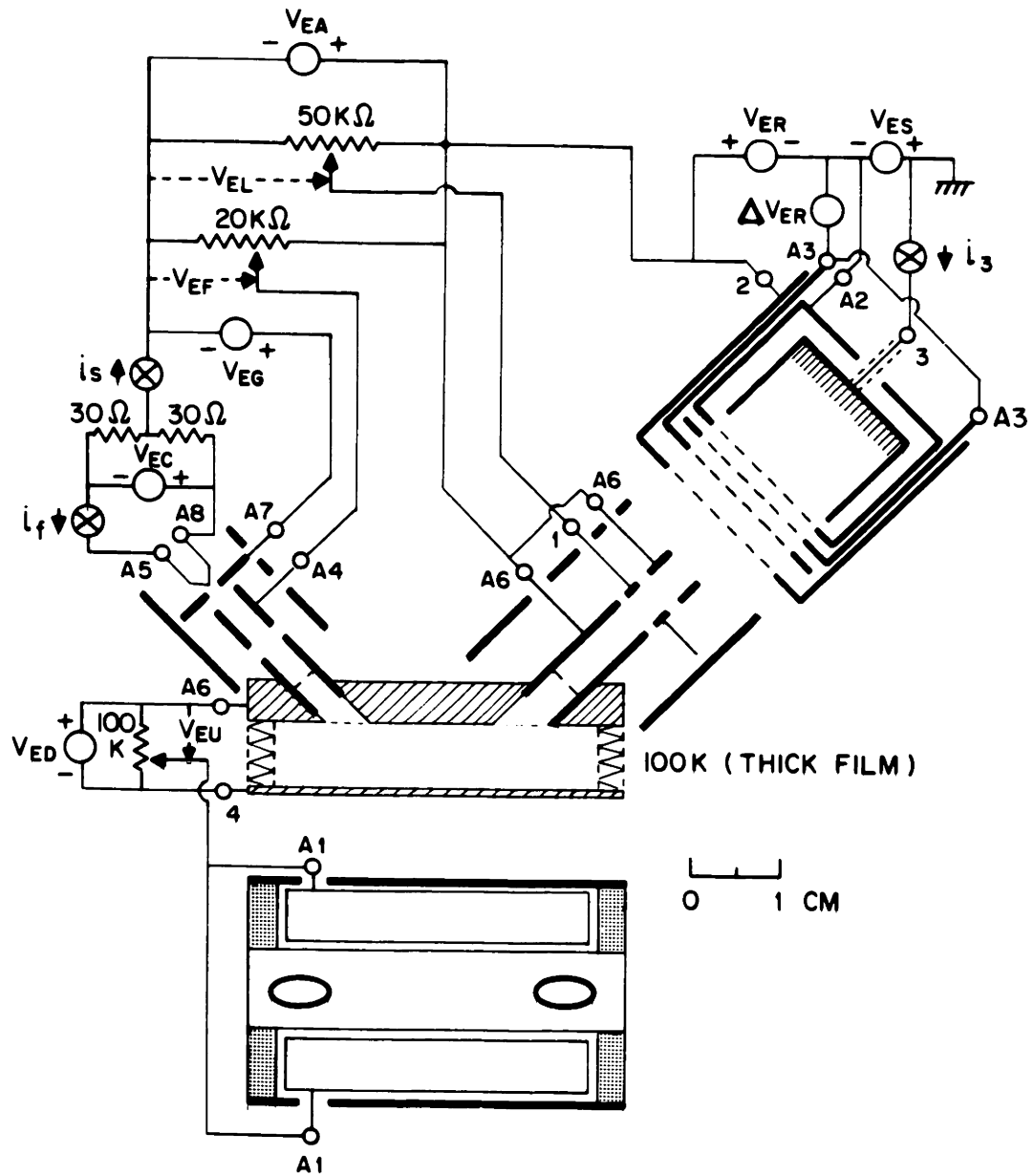


Fig. 50(a) Wiring diagram for the monochromator test

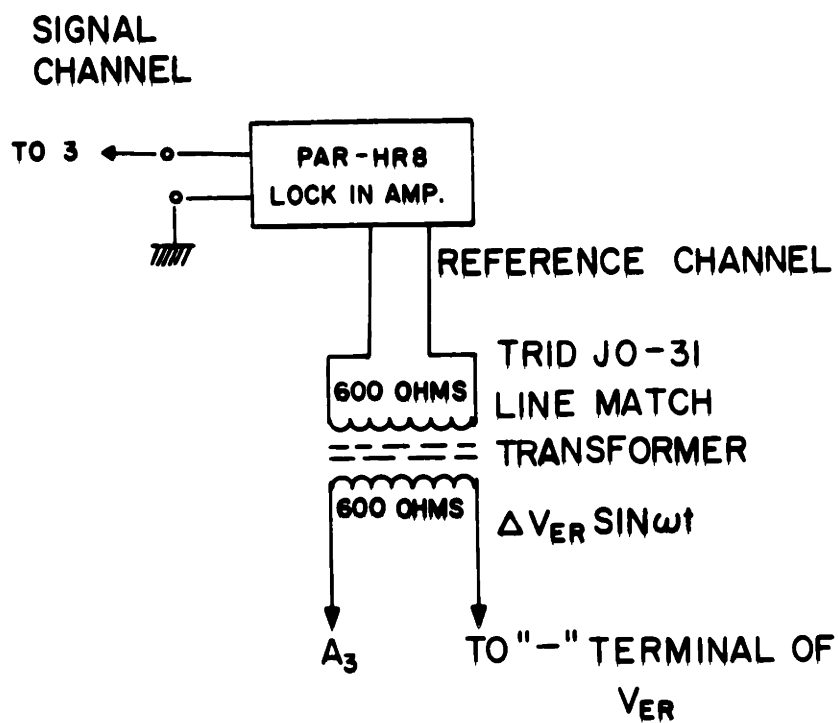


Fig. 50(b) Part of the wiring diagram with auto differentiation using a modulation technique.  $\Delta V_{ER}$  is from the internal reference signal of the PAR lock-in amplifier. The voltage ratio of the match transformer is unity.

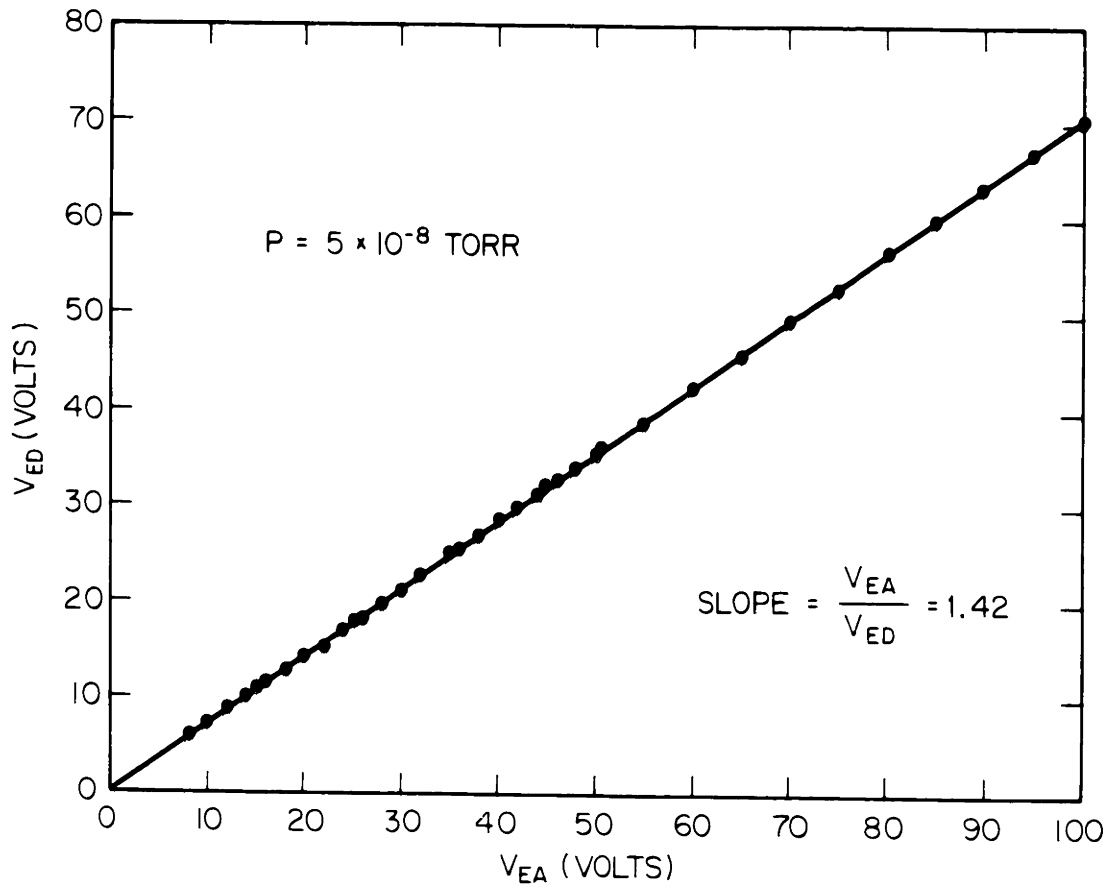


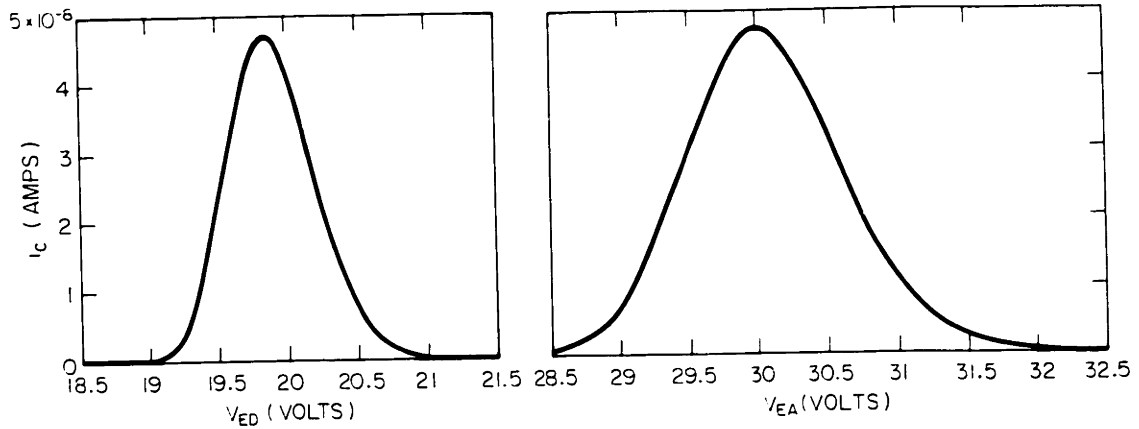
Fig. 51 Mirror voltage with respect to the beam energy. Linearity is shown.

TABLE IV Notations for Monochromator tests

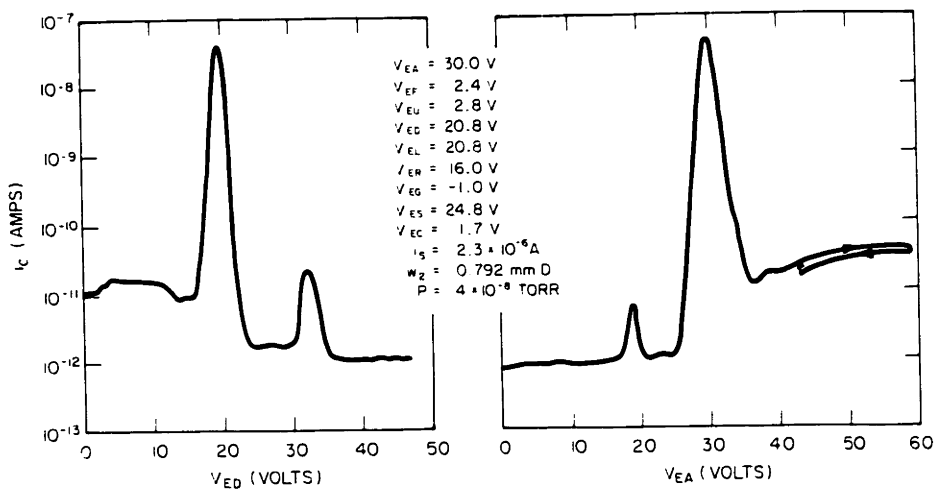
$V_{EA}$	provides the electron beam energy of the monochromator
$V_{EC}$	supplies filament voltage
$V_{EO}$	gives deflection mirror voltage
$V_{EF}$	controls electron gun focusing voltage
$V_{EL}$	supplies injection focusing voltage
$V_{ER}$	provides necessary retarding potential
$\Delta V_{ER}$	establishes differential retarding potential
$V_{ES}$	provides necessary secondary electron suppression voltage
$V_{EU}$	controls field compensation voltage
$i_f$	measures filament current
$i_s$	measures emission current
$i_c$	detects collector current

The beam profiles at  $V_{EA} = 30.0V$  are shown in Fig. 52(a) by sweeping  $V_{EA}$ . These profiles can be fitted to the Gaussian distribution function. The details of the profiles are also shown in the same figure (b) in the logarithmic scale. A subpeak was found at the higher voltage side of  $V_{ED}$  or at the lower voltage side of  $V_{EA}$ . This peak is probably the result of the primary electrons colliding with the inside cylinder wall, and reflecting through the output aperture. The background tail at the low voltage side of  $V_{ED}$  (and at the high voltage side of  $V_{EA}$ ) are the result of electrons colliding with the outside cylinder wall. All of these background currents are at least 3 order of magnitude

down from the selected peak current, thus they do not impose an important limit on energy selection.



(a)



(b)

Fig. 52 Beam profiles from the monochromator. (a) The electron collected current is recorded in an expanded scale by (i) scanning  $V_{ED}$  (the mirror voltage); and (ii) scanning  $V_{EA}$  (the beam energy). (b) The details of the profiles are shown in a logarithmic scale.



The half widths ( $\Delta V_{EA}$ ) are presented in Fig. 53. At low  $V_{EA}$ , the energy spread, which is normally independent of  $V_{EA}$ , becomes the sum of the voltage drop across the effective emitting area and the electron thermal energy (Maxwellian distribution). At high  $V_{EA}$ , on the other hand, most of the energy spread comes from the dispersion of the monochromator (i.e. approaching  $\Delta V_M = \eta V_{EA}$ ).

If the source and the monochromator energy spread are both assumed Gaussian, it can be shown that the resulting beam halfwidth (FWHM) is

$$\Delta V_r = \sqrt{(\Delta V_s)^2 + (\Delta V_M)^2} \quad , \quad (5.7)$$

where

$\Delta V_s$ : the energy spread of the electron source

$\Delta V_M$ : the intrinsic energy spread due to the monochromator.

From the data one can deduce  $\Delta V_M$ , which is also shown in Fig. 53.

With an aperture radius of 0.396 mm, the resolution was 1.7% after a linear interpolation. The zero offset of 0.2 volt is not precisely understood, but it probably results from minor changes in the emitting area for different  $V_{EA}$ . For high  $V_{EA}$ , the effective area is larger, in general, and the actual resolution should be better than that indicated above (as will be discussed in the retarded potential study which follows).

Parallel retarding potential grids were mounted on the same flange about 1 cm away from the injection lens. This arrangement was different from the conventional RPD technique, in that two grids were used to

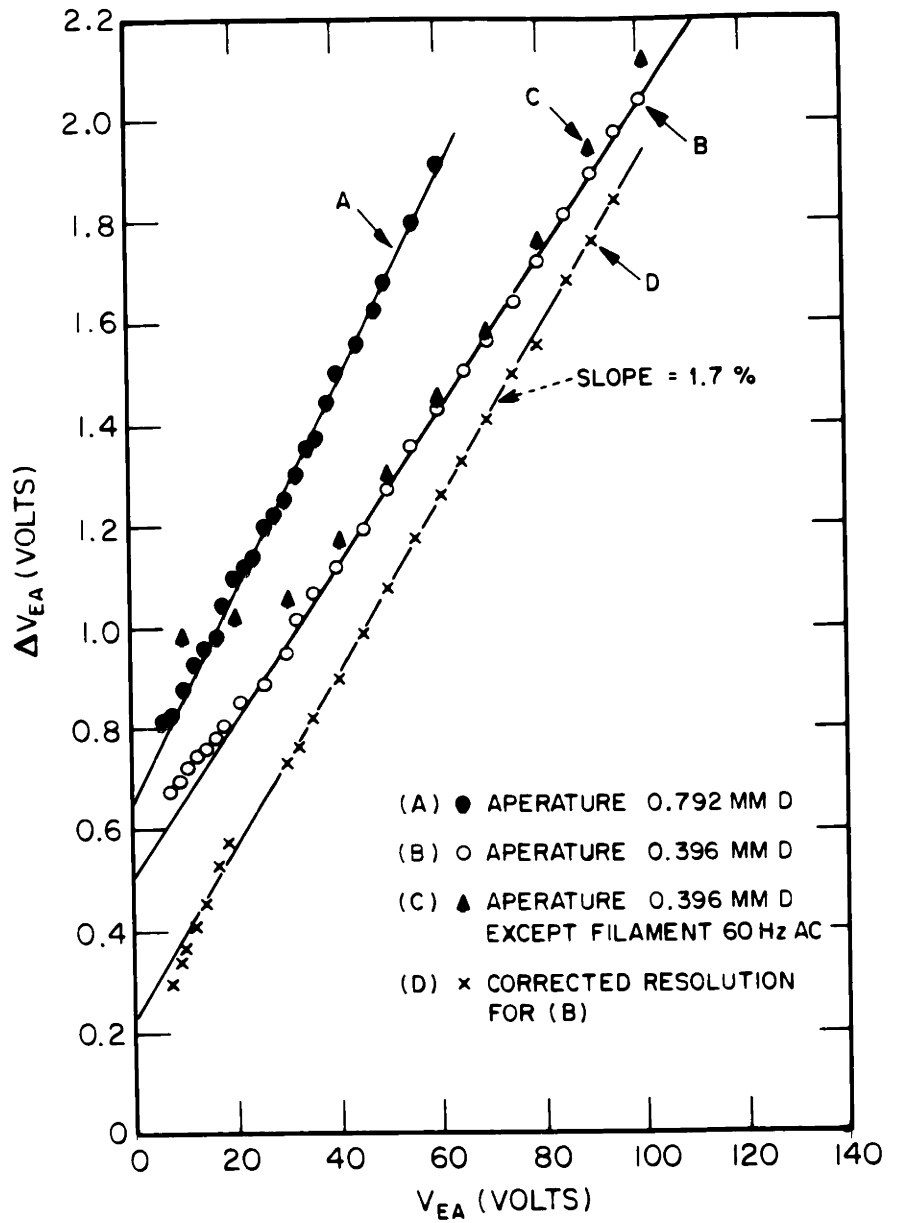


Fig. 53 Half width of the energy spread of the monochromator.

The result is measured as FWHM.

retard the beam. This results in less field penetration (due to the saddle point effect) and permits resolution as shown in appendix 2.

Both the test wiring diagram and an auto-differentiation technique are shown in Fig. 50. The output beam from the monochromator was retarded by  $V_{ER}$ . The retarded potential curve was then differentiated by the use of a small AC signal modulation ( $\Delta V_{ER}$ ), and then detected using a PAR HR-8 lock-in amplifier. This differentiation can be explained immediately by considering a Taylor series expansion,

$$i(V_{ER} + \delta V_{ER}) = i_o(V_{ER}) + \delta V_{ER} i_o'(V_{ER}) + \frac{(\delta V_{ER})^2}{2} i_o''(V_{ER}) + \dots \quad (5.8)$$

with  $\delta V_{ER} = \frac{\Delta V_{ER}}{2} \sin \omega t$ ,

$$i = i_o + \left(\frac{\Delta V_{ER}}{2}\right) i_o' \sin \omega t + \dots \quad (5.9)$$

Since  $\Delta V_{ER}$  is very small, the detection signal, neglecting the contribution of higher odd terms, is,

$$V_D \approx \Delta V_{ER} R_i i_o' \quad , \quad (5.10)$$

i.e.  $V_D \propto i_o'$  ,

where  $R_i$  is the input impedance of the lock-in amplifier. The energy window  $\Delta V_{ER}$  thus used was about 0.025 to 0.05 v peak-to-peak, and the modulating frequency was chosen away from the existing noise and power line harmonics. Typical retarding potential results are shown

in Fig. 54. Using this procedure, with the grids coated with Aquadag, the half width energy spread of the beam from the monochromator is plotted in Fig. 55. Similar results were also obtained with more scattered data when the nickel grids were clean. A constant energy spread of about 0.66 volts was observed over a range from  $V_{EA} = 65V$  to 90V. This was obviously due to the constant energy spread of the electron source (voltage drop across the filament and the thermal

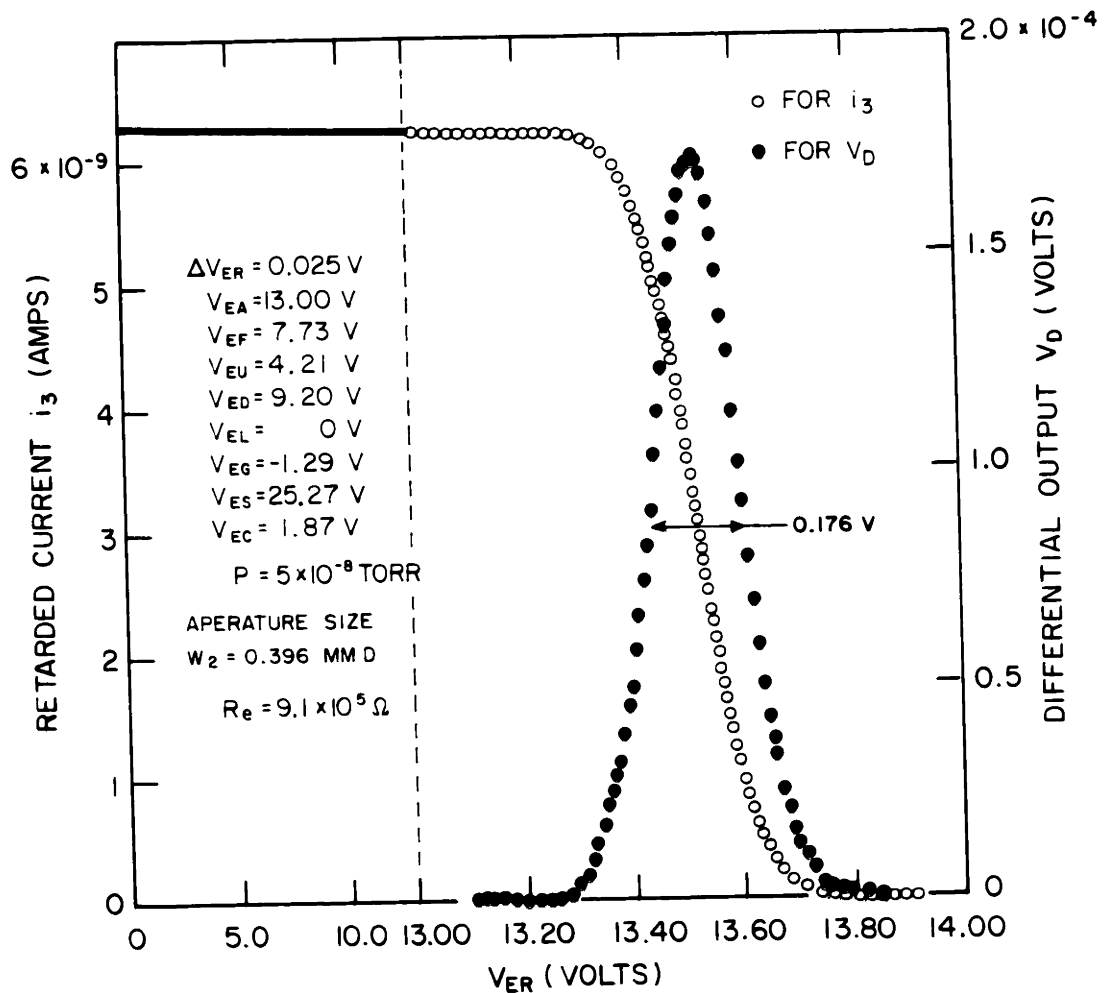


Fig. 54 Retarding potential result of the electron beam from the monochromator. At  $V_{EA} = 13.00V$ , the data indicate almost no secondary electrons.

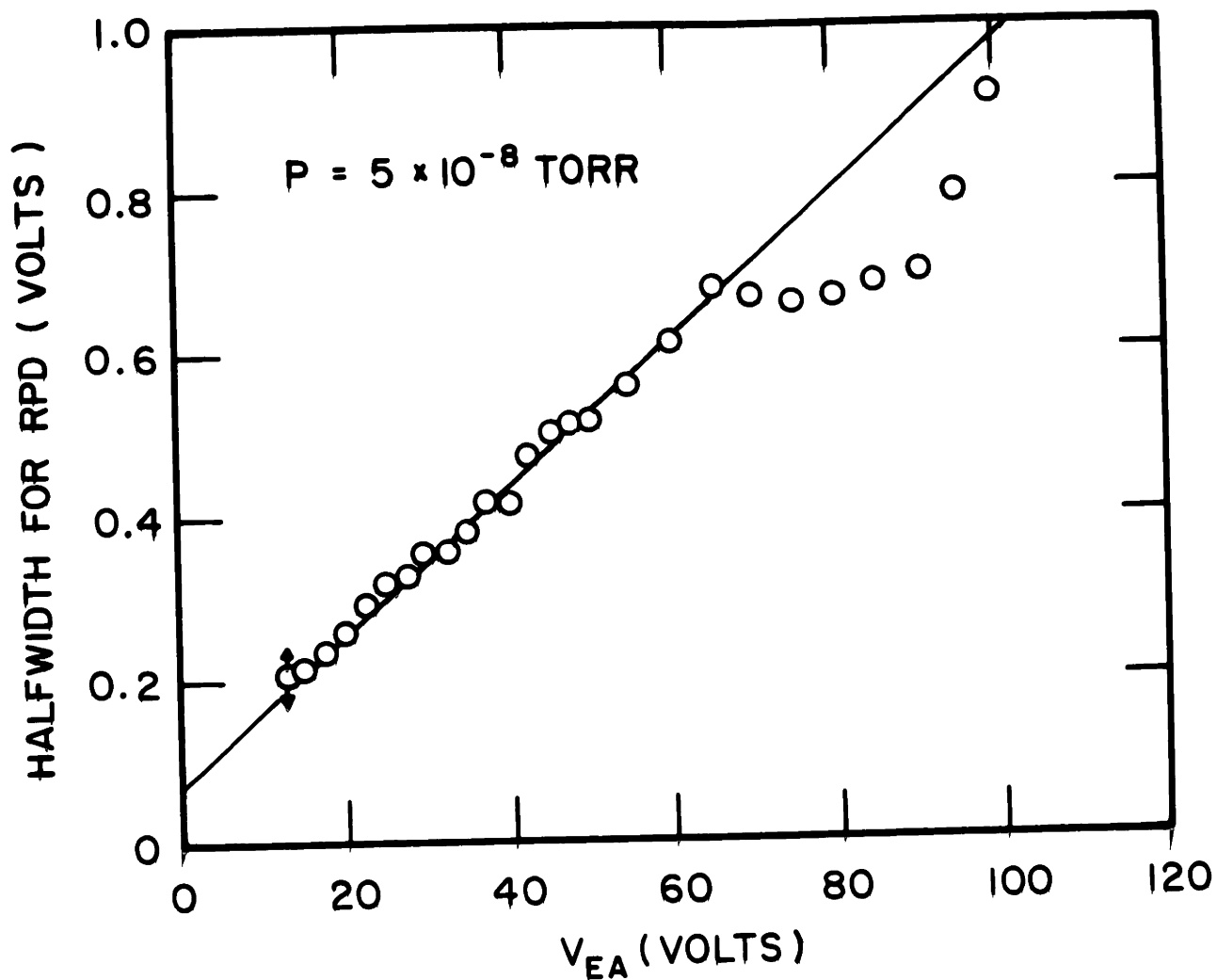


Fig. 55 Half width of the electron beam measured with the RPD method.

energy). At high energy, the energy pass-band of the monochromator is larger than this energy spread and the resulting beam carries the energy spread width. For  $V_{EA}$  higher than 90V, an unexpected rise in energy spread occurs which is not fully understood. This may be due to a lens effect at the retarding grids, or secondary electron effects. The rise is most certainly not due to the monochromator itself because, as

shown in Fig. 52, no such effect was observed when  $V_{ED}$  or  $V_{EA}$  was swept across the range indicated. The offset of 0.07V at zero  $V_{EA}$  was probably due to lens effects, space charge, a finite modulating signal, and other stray effects (which cause a finite resolution in the RPD method). These are discussed in appendix 4. The resolution observed from the RPD result was about 1%, and was better than that estimated from Fig. 53.

In comparison with the theoretically calculated resolution, the results from Fig. 53 are better by a factor of about 2. A similar result was recently obtained in the same type of analyzer.<sup>67</sup> To explain this, consider the dispersion expansion<sup>60</sup>

$$\Delta z = 5.6 a(\Delta E/E_0) - 15.4a(\Delta\alpha)^3 + 10.3a(\Delta E/E_0)\Delta\alpha$$

With a small semi-angular aperture, the resolution can be much better than that of the optimal condition shown by Hayward<sup>63</sup> when  $\Delta\alpha$  is fully used. Thus the effective resolution for a very small  $\Delta\alpha$  is

$$\eta = \frac{\Delta E}{E} \cong 1.5\%$$

This result shows uncertainty between 3% and 1.5% unless  $\Delta\alpha$  is well defined. This is in agreement with the result in Fig. 53. However, the better result from the RPD is still not understandable. Perhaps source size and the waist in the selection plane contribute to the improvement in resolution.

V.4 Source Requirements and Acceptance--Emittance Matching

The beam current can be expressed as

$$I = \frac{\pi}{16} B(v) E_{\alpha}^2 E_{\rho} \quad (5.11)$$

where  $B(v)$  is the brightness and  $E_{\alpha}$  is the acceptance area of the monochromator. To achieve a high output current, a monochromator with a high figure of merit as discussed earlier should be chosen. The emittance of the emission system should also be designed to match the acceptance of the monochromator. Furthermore, a high brightness source should be used.

V.4.1 Emission System--When operating at 2600°K, (life time about 5 hours), the emission current density of a tungsten cathode is about 700mA/cm<sup>2</sup>. The brightness can then be calculated as

$$\begin{aligned} B_1 &= \frac{J_1 [eV + kT]}{\pi kT} = \frac{J}{\pi} \left( \frac{V + \frac{T}{11605}}{\frac{T}{11605}} \right) \quad (5.12) \\ &\approx \frac{JV}{\pi} \left( \frac{11605}{T} \right) \quad V \gg 0.45 \text{ V} \\ &\approx 0.981 \text{ V} \quad (\text{amp/cm}^2\text{-sterad}) \end{aligned}$$

where  $V$  is the beam extraction voltage.

By using a Phillips impregnated cathode, much higher emission at much lower temperatures can be obtained. Using the M type, the emission

current density is,

$$J_2 = 10 \sim 20 \text{A/cm}^2, \quad \text{at } 1400^\circ\text{K.}$$

while the brightness is,

$$B_2 = \frac{J_2}{\pi} \text{V} \left( \frac{11605}{1400} \right) = 20 B_1$$

Hence, a factor of 20 in brightness can be gained. Furthermore, from the monochromator tests, the 0.65 volt drop across the emitting region was observed to be important; this drop is zero for the Phillips cathode. This implies that the average brightness of the tungsten cathode is further reduced by a factor of about 5. Therefore, the total gain of about 100 can be obtained in the output beam current. The brightness may be further increased with the use of a field emission cold cathode. However for field emission to be able to operate stably and for a sufficiently long life time, the vacuum system has to be better than the order of  $10^{-9}$  torr (because of sputtering on the emission tip by ionized ions). Since the present system has a large gas loading and no differential pumping is available, it is impracticable to attempt such a high vacuum. Thus the M type Phillip impregnated cathode was chosen.

The extraction stage is also very important. To avoid space charge limit at an extraction region of the cathode, a multiple stage decelerating technique similar to that used by Simpson et al<sup>68</sup> was adopted to improve the extraction and therefore to push the operating



current close to the space charge limit.

V.4.2 Acceptance of the Monochromator--The design of the multistage gun should be such that the acceptance of each stage matches the emittance in the previous stage. The acceptance of the monochromator can be determined by the optimal condition (i.e. by maximizing the transport current).

The current transport may be approximately written as

$$i = \frac{\pi}{16} B E_{\alpha} E_{\rho} \quad (5.13)$$

where B: brightness

$E_{\alpha}$ : Acceptance area in  $\alpha$ -direction independent of  $\rho$

$E_{\rho}$ : Acceptance area in  $\rho$ -direction independent of  $\alpha$

or

$$i = B \cdot 2\alpha(Z_g \cos\theta) E_{\rho} \quad (5.14)$$

$$\Delta Z = \Delta Z_g + \Delta Z_s$$

$$\Delta Z_s = A_{II} \alpha^2 + A_{III} \alpha^3 \quad (5.15)$$

Near  $42.2^\circ$ ,  $A_{II} = 0$ , and  $A_{III} \cong 21D \sin^3 \theta_o$ ,<sup>60</sup> then

$$i = B \cdot 2\alpha(\Delta Z - 2/T^3 D) \cos\theta_o \quad (5.16)$$

where  $D = E \frac{\Delta Z}{\Delta E} = \frac{a \cot \theta_o}{\sin^2 \theta_o (K^2 \cot^2 \theta_o - 1)}$  and  $T = \alpha \sin \theta$ .

Under the maximum transport condition\*, i.e.

$$\frac{\partial i}{\partial \alpha} = 0, \quad (5.17)$$

one obtains

$$\Delta Z = 84T^3D = 84 \sin^3\theta_o D \alpha^3 \quad (5.18)$$

With a circular aperture,  $d = 0.396$  mm, and  $\theta_o = 45^\circ$ ,  $Z$  is given by

$$\Delta Z = \frac{\pi}{4} \frac{d}{\cos\theta_o} = 0.439 \quad (\text{mm}), \quad (5.19)$$

where  $\frac{\pi}{4}$  is the geometric correction factor due to a circular aperture.

From Equ.(5.18), the semi-angular aperture may be calculated as,

$$\alpha = \frac{1}{\sin\theta_o} \left( \frac{0.439}{8.4 \times 6.2 \times 4.76} \right)^{1/3} = \frac{1}{\sin\theta_o} 0.564 \times 10^{-1} = 0.08 \quad (\text{rad}) \quad (5.20)$$

Since the second order spherical aberration vanishes under second order focussing from the dispersion and the third spherical aberration relations,

$$\Delta Z_s = A_{III} \alpha^3 = 7.65 \alpha^3 \quad (\text{mm}),$$

or for the distance perpendicular to the main ray

---

\* It is possible to maximize  $i \cdot \frac{1}{R}$ . However, since  $R$  is a weak function of  $\alpha$ , only a slight improvement can be made.

$$\Delta S_{\alpha} = (7.65 \cos \theta_0) \alpha^3 = 5.41 \alpha^3.$$

The acceptance in the  $\theta$ -direction can then be represented in Fig. 56(a).

For a  $2\pi$  cylindrical analyzer having a ring source, the acceptance in  $\rho$ -direction would be about  $4\pi r_0$ . In the present monochromator, only half the cylinder of the source is available, and the source is a plane disc. The resulting acceptance is shown in Fig. 56(b).

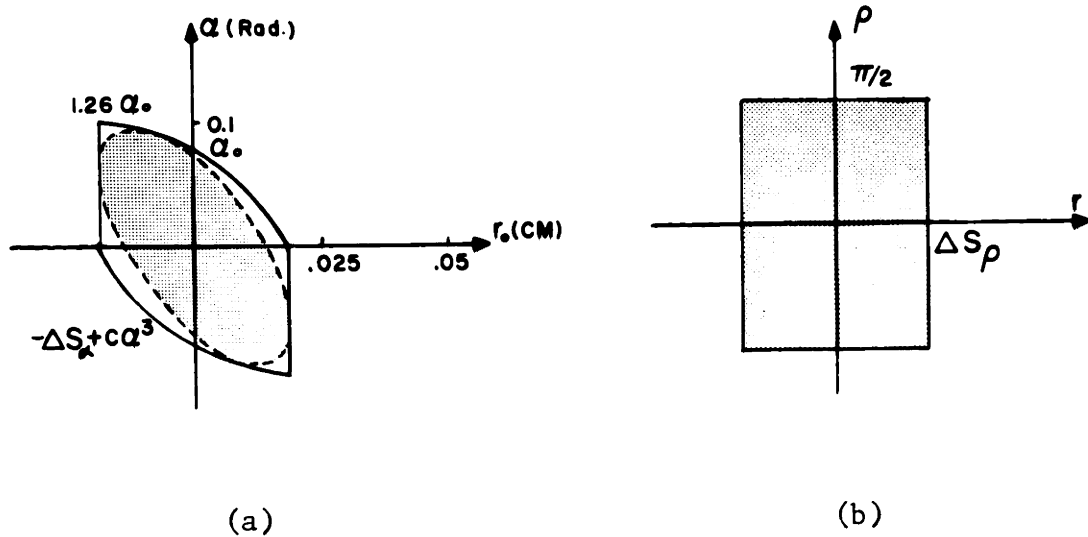


Fig. 56 (a) Acceptance of the cylindrical monochromator in the  $\alpha$ -direction  
 (b) Acceptance of the cylindrical monochromator in the median plane

The electron gun was designed to match the acceptance in  $\alpha$ -direction. When the object is considered as one waist of the beam, the image will be at the other. The designed optical properties can be found in the

work of Spangenberg<sup>54</sup> and Simpson<sup>68,70</sup>. Assuming the extraction stage to be set at 70 volts, the space charge limit current by the extraction is<sup>69</sup>

$$i = J_s \cdot A = 2.3V^{3/2} \cdot A, \quad (\mu A) \quad (5.21)$$

$$A = \frac{1}{4} \pi \left(\frac{1}{64}\right)^2 2.54^2 = 1.22 \times 10^{-3} \text{ (cm)}; V = 70 \text{ (V)}$$

$$i = 1.66 \quad (\mu A).$$

and the current limit through the monochromator with  $V = 10\text{eV}$  is<sup>69</sup>

$$\begin{aligned} i &\approx 38.5 V^{3/2} \alpha^2 \approx 0.78 \quad (\mu A) \\ &\approx 7.8 \times 10^{-7} \quad (A) \end{aligned} \quad (5.22)$$

It should be noted that the acceptance in the  $\rho$ -direction was not fully utilized. The reason for this is that the requirement for subsequent beam shapes of the ion optical system requires low emittance in both directions.

The electron gun layout is shown in Fig. 57. The general method and theory for matching acceptance and waist-to-waist transport will be considered elsewhere.<sup>71</sup>

The choice of the operation point can be made by compromising the energy pass-band and the transport current as

$$\delta V = RV \quad (5.23)$$

and  $\frac{B}{V} = \text{const} = C$

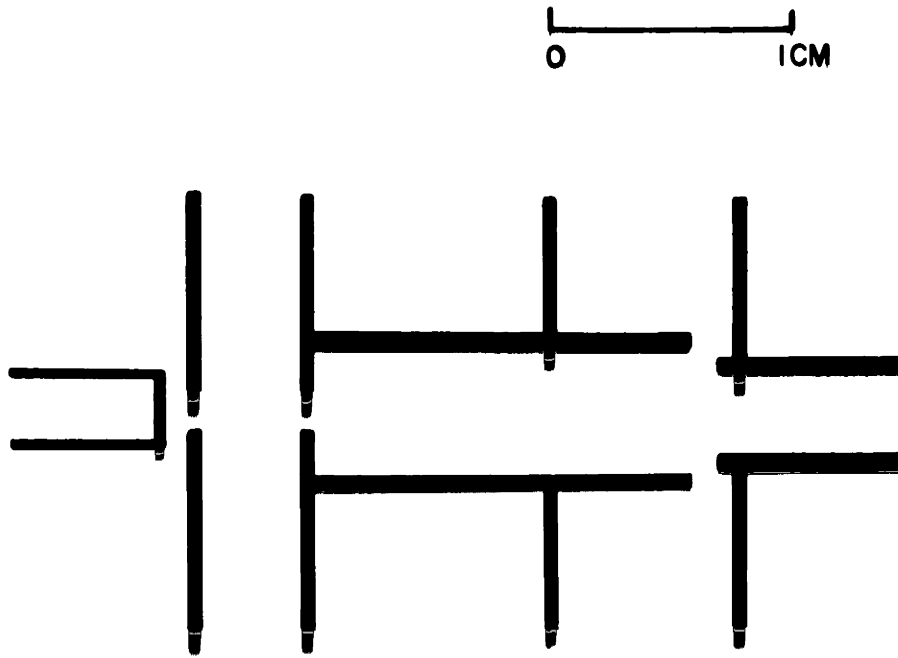


Fig. 57 Layout of the electron gun. The schematic configuration was designed by the match of the acceptance and the emittance.

It follows that

$$i/\delta V \propto \frac{C}{R} \quad (5.24)$$

That is, the  $i/\delta V$  is invariant for the monochromator with a given resolution as long as the space charge does not act as a limitation.

## VI. ION EXTRACTION OPTICS

Total ion collection is necessary for absolute cross section measurements. The conditions for this collection were formulated by considering emittance and acceptance of the optical systems in this chapter. Experimental results showed current saturation for an atomic beam and backgrounds. Full transmission through the mass spectrometer was observed to be possible for an atomic beam (with sacrifice of the resolution).

The existence of draw-out voltage affected the electron beam energy and extended the spread to a certain degree. It was found that  $V_{ID}$  should not be greater than 5 volts for threshold study. Penetration of potentials due to  $V_{IE}$  and  $V_{ED}$  were negligible.

### VI.1 Total Ion Collection and Ion Optics

The ionization chamber is made of three 25 $\mu$  diameter W-3%Re wires. The chamber is composed of a main (extraction) grid and two end grids insulated from one another. The insulation deteriorated after a period of operation due to deposition of the evaporating material from the flashed grids, and of scattered particles from atomic beams. As shown in Fig. 58 the main grid was wound by a wire in a quadrupole figure eight winding pattern. The spacing is about 1 mm in the main grid and 0.95 mm in the end grids. The main grid wire is about 75 cm in length and has a resistance of 150 ohms. Each of the end grid wires is about 15 cm in length and 32 ohms. Average transmission is approximately 97.5 %. Higher transmission for the electron beam can be obtained when the spacing is lined up with the electron beam aperture.

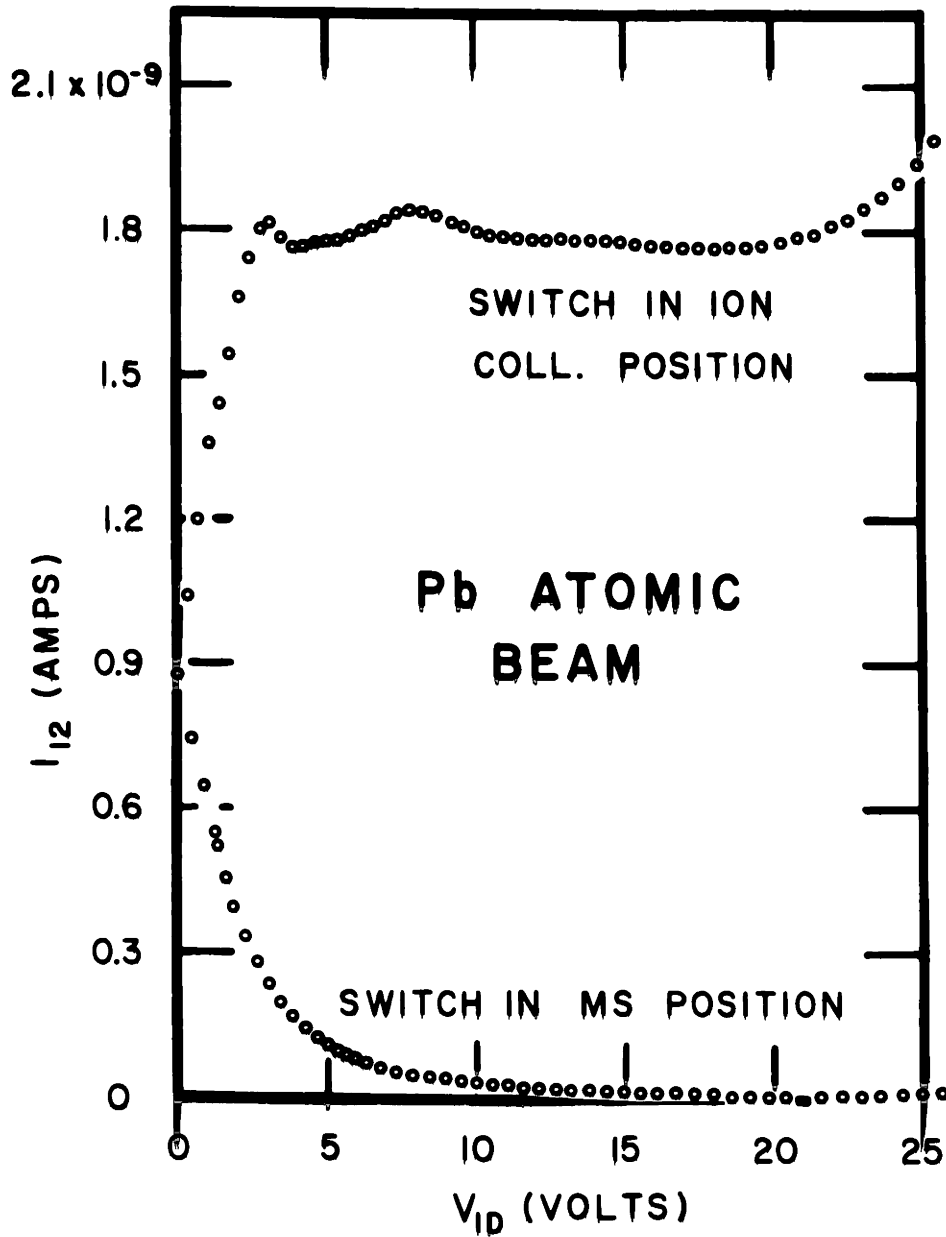


Fig. 59(a) The total ion collector current with respect to the extracting voltage for the Pb atomic beam.

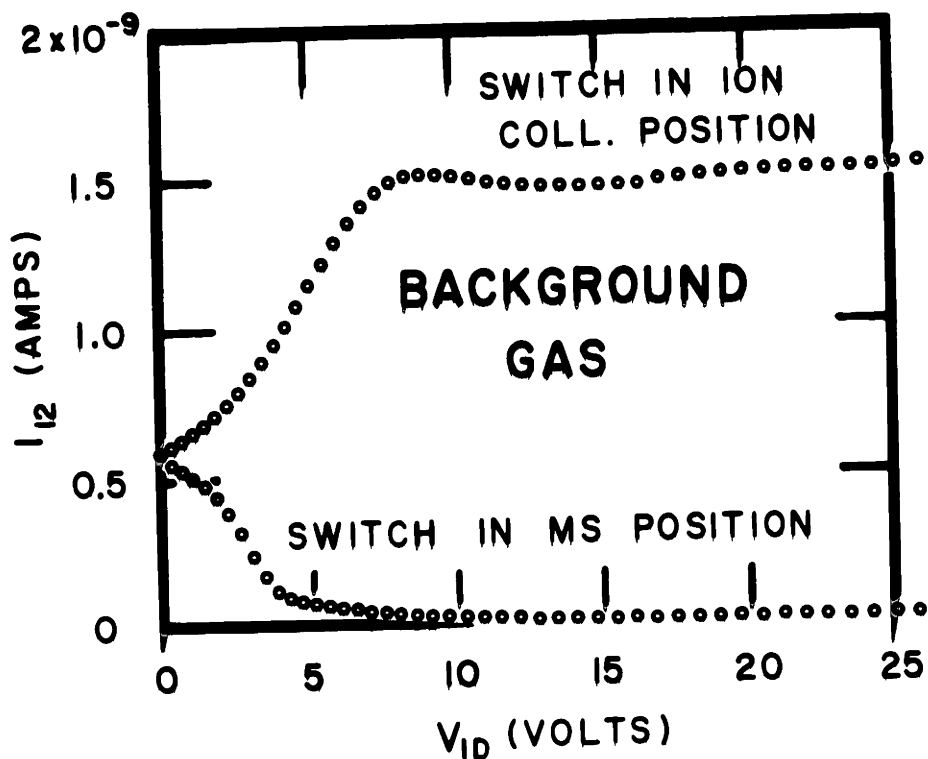


Fig. 59(b) The total ion collector current with respect to the extracting voltage for background gases.

saturation for an atomic beam occurred at about  $V_{ID} = 5$  volts. Two small peaks observed near  $V_{ID} = 3$  and 8 volts were probably the result of lens effects due to an end grid.

A rising tail for high  $V_{ID}$  ( $V_{ID} > 25V$ ) was observed due to the emission of potassium ions from the flashable grids. The emitted ion current with the threshold close to 25 volts is shown in Fig. 60. The emission mechanism is similar to that described in Chapter II (i.e.



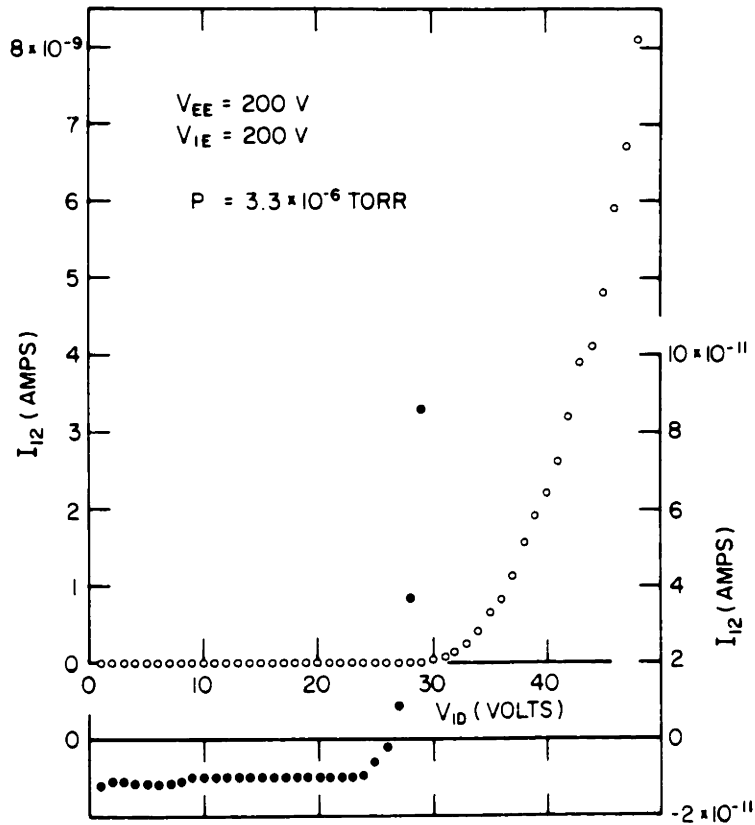


Fig. 60 Current collected as a function of  $V_{ID}$  with the electron gun off. The emission of potassium ions starts at  $V_{ID} = 25$  V. Open points go with the scale on the right, while solid points go with the scale on the left. The amount of ion emission is not steady.

surface ionization).

A simple two-cylinder lens was used to focus ions drawn out by the main grid to the quadrupole mass spectrometer. The linear relation of  $V_{IE}$  and  $V_{IF}$  which is shown in Fig. 61 reveals the lens properties. For

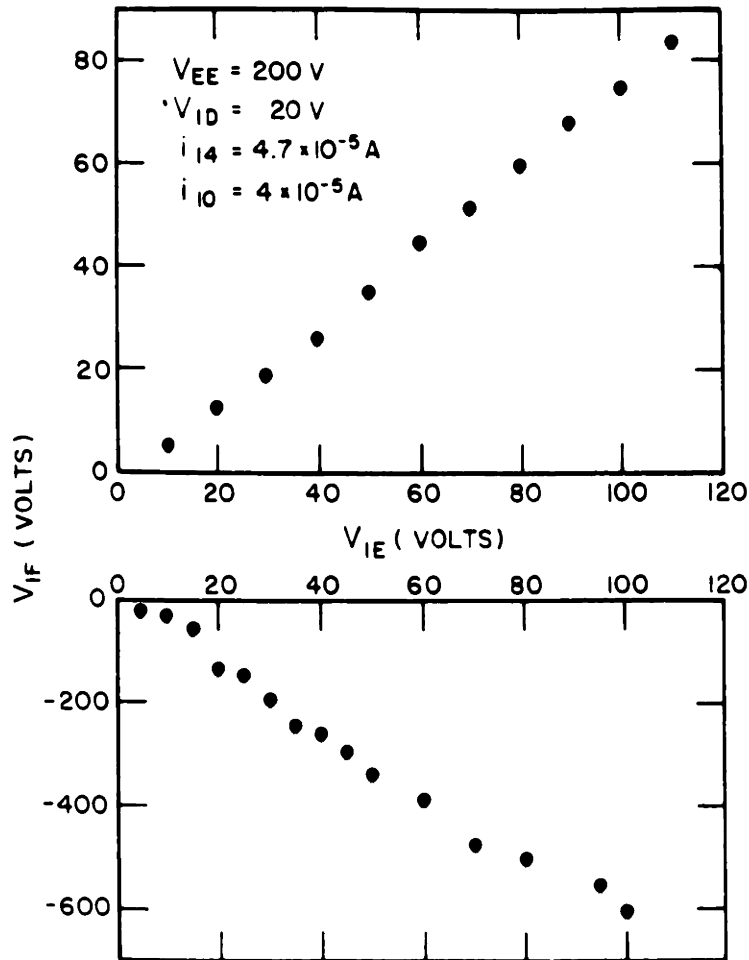


Fig. 61 Properties of the ion injection lens. Focusing can be achieved by both positive and negative  $V_{IF}$ .

a different ion energy, the focusing properties of  $V_{ID}$  can be observed in Fig. 62, in which the focus voltage was adjusted to give maximum output for  $V_{ID} = 15\text{V}$  and a given  $V_{IE}$ . The transmission depends on the ion energy shown in Fig. 63. At low ion energy, a linear relationship is expected following the Brightness Law. At high energies, an approximate saturation should be observed. It should be noted however, that at high energies, particle losses increase in the transport of the

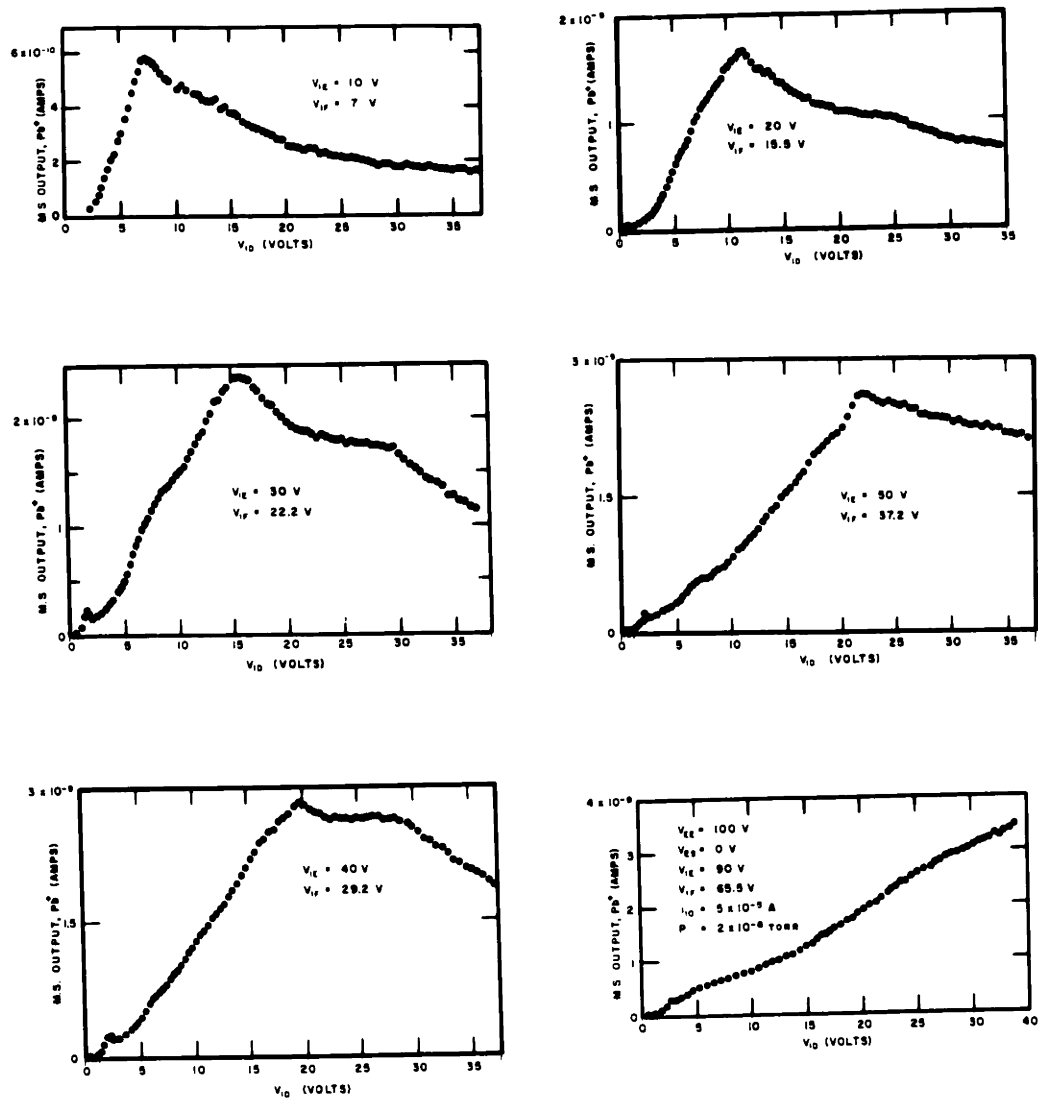


Fig. 62 The effect of ion energies on the mass spectrometer sensitivity. Focal points at different ion energies require different  $V_{IF}$ . From (a) through (f), spectrometer outputs with respect to  $V_{ID}$  are plotted for the different ion energies. In every case,  $V_{IF}$  is adjusted to give the maximum spectrometer output when  $V_{ID}$  is set to 15 volts.

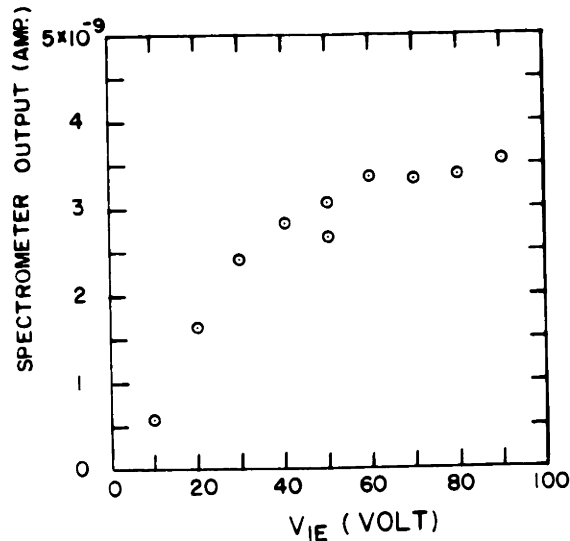


Fig. 63 Transmission of ion optical systems with respect to the ion energy.

the quadrupole mass spectrometer. At  $V_{IE} = 100V$ , backgrounds of about one part per 15 passed through and were detected. This is understandable since the emittance of backgrounds is much larger than the acceptance of the injection lens to the mass spectrometer. For an atomic beam, the transmission is increased to one part per five. As will be discussed in the next section, the emittance of the ion source for the atomic beam is much smaller than that for backgrounds.

A linear relationship between the mass spectrometer output and the electron beam current is necessary in order to have reliable cross section data. This linearity is observed in Fig. 64.

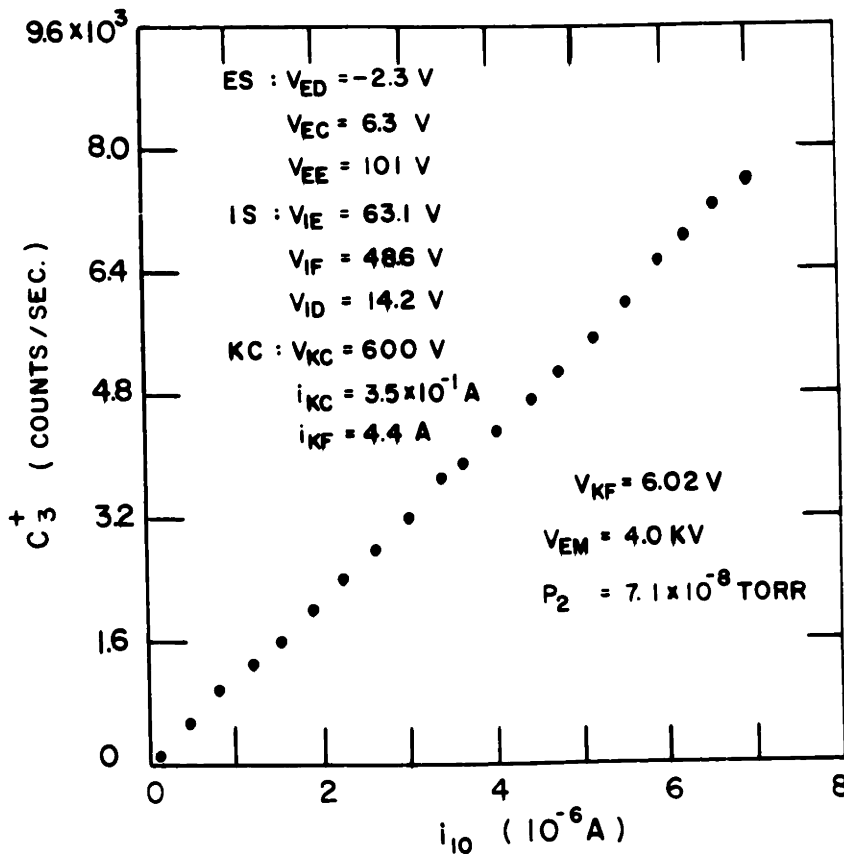


Fig. 64 Relation of the spectrometer output and the electron beam current. Linearity guarantees reliable cross section data.

## VI.2 Emittance and Acceptance of Ion Optics

From the geometrical configuration in Fig. 65, the acceptance area of the total ion collector (referring to the  $Q_1$ -plane) can be represented in Fig. 66\*. (The same acceptance area applied to the x-axis direction)

\* Note that the higher potential of ion collection will increase the acceptance area due to the accelerating field of  $V_{ES}$  and  $V_{IE}$ . These high  $V_{IE}$  and  $V_{ES}$  are necessary to provide an energy barrier for electrons.

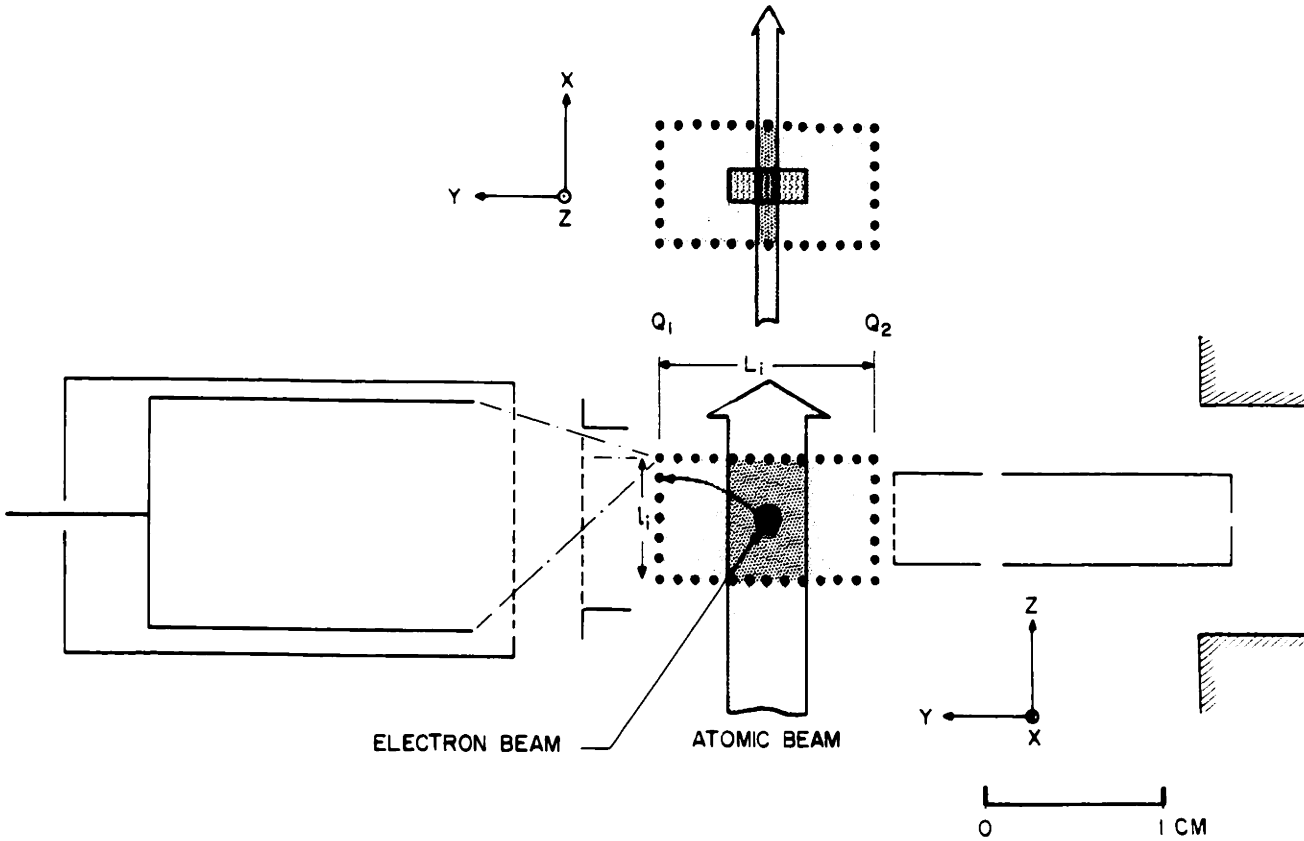


Fig. 65 Configuration diagram of the entire ion optical system, including the ionizer, the total ion collector, and the injection lens.

The brightness of ions in the ionizer is proportional to  $V_{ID}$ , (i.e. the emittance area increases inversely proportionally to  $V_{ID}$ ). Considering an electron beam of radius  $r_e$ , and then applying  $V_{ID}$  for ion collection, the ion trajectory may be obtained as

$$z = \left( \frac{4yeU_o L_i}{qV_{ID}} \right)^{1/2} \tag{6.1a}$$

and

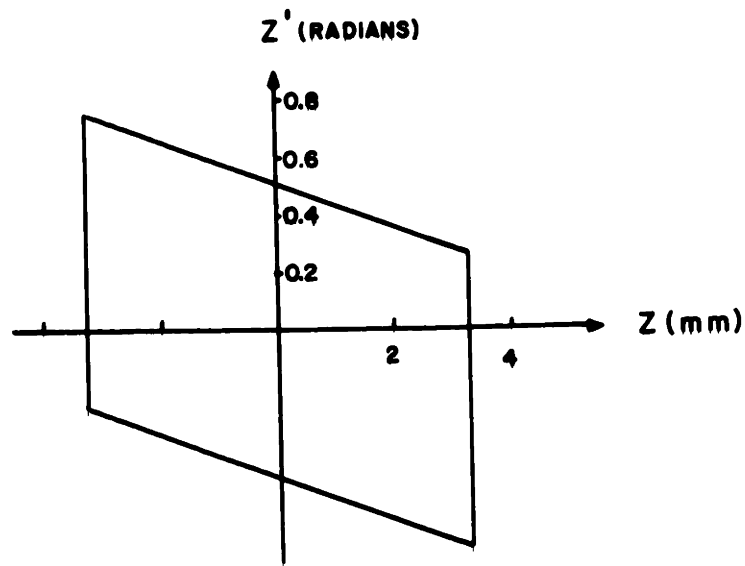


Fig. 66 Acceptance area of the total ion collector at the  $Q_1$ -plane. The same acceptance applies to other directions.

$$z' = \left( \frac{eU_o L_i}{qyV_{ID}} \right)^{1/2} \quad (6.1b)$$

specifically,  $y = \frac{L_i}{2} - r_e$ ,

$$z = \left( \frac{2eU_o L_i^2 \left(1 - \frac{2r_e}{L_i}\right)}{qV_{ID}} \right)^{1/2} \cong \left( \frac{2eU_o L_i^2}{qV_{ID}} \right)^{1/2} \quad (6.2a)$$

and

$$z' = \left[ \frac{eU_o}{qV_{ID} \left(1 - \frac{2re}{L_i}\right)} \right]^{1/2} \approx \left( \frac{eU_o}{qV_{ID}} \right)^{1/2} \quad (6.2b)$$

Thus the emittance area when referring to the  $Q_1$ -plane, depends on  $V_{ID}$ , and can be represented as in Fig. 67. Because of a larger thermal velocity in the beam direction for a neutral beam, the emittance area is shifted. Note that these emittances do not necessarily have the same area.

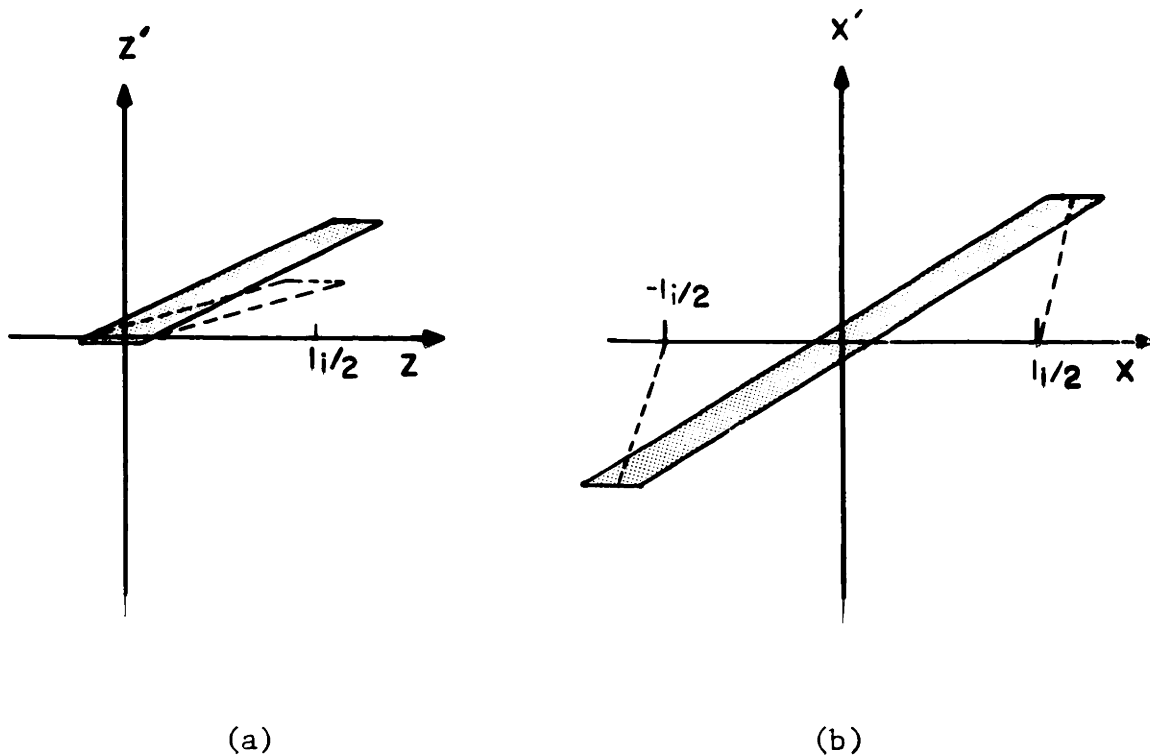


Fig. 67 z-axis emittances of ion sources; a) for an atomic beam,  
b) for background gases



For an atomic beam of temperature 2500°K, the average thermal energy for the Maxwellian distribution is

$$U_o = \frac{1}{2} \overline{mv^2} = \frac{1}{2} m \left( \frac{4kT}{m} \right) = 2kT = 0.431 \text{ eV}$$

and the momenta is mostly in the z-direction. In order to accomodate all of the ions, one sets  $V \geq U_o$ . The minimum  $V_{ID}$  required to assure that the emittance area is within the acceptance, (following Equ. 6.1a) can be obtained from Equ. 6.2a (for singly charged ions)

$$\frac{\rho_i}{2} \geq \left( \frac{2U_o L_i^2}{V_{ID}} \right)^{1/2} ,$$

or

$$V_{ID} \geq 8U_o \left( \frac{L_i}{\rho_i} \right)^2 , \quad (6.3)$$

numerically,

$$V_{ID} \geq 13.8 \text{ eV} ;$$

and from Equ. 6.2b

$$\alpha_o \geq \left( \frac{U_o}{V_{ID}} \right)^{1/2} ,$$

or

$$V_{ID} \geq \frac{U_o}{\alpha_o^2} . \quad (6.4)$$

Numerically with  $\alpha_o = 0.27 \text{ rad.}$  it becomes,

$$V_{ID} \geq 5.9 \text{ eV.}$$

It is obvious that Equ. 6.3 is a stronger requirement (i.e.  $V_{ID} \geq 13.8\text{eV}$ ).

As a check against the experimental result  $V_{ID}$  may be estimated for a Pb beam of temperature  $1100^\circ\text{K}$ . It is found that  $V_{ID} \geq 6.4 \text{ eV}$ . This agrees well with the data in Fig. 59. In the case of backgrounds,  $U_0$  is reduced by a factor of almost 10, while the source area is increased to the entire path length of electrons. Since the path length is the same or even larger than the ionizer dimensions (x-axis), total collection is almost impossible. As can be seen in Fig. 67, infinite  $V_{ID}$  will be required to squeeze the emittance to be within  $\frac{\lambda_i}{2}$  (i.e. zero volume of emittance). However, an experimental saturation may be observed as asymptotic behavior is approached (see Fig. 9(b)).

For the ion injection lens, the acceptance depends on injection momenta which are limited by the resolution of the quadrupole mass spectrometer. For the present mass spectrometer, one has<sup>50</sup>

$$\begin{aligned} U_t &\approx 3.5 \Delta M & (\text{V}) & , \\ U_a &\approx 1.35 \times 10^3 \Delta M & (\text{V}) & , \end{aligned} \tag{6.5}$$

and 
$$d = 0.8 \left( \frac{\Delta M}{M} \right) r_e ,$$

where  $U_t$  is radial energy;  $U_a$  is axial energy (i.e.  $V_{IE}$ ); and  $d$  is the diameter of an injection aperture. With resolution  $\Delta M = 0.5 \text{ amu}$ . (or  $R = \frac{1}{30}$ ), the requirements become

$$U_t \leq 1.75 \text{ (V)}, \quad U_a \leq 670 \text{ (V)}, \quad \text{and} \quad d \approx 1.2 \text{ mm.}$$

The acceptance area is represented in Fig. 68.

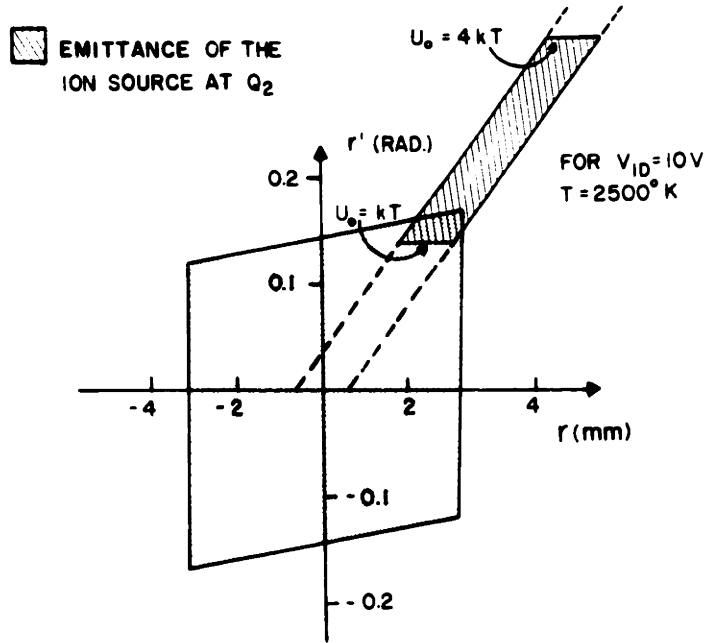


Fig. 68 Acceptance of the ion injection system. The  $Z'$  is limited by the quadrupole mass spectrometer.

From this figure it is obvious that most of the acceptance area is wasted.

Full transmission is possible if high  $V_{ID}$  and  $V_{IE}$  are chosen to satisfy the conditions stated. However  $V_{ID}$  values are also limited by the variation of the electron beam energy discussed in the next section. Careful shaping of the beam using other special techniques (e.g. deflection plane) can possibly achieve full transmission.

### VI.3 Potential Penetrations and Draw-Out Voltage Effects

Due to the existence of draw-out voltage, the actual electron beam energy was changed. The effect was severe in the low energy range where the threshold behavior was investigated. Due to this fact,  $V_{ID}$  was reduced, and the sensitivity for threshold study consequently decreased because of a low extraction and brightness voltage relation. Two types of error may be introduced in the beam energy: 1) the electron beam energy due to the offset of the center tape, and 2) the beam energy spread due to the finite size of the electron beam in the ionization chamber. As shown in Fig. 11, two 100-ohm resistors were used to bridge the center of the main grid.

Due to the geometric inexactness of construction, the center of the grid may be offset by a fraction  $\rho$ . The beam energy then becomes

$$V_e = V_{EE} + \rho V_{ID} \quad (6.6)$$

Assuming that the electron beam is 0.8 mm in diameter, the energy spread (FWHM) will be increased by

$$\Delta V = \frac{r_e}{L_i} V_{ID} = \sigma V_{ID} = 0.03 V_{ID}, \quad (6.7)$$

where  $L_i$  is the length of the ionization chamber and  $r_e$  is the electron beam radius. The actual increment of the beam energy spread may be smaller if the current distribution over the radius is better than uniform.

Investigation of these two effects were made on Ar gas whose threshold voltage is well known.<sup>72</sup> Constant leakage of the Ar was

admitted through a Granville-Phillips Automatic Pressure Controller (series 213) with a series 236 ionization gauge. Fig. 69 shows the threshold ionization cross section of Ar for different  $V_{ID}$ . The result indicates that  $\rho$  is usually very small ( $\rho < 0.002$ ), and  $\delta V$  may be in the order of 0.1 volt for  $V_{ID} = 5$  volts.

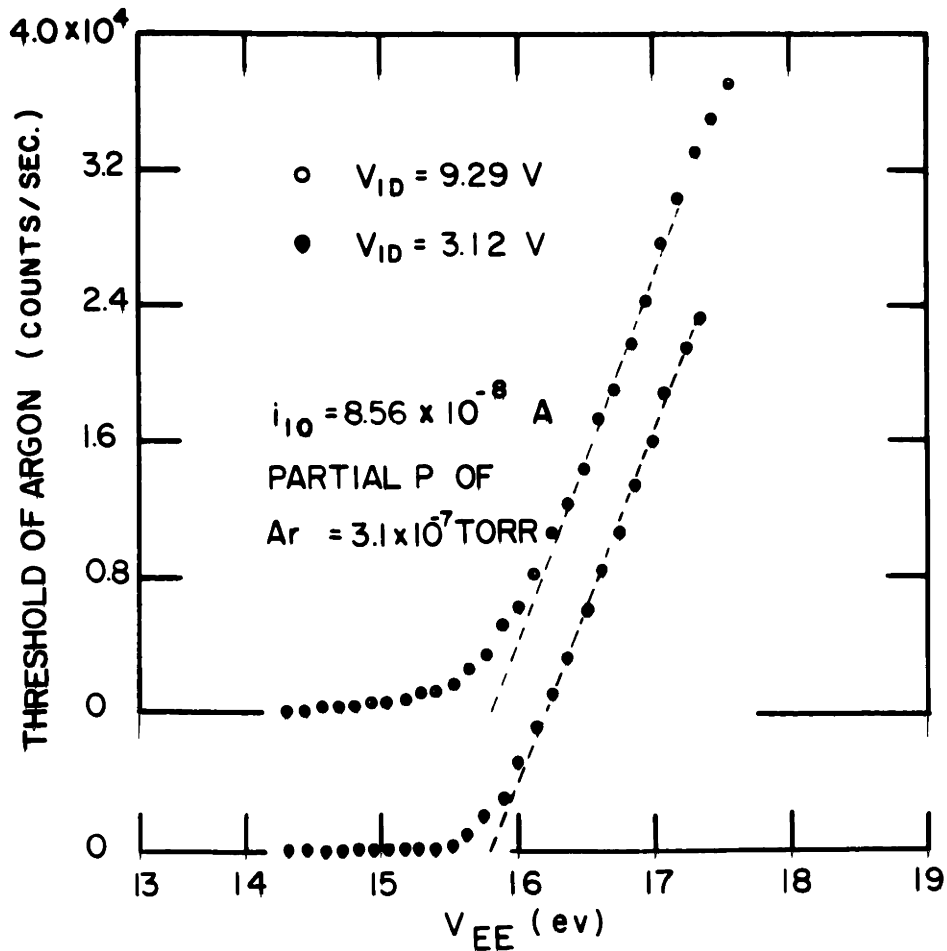


Fig. 69 Threshold behavior of Ar for different  $V_{ID}$ . Linear extrapolation to the threshold for various  $V_{ID}$  indicates that the fractional inaccuracy ( $\rho$ ) is small.

Penetration of the field due to  $V_{ED}$ ,  $V_{IE}$ , and  $V_{IF}$  can be estimated by using the two-dimensional grid formula discussed in appendix (A-14). It has been found to be negligible.

## VII. SIGNAL DETECTION AND ASSOCIATED INSTRUMENTATION

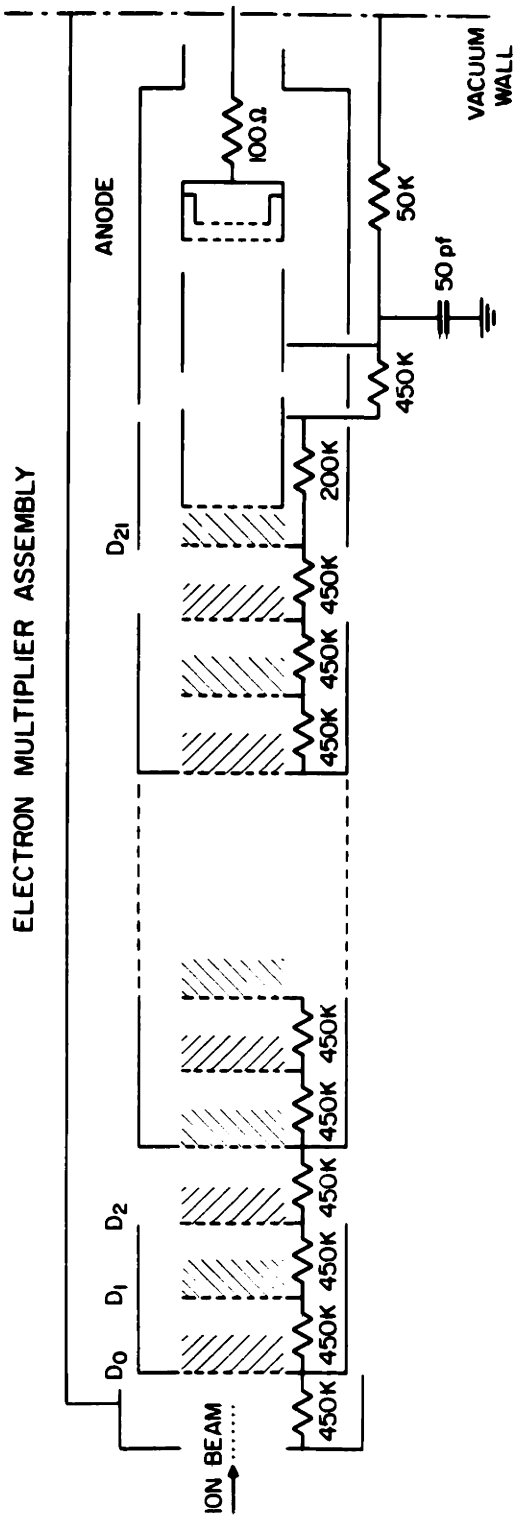
Ions passed through the mass spectrometer were detected with an electron multiplier. The multiplier and pulse electronics was carefully calibrated for its counting efficiency to avoid any uncertainty resulting from unknown yields of the conversion dynode for different ion species. Counting losses were due to statistical null yields of the first three dynodes (particularly of the conversion dynode), and the finite threshold of the counter.

Neutral beam intensity can be detected by several methods, (e.g. weight gain measurement, crystal thickness monitor, etc.). The crystal monitor method is about one hundred times more sensitive than the weight gain method and also more convenient.

### VII.1 Electron Multiplier Construction and Tests

A multiplier using EMI Venetian dynodes was assembled and mounted on the flange at the exit of the mass filter. These dynodes were chosen because of their ease of assembly, low cost, and large area (2.5 cm by 2.5 cm). Due to this large acceptance, no separate focusing system is required, and the multiplier may be placed directly after the quadrupole filter, even with its divergent output beam. A schematic diagram is shown in Fig. 70; the entire multiplier has 22 stages.

The resistive divider used to drive the dynodes consists of a linear chain carrying sufficient current to avoid the loading due to large signals. Although it did not influence operation in the counting mode, output linearity was important in the current amplifier mode (designed to be linear within 1%). Gradient electrostatic shields were used to



FE-3-9-69

Fig. 70 Electron Multiplier using EMI Venetian dynodes. Each of the three dynodes has a common gradient shield to avoid field emission.

Note: 1) total anode lead wire length is 22.8 cm, 2) multiplier surface to flange surface is 29.2 cm, 3) 50pf capacitor is a special ceramic capacitor (parallel stainless steel capacitor), 4) all 450k resistors are pyrofilm PT65 Hermetically Glass Sealed Deposited Carbon film Resistors, 5) 200k is two 100k Texas Instrument Corporation (series CG 1/8), 6) 100Ω is a CG 1/8 Texas Instrument Corp. resistor, 7) total resistance is 10.60 megΩ, 8) the interstage voltage is 4.24 x 10<sup>3</sup> (overall multiplier voltage).



ent field emission from the dynodes near the input. A weak lens, essentially just a drift space, was used between the last dynode and anode to allow the anode lead wire to be shortened to the minimum possible. This reduced the stray inductance and hence prevented the ringing after each pulse which might have given rise to erroneous counts. The focal length<sup>54</sup> of the lens used was about five times the anode diameter; it had no crossover.

The multiplier was then tested in the spectrometer high vacuum chamber. The gain was estimated statistically by averaging the impulse response with a simple RC circuit:

$$\bar{G} = \frac{C\bar{V}_0}{e} \quad (7.1)$$

where C is the capacity of the cable and oscilloscope, and  $\bar{V}_0$  is the average pulse peak voltage.

The variation of the gain with applied voltage for  $N_2^+$  is shown in Fig. 71. Gain characteristics taken about five months later are also represented. Little deterioration was observed.

## 2.2 Ion Counter

When the electron multiplier was connected as a particle counter amplifier in the Counting Mode<sup>50</sup> with the total voltage across the electron multiplier fixed; the detection efficiency was related to the impact energy as shown in Fig. 72. The saturation occurred at about 100 kV. Total detection efficiency was over 90% at this energy.

Similar saturation has been observed by other workers on comparable multipliers.<sup>73-75</sup> The loss of counts is also shown in Fig. 71. This

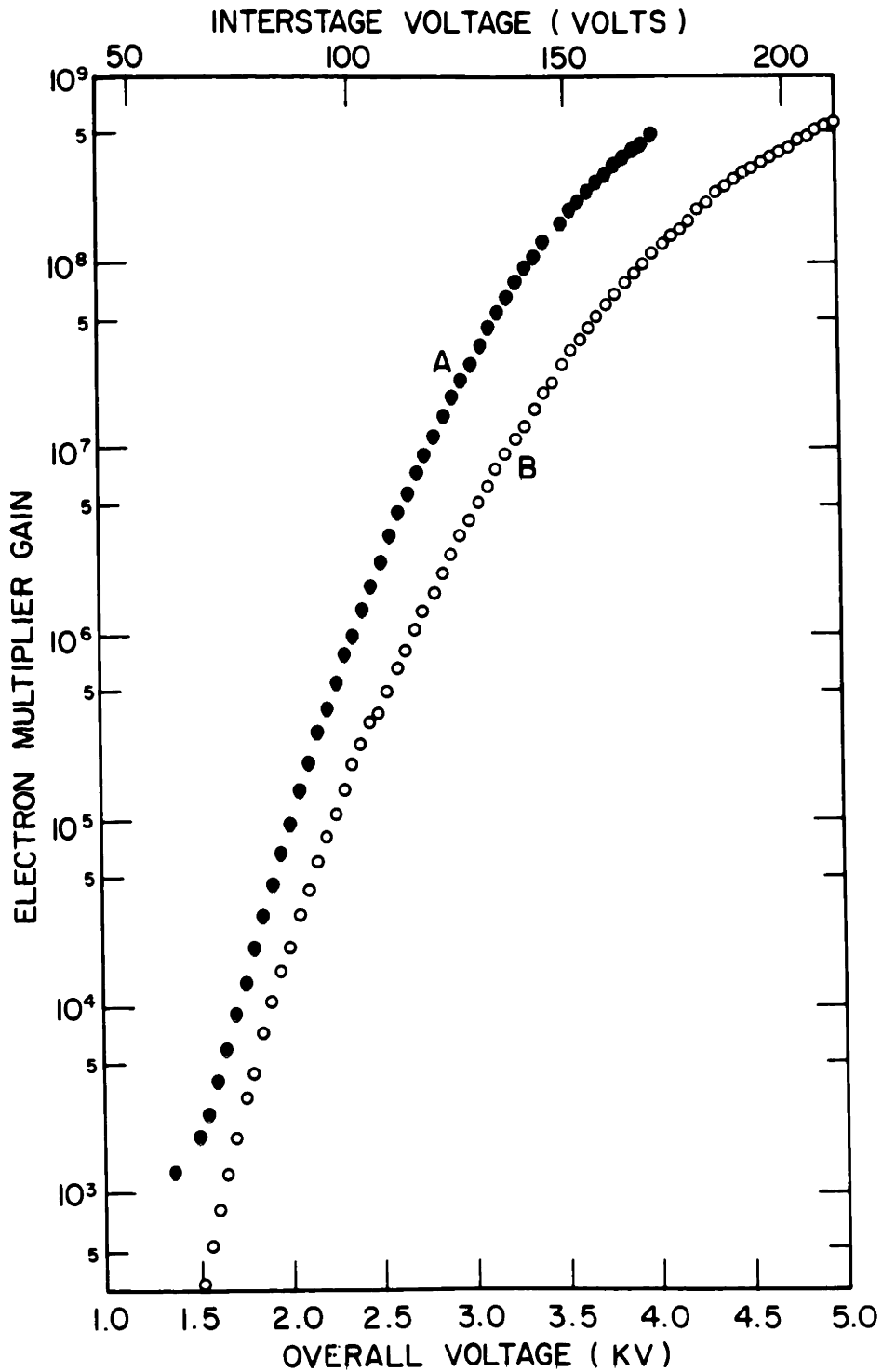
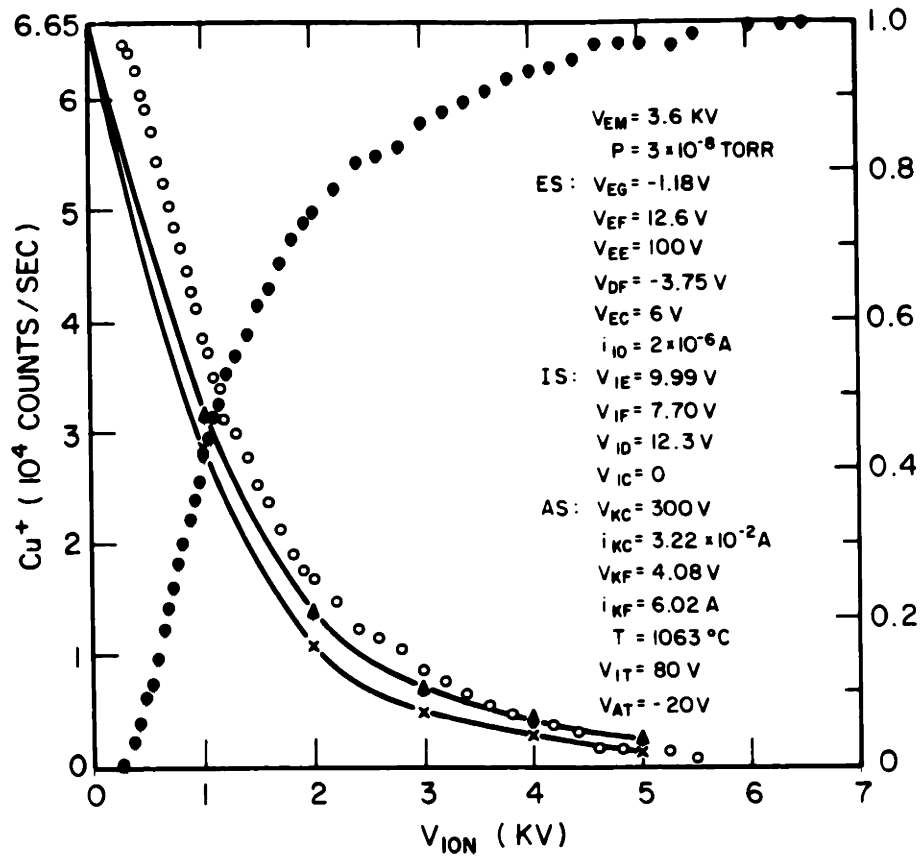


Fig. 71 Gain of the electron multiplier vs. overall voltage (inter-stage voltage is also shown) under  $^{28}\text{N}_2^+$  impact (A). Data B were taken about 5 months later and show only a relatively small deterioration.



FI-6-12-9

Fig. 72 Detection efficiency in counts/sec. (left scale), and percentage (right scale). Data shown as o are the experimentally measured losses. Data  $\Delta$  are the calculated results based on generating functions. Data x are also calculated results, but from a simple model considering all the loss to be due to the conversion (zero) dynode only (i.e.  $P(o) = e^{-\gamma}$ ).

loss can therefore be theoretically calculated if a Poisson distribution of secondary electrons is assumed.<sup>76</sup> The assumption of other secondary distributions would not greatly influence the results.

Consider distribution functions under ionic impact  $p_0(n)$  and under electron impact for each stage,  $p_1(n) = \dots = p_k(n)$ , where  $n$  indicates the number of electrons generated (the "zero" dynode is the ion conversion dynode which is under ionic impact). Then introduce the generating functions,<sup>78</sup>

$$g_0(s) = \sum_{n=0}^{\infty} p_0(n) s^n \quad (7.2)$$

$$g(s) = \sum_{n=0}^{\infty} p(n) s^n \quad (7.3)$$

In the case of a Poisson distribution

$$g(s) = \sum_{n=0}^{\infty} \frac{\gamma^n e^{-\gamma}}{n!} s^n = e^{-\gamma} e^{\gamma s} \quad (7.4)$$

$$g_0(s) = \sum_{n=0}^{\infty} \frac{\alpha^n e^{-\alpha}}{n!} s^n = e^{-\alpha} e^{\alpha s} \quad (7.5)$$

where  $\gamma$  is the secondary electron yield for electron impact,  $\alpha$  is the secondary electron yield for ion impact.

The generating function from the first dynode to the  $k^{\text{th}}$  dynode can then be shown to be:

$$G_k(s) = g[G_{k-1}(s)] = g[g[G_{k-2}(s)]] \quad (7.6)$$

$$= \sum_{n=0}^{\infty} P_k(n) s^n \quad (7.7)$$

$$P_k(n) = \frac{1}{n!} \left. \frac{d^n G_k(s)}{ds^n} \right|_{s=0} = \frac{G_k^{(n)}(s)}{n!} \Big|_{s=0} \quad (7.8)$$

where  $P_k(n)$  is the probability of generating  $n$  electrons at the  $k^{\text{th}}$  stage when the first stage is struck with a single electron. The differentiation can be obtained as,

$$\begin{aligned} \frac{d^n}{ds} G_k(s) &= \frac{d^n}{ds^n} g[G_{k-1}(s)] \\ &= \frac{d^{n-1}}{ds^{n-1}} \frac{d}{ds} (e^{-\gamma} e^{\gamma G_{k-1}(s)}) \\ &= \gamma \frac{d^{n-1}}{ds^{n-1}} [G_k(s) G_{k-1}^{(1)}(s)] \quad n \neq 0 \\ &= \sum_{i=0}^{n-1} \gamma C_i^{n-1} G_k^{(i)}(s) G_{k-1}^{(n-i)}(s) \end{aligned} \tag{7.9}$$

where  $C_i^{n-1}$  is a binomial expansion coefficient.

$$P_k(n) = \frac{\gamma}{n} \sum_{i=0}^{n-1} (n-i) P_k(i) P_{k-1}(n-i) \tag{7.10}$$

To include the zero dynode, consider the generating function for an entire multiplier:

$$G(s) = g_c[G_k(s)] = e^{-\alpha} e^{\alpha G_k(s)} = \sum_{n=0}^{\infty} P(n) e^{sn} \tag{7.11}$$

and then

$$P(n) = \frac{\alpha}{(n+1)!} \frac{d^n}{ds^n} G(s) G_k(s) \Big|_{s=0} \quad n \neq 0 \tag{7.12}$$

$$= \frac{\alpha}{n+1} \sum_{i=0}^n (n-i+1) P(i) P_k(n-i+1) \quad n \neq 0 \tag{7.13}$$

The pulse height distribution may therefore be obtained by consecutively applying (7.10) and (7.13). No calculation has yet been made, however

since a pulse height analyzer wasn't available to measure the experimental distribution. This distribution could also be obtained by adjusting the threshold of the counter. Unfortunately no precise calibration of threshold was available. If a precise pulse height distribution were available, one could also check the secondary yield distribution by unfolding techniques.

The theoretical loss may be easily found as  $n = 0$  in (7.11).

$$P(o) = g_o[G_k(o)] = e^{-\alpha} e^{\alpha G_k(s)} \Big|_{s=0} \quad (7.14)$$

$$= e^{-\alpha} e^{\alpha e^{-\gamma}} e^{-\gamma} \quad (7.15)$$

In the present case,

$$K = 21,$$

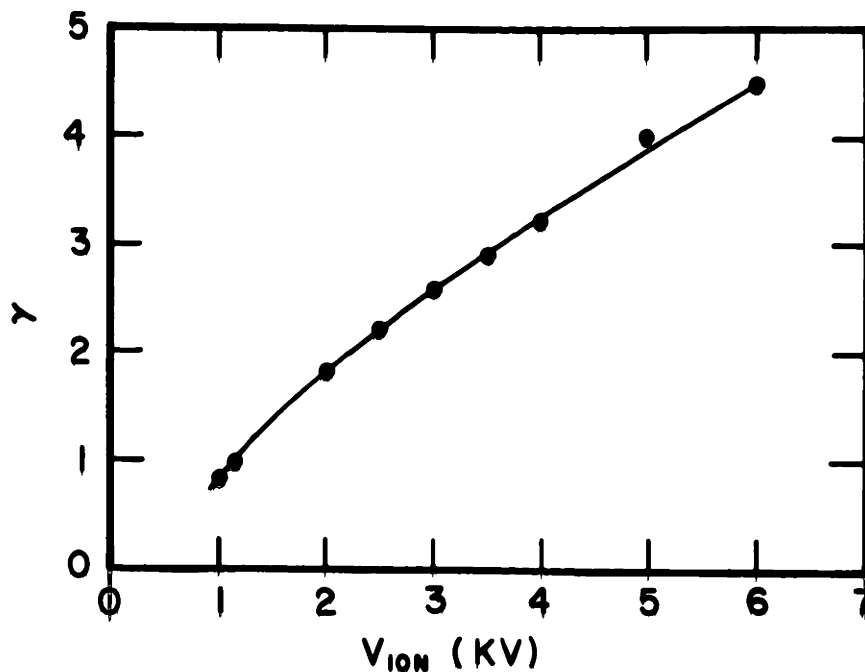
$\alpha$  is given as Fig. 73<sup>79</sup>,

$$\gamma = \sqrt{\frac{21 \times 1.5 \times 10^8}{2.98}} = 2.326 \text{ at } V_{EM} = 3.6 \text{ kV} \quad (7.16)$$

$$P(o) = e^{-\alpha} e^{0.1331\alpha} \quad (7.17)$$

The computation shows that the major loss comes from the "zero" dynode and the first three to four stages. Thus, for over 90% detection, the incoming ion energy should be over 3.5 kV. The loss due to the finite sensitivity of the counter here can be considered negligible as will be shown later. The discrepancy in the data at low energy is probably due to the divergent ion beam (the skew angular momenta from

the spectrometer output).



F2-6-24-9

Fig. 73 Secondary electron yield of BeCu by  $\text{Cu}^+$  ions. Data were interpolated between  $^{40}\text{Ar}^+$  and  $^{84}\text{Kr}^+$ .

The multiplier was next connected in the Amplifier-Counting Mode, and the gain of the multiplier was varied by adjusting the multiplier voltage. The counter output was then plotted against the voltage as shown in Fig. 74 (A).

(B) in Fig. 74 has the same characteristics as (A) except that the detection efficiency was calculated using a different ion impact energy. A portion of (B) is shown with a linear scale in (C).

Fig. 74 reveals an abnormally sharp rise when  $V_{EM} > 4.3$  kV. This sharp increase was not due to the field emission at the dynodes since

adjustment of the resolution of the spectrometer to infinity (zero transmission) confirmed that the background at this applied voltage is less than 0.2 count per second. Observation with a storage scope at 20msec/cm horizontal sweep, however, showed that there was a one-to-one correspondence between the electron multiplier and the counter

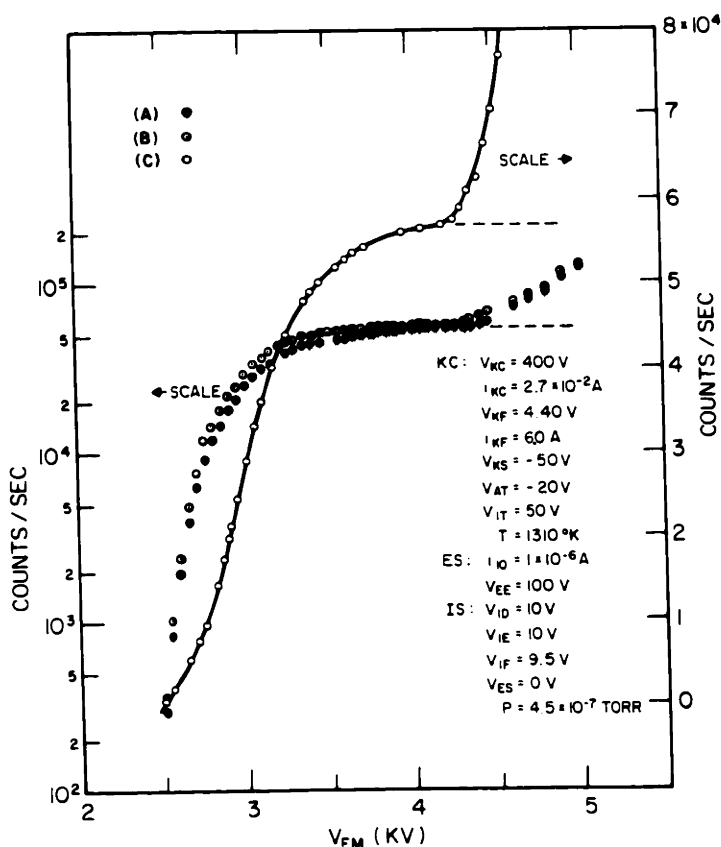


Fig. 74 Counting efficiency shown as a function of multiplier voltage.  $V_{EM} > 3.5$  kV guarantees that nearly every ion will generate an output pulse. The abnormal rise at 4.5 kV is probably due to the ringing of the preamplifier.

pulses at any  $V_{EM}$ . But, as  $V_{EM}$  increased from 4kV to 5kV, the output pulse height from the pulse standardizer was counting double pulses. The rate of counting however, was still less than 100 counts per second,



and thus the probability of having two particles arrive within such a short period of time (100 ns) was extremely low. Note also that, at this applied voltage, the gain of the multiplier did not rise sharply. It appears then, that these overlapping counts were caused by the ringing of the preamplifier and the anode lead wire when faced with a strong input pulse. The amplitude of the ringing apparently exceeded the threshold of the detector and registered as additional counts. Ion feedback, although possible, was not very likely in this instance, since the effect did not depend on the background pressure. (A reduction of the main amplifier gain also substantially decreased the effect.)

From Fig. 74, the required gain for full detection is about  $10^8$  with  $V_{EM} = 3.5$  kV. The loss derived from the finite sensitivity as indicated in Fig. 72 is thus confirmed to be negligible.

In summary, the EMI Venetian multiplier did not evidence much gain loss with repeated use. When the multiplier was used in the amplifier-counter mode for ion detection, the efficiency was more than 90%, as long as the  $V_{EM}$  was set greater than 3.6 kV. For even more accurate measurements, the counting mode is recommended with  $V_{ion} = 5$  kV and  $V_{EM} = 3.5$  kV.

### VII.3 Atomic Beam Detection

Calibration of absolute cross sections requires the information of neutral density  $n$ , which can in turn be determined from the neutral beam intensity (flux intensity) and its average velocity. There are several ways to do this:

(a) Weight Gain Measurements

Neutral density may be determined by condensing neutral atoms on a trap made of crinkled sheet metal to increase the accommodation coefficient. The neutral density can then be expressed as

$$n = \frac{\phi}{\bar{v}_b} = \frac{W N_a}{M A_a t \bar{v}_b} \quad (\text{particles/cm}^3) \quad (7.18)$$

where  $\phi$ : beam intensity (particles/cm<sup>2</sup>)

W: total weight gain in the trap (grams)

M: molecular mass (amu)

t: total condensation time (sec)

A<sub>a</sub>: Beam area  $\ell \times b$  (cm<sup>2</sup>)

N<sub>a</sub>: Avogadro's number  $6.0224 \times 10^{23}$  (molecules/gram-mole)

Substituting into the simple cross section formula, it becomes

$$\sigma = \frac{IMt \bar{A} \bar{v}_b}{i \ell W N_a} = \frac{IMt \bar{v}_b b}{i W N_a} \quad (\text{cm}^2) \quad (7.19)$$

and

$$\bar{v}_b = \sqrt{\frac{9\pi}{8} \frac{kT}{m}} \quad (\text{cm/sec})$$

The existing micro balance has an ultimate sensitivity of  $\pm 2 \times 10^{-6}$  gram, but is reliable only to  $\pm 10^{-5}$  grams. Thus for accuracies of a few percent, total weight gain should be in the order of  $10^{-3} \sim 10^{-4}$  gram. If one assumes a reasonable deposition of 0.001 gram/hour, the beam intensity (for C<sub>1</sub>) must be,

$$\phi = 3.68 \times 10^{14} \quad (\text{particles/cm}^2\text{-sec})$$

or at  $T = 2400^\circ\text{K}$ ,

$$n = 8.32 \times 10^9 \quad (\text{particles/cm}^3)$$

The source pressure may be estimated from Equ. 4.3

$$P_s \approx 3.06 \times 10^{-3} \text{ torr}$$

(b) Use of a Crystal Thin Film Thickness Monitor

In a piezoelectric device, the oscillation frequency depends on the mass of the crystal used.<sup>80</sup> Thus a change of mass due to deposition on the crystal results in a frequency shift. This shift can be measured. The change in oscillation period may be expressed as<sup>81</sup>

$$(d\tau) = \frac{m}{N\rho_c A} = \frac{\Phi \cdot A'}{N\rho_c A} \quad (7.20)$$

where  $N$  is a constant which depends on the crystal cut and material (for example, an AT cut quartz crystal has  $N = 1670 \text{ KHz mm}$ );  $\Phi$ , the beam intensity, is measured in  $\text{gram/cm}^2$ ; and  $A$  and  $A'$ , the effective crystal area and deposition area respectively, are in  $\text{cm}^2$ .

From (7.20) it follows that,

$$\Phi = N\rho_c \frac{A}{A'} (d\tau) = K(d\tau) \quad (\text{gram/cm}^2) \quad (7.21)$$

The ultimate sensitivity of the monitor depends, of course, on the stability of the electronics. The commercially available thickness monitor for thin films (Granville-Phillips Series 219) has a stability

of about  $\pm 4 \times 10^{-8}$  gram over an hour. For accuracy of a few percent, a condensed mass of  $10^{-5}$  gram/cm<sup>2</sup> is needed, and the required neutral density can then be estimated as

$$n^* = \frac{k(d\tau)}{tv_b} = \frac{R'\rho A}{tv_b A'} \quad (\text{gram/cm}^3)$$

where  $t$  is the total time of deposition and  $R'$  is the thickness (cm). Since the Granville-Phillips electronics are aluminum calibrated for ( $\rho = 2.702$  gram/cm<sup>3</sup>), the neutral density may be calculated from the direct thickness reading  $R$  using

$$n = 2.702 \times 6.0224 \times 10^{15} \frac{A}{A'} \gamma \frac{R}{tv_b} \frac{1}{M} \quad (\text{particles/cm}^3) \quad (7.23)$$

where  $\gamma$  is the accommodation coefficient.

It is important to notice that the required particle density ( $n$ ) does not depend on  $\rho$ . This is fortunate since there usually is a discrepancy between thin film and bulk material densities.

Use of a Crystal Monitor offers a higher sensitivity and permits the determination of the neutral density without venting the system. This latter advantage is particularly useful in cases where polymers are being studied and where multiple determinations of  $n$  are necessary as described in Chapter IV. On the other hand, there is an uncertainty in the accommodation coefficient because a high accommodation coefficient cannot be achieved by using crinkled sheet metal as in the weight gain method. Additional experiments may be needed to calibrate this coefficient.<sup>82</sup> Other schemes include the radioactive isotope dilution

(using  $C^{14}$ ) and the recently proposed torsion balance techniques<sup>83</sup>.

However, in the former case, the contamination due to the radioactivity in the isotope dilution is a disadvantage. In the latter case, the torsion balance has a complicated procedure of calibration and has lower, or at most, the same sensitivity. Only methods (a) and (b) were used in the carbon studies.

#### VII.4 Signal Detection

VII.4.1 Reference Channel--The reference signal necessary for the T-O-F study and the chopped beam technique is obtained using a tungsten light source phototransistor pair, as shown in Fig. 75. This signal

(the shutter function) is fed to the reference input of the lock-in amplifier. The chopping frequency can be varied from 100Hz to 6KHz by changing the motor drive frequency and substituting different chopper slots.

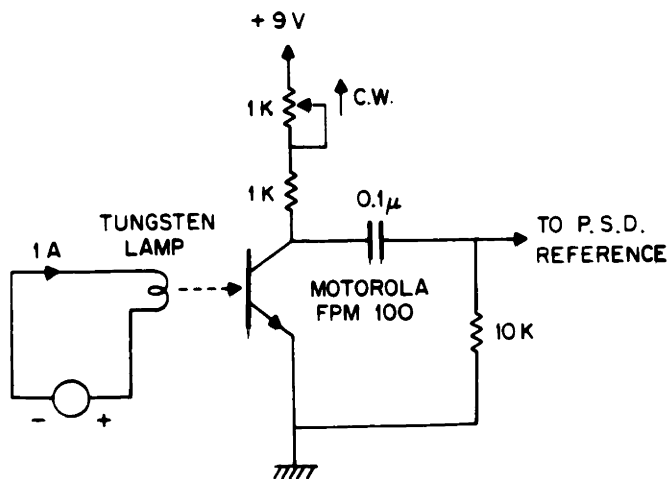


Fig. 75 Circuit for the lamp-phototransistor pair

VII.4.2 Signal Channel--The electron multiplier signal can be fed either to the pulse electronics or to a current amplifier as shown in Chapter III.

The wave form of the output signal was displayed using a synchronous wave form detector as shown in Fig. 76. The lower wave form came directly from the reference channel.



CHOPPER FREQUENCY= 800 Hz

X-AXIS : 0.2ms/sec. Y-AXIS : 0.46v/cm

Fig. 76 Signal output displayed with a waveform Eductor.

The lower wave form is the reference signal obtained from the light-phototransistor pair.

#### VII.5 Signal-to-Background Ratio

The advantage in signal-to-background ratio of using a modulated beam over an unmodulated beam can be easily seen from the following spectra. Fig. 77(a) shows the unmodulated beam spectra. The  $^{36}\text{C}_3^+$  contribution (from the molecular beam) peak here is only about 20% of the mass 36 peak shown; the remainder is background gas. This

was observed by moving the chopper a few degrees to completely stop off the beam. Spectra using a modulated beam and the synchronous detector are shown in Fig. 77(b). An improvement in the signal-to-background of  $5 \times 10^3$  has been achieved with an ion current about  $10^{-16}$  amp (approximately  $10^3$  counts/sec). A noise equivalent of about  $10^2$  counts/sec remains, most of which probably comes from the background current.

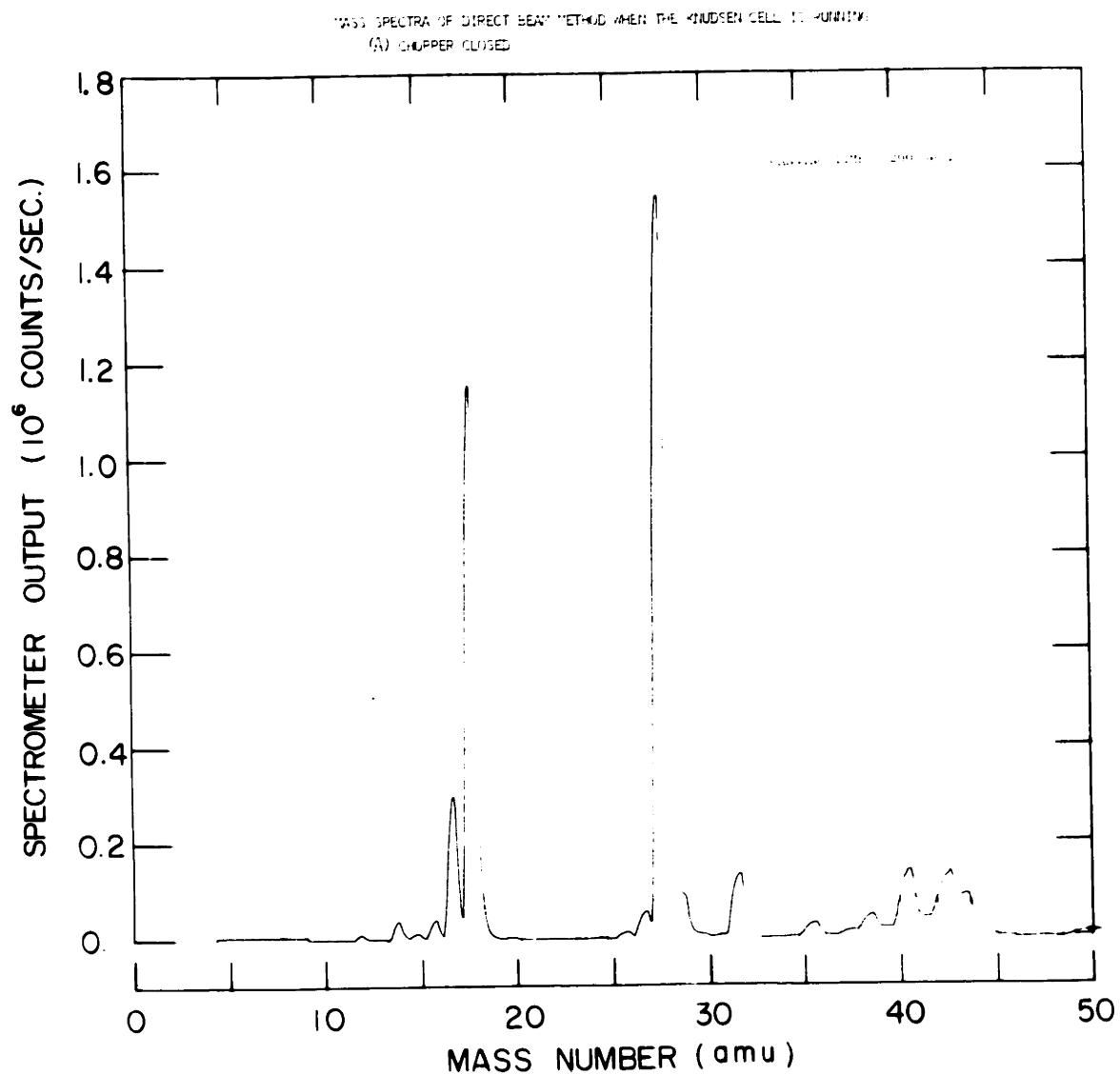


Fig. 77(a) Background spectra when the chopper is moved to interrupt the beam. Notice that the major backgrounds are  $N_2$  and  $H_2O$ .



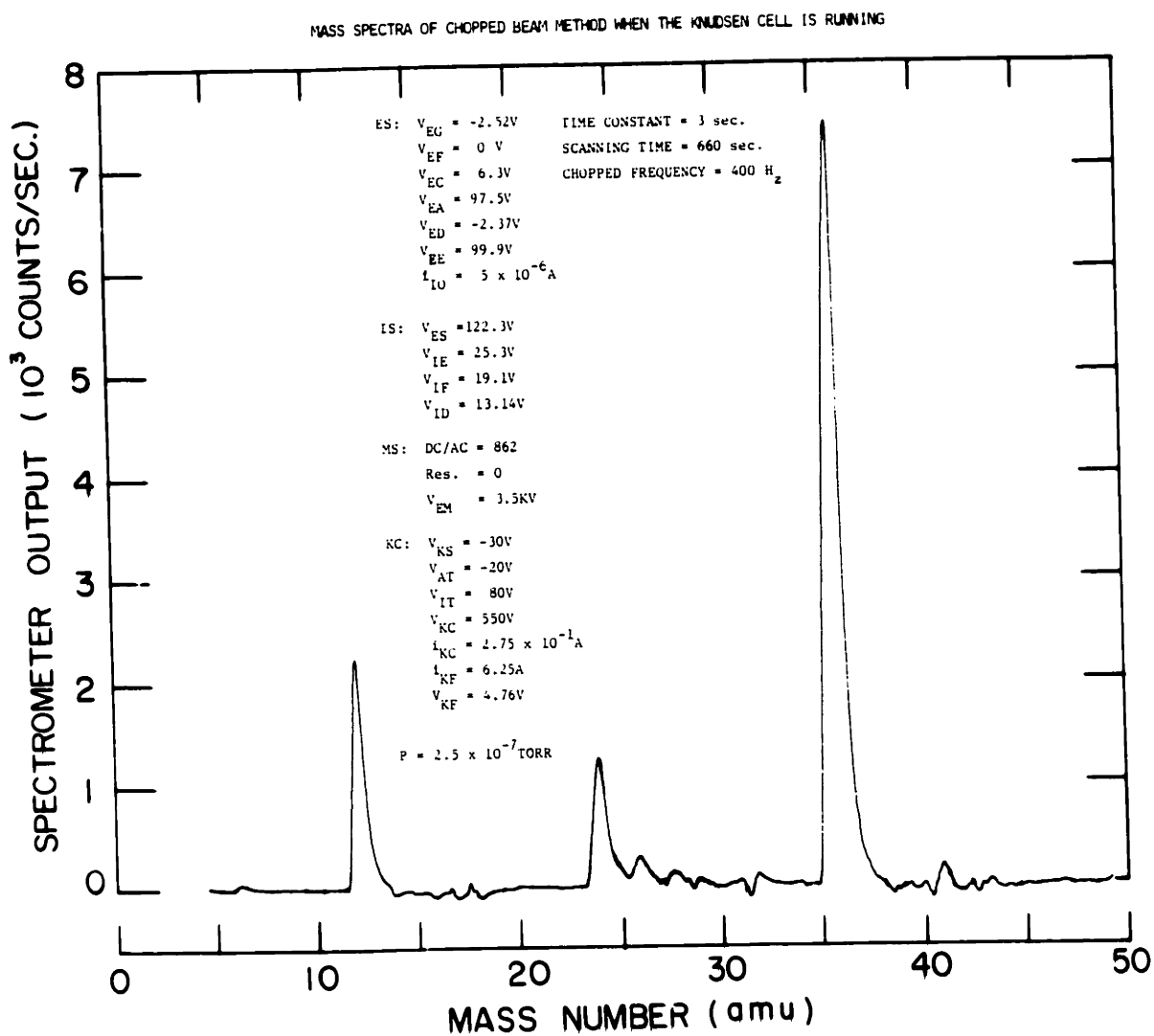


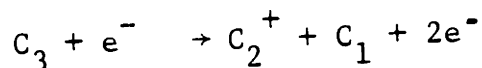
Fig. 77(b) Atomic beam spectra by the chopped beam technique. This run was made at low intensity to show the gain of signal-to-background ratio.

### VIII. IONIZATION CROSS SECTIONS

Ionization cross section data for carbon ( $C_1^+$ ,  $C_2^+$ ,  $C_3^+$  and  $C_1^{++}$ ) were measured by the techniques described in the previous chapters. Fragmentation is considered. Since no other experimental data are available, the results could only be checked against theoretical approximations. Modified Bethe, Born, and classical Cryzinski approximations are used.

#### VIII.1 Fragmentation Experiments

The time-of-flight experiments were made using a phase sensitive detector (PAR HR8 lock-in amplifier) as described in Chapter II. The phase shifts between species  $C_3$ ,  $C_2$  and  $C_1$  as functions of  $V_{EE}$  are given in Fig. 78.  $C_2^+$  ions from the fragmentation, e.g.



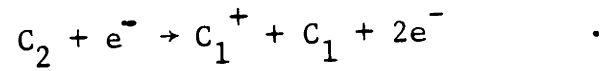
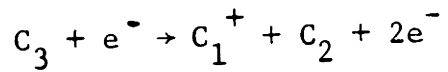
can be separated using

$$I_{2f}^+ = \left( 1 - \frac{\theta_{32}}{\theta_{32}^*} \right) I_2^+ \quad , \quad (8.1)$$

where  $\theta_{32}^*$  is a theoretical and  $\theta_{32}$  an experimental phase angle between  $C_3^+$  and  $C_2^+$ . Similarly,  $C_1^+$  from the fragmentation may be obtained as

$$I_f^+ = \left( 1 - \frac{\theta_{31}}{\theta_{31}^*} \right) I^+ \quad . \quad (8.2)$$

However, it is impossible to distinguish whether these ions are from  $C_3$  or  $C_2$  fragmentations, or from other reactions which produce  $C_1^+$  ions, e.g.



The fragmented ion current was then deduced.

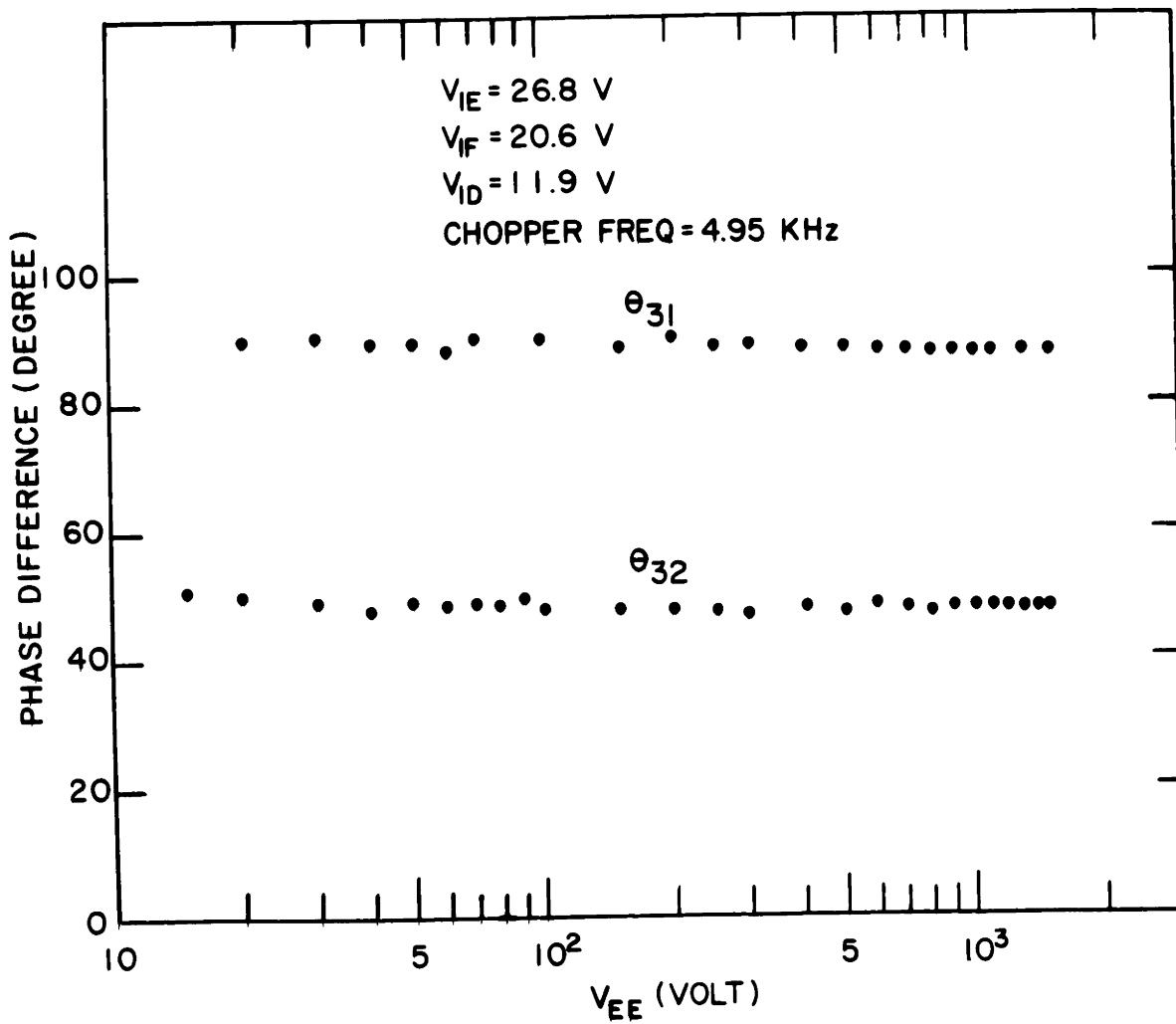
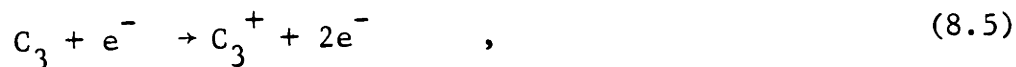
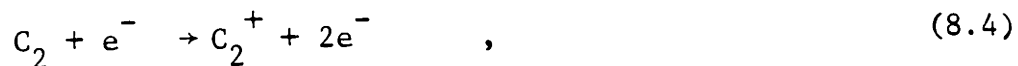
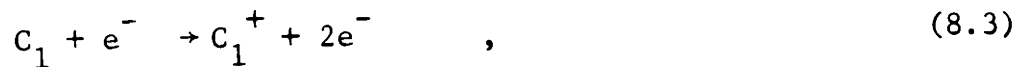


Fig. 78 Phase differences due to T-O-F with respect to  $V_{EE}$

VIII.2 Ionization Cross Section Data

The ionization cross sections of the following reactions,



and



were obtained and are presented in Figs. 79 through 82. The relative values were measured by both the direct and the chopped beam methods.

In the calibration of absolute values, the results of several runs showed a very close ratio of  $C_1^+ : C_2^+ : C_3^+$ . Thus the solutions of the simultaneous equations (2.44) were not stable as discussed in Appendix 6. Therefore the absolute values were, instead, calculated using the assumption that the relative cross sections are 3:2:1 for  $C_3^+$ ,  $C_2^+$ , and  $C_1^+$ , respectively. This assumption of these ratios agrees very well with experimental results at high energy for many elements and organic compounds as illustrated in Fig. 83.

On the other hand, Pottier<sup>84</sup> observed that cross section ratios of molecules to atoms were found to be less than two. However, no specific energy at which the ratios were taken was given. The results of Fig. 83 show that additivity holds with good accuracy at energies where the Born approximation is valid (c.f. VIII.4).

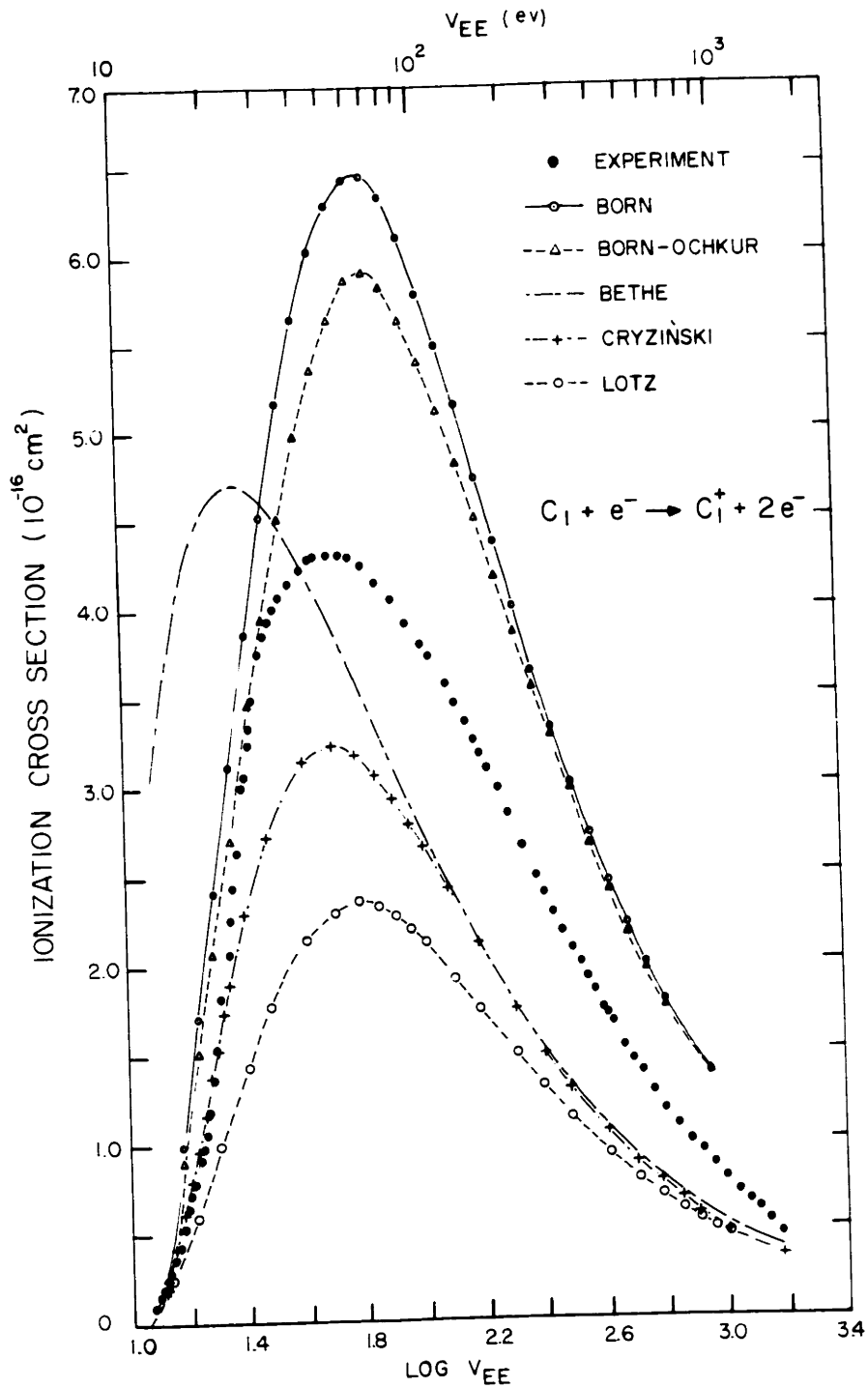


Fig. 79 Ionization cross section for  $C_1^+$ . Points are the experimental results; curves represent various approximations which will be discussed in the following sections.

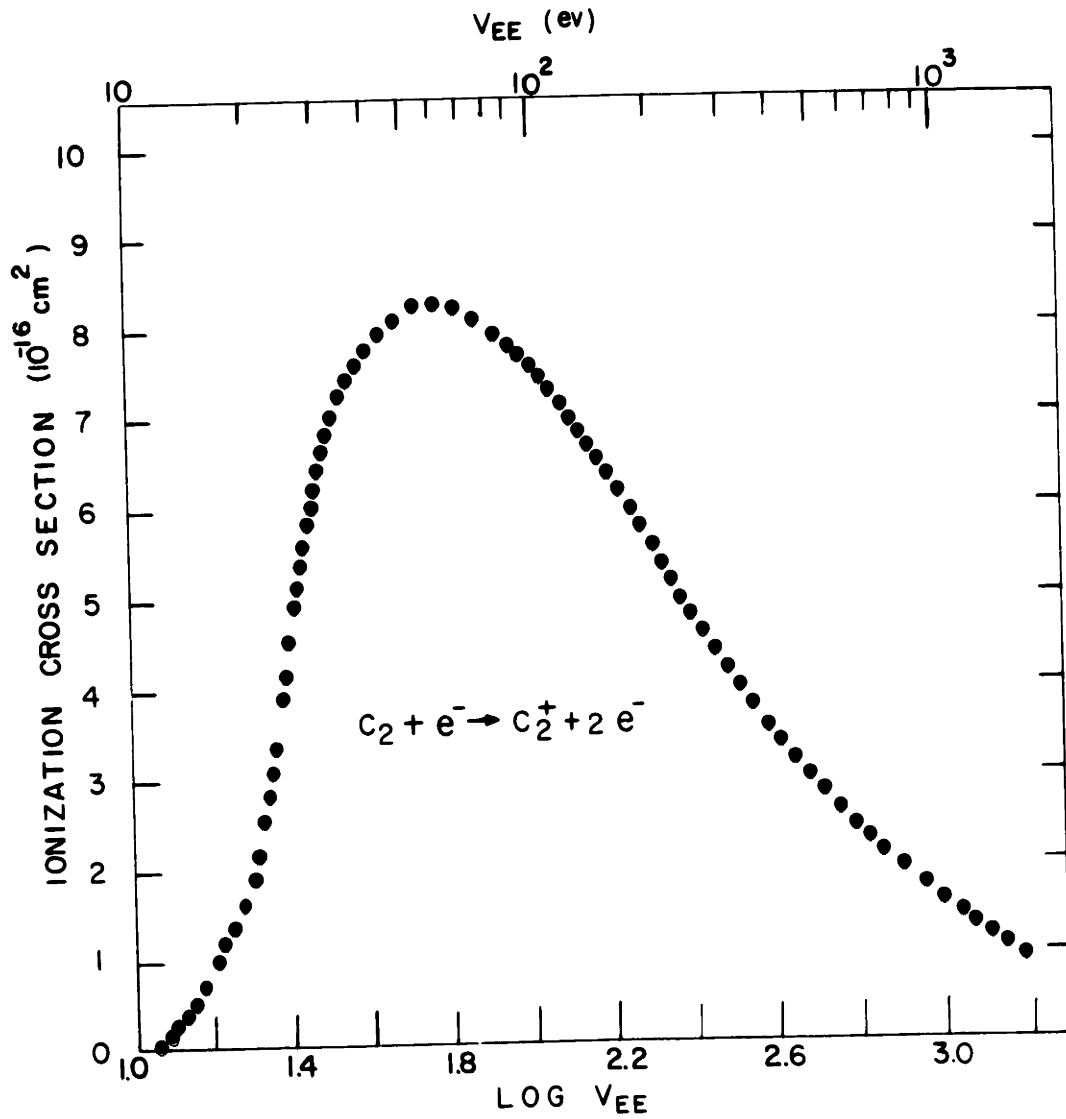


Fig. 80 Ionization cross section for  $C_2^+$

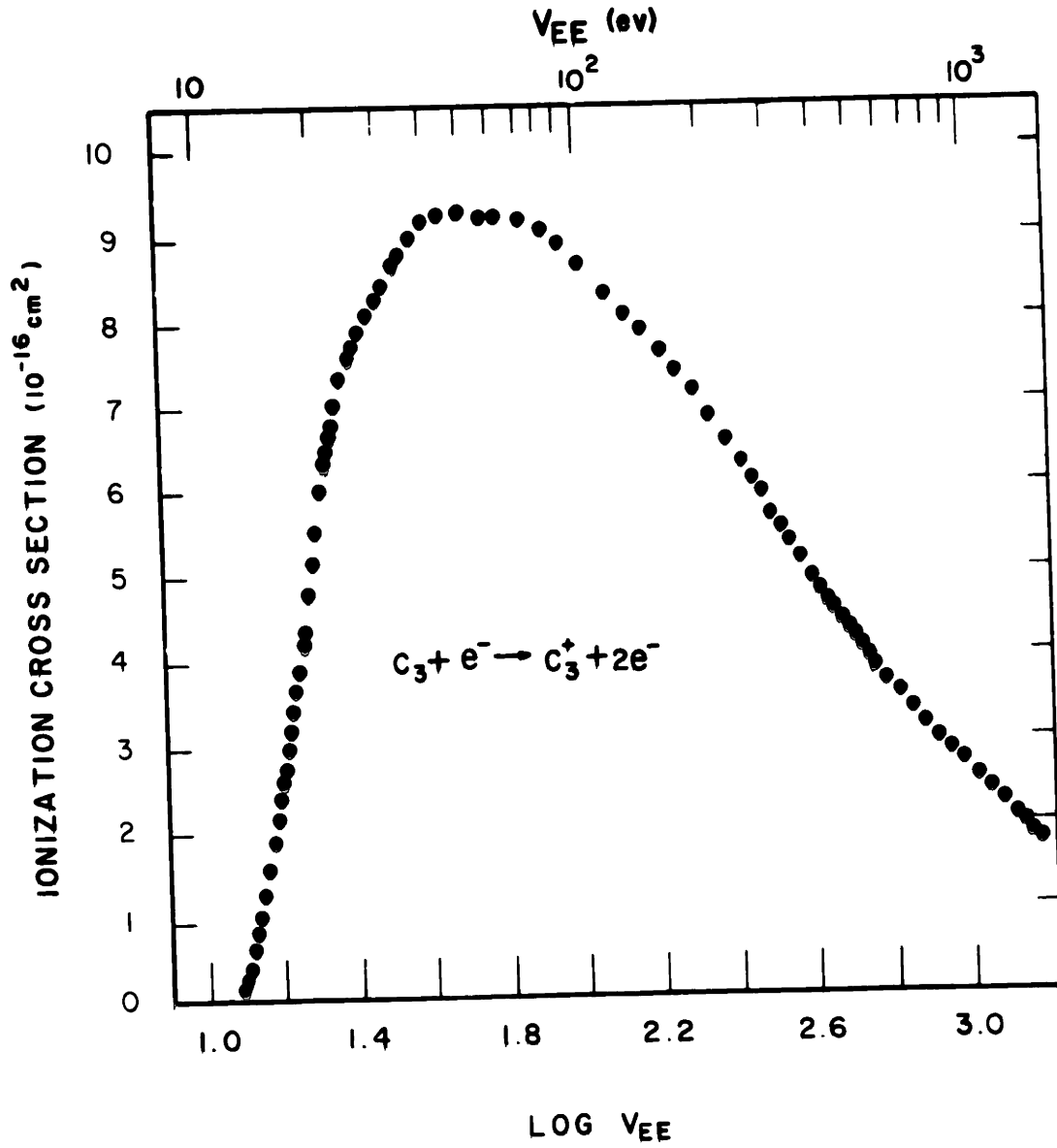


Fig. 81 Ionization cross section for  $C_3^+$

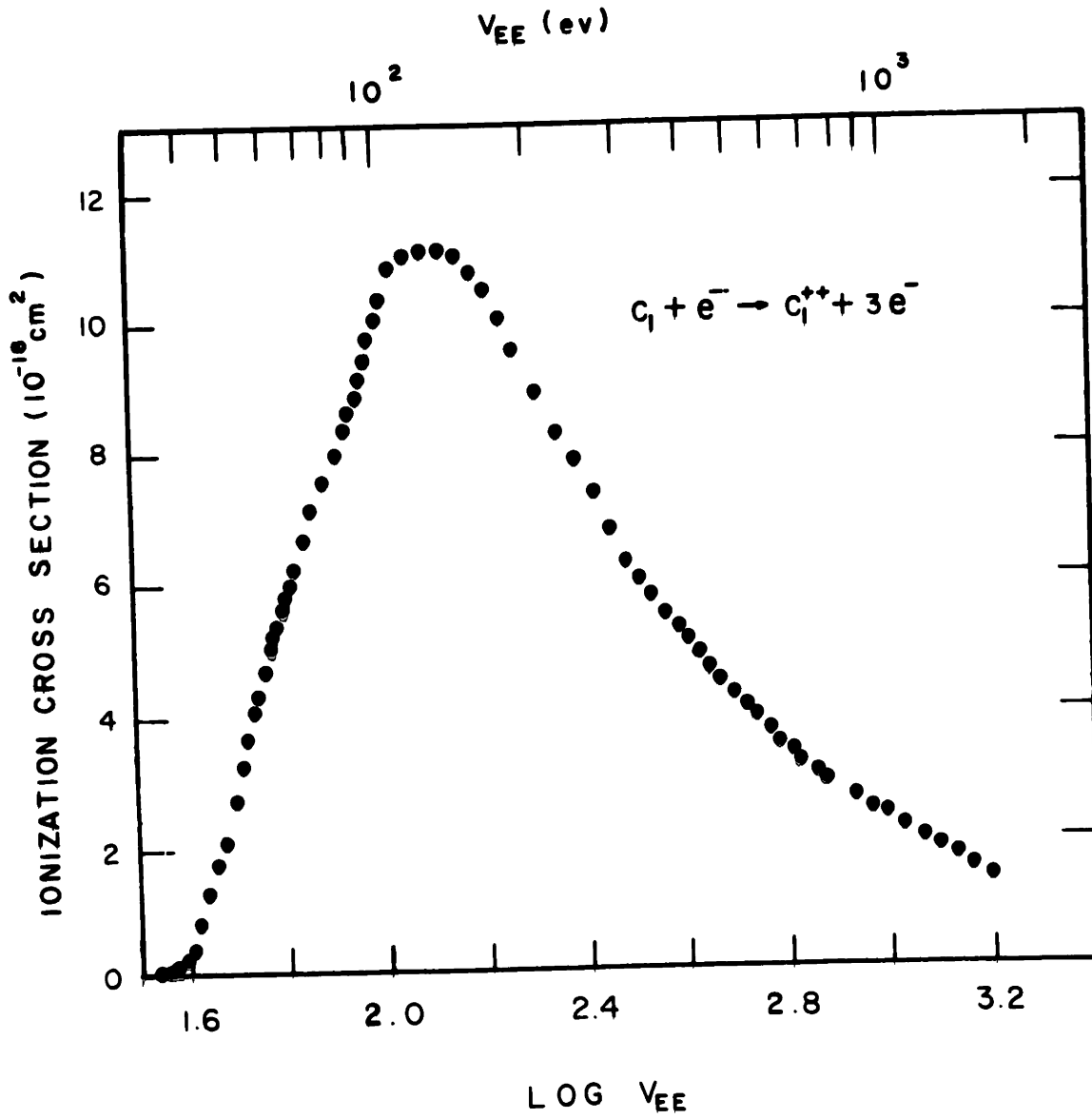


Fig. 82 Ionization cross section for  $C_1^{++}$



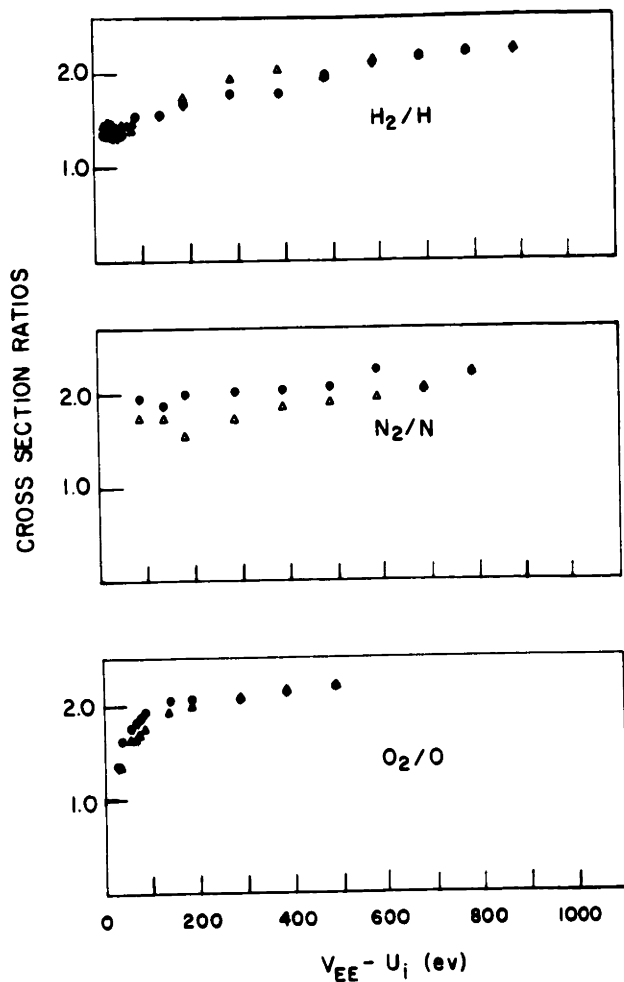


Fig. 83 Cross section ratios of various molecules to atoms. The additivity rule is shown to be almost true for high energies.

Similarly, contributions of  $C_2^{++}$  and  $C_3^{+++}$  were estimated by assuming their ratios to  $C_1^{++}$  as 2 and 3, respectively. Triple and higher order ionizations were considered to be negligible.

Since no other experimental data is available, no further direct comparisons could be made, however some theoretical calculations and estimates will be discussed in section VIII.4.

### VIII.3 Threshold Behavior

The monochromator described in section V.3 was used with an energy spread set at about 0.1 eV to achieve reasonable electron current, with a reasonable sensitivity. The monochromator was operated at a beam energy of about 7 eV. The absolute energy scale was calibrated with the threshold potential of argon which was admitted to the system through a leak valve regulated by a Granville-Phillips automatic pressure controller. The threshold potential of argon is taken to be 15.739 eV.<sup>72</sup> Correction of the energy scale due to the neutral beam energy can be shown to be negligible as follows: When the neutral atoms are considered to be stationary the resultant velocity can be expressed as

$$v_t = \sqrt{v_e^2 + v_n^2} = \left(\frac{2eE}{m}\right)^{1/2} \sqrt{1 + \frac{E_n m}{EM}},$$

and the energy is

$$eE_t = \frac{1}{2} m v_e^2 = (eE) \left[ 1 + \frac{E_n m}{EM} \right].$$

For  $C_{12}$ , it becomes

$$\begin{aligned} E_t &= E \left[ 1 + \frac{E_n}{E} \frac{1}{12 \times 1861} \right] \\ &= E + 4.48 \times 10^{-5} E_n \cong E \end{aligned}$$

where  $E_t$  is the electron impact energy, and  $E$  is the electron beam energy (i.e.  $V_{EE}$ ), and  $E_n$  is the neutral beam energy (at most 0.3 eV at a

temperature of 2800°K).

The overall energy deviation including those discussed in Chapter V, does not exceed 0.1 eV. The resulting threshold behavior for  $C_1^+$ ,  $C_1^{++}$ ,  $C_2^+$ , and  $C_3^+$  are shown in Figs. 84, 87, 85 and 86, respectively. The threshold potentials were found to be  $11.31 \pm 0.1$ ,  $12.05 \pm 0.1$ , and  $12.1 \pm 0.1$  eV for  $C_1^+$ ,  $C_2^+$ , and  $C_3^+$ , respectively. These are close to the values measured by Drowat *et al*<sup>29</sup> ( $11.3 \pm 0.6$ ,  $12.0 \pm 0.6$ , and  $12.6 \pm 0.6$  eV). Recent studies by Wachi and Gilmartin<sup>85</sup> showed that the appearance potential of  $C_3^+$  is about 12.1 eV.

The general shape of the ionization cross section predicted from quantum mechanics calculation is proportional to  $(E - U_i)$ . On the other hand, a classical calculation by Wannier<sup>86</sup> gave the dependence of  $(E - U_i)^{1.127}$ . Many experiments have been carried out to test the validity of the above results. No decisive conclusion could have been made because of:

- 1) spurious contributions to the energy spread of impact electrons,
- 2) uncertainty about the valid energy range, and
- 3) the observed cross section tails which may have arisen from multiple processes involving initial excitation just below the ionization potential.

The break in slope near 17 eV is probably a result of the 2s shell contribution. Wachi and Gilmartin<sup>85</sup> suggest that the break for  $C_3^+$  might be due to the fragmentation from higher polymers such as  $C_4$ ,  $C_5$ , etc. This seems unlikely, however, since the higher polymer intensities are much smaller than the intensity of  $C_3^+$ , and it is improbable that

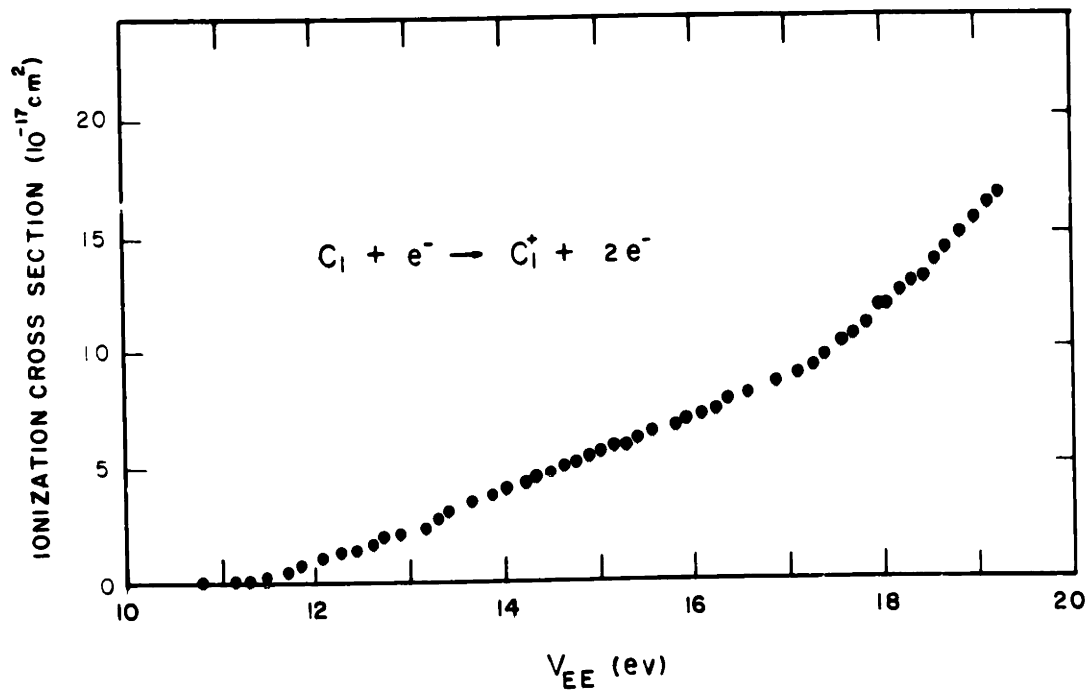


Fig. 84 Threshold cross section for  $C_1^+$

the fragmentation cross section would be much higher than the simple cross section (as evidenced in other molecules such as Na and Ha).

For double ionization, the threshold dependence is expected to be

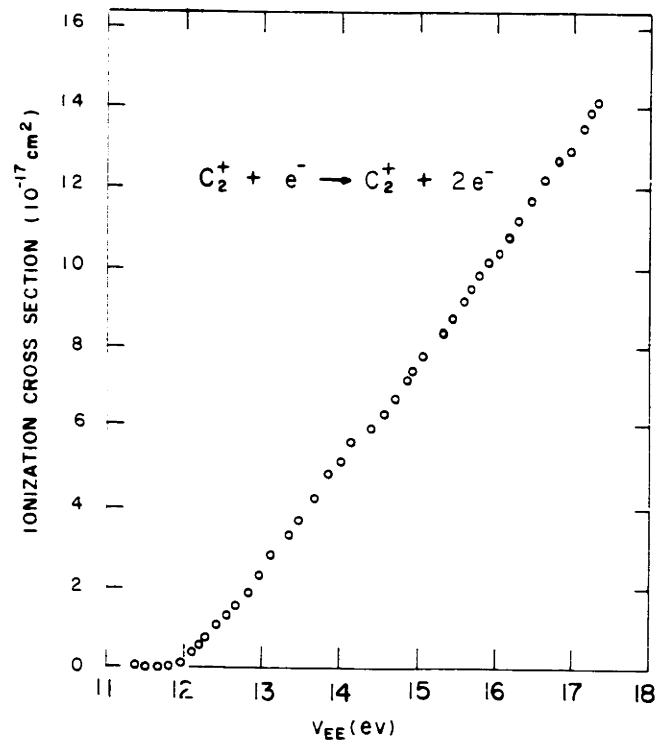


Fig. 85 Threshold cross section for  $C_2^+$

$(E - U_0)^2$ . In this case,  $\sqrt{\sigma^{++}}$  was plotted against  $(E - U_0)$  in Fig. 87.

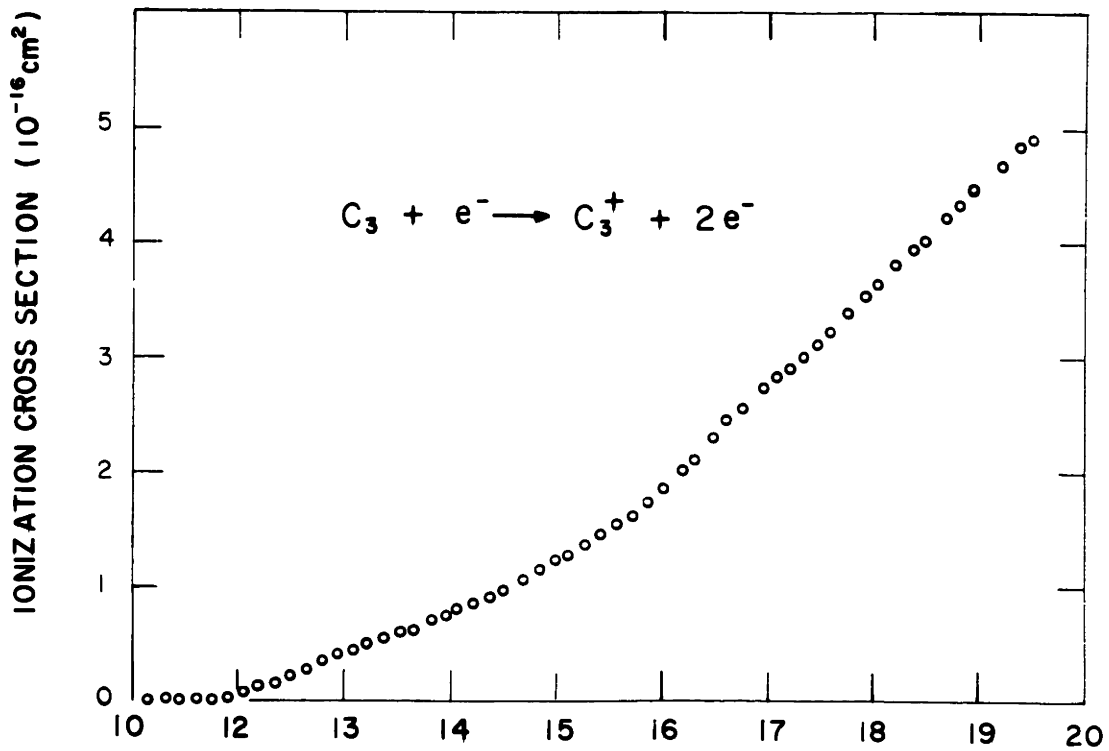


Fig. 86 Threshold cross section for  $C_3^+$

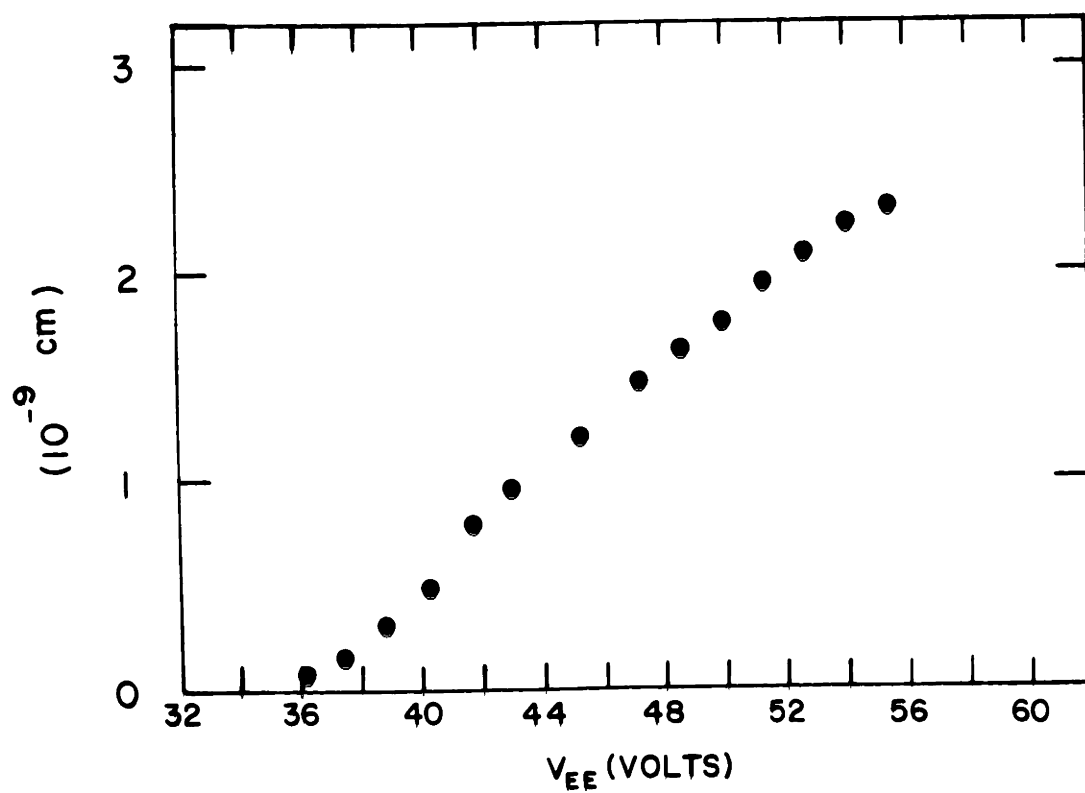


Fig. 87 Threshold behavior of doubly ionized ions ( $C_1^{++}$ )

#### VIII.4 Data Collection and Probable Errors

VIII.4.1 Procedures--The data were taken in three separate sections: from threshold to about 30 V, from 30 V to 1000 V, and from 1000 V up. Sufficient overlap provided convenient connection of these sections. The electron beam energy ( $V_{EE}$ ) was established by a programmable power supply which was in turn controlled by an analog scanner. While the energy was scanning, the beam current was held constant with a beam current controller. The ion signal from the counter was fed to a digital voltmeter, and then printed with the beam energy (measured by another digital voltmeter). Since every scan took a few minutes, systematic errors due to the drift of the neutral beam might have been introduced. In order to avoid this possibility, various techniques (averaging of the back and forth scans, choosing several reference points and taking them in reference to one specific point, etc.) were used. In order to reduce statistical error as much as possible the results were then smoothed by a fourth difference method<sup>88</sup> with a computer.

Absolute values were calibrated at  $V_{EA} = 60$  V. This calibration required measurements of  $I_{12}$  and of the ion species ratios. The total ion current was measured by a Keithley 601 Electrometer, subtracting the background ion current which was obtained by shutting off the neutral beam. Neutral beam intensity was detected by a Granville-Phillips film thickness monitor. Great care was exercised in calibrating the deposition area and in compensating for the reduction of counts due to temperature effects in the crystal.



VIII.4.2 Possible Errors and Uncertainties--All instrumentation stabilities were within  $\pm 2\%$  (twice the manufacturer specification). Systematic errors due to drifts of the atomic beam (and the electron beam) were carefully suppressed to within  $\pm 2\%$  using the procedure described in the previous section. Other possible errors induced from stray effects such as contamination and scattered electrons were observed to be small. Transmission of the electron and atomic beams through the ionizer induced an uncertainty of  $\pm 1\%$  because the electron path and beam profile were not precisely known. Thus, the relative cross section should have an accuracy of about  $\pm 3\%$ .

In the calibration of absolute cross sections, more uncertain quantities are involved. Because of the existence of a strong background gas due to outgassing, the ion current can only be measured within  $\pm 5\%$ . Furthermore, the transmission of the ion collection was not well defined through the two grids. Some other errors could have also been introduced when the ion species ratios were measured. During ion injection the emittances of the different species toward the mass spectrometer were not identical due to the inequality of their neutral beam velocities (c.f. section VI.2). In addition to the particle losses in the mass spectrometer, unequal emittances give rise to a deviation from the actual species ratios. This error in the ratios can be reduced to a few percent when high  $V_{ID}$  and  $V_{IE}$  are used. ( $V_{ID} \geq 15$  V,  $V_{IE} \geq 30$  V). Different masses were transmitted with respectively different efficiencies through the quadrupole mass spectrometer. The error generated by these variations amounted to a few percent. Other errors, involved in the

determination of species ratios from the unknown yields of the conversion dynode, were made negligible by the particle counting technique (Section VII.2).

An estimated accommodation coefficient of .90 was used. Although a more accurate value could have been obtained through calibration<sup>82</sup>, this estimate is known as correct to within a few percent.

As a result of the above, the absolute cross section measurements were accurate to  $\pm 10\%$ .

### VIII.5 Theoretical Approximation and Estimation

VIII.5.1 Classical Approximation--Classical theory<sup>88</sup> developed by Cryzinski on inelastic scattering has been in good agreement with many experimental works.<sup>89</sup> It would be worthwhile to compare this calculation with these experimental data. From the theory, the cross section contributed from the  $k^{\text{th}}$  shell for single ionization can be written as

$$\sigma_k^+ = \frac{6.56 \times 10^{-14}}{U_k^2} g\left(\frac{E}{U_k}\right), \quad (8.10)$$

$$g(x) = \frac{1}{x} \left(\frac{x-1}{x+1}\right)^{3/2} \left[ 1 + \frac{2}{3} \left(1 - \frac{1}{2x}\right) \ln(2.7 + (x-1)^{1/2}) \right] \quad (8.11)$$

where  $U_k$ : ionization potential for  $k^{\text{th}}$  shell in eV

$E$ : electron impact energy in eV

The total ionization cross section can therefore be summed over all the shells as,

$$\sigma^+(E) = \sum_k q_k \sigma_k^+ \quad (8.12)$$

where  $q_k$  is the number of electrons in the  $k^{\text{th}}$  shell.

The shell energies ( $U_k$ 's) used in this calculation were obtained from X-ray spectroscopy tabulated in Table V.<sup>90</sup>

TABLE V

Electron shell	$2p^2$	$2s^2$	$1s^2$
No. of electrons	2	2	2
Shell energy (eV)	11.26	16.59	288.

The computation result was plotted in Fig. 79, and, for comparison, in Fig. 88. In Fig. 88, contributions from the different shells are also given. A reasonably good agreement can be observed in comparison with the experimental results.

The summation rule of Equ. 8.12 implies the additivity of molecular cross sections.

#### VIII.5.2 Quantum Mechanical Calculation--Exact quantum mechanics

determination of ionization cross sections is not possible because of the computation complexity involved in dealing with many particle theories. Various approximations have been introduced. Among these, well known ones are Born, Bethe, Born-Oppenheimer, Born exchange, Born-Ochkur, improved final state, and plane wave approximations.

An excellent review, with particular emphasis on recent theoretical development, has been made by Rudge<sup>91</sup>. Massey and Burhop<sup>92</sup> also discuss all these theoretical aspects in detail. Only a few approximations

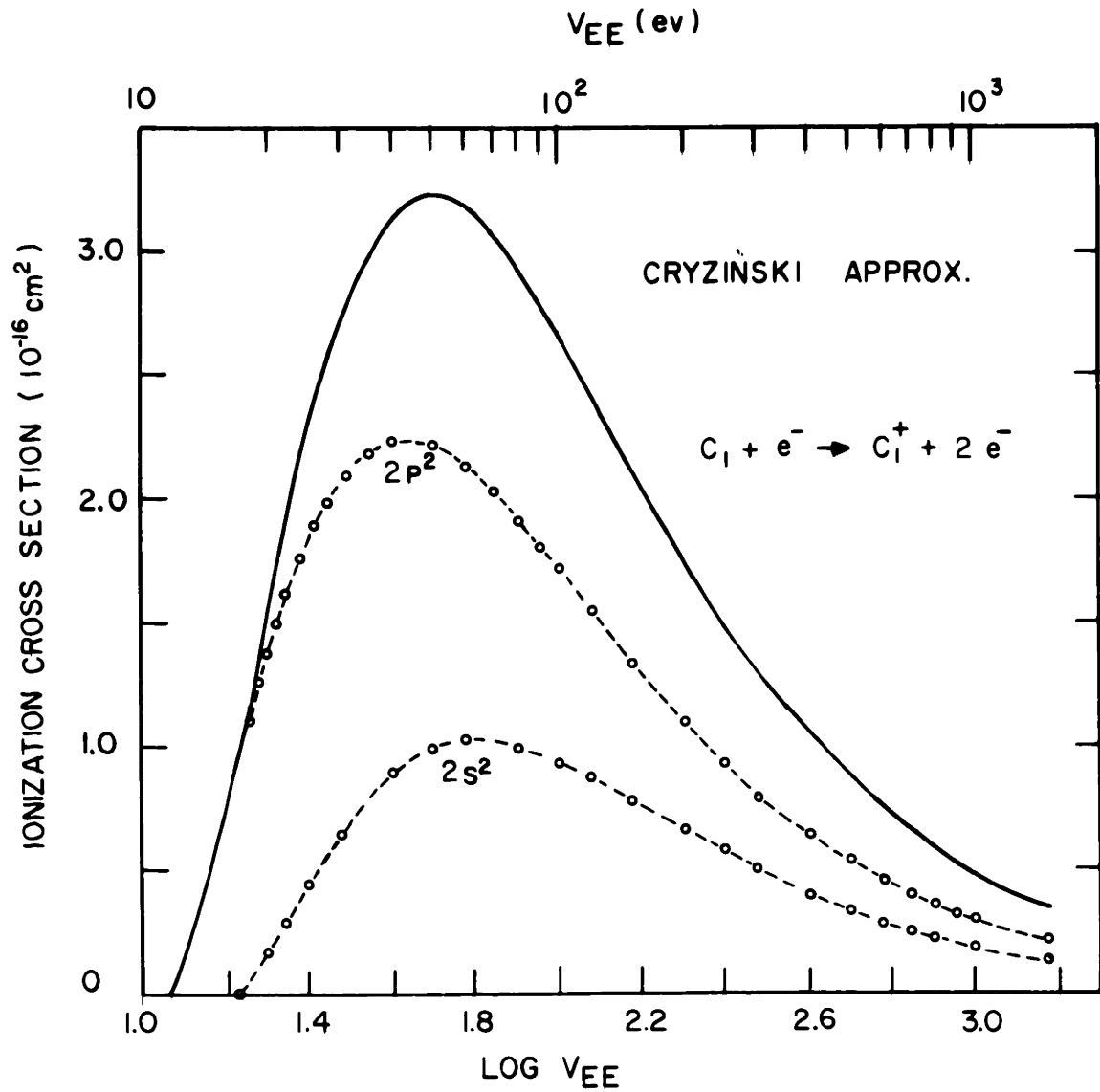


Fig. 88 Calculated cross section using the Cryzinski approximation. The contributions from individual shells are also shown.

will be discussed here.

The Born formulation has been used extensively<sup>92-94</sup>. Following the notation of Rudge and Seaton<sup>94</sup>, the Born approximation to the direct scattering amplitude is

$$f_B(\vec{k}', \vec{k}) = -\frac{2}{k^2} \int \psi_f^*(X) \sum_{j=1}^N \exp(i\vec{K} \cdot \vec{r}_j) \psi_j(X) d\vec{r}_1 d\vec{r}_2 \dots d\vec{r}_N \quad (8.16)$$

where  $\vec{K} = \vec{k}_i - \vec{k}$ ;  $X = (x_1, x_2 \dots x_N)$

The cross section, when neglecting exchange, can then be expressed as

$$\sigma = \frac{1}{k_i} \int_0^{E_0} k k' d\epsilon \int |f(\vec{k}', \vec{k})|^2 d\hat{k} d\hat{k}' \quad (8.17)$$

where  $\vec{K} = \vec{k}_i - \vec{k}$ ;  $E_0 = \frac{1}{2}(k^2 + k'^2) = \frac{1}{2} k_i^2 - U_i$ ; and  $E = \frac{1}{2} k_i^2$ .

Besides the error from the approximated wave functions thus used, the Born approximation gives rise to substantial error (usually too high) in low energies, and incorrect threshold behavior. This is due to neglecting the electron exchange.

Since the spin-orbit coupling is neglected in the Born approximation, conservation of the spin is required. Electron exchange between incident and ejected electrons will result in a transition of different multiplicity terms and therefore influence the cross section. Several approximations have been considered to estimate the exchange amplitude. Oppenheimer's approximation of exchange amplitude leads to<sup>95</sup>

$$g^+ (\vec{k}, \vec{k}') = \frac{1}{2} \exp \{i\tau(\vec{k}, \vec{k}')\} f(\vec{k}, \vec{k}')$$

$$|g^- (\vec{k}, \vec{k}')| = |g^+ (\vec{k}, \vec{k}')|$$

where  $\tau(\vec{k}, \vec{k}')$  is a phase factor, and where amplitudes  $g^\pm(\vec{k}, \vec{k}')$  describe exchange transition to singlet (+) and triplet (-) continuum states for a 2-electron system. Ochkur<sup>96</sup> then obtained a simple result at not too low energy as

$$g(\vec{k}, \vec{k}') = \frac{k^2}{2k_i} f(\vec{k}, \vec{k}') \quad (8.18)$$

The factor of two is due to the two electrons.

When the exchange is taken into consideration, the cross section may be expressed as<sup>97</sup>

$$\sigma = \frac{1}{k_i} \int_0^{E_0/2} k k' d\epsilon \int d\hat{k} d\hat{k}' [ |f(\vec{k}', \vec{k}) - g^+(\vec{k}', \vec{k})|^2 + \frac{3}{2} |g^-(\vec{k}', \vec{k})|^2 ] \quad (8.19)$$

With the substitution of Equ. 8.19 it becomes

$$\sigma_0 = \frac{1}{k_i} \int_0^{E_0/2} k k' d\epsilon \iint d\hat{k} d\hat{k}' |f(\vec{k}, \vec{k}')|^2 \left(1 - \frac{K^2}{k_i^2} + \frac{K^4}{k_i^4}\right) \quad (8.20)$$

where the subscript "0" is the Ochkur approximation.

The total cross sections of  $\sigma_B$  and  $\sigma_0$  may be summed over the outer and the inner shell contributions. It should be noted that the inner shell cross section was obtained by adding the contribution from the

direct ionization processes to that from the auto-ionization. The auto-ionization cross section was obtained by extrapolation of  $\epsilon \rightarrow -\frac{1}{n}$ , i.e.

$$\sigma(E, \epsilon) \rightarrow \sigma(E, -\frac{1}{n}) \quad (8.21)$$

Peach<sup>93,94</sup> used an undistorted coulomb function for an ejected electron for actual numerical evaluation, i.e.

$$\phi(\vec{k}, \vec{r}) = \exp(\frac{\pi}{2k}) \Gamma(1 - \frac{i}{k}) \exp(i\vec{k} \cdot \vec{r}) {}_1F_1[\frac{i}{k}, 1; i(kr - \vec{k} \cdot \vec{r})] \quad (8.22)$$

Then, making the parentage expansion for initial and final state wave functions as

$$\psi_i(\ell^q SL) = \sum_{\bar{S}\bar{L}} (\ell^q \bar{S}\bar{L} | \ell^{q-1}(SL) \ell SL) \psi_i(\ell^{q-1} \bar{S}\bar{L} \ell SL) \quad (8.23)$$

$$\psi_f(\vec{x}_1 \dots \vec{x}_N) = \frac{1}{N^{1/2}} \sum_{i=1}^N (-1)^{n-i} \psi(\ell^{q-1} SL) \times (\bar{k}, \bar{x}_i) \quad (8.24)$$

and

$$\chi(\vec{k}, \vec{x}_i) = \chi(\vec{k}, \vec{r}_i) \delta(\sigma | m_s) \quad (8.25)$$

where  $\delta(\sigma | m_s)$  is normalized spin wave function and  $(\ell^q SL | \ell^{q-1}(\bar{S} \bar{L}) \ell SL)$  is a fractional parentage coefficient<sup>98</sup>. The calculated results are shown in Fig. 79, for comparison and in Fig. 89 (indicating the inner shell contribution).

From the scattering amplitude in Equ. 8.16, the cross section may also be expressed as,<sup>99</sup>

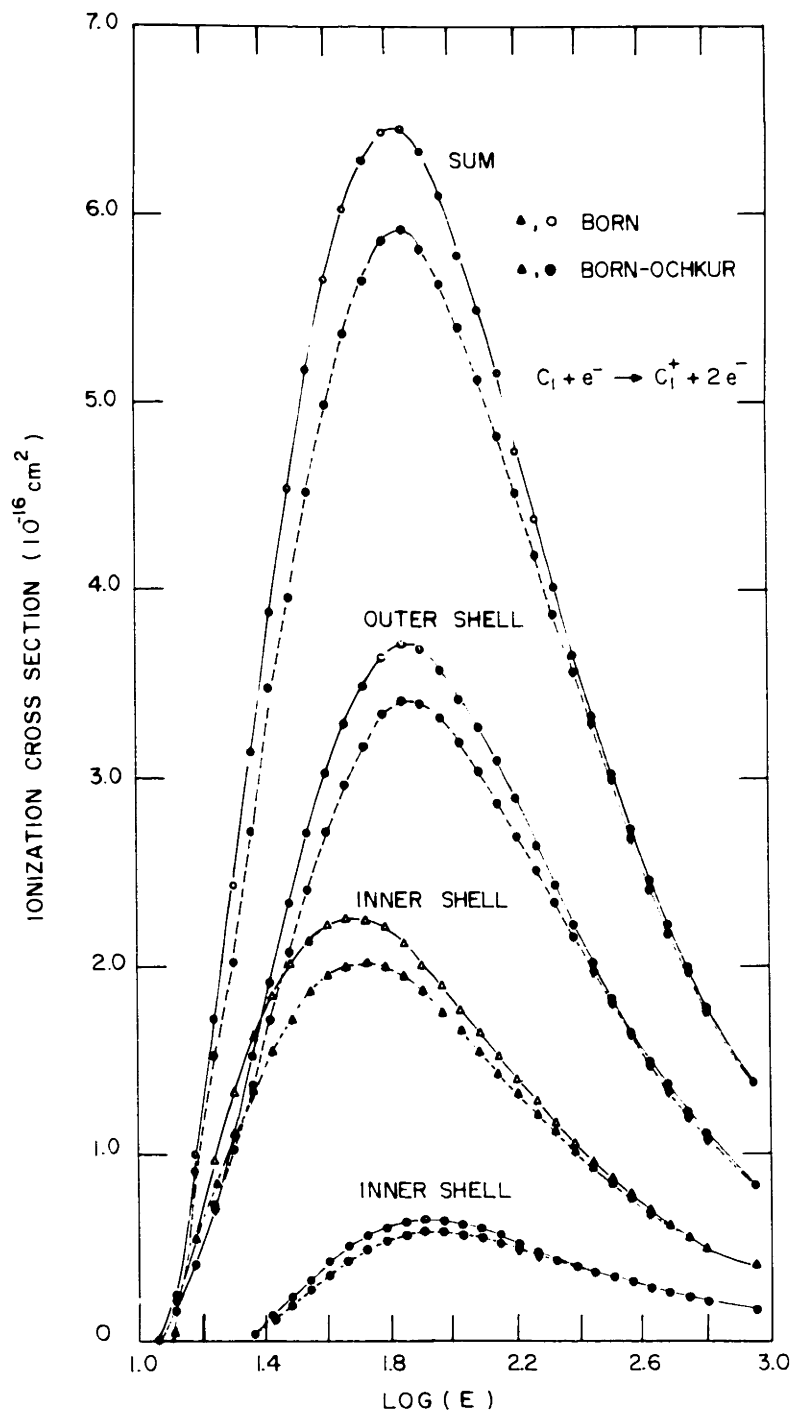


Fig. 89 Calculated cross section using the Born and the Born-Ochkur approximations. Inner shell contributions are also indicated.



$$\sigma = \frac{8\pi}{E} N_{n\ell} \int dk \int_{K_{\min}}^{K_{\max}} |\epsilon_{n\ell}(K)|^2 \frac{dK}{K^3}, \quad (8.26)$$

where

$$\epsilon_{n\ell}^k(K) = \frac{1}{2\ell + 1} \sum_{m=-\ell}^{\ell} \left| \int_{K_{\min}}^{K_{n\ell}} e^{iKz} \psi_{n\ell m} \psi_k^* dr \right|^2$$

$$K_{\min} = k - k_{n\ell} \cong \frac{Ek_1 - E_{n\ell}}{k_0}$$

$$K_{\max} = k + k_{n\ell} .$$

Since the integral in Equ. 8.27 will be small for  $K^2 \gg 2V_i = k_0^2$ , one may estimate the cross section contribution by neglecting  $K > K_0$ . Under this condition, expanding the exponential term in Equ. 8.27, Equ. 8.26 becomes

$$\sigma_{n\ell} \Big|_{K < k_{n\ell}} = \frac{8\pi R N_{n\ell}}{E} \int_0^\infty dk \int_{K_{\min}}^{K_{\max}} \frac{1}{2\ell + 1} \sum |Z_{n\ell, K}|^2 \frac{dK}{K}; \quad (8.27)$$

$$Z_{n\ell, K} = \int z \psi_{n\ell m} \psi_K^* dr .$$

The cross section may be put into the following form,

$$\sigma_{n\ell} = 4\pi \frac{a_0^2 R}{E} |M_{n\ell}^2| \ln \frac{4E}{C_{n\ell}} \quad (\text{cm}^2) \quad (8.28)$$

with

$$|M_{n\ell}|^2 = \frac{N_{n\ell}}{a_0^2} \int_0^\infty \frac{1}{2\ell+1} \sum_m |Z_{n\ell,k}|^2 dk$$

$$\ln C_{n\ell} = \frac{\frac{N_{n\ell}}{a_0^2} \int_0^\infty \frac{1}{2\ell+1} \sum_m |Z_{n\ell,k}|^2 \ln \frac{E_k - E_{n\ell}}{(-E_{n\ell})} dk}{|M_{n\ell}|^2}$$

where  $a_0$  is the radius of a hydrogen atom, and  $R$  is Rydberg. This is the Bethe approximation.

Since neglect of contribution from high  $K$  was assumed, the result introduced a significant error. Recently Gaudin and Botter<sup>100</sup> have added the cross section for larger  $K$ . This contribution may be shown to be

$$\sigma_{n\ell} |_{K > k_{n\ell}} = \frac{8\pi R}{E} N_{n\ell} \int_{K_{\min}}^{K_{\max}} \frac{dK}{K^3} \quad (8.29)$$

For high incident energies such that  $K_0 \gg k_{n\ell}$  it becomes,

$$\sigma_{n\ell} |_{K > K_{n\ell}} = \frac{4\pi R}{E} a_0^2 N_{n\ell} \cdot \frac{R}{(-E_{n\ell})} \quad (8.30)$$

The resultant summation is

$$\sigma_{n\ell} = 4\pi \frac{a_0^2 R}{E} |M_{n\ell}|^2 \ln \frac{4E}{C_{n\ell}}, \quad (8.31)$$

where

$$M_{n\ell} = \frac{N_{n\ell}}{a_0^2} \int_0^\infty dk \left( \frac{1}{2\ell+1} \right) \sum_{m=-\ell}^{\ell} |Z_{n\ell}|^2$$

$$\ln C_{nl}^i = \frac{(2 N_{nl}/a_o^2) \int_0^\infty dk \left(\frac{1}{2l+1}\right) \sum_{m=-l}^l |Z_{nl}|^2 \ln(E_k - E_{nl})}{|M_{nl}|^2}$$

$$- (-E_{nl}) - \frac{N_{nl} R}{(-E_{nl}) |M_{nl}|^2}$$

The summation of all the quantum number results is

$$\sigma = \frac{4\pi a_o^2}{E} |M_i|^2 \ln \frac{4E}{C_i}, \quad (8.32)$$

where

$$|M_i|^2 = \sum_{n,l} |M_{nl}|^2,$$

$$\ln C_i = \frac{\sum |M_{nl}|^2 \ln C_{nl}}{|M_i|^2}.$$

The numerical computation for carbon, using hydrogenic-like wave functions for bound states and an undistorted coulomb wave function as an ejected electron wave function, was carried out and shown again in Fig. 80.

Otvos and Stevenson<sup>16</sup> calculated the cross sections relative to a hydrogen atom by summing the cross section of the contribution from valence electrons weighted by the mean square radii of these electrons. The radii of the electrons were estimated from hydrogen-like wave

functions (with given quantum numbers  $n\ell$ ). If the single ionization cross section for hydrogen were taken from Fite and Brackmann<sup>101</sup>, the cross section of carbon would be estimated to be  $2.76 \times 10^{-16} \text{ cm}^2$  at  $E = 100 \text{ eV}$ .

### VIII.6 Empirical Formulation

There have been several empirical attempts to formulate ionization cross sections (e.g. Drawin in 1961<sup>102</sup> and Lotz in 1968<sup>103</sup>). Drawin's formula of two parameters gave very good results (with the exception of values near the threshold). Lotz recently proposed a three-parameter formula for the calculation of ionization cross sections. This formula was obtained by observing some empirical regularities, and asymptotic behavior of cross sections (at high energies) predicted by theoretical approximations (such as those of Born, Bethe, and Cryzinski). In this manner the cross section may be expressed as

$$\sigma = \sum_{k=1}^n a_k q_k \frac{\ln(E/U_k)}{EU_k} \{1 - b_k \exp[-c_k(E/U_k - 1)]\}; \quad (8.33)$$

$$E \geq U_k, \quad ,$$

where  $E$  is the energy of the impact electron;  $U_k$  is the binding energy of electrons in the  $k^{\text{th}}$  subshell;  $q_k$  is the number of equivalent electrons in the  $k^{\text{th}}$  subshell; and  $a_k$ ,  $b_k$  and  $c_k$  are associated constants which were determined empirically. Extensions of this were made to predict other unknown cross sections by comparison of other experimentally existing isoelectric species as well as equally charged species. The

results thus obtained show an excellent agreement with experimental data (± 10%, which is twice the probable error). Prediction of the single ionization of carbon was also obtained with

$$a_1 = 3.5; \quad b_1 = 0.7; \quad c_1 = 0.4; \quad q_1 = 2$$

$$a_2 = 4.0; \quad b_2 = 0.7; \quad c_2 = 0.5; \quad q_2 = 2$$

and is shown in Fig. 80. It is obvious that this empirical formulation does not show the fine structure of the cross sections.

#### VIII.7 Comparison and Discussion

In summary, Cryzinski and Lotz's results agree reasonably well with the experimental values, while the quantum mechanical approximations of Born, Born-Ochkur, and Bethe all show a much higher value at the low energy range close to the threshold. The significant deviation of the threshold behavior from the quantum mechanics approximations is the consequence of neglecting electron exchanges. Even in the Ochkur approximation, only the first expansion term of Oppenheimer's exchange amplitude is used. It therefore does not give a good representation of correct cross sections at low energies.

## IX. SUMMARY AND FUTURE IMPROVEMENT

In the measurement of ionization cross sections described in this dissertation, it appears that a large amount of the probable error resulted from the ion current measurement. The signal ion current from the neutral beam could stand only about 20% of the total measured current (from the neutral beams and background) because of the strong background which was caused by outgassing. An attempt to increase the neutral beam intensity resulted in running-away of the power supply (as discussed in Chapter IV.), unstable ion current, and great sample consumption. It is suggested that 1) a constant-power power supply should be made available, and 2) differential pumping may be installed in the neutral beam source chamber to reduce the pressure near the ion source.

In the investigation of possible fragmentation using this particular T-O-F technique, high sensitivity cannot be achieved because precise separation of different species in the Maxwellian distribution cannot be made better than a few percent. This is due to the fact that the Maxwellian distribution has a continuous spectrum. In order to study the fragmented ionization by electron impact, it is suggested that the generation of single molecular species is mandatory. Furthermore, it would be helpful to study other simple diatomic gases ( $H_2$ , for instance) especially in the aspects of theoretical understanding. The fragmented ions may then be investigated to a sensitivity depending on the existing amount of lower polymer neutrals, whose ions can be the result of fragmentation. When the amount of existing lower polymers and atomic species are significant, they can be measured at best to a

few percent of the simple ionization products by the present T-O-F technique.

Energy-distribution differentiation has been attempted to investigate fine structure near the threshold potential. A small AC carrier was added to the electron beam energy ( $V_{EE}$ ), and the ion signal was then detected with a lock-in amplifier similar to that described in section V.3. Good data are lacking because of a low signal-to-noise ratio. It is possible to gain a higher signal-to-noise ratio by 1) increasing the neutral beam intensity with a large sample supply when the neutral beam source can be revised accordingly, and 2) sacrificing the resolution of the electron beam energy.

Other techniques using two electron beams to measure absolute ionization cross sections were described elsewhere<sup>104-106</sup> (multiple cross beam or exponential depletion technique). In these methods, although no information on neutral beam density is required, other uncertainties and a high signal-to-noise ratio may render it no better or no more convenient than the technique presently used. (A film thickness monitor can be used especially to measure mass condensation with much higher sensitivity.)

APPENDIX 1

Calibration Experiments Using Copper

Before doing the carbon work described in the text, a small piece of Cu was put in the Carbon Knudsen cell to calibrate the ion source and to tune the mass spectrometer for sensitivity. Due to the ionizer geometry, peak sensitivity for atomic beam detection does not correspond to peak sensitivity with background gas.

During the copper experiment, the melting point can be easily determined by observing the cooling or heating characteristics with an optical pyrometer. Such a curve is shown in Fig. A-1.

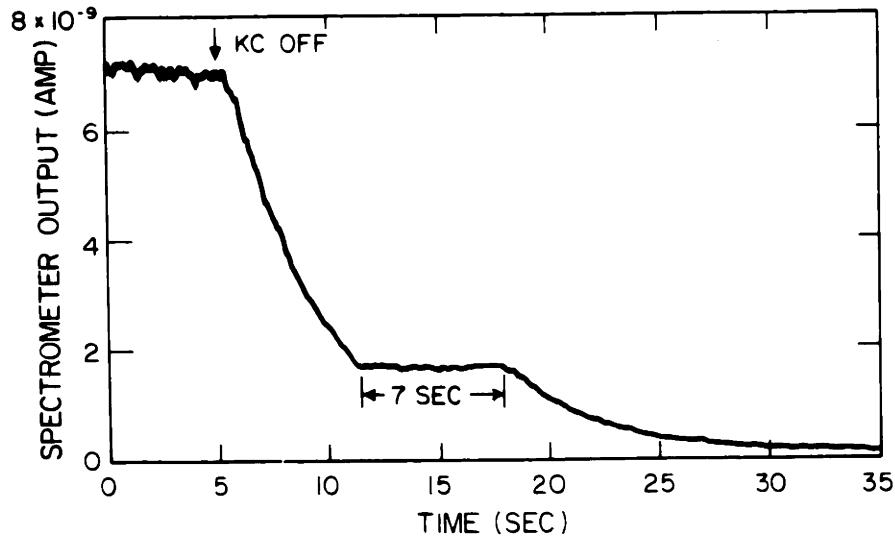


Fig. A-1(a) Spectrometer output showing the effect of melting point when cooling.

The above observation has several applications:

- 1) Temperature calibration



Since the melting point is known, the cell temperature can be calibrated at this point regardless of its emissivity. A temperature range close to this point can then also be calibrated using the vapor pressure.

## 2) Determination of weight losses

A measurement of either the melting or the solidification time along with the knowledge of the heat of fusion and the power input is sufficient to determine the amount of molten material. If both are measured, the results can be checked against each other. Let  $P_m$  be the power required to just maintain temperature at the melting point; let  $P_{in}$  be the power input.  $P_{in}$  is greater than  $P_m$  if material is being melted, thus the mass of the molten material is

$$m = \frac{P_{in} - P_m}{H} \cdot \Delta t_h, \quad (A.1)$$

where  $H$  is the heat of fusion and  $\Delta t_h$  is the melting time. Note that this time interval can be expanded or reduced by adjusting  $P_{in}$ .

Similarly, looking at the cooling curve, one obtains

$$m = \frac{P_m}{H} \cdot \Delta t_c \quad (A.2)$$

where  $\Delta t_c$  is the solidification time.

## 3) Stable beam operation

A stable beam is necessary for absolute cross section measurements to provide stable ion currents and to allow a precise weight gain to yield an accurate neutral beam intensity. At the melting point, the vapor

pressure is nearly constant even if small power fluctuations occur.

Unfortunately these advantages cannot be applied to the study of carbon, because the melting point is too high, but they can be useful in high temperature mass spectrometry and in the measurement of other cross sections.

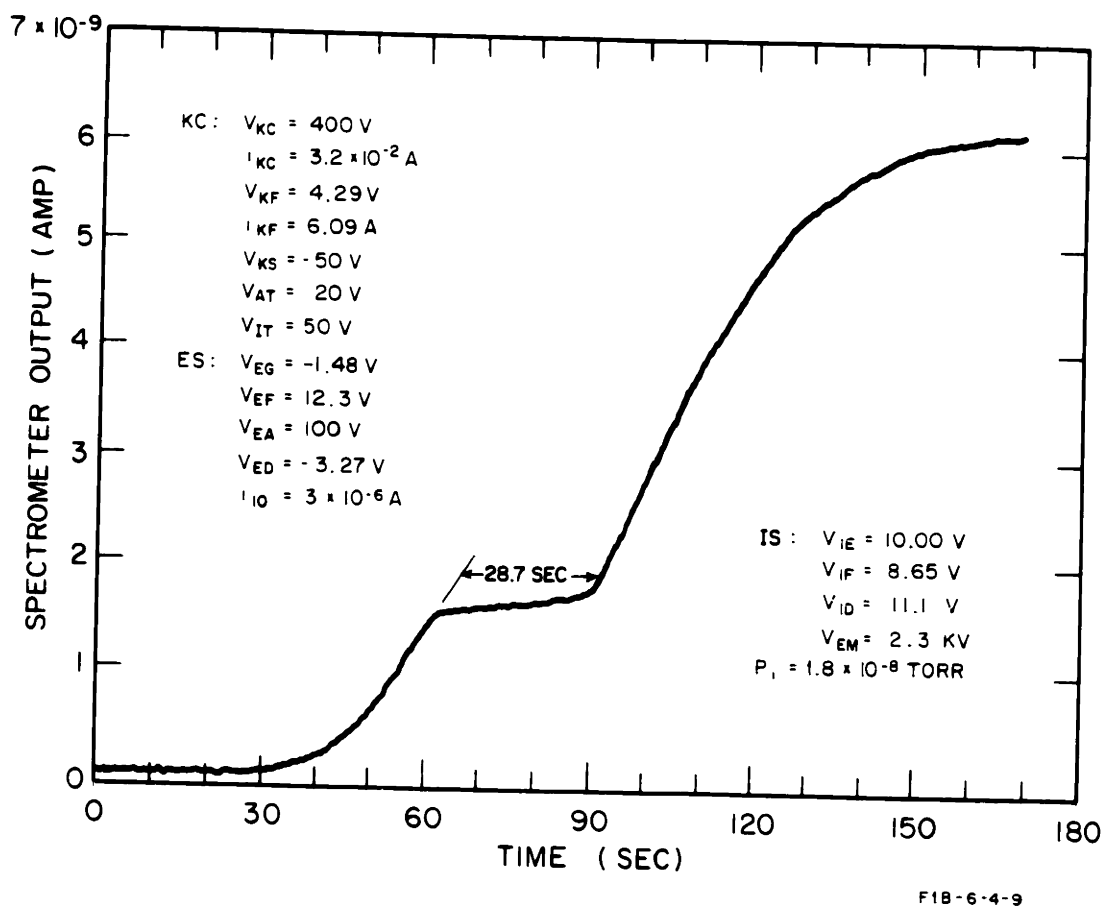


Fig. A.1(b) Output when heating at constant power

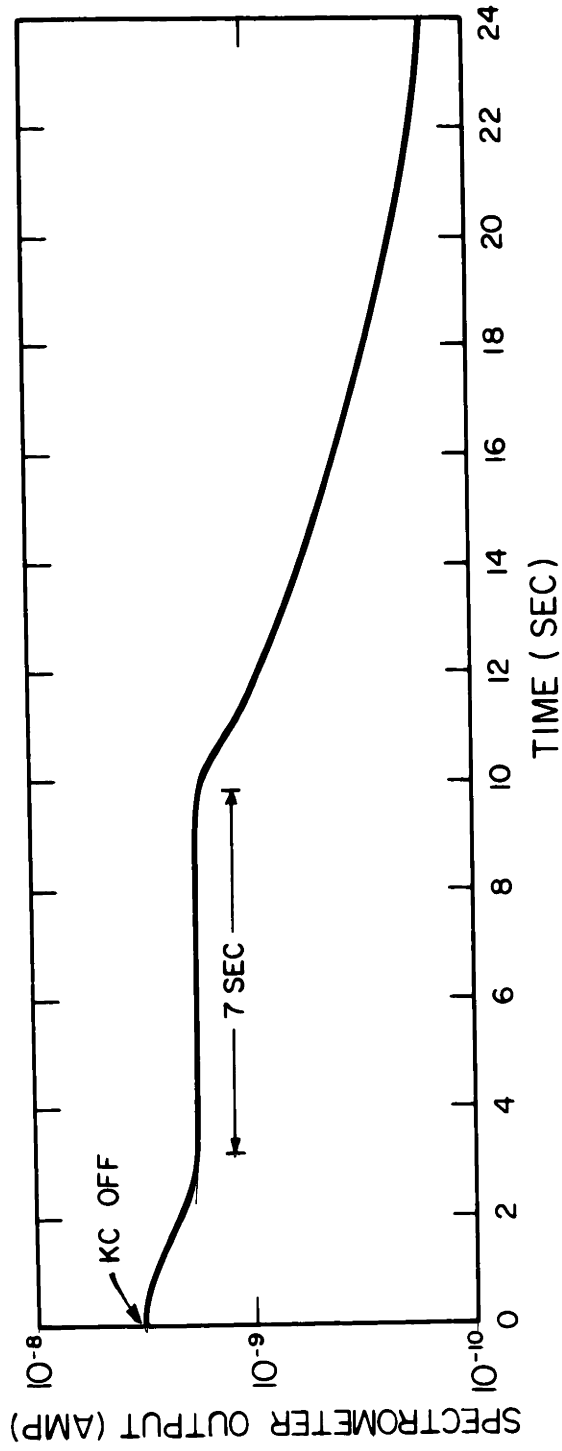


Fig. A.1(c) Spectrometer output showing the effect of the melting point when cooling using a logarithmic ordinate scale.

APPENDIX 2

Retarding Potential Method

As shown in Fig. A.2, several effects should be taken into consideration when using the RPD method.

(A) Momentum Changes:

Each aperture of each grid forms an aperture lens. For a two-dimensional grid, the focal length can be approximately expressed as<sup>107-109</sup>

$$f = \frac{2\sqrt{2} v}{V_1' - V_2'} \quad (\text{A.3})$$

A parallel ray going to the grids will have a divergent angle due to this lens effect

$$\theta \approx \frac{d}{f} = \frac{d(V_1' - V_2')}{2\sqrt{2} v} \quad (\text{A.4})$$

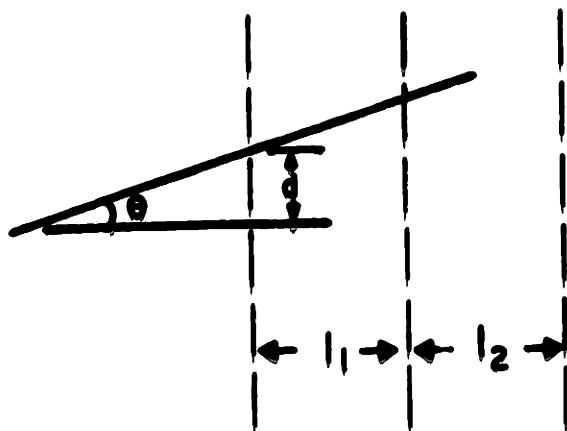


Fig. A.2 Schematic diagram of a conventional retarding potential difference technique.

The ray coming in with a divergent angle  $\alpha$  is considered to be due to the optical lens in the previous stage. In the worst possible case, the change of axial momentum is

$$\delta P_z = P_z (1 - \cos\theta) + P_z (1 - \cos\alpha) \quad , \quad (A.5)$$

and

$$\frac{\delta V}{V} = \frac{P_z^2 (2 - \cos\theta - \cos\alpha)^2}{P_z^2} = \theta^2 + \alpha^2 \quad . \quad (A.6)$$

Substituting Equ. A.4 into Equ. A.6, it becomes

$$\frac{\delta V}{V} = \alpha^2 + \frac{d^2}{8V^2} (V_1' - V_2')^2 \quad . \quad (A.7)$$

Then the energy width due to a divergent beam with lens effect can be

$$\delta V = V \left[ \alpha^2 + \frac{d^2}{8V^2} (V_1' - V_2')^2 \right] \quad (A.8)$$

$$\delta V = V \left[ \alpha^2 + \frac{1}{8} \left( \frac{d}{\ell} \right)^2 \right] \quad (A.9)$$

Specifically,  $\alpha = 0.1$  rad.,  $d = 0.025$  cm, and  $\ell = 0.38$  cm,

$$\delta V = V \left[ \alpha^2 + \frac{1}{8} \left( \frac{0.025}{0.38} \right)^2 \right] = 0.01444V \quad (A.10)$$

#### (B) Field Penetration (Saddle Point)

For the PDD schematic in Fig. A.2, the potential distribution along

the z-axis for a single aperture may be written as<sup>110</sup>

$$\phi_a(z) = V_o - \frac{V_1' + V_2'}{2} z + \frac{R}{\pi}(V_1' - V_2') \left[ \frac{z}{R} \arctan\left(\frac{z}{R}\right) - 1 \right] \quad (\text{A.11})$$

Set  $Z = 0$

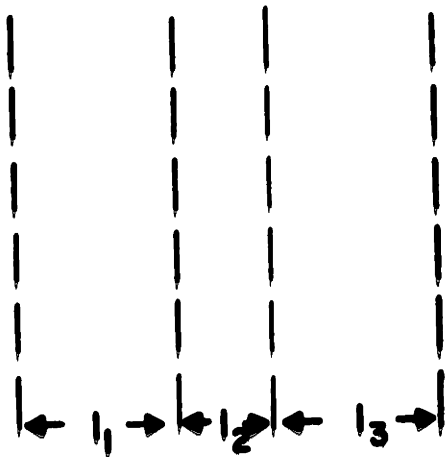
$$\phi_a(0) = V_o + \frac{R}{\pi}(V_1' - V_2') \quad ;$$

or

$$\delta\phi_a = \phi_a(0) - V_o = \frac{R}{\pi}(V_1' - V_2') \quad (\text{A.12})$$

In the case of the technique shown in Fig. A.2, one has

$$V_1' = -V_2' = \frac{V_o}{\ell}$$



Equ. A.12 becomes

$$\delta\phi_a = \frac{2}{\pi} \frac{R}{\ell} V_o$$

In the case of square grids, one can approximate this by using the radius of a circle of equal area.

Thus one has

$$\delta\phi_s = \frac{1}{2.78} \frac{d}{\ell} V_o \quad (\text{A.13a})$$

Fig. A.3 Revised form of a retarding potential difference method.

or numerically,

$$\delta\phi_s = 0.024 V_o \quad (\text{A.13b})$$

The result shows that the resolution is essentially limited by the saddle point effect in the conventional RPD. This can be circumvented by retarding the collector and successive grids. However space charge may then become the dominating obstacle. Fig. A-3 then shows a revised RPD schematic. In this case, both the second and the third grids are at the same potential and the saddle point potential can be greatly smoothed, hence the resolution is enhanced. With  $\lambda_2 \gg d$ ; and  $\lambda_1 = \lambda_3$  one has, following Kanaya et al<sup>111</sup> and Regenstreif<sup>112</sup>,

$$\phi(o) = k^2 V_o \quad ; \quad (\text{A.14})$$

$$k^2 = 1 - \frac{1}{2} \frac{r_1 \{2r_1 + 2Z_1 \tan^{-1}(\frac{Z_1}{r_1}) - \pi Z_1\}}{\{Z_2 \tan^{-1}(\frac{Z_2}{r_1}) + r_1\} \{4Z_1 \tan^{-1}(\frac{Z_1}{r_1}) + 4r_1 - \pi Z_1\} - 2\{Z_1 \tan^{-1}(\frac{Z_1}{r_1}) + r_1\}^2} \quad (\text{A.15})$$

with

$$R_1 = 0.005''; \quad \lambda_1 = 0.075''; \quad \lambda_2 = 0.187''$$

$$r_1 = \frac{d}{2}; \quad Z_1 = \frac{\lambda_1}{2} \quad ; \quad Z_2 = Z_1 + \lambda_2$$

Numerical evaluation leads to

$$k^2 = 1 - 7.78 \times 10^{-4} \quad .$$

The voltage penetration is only 0.0798%. Therefore, in this case, the saddle point ripple can be considered to be negligibly small.

(C) Space charge

Space charge in the beam and potential barriers in the retarded field influences the actual beam spread as discussed by Mason.<sup>113</sup>

Expansion of beam profiles due to space charges was discussed by Pierce<sup>54</sup> and Walsh<sup>114</sup>. This expansion of the beam profile in a retarded field is greater than it is in the field-free case.

(D) Scattered and secondary electrons

Inelastic and elastic scattering of electrons with grids results in primary reflection and true secondary electrons. This will effectively introduce a amount of the energy spread which is likely to be a weal energy function. Other stray effects such as those due to a magnetic field (discussed by Anderson and Eggleton<sup>115</sup>, and Simpson<sup>108</sup>) and those due to contamination will change the energy distribution and contribute to spurious energy spreads. In conclusion, when the RPD is used, the limitations and stray effects must be understood before attempting to judge the energy width.



APPENDIX 3

Influence of a Circular Aperture

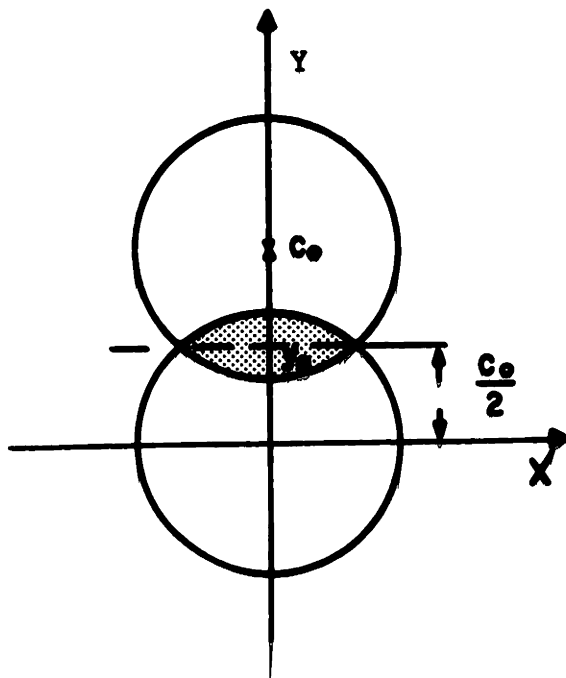
When the two circles shown in Fig. A.4 (having the same unity area) are convolved, the area of overlap, from the equations of the circles, becomes

$$A_{sh} = 4 \int_{y_0}^1 x \, dy$$

$$= 2 \left[ \frac{\pi}{2} - \frac{C}{2} \sqrt{1 - \left(\frac{C}{2}\right)^2} - \sin^{-1} \frac{C}{2} \right]$$

when the two circles overlap completely, their area is  $\pi$ . For half transmission, set  $A_{sh} = \frac{\pi}{2}$ , or

$$\frac{C}{2} \sqrt{1 - \left(\frac{C}{2}\right)^2} + \sin^{-1} \frac{C}{2} = \frac{\pi}{4}$$



Numerical evaluation yields

$$C \cong 0.8 \approx \frac{\pi}{4}$$

which implies that the resolution defined as FWHM is about 0.8 of that of the slit aperture case.

Fig. A.4 Convolution of two circles

APPENDIX 4

Knudsen Cell II Control

A versatile feedback controller was constructed for control of emission, temperature, spectral output, or similar parameters. The unit adapts a commercial power supply as a current amplifier. A block diagram is given in Fig. A.5.

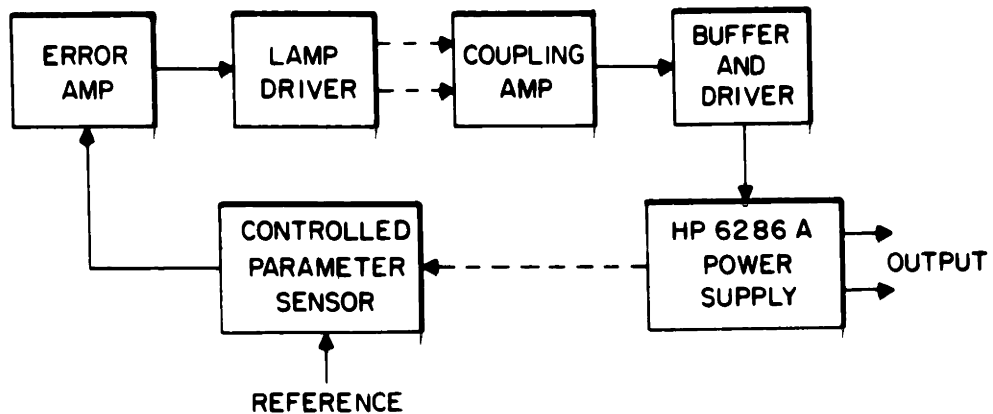


Fig. A.5 Block diagram of the Knudsen cell II control.

The input and output may be floated at different voltages up to 1KV limited by the transformer insulation. A Hewlett Packard Model 6286A power supply was connected for remote voltage programming operation to operate as a current amplifier.

The controller may be used to maintain a desired parameter constant (such as  $i_{KC}$  or  $T_{KC}$ , etc.) by controlling filament power and sensing changes with a suitable sensor. As discussed in the text, once the

cut-off point is reached, the unit will no longer regulate, and a constant-power power supply or some other system is required. The circuitry is shown in Fig. A.6.

This unit was operating in constant  $i_{KC}$  mode. No oscillating or hunting was encountered. However, when the sensor circuitry is changed, new phase shifts may be introduced, and these occasionally result in unstable situations. Thus a compensation network has been included for the necessary phase corrections.



APPENDIX 5

Constant-Power Power Supply

The general block diagram of a constant power supply is shown in Fig. A.7.

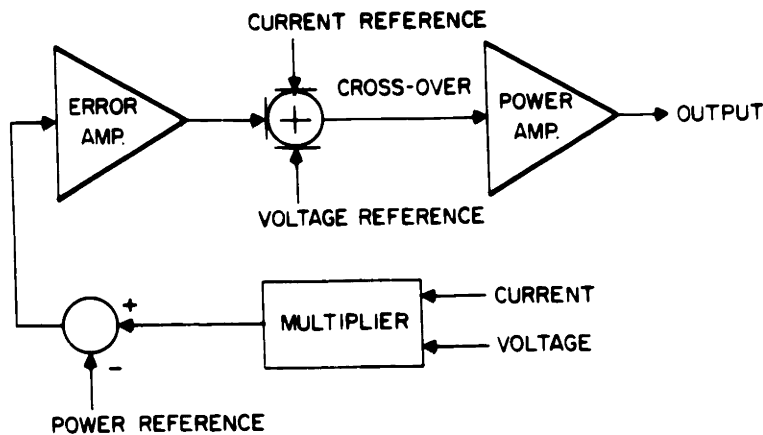


Fig. A.7 Block diagram of a constant-power power supply

The supply should be designed to automatically cross over to voltage or current regulation if either voltage or current becomes too large while operating at constant power. Thus the supply will function on one of the three piece-wise characteristics (1,2,3) shown in Fig. A.8. There are two crossover points. If the power line is set far above the current and voltage limits, the unit will operate as an ordinary voltage or current supply with only one crossover. One way to construct this unit would be to adapt a commercial programmable supply with the addition of a current-voltage product sensor at the crossover point.

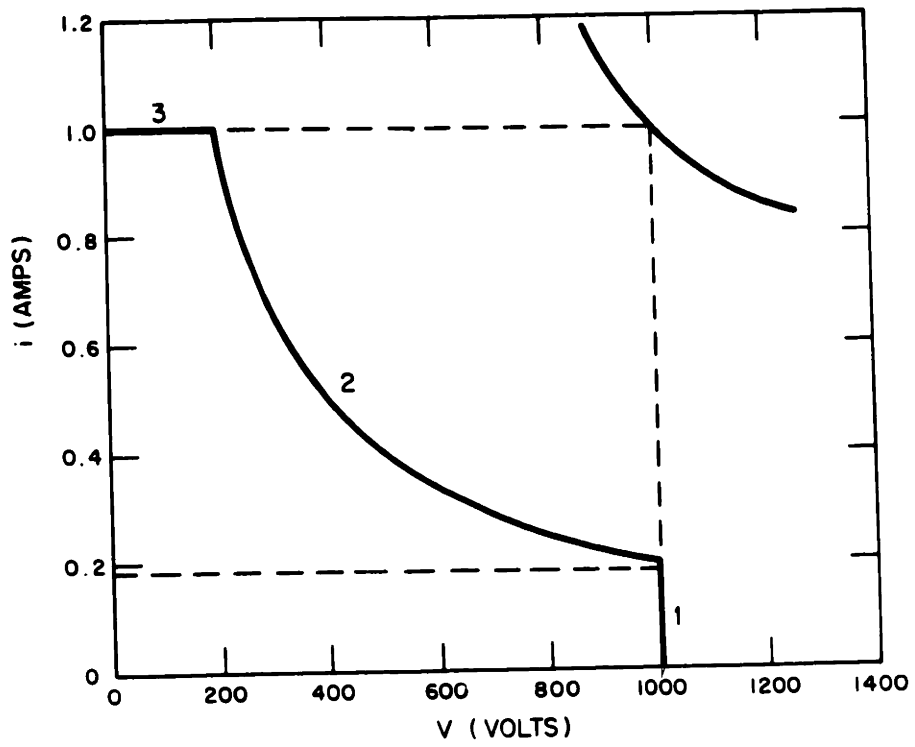


Fig. A.8 General characteristics of the constant-power power supply

APPENDIX 6

Neutral Beam Intensity Ratios

Attempts to directly determine intensity ratios for various components in the neutral beam were carried out as follows. Many runs were made to obtain both the total neutral intensity and the ion ratios for several samples at different temperatures. Then, solutions were obtained from Eqs. 2.43 to 2.45, i.e.

$$\phi_1 + \phi_2 + \phi_3 = \Phi$$

$$\chi_1' \phi_1' + \chi_2' \phi_2' + \chi_3' \phi_3' = \Phi' / \sqrt{\frac{T'}{T}}$$

$$\chi_1'' \phi_1'' + \chi_2'' \phi_2'' + \chi_3'' \phi_3'' = \Phi'' / \sqrt{\frac{T''}{T}}$$

where the  $\phi$ 's are in  $\text{gm}/\text{cm}^2\text{-sec}$ . Finally, the neutral intensities were calculated as tabulated in Table A-1 (along with the original data).

Table A-1

Data Set	Entry Data			
	$\phi(\text{gm}/\text{cm}^2\text{-sec})$	$\chi_1$	$\chi_2$	$\chi_3$
1	51.6	1	1	1
2	18.4	0.488	0.5318	0.4075
3	5.9	0.1945	0.1895	0.127
4	32.4	0.7294	0.688	0.717
5	32.0	0.788	0.711	0.577

Solutions

Sets	$\phi_1$	$\phi_2$	$\phi_3$
1,2,4	-161.9	8.46	128.8
1,2,3	28.76	-38.73	61.56

Unfortunately the solutions to these equation came out with negative intensities (an obviously erroneous result). This instability results from the fact that all of the  $\chi$ 's have very close ratios, and hence small perturbations from various experimental inaccuracies can have a large effect.

Additional experiments using other materials which have larger differences in their ion ratios could overcome this difficulty. Such materials might be TAC, WC, or other markedly different types of graphite.



Solutions

Sets	$\phi_1$	$\phi_2$	$\phi_3$
1,2,4	-161.9	8.46	128.8
1,2,3	28.76	-38.73	61.56

Unfortunately the solutions to these equation came out with negative intensities (an obviously erroneous result). This instability results from the fact that all of the  $\chi$ 's have very close ratios, and hence small perturbations from various experimental inaccuracies can have a large effect.

Additional experiments using other materials which have larger differences in their ion ratios could overcome this difficulty. Such materials might be TAC, WC, or other markedly different types of graphite.

APPENDIX 7

Instruments and Power Supplies

P.O.L. Index Number

Electron Source (scanning  $V_{EA}$ )

$V_{EG}$ (DC power supply)	HP-6207B-1
$V_{EA}$ (DC power supply)	KP-1500-1
$V_{EC}$ (6.3V battery supply)	
$V_{EF}$ (resistor divider through $V_{EA}$ )	

Electron Source ( $V_{EA}$  fixed)

$V_{EG}$ (DC power supply)	ER-110PM-1
$V_{EA}$ (DC power supply)	HP-6110A-1
$V_{EF}$ (DC power supply)	KP-325-1
$i_{10}$ (electrometer)	KE-601-2
$i_{14}$ (microammeter)	WN-XMR-2
Electron Beam Control	SP-XEC-1

Ion Source

$V_{ES}$ (DC power supply)	ER-110PM-4
$V_{IE}$ (DC power supply)	ER-110PM-6
$V_{IF}$ (DC power supply)	ER-110DM-5
$V_{ID}$ (DC power supply)	ER-110DM-3
$I_{12}$ (electrometer)	KE-601-3

Knudsen Cell Source

$V_{KS}$ (DC power supply)	LM-50-1
----------------------------	---------

$V_{AT}$ (DC power supply)	UE-620A-1
$V_{IT}$ (120V battery supply)	SP-120-1
$V_{KC}$ (DC power supply)	( KP-800B-1 SR-300-1
$V_F$ (DC power supply)	HP-6286A-1
Knudsen Cell Emission Controller	SP-XKC-1
 Detection Electronics	
$V_{EM}$ (DC power supply)	NE-RE5001-1
Lock-in Amplifier	PA-HR8-1
Quadrupole Mass Spectrometer	SP-XMS-2
Function Generator	HP-3310A-1
Audio Amplifier	MC-50W-2
 Vacuum Measurement	
$P_1$ (ionization gauge controller)	GP-01006-1
$P_2$ (ionization gauge controller)	GP-01260-1
 General Data Equipment	
Digital Voltmeter	DG-252-1
Digital Voltmeter	DG-252-2
Data Printer	DG-611-1
Mosely X-Y Recorder	MS-7001A-1
Analog Scanner	SP-XSG-1
Oscilloscope	TX-RM503-1

REFERENCES

1. J. T. Tate and P. T. Smith, Phys. Rev., 39 290 (1932).
2. F. H. Field and J. L. Franklin, Electron Impact Phenomena and the Properties of Gaseous Ions, Academic Press Inc., N.Y., 1956.
3. H. S. W. Massey and E. H. S. Burhop, Electronic and Ionic Phenomena, Oxford University Press, 1952.
4. H. S. W. Massey, "Excitation and Ionization of Atoms by Electron Impact" in Handbuch der Physik, Vol. XXXVI, Springer-Verlag, Berlin, 1956, pp. 307-408.
5. J. D. Craggs and H. S. W. Massey, "The Collisions of Electrons with Molecules", in Handbuch der Physik, Vol. XXXVII, Springer-Verlag, Berlin, 1959, pp. 314-415.
6. W. L. Fite, "The Measurement of Collisional Excitation and Ionization Cross Sections" in Atomic and Molecular Processes (Edited by D. R. Bates), Academic Press, New York, 1962.
7. R. I. Reed, Ion Production by Electron Impact, Academic Press, New York, 1962.
8. J. B. Hasted, Physics of Atomic Collisions, Butterworth, Washington, 1964.
9. S. C. Brown, Basic Data of Plasma Physics, M. I. T. Press, Cambridge, 1967.
10. E. W. McDaniel, Collision Phenomena in Ionized Gases, John Wiley and Sons, N. Y., 1964.
11. L. J. Kieffer and G. H. Dunn, Reviews of Mod. Phys., 38 1 (1966).

12. M. J. Seaton, "The Theory of Atomic Collisions", In Atomic and Molecular Processes (Edited by D. R. Bates), Academic Press, New York, 1962.
13. N. F. Mott and H. S. W. Massey, The Theory of Atomic Collisions, Oxford University Press, Oxford, 1965; H. S. W. Massey, E. H. S. Burhop, and H. B. G. Gilbody, Electron and Ionic Impact Phenomena, Vol. 1, Clarendon Press, Oxford, 1969.
14. L. J. Kieffer, Bibliography of Low Energy Electron Collision Cross Section Data, National Bureau of Standard, Miscellaneous Publications, 280 (1967); G. E. Chamberlain and L. J. Kieffer, JILA Information Center Report No. 10 (1970), No. 6 (1969), University of Colorado, Boulder, Colorado; Bibliography of Atomic and Molecular Processes, Atomic and Molecular Processes Information Center, Oak Ridge National Lab Reports, (1967, 1968, 1969).
15. F. E. Stafford, J. Chem. Phys., 45 859 (1966).
16. J. W. Otvos and D. P. Stevenson, J. Am. Chem. Soc., 78 546 (1956).
17. An N. Nesmeyanov, Vapor Pressure of the Elements, Chapter 5, Publishing House of U.S.S.R. Academic of Science, Moscow, Translated by V. I. Carasso, Academic Press, N. Y., 1963.
18. M. Heh, P. E. Blackburn, D. P. Dingley, and H. L. Johnston, J. Phys. Chem., 59 97 (1955).
19. T. Doerhaerd, P. Goldfinger, and F. Waelbroeck, J. Chem. Phys., 20 757 (1952).
20. P. Goldfinger, Mem. Soc. Roy. Sci. Liege, 15 378 (1955) and F. Waelbroeck, J. Chem. Phys., 20 757 (1952).

21. D. M. Kern, J. Chem. Edu., 33,272 (1956).
22. L. Brewer, J. Chem. Phys., 20 578 (1952).
23. R. J. Thorn and G. H. Winslow, J. Chem. Phys., 23 1369 (1955).
24. K. S. Pitzer and Enrico Clementi, J. Am. Chem. Soc., 81 4477 (1959).
25. R. P. Burns, A. J. Jason, and M. G. Inghram, J. Chem. Phys., 40  
1161 (1964).
26. J. Drowart, Mass Spectrometric Studies of Vaporization of Inorganic  
Substances at High Temperature, in Condensation and Evaporation of  
of Solids, E. Rutner, P. Goldfinger, J. P. Hirth, edited by Gordon  
and Breach, N. Y. and London (1964).
27. W. A. Chupka and M. G. Inghram, J. Chem. Phys., 21 371 (1953); 21  
133 (1953); 22 1472 (1954); J. Phys. Chem., 59 133 (1955).
28. R. E. Honig, J. Chem. Phys.,22 126 (1954).
29. J. Drowart, R. P. Burns, G. DeMaria, and M. G. Inghram, J. Chem.  
Phys., 31 1131 (1959).
30. L. Brewer, J. T. Hicks, and O. H. Krikorian, J. Chem. Phys., 36  
182 (1962).
31. L. Brewer and J. L. Engelke, J. Chem. Phys., 36 992 (1962).
32. P. Goldfinger and M. Jeunehomme, in Advances in Mass Spectrometry,  
page 534, edited by R. M. Waldron, Pergamon Press, N. Y. (1959).
33. W. A. Chupka, J. Berkowitz, D. J. Meschi, and H. A. Tasman, Advances  
in Mass Spectrometry, Vol. 2, page 39, edited by R. M. Elliott,  
Pergamon Press, N. Y. (1963).
34. F. M. Wachi and D. E. Gilmartin, Carbon, 8 141 (1970).
35. W. L. Baun and D. W. Fisher, J. Chem. Phys., 35 1518 (1961).

36. W. L. Baun, F. N. Hodgson, and M. Desjardins, *J. Chem. Phys.*, 38 2787 (1963).
37. E. Doernenburg and H. Hintenberger, *Z. Naturforschg*, 14a 765 (1959);  
E. Doernenburg, H. Hintenberger, J. Frarzen, *Z. Naturforschg*, 16a 532 (1961).
38. R. E. Honig and J. R. Woolston, *Applied Phys. Letters* (Netherland), 2 138 (1963); B. E. Knox, *Mater. Res. B.*, 3 329 (1968).
39. J. Berkowitz and W. A. Chupka, *J. Chem. Phys.* 40 2735 (1964); A. G. Robiette and H. L. Strauss, *J. Chem. Phys.*, 44 2826 (1966); H. L. Strauss, *J. Chem. Phys.*, 46 2473 (1967).
40. E. J. Kohl, O. M. Uy, and K. D. Carlson, *J. Chem. Phys.*, 47 2667 (1967).
41. J. Drowart, G. Demaria, A. J. Boerboom, M. G. Inghram, *J. Chem. Phys.*, 30 308 (1959); A. Kant and B.H. Strauss, *J. Chem. Phys.*, 45 822 (1966).
42. P. Goldfinger, M. Ackerman, and M. Jeunehomme, Final Tech Rep. Contract AF61(052)-19 Jan. 1959; P. Goldfinger and M. Jeunehomme, *Trans. Faraday Soc.*, 59 2851 (1963).
43. J. Berkowitz and W. A. Chupka, *J. Chem. Phys.*, 45 4289 (1966); 40 287 (1964); 39 283 (1963).
44. E. C. Ko, *J. Franklin Inst.*, 217 173 (1934).
45. R. C. Miller and P. Kusch, *Phys. Rev.*, 99 1314 (1955); *J. Chem. Phys.*, 25 860 (1956); 27 281 (1957).
46. M. Eisenstadt, G. M. Rothberg, and P. Kirsch, *J. Chem. Phys.*, 29 797 (1958); V. S. Rao and R. C. Schoonmaker, *J. Chem. Phys.*, 33 1718 (1960).
47. M. H. Boyer, E. Murad, Y. H. Inami, and D. L. Hildenbrand, *Rev. Sci. Instr.*, 39 26 (1968).
48. N. F. Ramsey, Molecular Beams, Oxford University Press, London (1956).

49. O. F. Hagen and A. K. Varma, *Rev. of Sci. Instr.*, 39 47 (1968).
50. C. E. Woodward, Development of a Quadrupole Mass Spectrometer, Ph.D. Thesis, E. E. Department, M. I. T. (1964).
51. V. W. Hughs and H. L. Schultz, (ed.), Methods of Experimental Physics, Vol. 4A, Academic Press, New York (1967).
52. Heat Transfer, M. Jakob, John Wiley, New York, (1957).
53. Thermophysical Properties of High Temperature Solid Materials, Thermophysical Properties Research Center, Purdue University (TPRC), Vol. 1, ed. by Y. S. Touloukian, The MacMillan Company, N. Y. (1967).
54. K. R. Spangenberg, Vacuum Tubes, John Wiley and Sons Co., New York (1948); J. R. Pierce, Theory and Design of Electron Beams, D. Van Nostrand Co., New York, (1949).
55. C. K. Crawford, Particle Optics Laboratory Technical Report #1 (ARML-TR-67-376), Cambridge, Mass. (1967).
56. M. Kamisky, Atomic and Ionic Impact Phenomena on Metal Surfaces, pp. 120, Academic Press, N. Y. (1965).
57. D. Lazarus, Diffusion in Metals, in Solid State Physics, Vol. 10, p. 71, F. Seitz and F. Turnbull (ed), Academic Press, New York (1960); N. L. Patterson, Diffusion in Metals, loc. cit., Vol. 22, p. 409, Academic Press, New York, (1968); P. R. Ghatge, *Phys. Rev.*, 133 A 1167 (1964); R. M. Barrer, Diffusion in and through Solids, Cambridge, University Press (1951).
58. E. F. Greene, *Rev. of Sci. Instrum.*, 32 860 (1961).
59. H. F. Winter et al., *J. Appl. Phys.*, 34 1810 (1963); D. Lichtman and T. R. Kirst, *J. Appl. Phys.*, 34 2323 (1965); M. Kaminsky, Advances in Mass Spectrometry, Vol. 1, p. 125, J. D. Waldron (ed.), Pergamon



Press (1960).

60. H. Z. Sar-El, Rev. Sci. Instr., 38 1210 (1967).
61. V. V. Zashkvara, M. I. Korsunskii, and O. S. Kosmachev, Sov. Phys. Tech.-Phys. (English Transl.), 11 96 (1966).
62. V. V. Zashkvara and V. S. Red'kin, Sov. Phys.-Tech. Phys. (English Transl.), 14 1089 (1970).
63. S. Aksela, M. Karras, M. Pessa, and E. Suoninen, Rev. Sci. Instr., 41 351 (1970).
64. F. R. Paolini and G. C. Theodoridis, Rev. Sci. Instr., 38 579 (1967).
65. H. Hafner, J. A. Simpson, and C. E. Kuyatt, Rev. Sci. Instr., 39 33 (1968).
66. H. Z. Sar-El, Rev. Sci. Instr., 41 561 (1970).
67. P. Kudirka, M.S. Thesis, E. E. Department, M. I. T. (1970).
68. J. A. Simpson and C. E. Kuyatt, Rev. Sci. Instr., 34 265 (1963).
69. C. E. Kuyatt and J. A. Simpson, Rev. Sci. Instr., 38 103 (1967).
70. A. Septier (ed.), Focusing of Charged Particles, Vol. 1, Academic Press, New York (1967).
71. A. P. Banford, The Transport of Charged Particle Beams, E. & F. N. Spon Co., London (1966).
72. S. N. Fonder and B. H. Hall, Phys. Rev., 122 512 (1961).
73. V. Afrosimov, I. P. Gladkovskii, Yu. S. Gordeev, I. F. Kalinkevich, and N. Y. Fedorenko, Soviet Phys. JETP., 5 1378 (1961)
74. D. S. Evans, I.E.E.E. Transactions on Nuclear Science, Feb., 34 (1964).
75. C. N. Burrous, A. J. Lieber, and V. T. Zavianstaff, Rev. Sci. Instr., 38 1477 (1967).

76. H. Greupner, Z. fur Physik, 214 427 (1968).
77. C. Julliot, M. Cantin, R. Ducros, and C. Jehanno, IEEE Trans. on Nucl. Sci., June, 169 (1964); Z. Bay and G. Papp., loc. cit., June, (1964).
78. G. A. Morton and J. A. Mitchell, RCA Rev., 9 632 (1948); T. Jorgensen, Jr., Am. J. Phys., 16 285 (1948); F. J. Lombard and F. Martin, Rev. of Sci. Instr., 32 200 (1961).
79. M. J. Higatsberger, H. L. Demorest, and A. O. Nier, J. of Appl. Phys., 25 883 (1954); E. S. Chambers, Phys. Rev., 133 A1202 (1964); S. C. Brown, Basic Data in Plasma Physics, p. 128, M. I. T. Press, Cambridge, Mass. (1967).
80. W. G. Cady, Piezoelectricity, Vol. 1 and 2, Dover Inc., New York (1964).
81. Instruction Manual for Film Thickness Monitor (series 219), Granville - Phillips Co., Boulder, Colorado 80303 (US..A).
82. S. Chandra and G. D. Scott, Can. J. Phys., 36 1148 (1958).
83. C. Schmidt, Rev. Sci. Instr., 40 1327 (1969).
84. R. F. Pottie, J. Chem. Phys., 44 916 (1966).
85. F. M. Wachi and D. E. Gilmartin, Carbon, 8 141 (1970).
86. G. H. Wannier, Phys. Rev., 90 817 (1953).
87. C. Lanczos, Applied Analysis, Prentice-Hall Inc., Englewood Cliffs, N. J. (1965).
88. M. Cryzinski, Phys. Rev., 115 374 (1959); 138 A305, A322, A336, (1965); Atomic Collision Processes, p. 226, M. R. C. McDowell, (ed.), Proc. of 3rd Intern. Conf. Phys. of Electric and Atomic Collision (1964),

North-Holland Co.

89. R. H. McFarland, Phys. Rev., 139 A40 (1965); J. W. Sheldon and J. V. Dugan Jr., J. Appl. Phys., 36 650 (1965); F. E. Stafford, J. Chem. Phys., 45 859 (1966).
90. W. Lotz, J. Opt. Soc. Am., 38 915 (1968).
91. M. R. H. Rudge, Revs. Mod. Phys., 40 564 (1968).
92. H. S. W. Massey, E. H. S. Burhop, and H. B. Gilbody, Electronic and Ionic Impact Phenomena, Vol. 1, Clarendon Press, Oxford (1969).
93. G. Peach, J. Phys. (B), 1 1088 (1968); 3 328 (1970).
94. G. Peach, Proc. Phys. Soc., 85 709 (1965); 87 375 (1966); 87 381 (1966).
95. M. R. H. Rudge and M. J. Seaton, Proc. Roy. Soc. (London), A283 262 (1965).
96. V. I. Ochkur, Sov. Phys. JETP, (English Transl.), 18 503 (1964).
97. R. K. Peterkop, Sov. Phys. JETP (English Transl.), 14 1377 (1962); Proc. Phys. Soc., 77 1220 (1961); I. H. Sloan, Proc. Phys. Soc., 85 435 (1965).
98. G. Racah, Phys. Rev., 63 367 (1943); B. W. Shore and D. H. Menzel, Principles of Atomic Spectra, John Wiley and Sons, Inc., New York, (1968).
99. N. F. Mott and H. S. W. Massey, The Theory of Atomic Collisions, p. 476, Oxford University Press, Oxford (1965).
100. A. Gaudin and R. Botter, J. Chim Phys., 65 1112 (1968); 65 1118 (1968).
101. W. L. Fite and R. T. Brackmann, Phys. Rev., 112 1141 (1958).
102. H. W. Drawin, Z. Phyk., 164 513 (1961).
103. W. Lotz, Z. Phyk., 216 241 (1968); 206 205 (1967).
104. C. K. Crawford and C. E. Woodward, The Multiple-Crossed-Beam Method

- for Measuring Electron-Ionization Cross Sections, Tech. Rept., 175  
Lab. Insulation Research, M. I. T. (1962).
105. K. L. Wang, M. D. Brody, and C. K. Crawford, Electron Impact  
Ionization Cross Sections, Tech. Rept. AFM.-TR-69-5, Particle Optics  
Lab., M. I. T. (1969).
106. L. H. Rovner and J. H. Norman, J. Chem. Phys., 52 2946 (1970).
107. V. Orlinov, Sov. Phys-Solid Sta. (English Tranl.), 3 880 (1960).
108. J. A. Simpson, Rev. Sci. Instr., 32 1283 (1961).
109. H. Mendlowitz, Rev. Sci. Instr., 29 701 (1958).
110. V. K. Zworykin et al., Electron Optics and the Electron Microscope,  
p. 385, John Wiley and Sons, New York (1945).
111. K. Kanaya, et al., J. Sci. Instr., 43 416 (1966).
112. E. Regenstreif, Annls Radioélect., 6 51-83, 114-55 (1951).
113. D. W. Mason, Plasma Phys., 6 553 (1964).
114. T. R. Walsh, Plasma Phys, 5 17 (1963).
115. N. Anderson and P. P. Eggleton, Int. J. Electronics, 22 497 (1967);  
Rev. Sci. Instr., 38 1524 (1967); N Anderson, P. P. Eggleton, and  
R. G. W. Keesing, ibid, 38 924 (1967).

BIOGRAPHICAL NOTE

Kang-Lung Wang was born in Lukang, Taiwan, China on July 3, 1941. After completion of elementary and secondary schooling he attended Chen Kung University in Taiwan where he received his Bachelor's degree in 1964. From July of 1964 to July of 1965 he served as an electronics officer (2<sup>nd</sup> lieutenant) in the Air Force of the Republic of China.

He came to M.I.T. in September of 1965 and received his Master's degree here in 1966. Since September 1965 he has been employed at M.I.T. as a Research Assistant (September 1965 - June 1967; September 1967 - January 1968; and July 1968 - August 1970), a Teaching Assistant (February 1968 - June 1968), and a DSR Staff Member (June 1967 - September 1967). During his stay at M.I.T. he married Shen-Wei Chien.

He attended the Winter Institute Quantum Theory Project in Gainesville, Florida in January 1970 and is currently a member of the I.E.E.E. and Sigma Xi.

Mr. Wang has accepted an offer for a Research Associateship in the Particle Optics Laboratory at M.I.T. (where most of his thesis work was done) upon receipt of his doctorate.

ED OF FILM

EASE REWIN



